NORTHWESTERN UNIVERSITY

Atom-Probe Tomographic Investigations of a Precipitation-Strengthened HSLA-115 Steel and a Ballistic-Resistant 10 wt. % Ni Steel for Naval Applications

A DISSERTATION

SUBMITTED TO THE GRADUATE SCHOOL

IN PARTIAL FULFILLMENT OF THE REQUIREMENTS

for the degree

DOCTOR OF PHILOSOPHY

Field of Materials Science and Engineering

By

Divya Jain

EVANSTON, ILLINOIS

September 2017

Abstract

High performance structural materials are needed for Naval applications which require an excellent combination of yield strength, low-temperature impact toughness, ductility, ballistic-resistance, and weldability. This research investigates precipitation-strengthened HSLA-115 steels and ballistic-resistant 10 wt. % Ni steels, which have emerged as promising alternatives to the widely used HSLA-100 steels for Naval applications.

HSLA-115 is a Cu-bearing high-strength low-carbon martensitic steel and has been used in the flight deck of the recently built U.S. Navy CVN-78 aircraft carrier. It is typically used in conditions with overaged Cu precipitates, to obtain acceptable impact toughness and ductility at 115 ksi (793 MPa) yield strength. However, overaging of Cu precipitates limits its strength and applications. This research demonstrates that aging at 550 ^{o}C facilitates the co-precipitation of sub-nanometer sized M_2C carbides and Cu precipitates in high number density (~10^{23} m^{-3}) in HSLA-115. 3-D atom-probe tomography (APT) investigation reveals that Cu precipitates form first, followed by the nucleation of M_2C carbides, which are co-located with Cu precipitates and are distributed heterogeneously at lath-boundaries and dislocations, indicating heterogeneous nucleation of M_2C. Carbon redistribution during quenching (following the austenitization) and subsequent aging at 550 ^{o}C is followed using APT. Segregation of C (3-6 at. % C) is observed at martensitic lath-boundaries in the as-quenched and 0.12 h aged conditions. On further aging, C redistributes, forming cementite and M_2C carbides, whose composition and morphology evolves with aging time. Precipitation kinetics of M_2C carbides is intertwined with Cu precipitates;

temporal evolution of Cu precipitates and M_2C carbides is characterized in terms of their mean radii, number densities, and volume fractions and correlated with the bulk mechanical properties.

Precipitation of M_2C carbides offsets the softening due to overaging of Cu precipitates and tempering of the martensitic matrix. This results in an extended yield strength plateau, compared to alloys relying solely on Cu precipitation strengthening (for example, NUCu-140 steels) and is highly beneficial as impact toughness improves significantly in overaged conditions with respect to Cu precipitates. Optimum mechanical properties (yield strength 141 ksi or 972.1 MPa, elongation to failure 24.8 %, and impact toughness 188.0 J at −18 ^{o}C) are attained after 3 h aging at 550 ^{o}C. Incorporating finely dispersed M_2C carbides with Cu precipitates, thus provides a promising pathway for use of Cu-bearing Naval HSLA-115 steels in higher strength applications, while still meting toughness and ductility requirements.

Low-carbon 10 wt. % Ni steels are optimally processed via a multi-step intercritical *Quench Lamellarizing Tempering* (QLT)-treatment to form a fine dispersion of thermally stable Ni-enriched austenite in a tempered martensitic matrix. Deformation-induced martensitic transformation of this austenite is key to its superior overall mechanical properties, specifically ballistic resistance over HSLA-100 steels. This research elucidates the basic physical principles controlling the thermal stability and kinetics of Ni-stabilized austenite, formed during the QLT-treatment. The role of Ni-enriched austenite and fresh martensitic regions, inherited from the first isothermal intercritical step (L) at 650 ^{o}C, in forming thermally stable austenite during the second isothermal intercritical step (T) at 590 ^{o}C is highlighted using dilatometry, synchrotron X-ray diffraction, 3-D atom-probe tomography (APT), and thermodynamic and kinetic modeling using ThermoCalc and Dictra. Results indicate the growth of nm-thick austenite layers during T-step

tempering (predominantly in the Ni-enriched fresh martensitic regions), with austenite retained from L-step acting as a nucleation template. Thermal stability of austenite is estimated by predicting its martensite-start (M_s) temperature, using the approach formulated by Ghosh and Olson. This approach is particularly useful as empirical relations cannot be extrapolated for the highly Ni-enriched austenite investigated in the present study. Co-located and mixed MC/M_2C-type carbides (M is Mo, Cr, V), comprising of a M_2C carbide shell and a MC carbide core are observed after isothermal tempering at both 590 and 650 ^oC. Since MC carbides are inherited from the as-quenched condition, the nucleation of M_2C-type carbides is likely assisted by the MC carbides during tempering at these temperatures.

Local redistribution of C, Ni, and Mn in the single-pass heat-affected-zone (HAZ) microstructures of QLT-treated 10 wt. % Ni steels is investigated using site-specific 3-D APT to assess the thermal stability of austenite (Ni-rich regions) in HAZs. M_s temperature calculations predict that austenite in the HAZs is susceptible to martensitic transformation upon cooling to room temperature, unlike the austenite in the QLT-treated base metal. While C in the QLT-treated base metal is consumed primarily in MC/M_2C-type carbides, its higher concentration in the Ni-rich regions observed in the HAZs indicates the dissolution of carbides, particularly the M_2C carbides. The role of M_2C carbides and austenite stability is discussed in relation to the increase in microhardness in single-pass HAZs relative to the QLT-treated base metal. A better understanding of austenite stability and C redistribution after single-pass weld cycles will assist in designing multiple-weld cycles and Gleeble-weld simulations for these novel 10 wt. % Ni steels.

Acknowledgments

I am extremely grateful to my thesis advisor, Professor David N. Seidman, for his guidance, support, and encouragement throughout my research. Your enthusiasm, knowledge, and positive attitude is inspiring and uplifting. Your trust and calmness helped me face challenges during my research. Your constructive feedback regarding my writing and presentation style helped me improve on those skills.

Prof. Dieter Isheim, thank you for teaching me fundamentals of atom-probe tomography (APT), associated sample preparation, and data analysis. I always found you approachable to ask queries and take suggestions during my research. I learnt a lot from the excellent discussions with you and your constructive criticism improved my writing and data analyzing skills.

I would like to thank Prof. David Dunand, Prof. John N. DuPont, and Prof. Greg Olson for willing to serve on my thesis committee. Prof. Dunand, your constructive criticism during my qualifier helped me improve my presentation skills. Prof. DuPont, our collaborations on welding studies helped me learn about the complexity of the welding processes and associated phase transformations. Thank you for your guidance on these projects. Prof. Olson, your research work is an outstanding source of knowledge about the metallurgy of steels and in particularly, martensitic transformations. Materials Design course taught by you was a great learning experience.

I would like to thank all those individuals who helped me with my research:

- Dr. Sung-Il Baik for his help with Focused Ion Beam Microscopy and APT
- Dr. Denis T. Keane for his help with synchrotron X-ray diffraction (XRD) at the Advanced

Photon Source (APS) at Argonne National Laboratory

- Prof. Gautam Ghosh for his help with martensite-start temperature calculations and providing the kMART thermodynamic database
- Mr. Mark Seniw for his help with tensile and Charpy impact testing
- Dr. Carla Shute for her help with metallography
- Mr. Ben Myers and Mr. Eric Miller for their help with Scanning Electron Microscopy (SEM) and Focused Ion Beam Microscopy
- Allen Hunter, Liza Plotnikov, Peter Bocchini, and Daniel Sauza to help me get acclimatized with a foreign environment. All other Seidman group members, past and present

To my parents, Dr. Rajendra Jain and Dr. Shobha Jain, I feel extremely blessed to be your son. Your love, encouragement, and support is the primary reason for all my accomplishments. You both have been a constant source of inspiration and strength in my life. To my brother, Kunal, I love you very much and wish that we can spend more time together. My childhood was filled with fun and happiness because of you and I will always cherish those memories. To Sadhana aunty, I feel blessed to have received your unconditional love throughout my life. I have had great memories with you and Amitabh Uncle, who I always remember with fondness and for his charming personality. To my friends, your friendship and time spent together has given me some of the best memories that I will cherish for my entire life. Arindam and Bharath, thank you for your friendship and for being there for me all these years of my graduate study. Shireesh, I feel blessed to have been friends with you since childhood. Amit, Nitesh, Abhay, Rohit, Ayush,

Arunoday, Ashish, I have had great times with you all on the cricket field. Ankush, Nitish, Achal, Gaurav, Himanshu, thank you for your friendship and great times at IIT Kanpur.

I would like to acknowledge financial support for this research by the Office of Naval Research (ONR), through Grants N00014-12-1-0475 and N00014-12-1-0425 and useful discussions with the program manager, Dr. William Mullins. Atom-probe tomographic measurements were performed at the Northwestern University Center for Atom-Probe Tomography (NUCAPT). The LEAP tomograph at NUCAPT was purchased and upgraded with funding from NSF-MRI (DMR-0420532) and ONR-DURIP (N00014-0400798, N00014-0610539, N00014-0910781) grants. Instrumentation at NUCAPT was supported by the Initiative for Sustainability and Energy at Northwestern University (ISEN). This research made use of Northwestern's NUANCE-EPIC and OMM facilities. NUCAPT, EPIC and OMM received support from the MRSEC program (NSF DMR-1121262) through Northwestern's Materials Research Center. NUCAPT and NUANCE received support from the Soft and Hybrid Nanotechnology Experimental (SHyNE) Resource (NSF NNCI-1542205). NUANCE received support from the International Institute for Nanotechnology (IIN); the Keck Foundation; and the State of Illinois, through the IIN. X-ray diffraction experiments were performed at the DuPont-Northwestern-Dow Collaborative Access Team (DND-CAT) Synchrotron Research Center located at Sector 5 of the Advanced Photon Source (APS).

Table of Contents

List of Figures

Figure 3.8- 3-D APT reconstruction of 0.25 h HSLA-115 specimen at 823 K (550 ^{o}C). Copper precipitates and M_2C carbides are delineated by 10 at.% Cu isoconcentration- (red) and by 5 at.% (C + Cr + Mo) isoconcentration-surfaces (dark-green), respectively. Iron atoms are displayed in blue: only a small fraction is shown for clarity. A coarse cementite precipitate is delineated by a 5 at.% C isoconcentration-surface (black). To the extreme left, the distribution of carbon atoms (black), in and around the cementite particle is displayed.

Figure 3.9- 3-D APT reconstructions of 3 h HSLA-115 specimen at 823 K (550 ^{o}C) C, (a) Nanotip 1; (b) Nanotip 2. Copper precipitates and M_2C carbides are delineated by 10 at.% Cu isoconcentration- (red) and by 5 at.% (C + Cr + Mo) isoconcentration-surfaces (dark-green), respectively. Iron atoms are shown in blue: only a small fraction is shown for clarity.

Figure 3.10- 3-D APT reconstructions of 16 h HSLA-115 specimen at 823 K (550 ^{o}C), (a) Nanotip 1; (b) Nanotip 2. Copper precipitates and M_2C carbides are delineated by 10 at.% Cu isoconcentration- (red) and by 5 at.% (C + Cr + Mo) isoconcentration-surfaces (dark-green), respectively. Iron atoms are displayed in blue: only a small fraction is shown for clarity.

Figure 3.11- Proxigram concentration profiles (at.%) of C, Cr, Mo and Cu obtained from 5 at.% (C + Cr + Mo) isoconcentration-surfaces, which are used to delineate the M_2C carbides in HSLA-115 samples aged at 823 K (550 ^{o}C) for: (a) 1 h; (b) 3 h; (c) 16 h; and (d) 64 h. The Fe concentration profile is displayed in 11(d). Fiducial marker is placed vertically at the zero of the proxigrams, which is chosen as the inflection point of the Fe-concentration profile.

Figure 3.12- Evolution of the number density of Cu precipitates, $N_v(t)$, with aging time for HSLA-115 and NUCu-140 at 823 K (550 ^{o}C). The APT experiments for NUCu-140 steel for aging times < 3 h are from Hunter's PhD Thesis [42].

Figure 4.1- Yield Strength (YS) at room temperature and Charpy impact energy at 255 K (-17.8 ^{o}C) for HSLA-115 in the as-quenched condition and after aging at 823 K (550 ^{o}C) for 0.25, 3, and 16 h.

Figure 4.2- Synchrotron X-ray diffraction scans of the as-quenched HSLA-115 sample and those aged at 823 K (550 ^{o}C) for 0.25, 3, and 16 h. The subscripts, θ_{cem} and NbC on the reflection indices in (a) refer to niobium carbide and cementite respectively, while the subscripts, γ and α in (b) refer to austenite and ferrite respectively.

Figure 4.3- 3-D APT reconstruction of the as-quenched HSLA-115 sample. C-enriched regions are delineated by 1 at. % C isoconcentration surfaces (black). Niobium carbonitride precipitates

are delineated by 15 at. % (Nb + C) isoconcentration surfaces (brown). Only a fraction of the Fe atoms is displayed (blue dots) and the other alloying element atoms are omitted for the sake of clarity.

Figure 4.4- Proximity histogram concentration profiles (at. %) of Fe, C, Ni, Cu, Mn, Cr, Si, and Mo for C-enriched regions-1, 2, and 3 in Figure 4.3 and their vicinity are displayed in (a), (b), and (c) respectively. These C-enriched regions are delineated by 1 at. % C isoconcentration surfaces in Figure 3, which is the 3-D APT reconstruction of the as-quenched HSLA-115 sample. Ordinate axis of the plots displaying C, Ni, and Cu concentration profiles is drawn on a log-scale for clear visualization of the C concentrations in α-Fe matrix in vicinity of C-enriched regions.

Figure 4.5- (a) 3-D APT reconstruction (two orthogonal views) of the HSLA-115 sample aged at 823 K (550^{o}C) for 0.12 h. Carbon atoms are displayed as black dots, Cu precipitates are delineated by 7 at. % Cu isoconcentration surfaces (red) and the other alloying element atoms are omitted for the sake of clarity; (b) Proximity histogram concentration profiles (at. %) of Fe, C, Ni, Cu, Mn, Cr, Si, and Mo for C-enriched region in (a) and its vicinity (excluding the Cu precipitates, which were removed from the dataset before the proxigram analysis using the IVAS program).

Figure 4.6- (a) Atom-probe tomographic mass spectrum of the niobium carbonitride precipitate, observed in the as-quenched HSLA-115 sample and is indicated by an arrow in Figure 4.3. Mass peaks associated with Nb, C, and N are labelled in the mass spectrum, while those of other minor elements in the precipitate, such as Fe, Mo, Cr, and V are not labelled for the sake of clarity; (b) Proximity histogram concentration profiles (at. %) of Fe, Nb, C, and N for the niobium carbonitride precipitate and its vicinity. A fiducial marker is placed vertically at the origin (0) of the proxigram, which is chosen as the inflection point of the Fe-concentration profile.

Figure 4.7- (a) 3-D APT reconstruction of the HSLA-115 sample aged at 823 K (550^{o}C) for 0.25 h. The cementite precipitate is delineated by a 5 at. % C isoconcentration surface (black). Copper precipitates and M_2C carbides are delineated by 10 at. % Cu isoconcentration surfaces (red) and 5 at. % (C + Cr + Mo) isoconcentration surfaces (dark-green) respectively. Only a fraction of the Fe atoms is shown (blue dots) and the other alloying element atoms are omitted for the sake of clarity; (b) Proximity histogram concentration profiles (at. %) of Fe, C, Mn, Cr, Mo, and Si for the cementite precipitate and its vicinity. A fiducial marker is placed vertically at the origin (0) of the proxigram, which is chosen as the inflection point of the Fe-concentration profile.

Figure 4.8- Atom-probe tomographic mass spectrum of the cementite precipitate observed in the HSLA-115 sample aged at 823 K (550^{o}C) for 0.25 h.

Figure 4.9- 3-D APT reconstructions of HSLA-115 samples aged at 823 K (550 ^{o}C) for: (a) 0.12 h; (b) 0.25 h; (c) 3 h; (d) 16 h (nanotip 1); (e) 16 h (nanotip 2); (f) 64 h; (g) 256 h (nanotip 1); and (h) 256 h (nanotip 2). Only a fraction of the Fe atoms is shown (blue dots) and the other alloying element atoms are omitted for the sake of clarity. Copper precipitates are delineated by 10 at. % Cu isoconcentration surfaces (red). M_2C carbides are delineated by 5 at. % (C + Cr + Mo) isoconcentration surfaces (dark-green) in all reconstructions except in (e), where 7 at. % (C + Cr + Mo) isoconcentration surfaces are used to delineate M_2C carbides.

Figure 4.10- Proximity histogram concentration profiles (at. %) of C, Mo, and Cr for the ten largest M_2C carbide precipitates and their vicinity in HSLA-115 samples aged at 823 K (550 ^{o}C) for: (a) 0.25; (b) 1; (c) 3; and (d) 16 h (nanotip 1).

Figure 4.11- Proximity histogram concentration profiles (at. %) of Fe, Mo, C, and Cr for: (a) M_2C carbide (indicated by an arrow in Figure 4.9(e)) and its vicinity; (b) M_2C carbide (indicated by an arrow in Figure 4.9(f)) and its vicinity. Figure 4.9(e and f) are the 3-D APT reconstructions of HSLA-115 samples aged at 823 K (550 ^{o}C) for 16 and 64 h respectively. A fiducial marker is placed vertically at the origin (0) of the proximity histograms, which is chosen as the inflection point of the Fe-concentration profile.

Figure 4.12- Atom-probe tomographic mass spectrum of the M_2C carbide precipitate observed in the HSLA-115 sample aged at 823 K (550 ^{o}C) for 64 h, which is indicated by an arrow in Figure 4.9(f). It is noted that the abscissa scale chosen is not linear to enlarge portions of the mass spectrum for clarity.

Figure 4.13- Atomic ratios, (Mo + Cr)/C and Mo/Cr for the ten largest M_2C carbides and their vicinity in HSLA-115 samples aged at 823 K (550 ^{o}C) for: (a) 0.25 h; (b) 1 h; (c) 3 h; and (d) 16 h (nanotip 1). The portions of the diagrams on the right-hand side of the vertical fiducial markers in these plots represent the core of the M_2C carbide precipitates with nearly constant (Mo + Cr)/C values.

Figure 4.14- Temporal evolution of atomic ratios: (a) (Mo + Cr)/C; and (b) Mo/Cr in the M_2C carbide precipitates for HSLA-115 aged at 823 K (550 ^{o}C). For aging times of 1, 3, and 16 h, these values are the mean values obtained from the analysis of the two APT nanotips for each of these aging times. Coarser blocky carbide precipitates observed to the bottom right in Figure 4.9(d) and the one indicated by an arrow in Figure 4.9(e) have been excluded from this analysis to obtain a clearer analysis of the smaller carbide precipitates and to distinguish precipitates at different stages of their growth.

Figure 5.1- SEM micrographs of: (a) QL; (b) QT; and (c) QLT-treated 10 wt. % Ni steel etched with a 2% Nital solution.

Figure 5.2- Dilatometric responses of the 10 wt. % Ni steel (in blue) exhibiting austenite formation during intercritical isothermal steps at 923 K (650 ^{o}C) and 863 K (590 ^{o}C). Some of the austenite transforms to martensite during quenching, after isothermal aging at 923 K (650 ^{o}C). This transformation commences at 461 K (188 ^{o}C), the martensite-start (M_s) temperature. Dilatometry performed by Dr. Zhang, NSWCCD.

Figure 5.3- Synchrotron X-ray diffraction scans of the 10 wt. % Ni steel after different stages of the QLT-treatment, including the QLT-treated sample that was subsequently quenched to 188.7 K (-84.4 ^{o}C), prior to the X-ray diffraction analysis. The NIST standard sample is also analysed for calibration purposes.

Figure 5.4- 3-D APT reconstructions of the QL-treated 10 wt. % Ni steel: (a) QL-1 sample, Fe atoms (10 %) are displayed as blue dots, Ni atoms (100%) are displayed in green; (b) QL-2 sample, Fe atoms (3 %) are displayed as blue dots, Ni atoms (30%) are displayed in green. The heterophase interface (indicated by a dashed curve) between the tempered martensite matrix, α-Fe, and the Ni-rich region is delineated by 9 and 11 at. % Ni isoconcentration surfaces in (a) and (b), respectively. Metal carbides are delineated by a 10 at. % (C plus Cr plus Mo plus V) isoconcentration surfaces (black) in both reconstructions.

Figure 5.5- Proximity histogram concentration profiles obtained from 9 and 11 at. % Ni isoconcentration surfaces in: (a) QL-1; and (b) QL-2 10 wt. % Ni steel samples, respectively, displaying the concentration profiles of Fe, Ni, Mn, Cr, Mo, Si, C, Cu, and V across the α-Fe matrix and Ni-rich region. Metal carbides were excluded from the datasets before obtaining the proximity histograms.

Figure 5.6- 3-D APT reconstructions of the QLT-treated 10 wt. % Ni steel: (a) QLT-1 sample, Fe atoms (10 %) are displayed as blue dots, Ni atoms (80%) are displayed in green; (b) QLT-2 sample, Fe atoms (5 %) are displayed as blue dots, Ni atoms (50%) are displayed in green. The heterophase interface (indicated by a dashed curve) between the tempered martensite matrix, α-Fe, and the Ni-rich region is delineated by 11 at. % Ni isoconcentration surface in both (a) and (b). Metal carbides are delineated by a 10 at. % (C plus Cr plus Mo plus V) isoconcentration surfaces (black) in both reconstructions.

Figure 5.7- Proximity histogram concentration profiles obtained from 11 at. % Ni isoconcentration surfaces in: (a) QLT-1; and (b) QLT-2 10 wt. % Ni steel samples, displaying the concentration

profiles of Fe, Ni, Mn, Cr, Mo, Si, C, Cu, and V across the α-Fe matrix and Ni-rich region. Metal carbides were excluded from the dataset before obtaining the proximity histograms. Shaded regions on the Ni-rich side in (a) and (b) represent the composition of austenite formed during the T-step tempering at 863 K (590 ^{o}C).

Figure 5.8- Linear concentration profiles of Mo, C, V, Cr, and Ni across the tempered martensite (α-Fe), Ni-rich region (austenite), and an M_2C-type carbide precipitate in the QL-2 10 wt. % Ni steel sample exhibiting strong partitioning of C and Ni toward and away from the carbide phase, respectively.

Figure 5.9- DICTRA simulations during T-step tempering at 863 K (590 ^{o}C) displaying a Ni concentration profile after: (a) 0 s; (b) 1 h; and (c) 100 h. A DICTRA simulation after 1 h in (b) indicates that austenite grows predominantly into the fresh-martensitic region.

Figure 5.10- Dilatometric responses of the 10 wt. % Ni steel (in blue) for, (a) optimal QLT-treatment involving a quench to room temperature following the L-step (isothermal heating at 923 K (650 ^{o}C)). Some of the austenite transforms to martensite during quenching; this transformation commences at 461 K (188 ^{o}C), the martensite-start (Ms) temperature; (b) QLT-treatment without the quench to room temperature after the L-step. No austenite formation occurs during the T-step (isothermal heating at 863 K (590 ^{o}C)). Dilatometry performed by Dr. Zhang, NSWCCD.

Figure 5.11- DICTRA simulations during T-step tempering at 863 K (590 ^{o}C) displaying a Ni concentration profile after: (a) 0 s; (b) 1 h; and (c) Ni concentration profile obtained from an APT investigation of the QLT-treated 10 wt. % Ni steel (QLT-2 sample, Figure 5.7(b)). Nickel concentration profiles obtained from both APT and DICTRA simulations indicate the formation of nanolayers of austenite with a higher Ni concentration on top of the retained austenite from the L-step containing lower Ni concentration.

Figure 6.1- SEM micrograph of the QLT-treated 10 wt. % Ni steel-1 (base metal). Brighter appearing phase, dispersed in the matrix is the Ni-rich constituent, consisting of austenite and martensite, with the latter formed during the quenching following the L-step [6, 225]

Figure 6.2- SEM micrographs of QLT-treated 10 wt. % Ni steel-1, (a) Base Metal (BM); (b) HAZ-1 region; (c) HAZ-2 region. The relative positions of HAZ-1 and HAZ-2 regions with respect to BM are indicated in Figure 3, with HAZ-2 region lying in closer proximity to the fusion zone.

Figure 6.3- Microhardness trace across the autogenous Gas Tungsten Arc Weld (GTAW) of QLT-treated 10 wt. % Ni steel-1, provided by Erin Barrick, Lehigh University.

Figure 6.4- (a) 3-D APT reconstruction of the QLT-treated 10 wt. % Ni steel-2. Fe (5 %) and Ni (50%) atoms are displayed in blue and green respectively. The heterophase interface between the tempered martensite matrix, α-Fe, and the Ni-rich region is delineated by 11 at. % Ni isoconcentration surface (shown schematically by a dashed curve). Metal carbides are delineated by 10 at. % (C plus Mo plus Cr plus V) isoconcentration surfaces (black); (b) Proximity histogram concentration profiles of Fe, Ni, Mn, and C across the α-Fe matrix and the Ni-rich region. Shaded regions on the Ni-rich side represent the composition of austenite formed during the T-step tempering at 863 K (590 ^{o}C).

Figure 6.5- 3-D APT reconstructions of QLT-treated 10 wt. % Ni steel-1, (a) Base Metal (BM), Fe (20 %) and Ni (100%) atoms are displayed in blue and green respectively; (b) HAZ-1 (nanotip-1), Fe (10 %) and Ni (80%) atoms are displayed in blue and green respectively, metal carbides are delineated by 10 at. % (C plus Mo plus Cr plus V) isoconcentration surfaces (black); (c) HAZ-2 (nanotip-1), Fe (20 %) and Ni (100%) atoms are displayed in blue and green respectively. The heterophase interface between the tempered martensite matrix, α-Fe, and the Ni-rich region is delineated by 13, 11, and 11 at. % Ni isoconcentration surfaces in a, b, and c respectively (shown schematically by dashed curves).

Figure 6.6- Proximity histogram concentration profiles of Fe, Ni, Mn, and C across the α-Fe matrix and the Ni-rich region for the QLT-treated 10 wt. % Ni steel-1, (a) Base metal (BM); (b) HAZ-1 (nanotip-1); (c) HAZ-2 (nanotip-1).

Figure 6.7- 3-D APT reconstructions of QLT-treated 10 wt. % Ni steel-1, (a1) HAZ-1 (nanotip-2), Fe (10 %) and Ni atoms (80 %) are displayed in blue and green respectively, metal carbides are delineated by 10 at. % (C plus Mo plus Cr plus V) isoconcentration surfaces (black); (b1) HAZ-2 (nanotip-2), Fe (15 %) and Ni atoms (100 %) are displayed in blue and green respectively. The heterophase interface between the tempered martensite matrix, α-Fe, and the Ni-rich region is identified by 9 and 12 at. % Ni isoconcentration surfaces in (a1) and (b1) respectively (shown schematically by dashed curves). Proximity histogram concentration profiles of Fe, Ni, Mn, and C across the α-Fe matrix and the Ni-rich region for, (a2) HAZ-1 (nanotip-2); (b2) HAZ-2 (nanotip-2).

Figure 6.8- (a) 3-D APT reconstruction of the as-quenched 10 wt. % Ni steel-2. Fe atoms (0.2 %) are displayed in blue and MC-type carbides are delineated by 7 at. % (C plus Mo plus V) isoconcentration surfaces (dark-red); (b) Magnified view of the encircled region in (a); (c) Proxigram concentration profiles of C, Mo, V, and Cr across the α-Fe matrix and MC carbides.

Figure 6.9- 3-D APT reconstructions of quenched and isothermally tempered 10 wt. % Ni steel samples at, (a) 811 K (538 ^{o}C) for 1 h; (b) 863 K (590 ^{o}C) for 1 h; (c) 923 K (650 ^{o}C) for 0.5 h; (d) 923 K (650 ^{o}C) for 0.5 h and 863 K (590 ^{o}C) for 1 h. Fe atoms are displayed in blue (only a fraction is shown for clarity). Metal carbides are delineated by 10 at. % (C plus Mo plus Cr plus V) isoconcentration surfaces (black). It is noted that all samples are from steel-2, except (a), which is obtained from a 10 wt. % Ni steel, whose overall composition is 0.07C-10.31Ni-1.12Mo-0.07V-0.61Mn-0.60Cr-0.22Si (wt. %).

Figure 6.10- (a) Distribution of V (dark-red), C (black), and Fe (blue) atoms in a mixed MC/M_2C-type carbide, observed in the 10 wt. % Ni QLT-treated steel-2 sample; (b) Linear concentration profiles of Fe, C, Mo, V, and Cr, obtained from the selected region of interest, in the direction of the arrow in (a). These profiles reveal the mixed nature of the carbide, consisting of M_2C carbide in the outer shell and MC carbide in the inner core.

Figure 6.11- 3-D APT reconstructions of QLT-treated 10 wt. % Ni steel, (a) base metal (steel-2): (a1) nanotip-1, (a2) nanotip-2; (b) HAZ-1 (steel-1): (b1) nanotip-1, (b2) nanotip-2; (c) HAZ-2 (steel-1): (c1) nanotip-1, (c2) nanotip-2. Fe atoms are displayed in blue (only a fraction is shown for clarity) and metal carbides are delineated by 10 at. % (C plus Mo plus Cr plus V) isoconcentration surfaces (black).

List of Tables

Table 5.3- Volume percent of austenite in 10 wt. % Ni steel samples after different stages of the QLT-treatment, as obtained by synchrotron X-ray diffraction (XRD) experiments performed at the Advanced Photon Source at Argonne National Laboratory.

Table 5.4- Chemical compositions (at. %) of Ni-rich region (austenite formed during L-step at 923 K (650 ^{o}C)) and the tempered martensite matrix, α-Fe in the QL-treated 10 wt. % Ni steel, as measured by APT. Martensite-start (M_s) temperatures, as calculated using the Ghosh-Olson thermodynamic and kinetic approach are also shown. Compositions of austenite and α-Fe, obtained from equilibrium thermodynamic calculations at 923 K (650 ^{o}C) using ThermoCalc are also listed.

Table 5.5- Chemical compositions (at. %) of Ni-rich regions (austenite formed during T-step at 863 K (590 ^{o}C) and retained austenite from L-step at 923 K (650 ^{o}C)) and the tempered martensite matrix, α-Fe in the QLT-treated 10 wt. % Ni steel samples, as measured by APT. Martensite-start (M_s) temperatures, as calculated using the Ghosh-Olson thermodynamic and kinetic approach are also shown. Compositions of austenite and α-Fe, obtained from equilibrium thermodynamic calculations at 863 K (590 ^{o}C) using ThermoCalc are also listed.

Table 5.6- Comparison of M_s temperature predictions for austenite obtained after the T-step at 863 K (590 ^{o}C) in the QLT-treated 10 wt. % Ni steel samples using the Ghosh-Olson approach and empirical relations.

Table 6.1. Chemical compositions of 10 wt. % Ni steels (steel-1 and steel-2), as measured from optical emission spectroscopy.

Table 6.2. Compositions (at. %) of Ni-rich regions and tempered martensite, α-Fe for QLT-treated base metal for steel-1 and steel-2.

Table 6.3. M_s temperature calculations for the Ni-rich regions observed from APT, using the Ghosh-Olson approach [205-207].

Chapter 1

Introduction

High performance structural materials are needed for U. S. Naval applications, such as ship hulls and decks, which require an excellent combination of yield strength, low-temperature impact toughness, ductility, blast and fragment (ballistic)-resistance, and weldability [1-6]. In recent years, HSLA-115 steels and 10 wt. % Ni steels have emerged as promising alternatives to the widely used HSLA-100 steels for Naval applications.

1.1 Precipitation-Strengthened HSLA-115 steel

HSLA-115 is a newly developed high-strength low-alloy structural steel derived from martensitic Cu-bearing HSLA-100 [2] and has been used in the flight deck of the CVN-78 aircraft carrier [7]. To meet the strength requirements, HSLA-100 and HSLA-115 steels utilize precipitation-strengthening from Cu precipitates [8-10] and are typically used in conditions with overaged Cu precipitates, to obtain acceptable impact toughness and ductility. However, rapid decrease in strength occurs in the overaged microstructure with respect to Cu precipitates, which limits their applications [11-13].

Mo and Cr in HSLA-115 steels can potentially be utilized to form stable alloy carbides, such as M_2C (M = Mo, Cr, Fe) carbides, when the steel is tempered in a suitable temperature range of approximately 773-873 K (500-600 ^oC) [14]. Fine dispersions of these carbides are known to provide secondary hardening in tempered martensitic steels and are also considered beneficial for impact toughness as their precipitation can result in the dissolution of the brittle coarse cementite

phase [14, 15]. Suitable aging temperatures to utilize Cu precipitation strengthening range from 723 to 923 K (450 to 650 ^{o}C) [12, 16, 17] and thus it seems possible to co-precipitate M_2C carbides and Cu precipitates in HSLA-115, as had been observed for a BA-160 steel [18] and a ultrahigh-strength carburized steel [19]. 3-D atom-probe tomography (APT) with its sub-nanometric scale resolution and excellent mass resolving power is a unique instrument to investigate microstructures in such precipitation-hardened alloys [20-23]. This research explores the possibility of co-precipitating M_2C carbides with Cu precipitates in HSLA-115 and investigates its effects on the bulk-mechanical properties of HSLA-115 and on the evolution of Cu precipitates. A fundamental understanding of the various precipitating processes in correlation with the bulk-mechanical properties will help in optimizing the processing of these steels and in exploring their potential for U.S. Naval systems and other structural applications.

1.2 Ballistic Resistant 10 wt. % Ni steel

In addition to increasing the yield strength, there is also a great need to develop steels with superior ballistic protection for Naval structural applications to limit damages caused by terrorist activities. Deformation due to the impact of high velocity fragments can cause shear localization, which then leads to plastic shear instability and flow localization within thin adiabatic shear bands [24-26]. This results in the shear plugging failure, in which material ahead of the projectile is ejected as one solid piece with little energy absorption [25-27]. There are two mechanisms that have been proposed that can cause shear localization during high strain rate deformation. First is the thermal softening due to temperature rise associated with plastic deformation under adiabatic conditions, which can override strengthening from increased strain rates [25, 28]. The other mechanism, proposed by Cowie et al.[29] attributes microvoid softening to shear instability in which void

nucleation rather than void growth acts as a destabilizing event. To delay the onset of shear instability and thus enhance ballistic (fragment penetration) resistance, the phenomena of TRIP (transformation-induced plasticity) can be utilized. TRIP is known to stabilize the plastic flow behavior via mechanically-assisted transformation of austenite to martensite [30-32]. In recent years, several research efforts have been performed to develop steels for the Navy that utilize TRIP effect to optimize performance in both tensile and shear stress states and increase blast and fragment resistance. These can broadly be categorized into two classes of steels: fully austenitic TRIP steels [5, 33, 34] and TRIP-assisted martensitic steels containing dispersed austenite [6, 35]. Low-carbon (<0.1 wt. % C) 10 wt. % Ni-Cr-Mo-V martensitic steels (referred to as '10 wt. % Ni steels' herein), investigated in the present research belongs to the class of TRIP-assisted martensitic steels. These have emerged as promising alternatives to HSLA-100 steels with increase of over 15 % in both yield strength and 20 mm fragment simulation projectile ballistic limit V_{50} [6].

Optimal heat treatment for 10 wt. % Ni steels is a multistep intercritical treatment, referred to as the *Quench-Lamellarizing-Tempering* (QLT)-treatment, and produces fine and dense dispersion of thermally stable austenite in a tempered martensite matrix.[6] Austenite reversion and its thermal stability attained during the QLT-treatment is key to its superior overall mechanical properties, especially its ballistic (fragment penetration) resistance [6]. This research focuses on understanding austenite formation during the QLT-treatment using dilatometry, synchrotron X-ray diffraction, 3-D atom-probe tomography (APT), and thermodynamic and kinetic modeling using ThermoCalc and Dictra. A basic physical understanding of the thermal stability of austenite and kinetics of its formation during the QLT-treatment will provide basis for computational design of these steels for further optimization and for exploring their potential in other applications. The

implementation of 10 wt. % Ni steel for Naval applications will depend on the ease of its weldability. Critical to the thermal stability of austenite is its composition, which can be severely affected in the weld heat-affected-zones (HAZs). Austenite stability and carbon redistribution after single-pass weld cycle in the HAZs is investigated by site-specific APT, which will assist in designing *Gleeble* weld simulations and multiple weld-cycles for these novel 10 wt. % Ni steels.

1.3 Present Thesis Structure

The thesis is divided into the following chapters:

- Chapter 2 provides relevant background on HSLA-115 steels and 10 wt. % Ni steels.
- Chapter 3 demonstrates that aging at 550 ^{o}C facilitates the co-precipitation of Cu precipitates and M_2C carbides in HSLA-115 and describes its effects on mechanical properties.
- Chapter 4 provides a comprehensive compositional analysis of carbon redistribution and associated carbide precipitation during isothermal aging of HSLA-115 at 550 ^{o}C.
- Chapter 5 describes the basic physical principles behind the thermal stability and kinetics of austenite formation during the multi-step QLT-treatment for 10 wt. % Ni steels.
- Chapter 6 describes the local redistribution of C, Ni, and Mn in the single-pass weld heat-affected-zones (HAZs) of the 10 wt. % Ni steels and its implications on thermal stability of austenite in HAZs. MC and M_2C-type carbides in 10 wt. % Ni steels are characterized by APT.
- Chapter 7 provides suggestions for future work.

Chapter 2

Background

2.1 HSLA-100 and HSLA-115 steels

More than two decades ago, the U.S. Navy replaced the higher C steels (0.14-0.20 wt.% C), designated as High Yield Strength steels (HY-80 and HY-100) by lower C concentration (<0.06 wt.% C) steels: specifically, High Strength Low Alloy steels (HSLA-80 and HSLA-100) [1, 11]. The numerals 80 and 100 designate the minimum obtainable tensile yield strength (YS) in ksi (1 ksi = 6.9 MPa). Carbon concentration was reduced in HSLA steels to decrease the susceptibility of the heat-affected-zone in welds to hydrogen cracking, simplifying welding procedures as is indicated by the Graville diagram [36]. Enhanced weldability reduces the preheating requirements and consequently the processing cost [37]. To compensate for the lower C concentration, Cu additions were done to HSLA-steels to utilize precipitation strengthening and meet the strength requirements [8-10]. Figure 2.1 shows the limited solubility of Cu in α-Fe [38, 39].

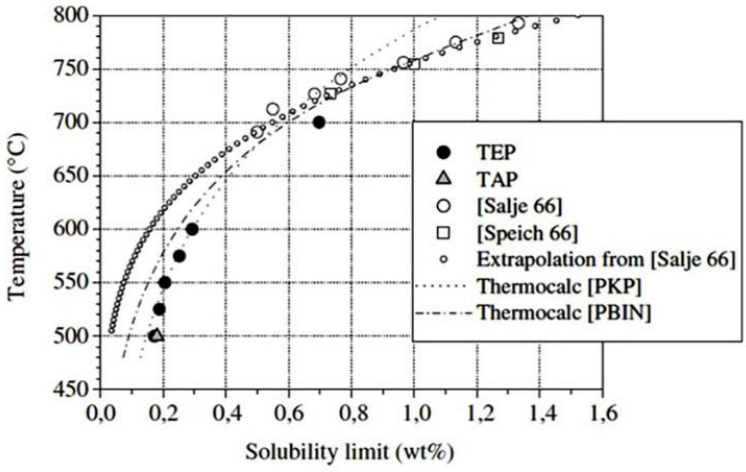

Figure 2.1- Solubility limit of Cu in α-Fe, deduced from thermoelectric power (TEP) and tomographic atom probe (TAP) measurements [39].

Niobium was added in small amounts as it forms stable carbonitride precipitates, Nb(C,N), during the solutionizing and hot-rolling treatments. These precipitates impede austenite grain growth during austenitization at high temperatures, and thus refine grain size, benefitting both strength and toughness [40-42]. Since the approval of HSLA-100 for surface combatant ships in 1989, efforts were made by the U.S. Navy to develop steels with similar compositions as HSLA-100 but with higher yield strength, while maintaining desirable impact toughness and weldability. These efforts led to the development of an HSLA-115 steel, whose composition is slightly richer in Cu, Ni, and Mo than HSLA-100 (composition-2) [2]. HSLA-115 was approved for plate production in 2009 [2] and has been used in the flight deck of the CVN-78 aircraft carrier [7].

Traditionally, commercial processing practices of HSLA-100 steels have employed an austenitizing, water-quenching and an aging treatment at temperatures exceeding 873 K (600 ^{o}C) to obtain desirable impact toughness, Figure 2.2 [8, 11, 12]. The microstructure thus produced consists of overaged Cu precipitates in a tempered martensite matrix. However, the overaging of Cu precipitates results in rapid decrease in strength (see Figure 2.2), which limits the applications of these steels [11-13]. A more detailed description of the development of the Naval HSLA-100 steels can be found elsewhere [1, 4].

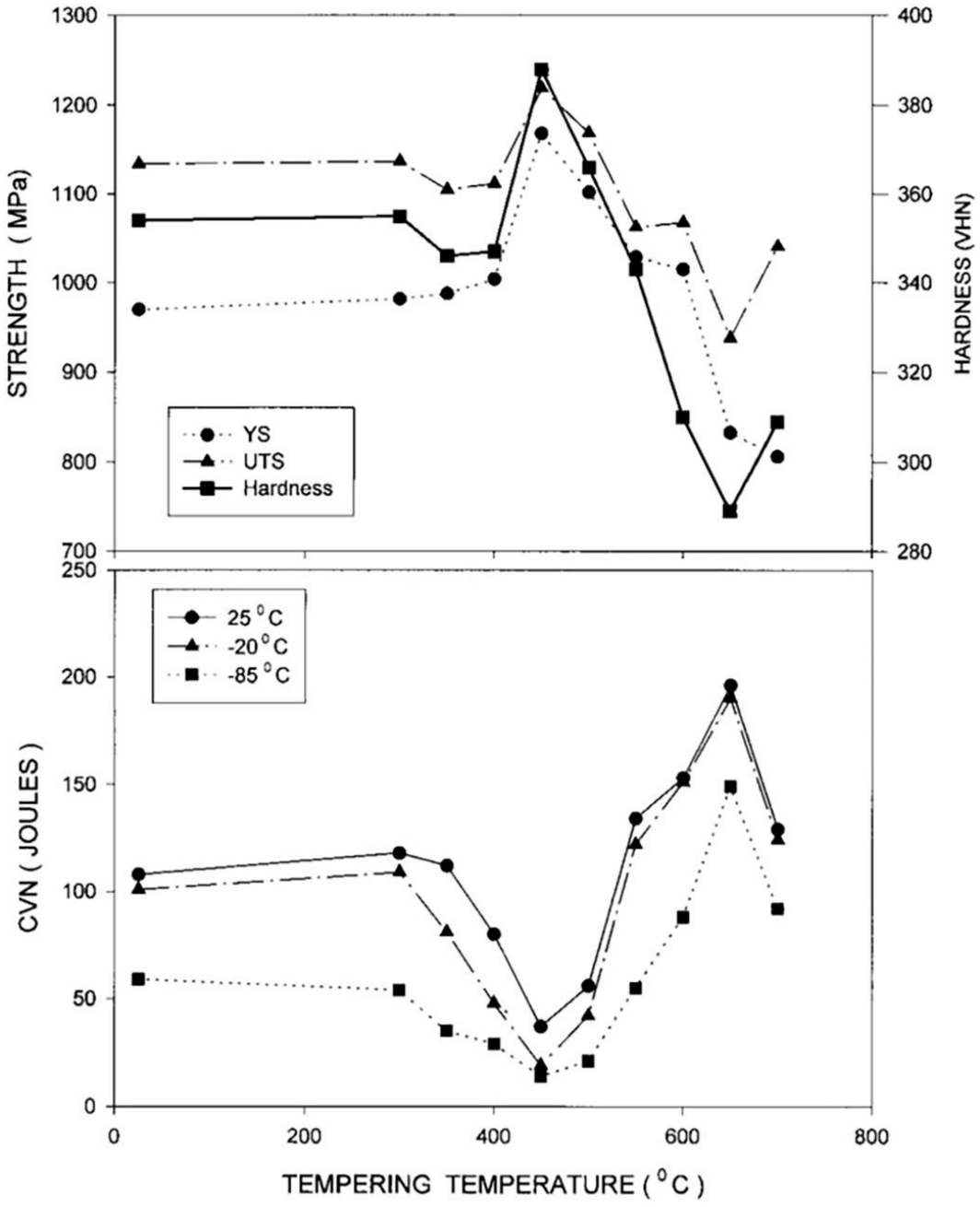

Figure 2.2- Variation of Yield Strength (YS), Ultimate Tensile Strength (UTS), Vickers Hardness (VHN), and Charpy V-Notch (CVN) Impact Energy of HSLA-100 steel with tempering temperature. The samples were tempered for 1 h followed by water quench [12].

Previous research on the as-received HSLA-115 steel aged at 660 ^{o}C for 49 minutes revealed overaged Cu precipitates with volume equivalent spherical radius of 4.36±2.05 nm and a number density of 2.0±0.5 *10^{22} m^{-3}, and the rare occurrence of co-located precipitates of AlN, Cu, M_2C, and NbC, Figure 2.3 [43].

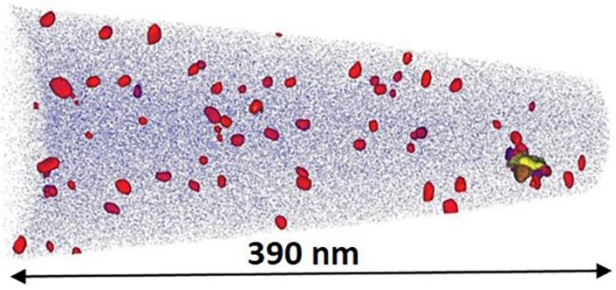

Figure 2.3- 3-D APT reconstruction of the as-received HSLA-115 steel aged at 660 ^{o}C for 49 minutes. Cu precipitates are delineated by 20 at% isoconcentration surfaces (red) and a fraction of the Fe atoms are shown (blue dots). A single cluster consisting of co-located precipitates of AlN (yellow), Cu (red), M_2C (purple), and NbC (brown) is observed [43].

To explore the potential of HSLA-115 steels for higher strength applications, co-precipitation of secondary hardening M_2C carbides (M is Mo, Cr) with Cu precipitates is explored in the present study. Mo and Cr were originally added to HSLA-100 steel to increase its hardenability to obtain a martensitic matrix on quenching [11]. These elements, if present in sufficient quantities can also form stable alloy carbides, such as M_2C (M = Mo, Cr, Fe) carbides, when the steel is tempered in a suitable temperature range of approximately 773-873 K (500-600 ^{o}C) [14]. A steel that was first designed to utilize precipitation strengthening from both Cu precipitates and M_2C carbides was the low-carbon blast resistant BA-160 steel, Figure 2.4 [18, 44]. A more detailed description of Cu precipitates and M_2C carbides in b.c.c (α)-Fe is provided below.

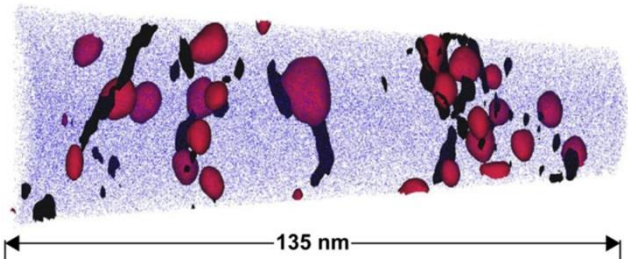

Figure 2.4- 3-D APT reconstruction of BA-160 steel after aging at 550 °C for 30 min and 450 °C for 320 h. The blue dots, red surfaces, and black surfaces represent Fe atoms, 10 at. % Cu isoconcentration surfaces, and 1 at. % C isoconcentration surfaces, respectively [18].

2.2 Copper Precipitates in b.c.c. (α)-Fe

It is now well known that Cu nucleates as coherent (b.c.c.) spheroidal precipitates in α-Fe. [45-47] The first direct evidence of the b.c.c. structure was provided by Pizzini et al.[47], who used Extended X-ray absorption fine structure (EXAFS) technique to observe the changes in the bonding in the neighborhood of Cu atoms in Fe-Cu and Fe-Cu-Ni alloys and concluded that Cu precipitates during early aging times had a b.c.c. structure. It was only at long aging times that they observed Fourier Transforms resembling the f.c.c. structure. Earlier Transmission Electron Microscopy (TEM) studies on Fe-Cu alloys [45, 48] revealed that at equilibrium, f.c.c. Cu precipitates acquire rod morphology with hemispherical caps and have a Kurdjumov-Sachs (K-S) orientation relationship with α-Fe, which is, $(111)_{Cu} \parallel (110)_{\alpha\text{-Fe}}$ and $[110]_{Cu} \parallel [111]_{\alpha\text{-Fe}}$. Further revelation for the structural evolution of Cu precipitates in α-Fe was made by Othen et al.[49, 50] using High Resolution TEM (HRTEM). They reported that b.c.c. Cu precipitates larger than 4 nm in diameter undergo martensitic transformation to twinned 9R structures, Figure 2.5 [49]. They also reported the occurrence of a second martensitic shear transformation to a 3R structure for precipitates larger than 17 nm diameter, which acquire an ellipsoidal morphology as they grow and finally transform to the more elongated rod-shaped equilibrium f.c.c. structure [50].

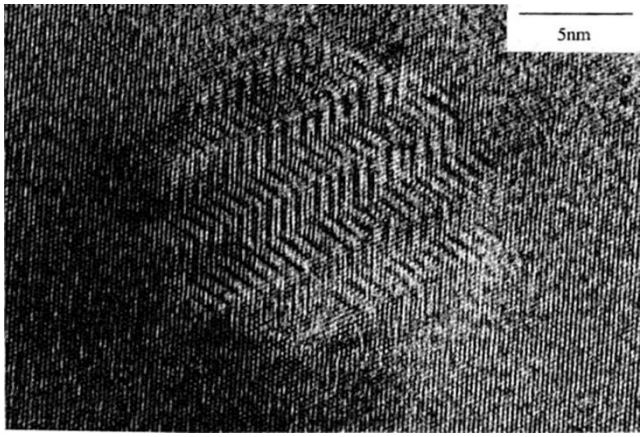

Figure 2.5- High Resolution Electron Micrograph (HREM) showing herring-bone fringe pattern within the Cu particle. The spacing and direction of the fringes are consistent with a twinned 9R structure [49].

The composition of b.c.c. Cu precipitates in α-Fe has been a matter of debate for decades, primarily due to the contradiction in the results obtained by atom probe and small-angle neutron scattering (SANS) studies. Earliest atom-probe investigation on Fe- 1.4 at. % Cu alloys was done by Goodman et al.[46, 51] They reported significant Fe (~50 at. %) in the Cu precipitates. Similar high Fe concentrations in the Cu precipitates during early aging times have also been obtained in the more recent atom-probe studies [18, 52, 53]. Mulholland et al.[18] using atom-probe showed that the core composition of the Cu precipitate becomes richer in Cu with increasing precipitate's radius, Figure 2.6.

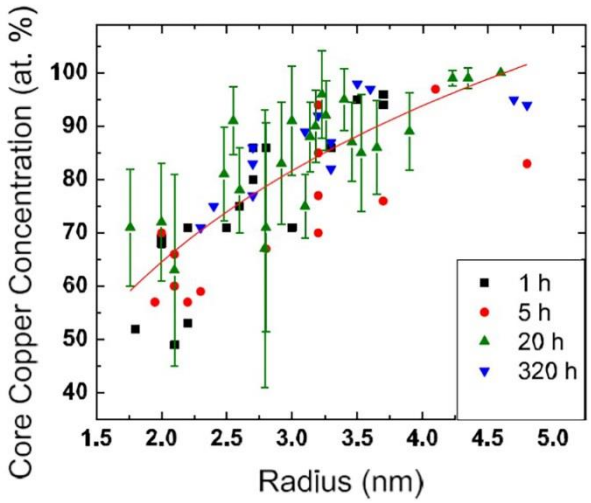

Figure 2.6- Copper precipitate core concentrations versus the radius, R, of each precipitate for the BA-160 steel aged at 450 ^{o}C for the indicated times. A prior tempering at 550°C for 30 min was performed before aging at 450 ^{o}C. Each data point is for a single Cu precipitate [18].

In contrast, negligible Fe concentrations have been reported in Cu precipitates from SANS studies [54, 55]. While the composition of Cu precipitates at early aging times, as determined by APT, may be affected by the artificial inclusion of matrix-Fe atoms due to ion-trajectory overlaps [56], the SANS based analysis assumes the Cu precipitates in α-Fe to be non-ferromagnetic, which is highly questionable in light of the significant Fe concentrations reported from atom-probe studies. Computer simulations have also yielded contradictory results; Monte Carlo simulations done by Soisson et al.[57] in Fe-1.34 at.% Cu alloy reported negligible Fe content in copper precipitates, while the more recent first principle calculations by Liu et al.[58] predicted that b.c.c. solid solutions of Fe-Cu with Cu concentrations greater than 50 at. % are mechanically unstable, as their elastic shear modulus, C', is negative.

There are two different strengthening mechanisms that have been proposed for Cu precipitate strengthening in α-Fe. The earlier mechanism proposed by Russel and Brown [59] is attributed to

the shear elastic modulus mismatch between α-Fe and Cu precipitates. Smaller shear modulus of Cu precipitates than the α-Fe matrix decreases the dislocation line energies inside the Cu precipitates. They, however, used f.c.c. Cu shear modulus due to the non-availability of the data for b.c.c. Cu. An alternative mechanism is proposed by Harry and Bacon [60, 61], in which they attributed the strengthening to the energetically favorable transformation of b.c.c. Cu precipitates to a distorted, close packed, f.c.c.-like structure when sheared by a dislocation.

2.3 M_2C carbides (M=Mo, Cr) in b.c.c. (α)-Fe

M_2C carbides have a hexagonal close packed structure of metal atoms with carbon atoms occupying a fraction of total octahedral sites depending on the chemical composition [62]. Precipitation of M_2C carbides requires diffusion of both carbon and substitutional alloying elements. Since the latter diffuse slowly as compared to the fast interstitial diffusion of carbon, the diffusion of substitutional alloying elements controls the growth of these carbides [14]. Generally, these alloy carbides nucleate at dislocation sites, the basic driving force for such precipitation being the lowering of the strain energy [63]. Several studies have shown that Mo_2C precipitates in α-Fe assume the morphology of rods or needles and grow along $<100>_{\alpha\text{-Fe}}$, Figure 2.7 [64, 65]. It is generally believed that M_2C carbides nucleate coherently in the ferritic matrix [62, 66, 67]. In a TEM study of AF1410 steel, the change from coherency to incoherency was identified by a shift in the lattice parameter of M_2C carbides [62]. Nagataki et al.[67] in their x-ray diffraction study observed changes in x-ray line broadening which was linked to the coherency loss of these carbides.

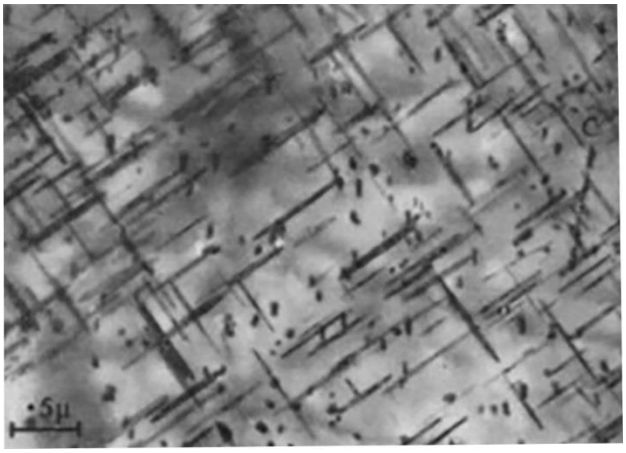

Figure 2.7- TEM micrograph of ferrite <100> zone containing two sets of Mo_2C needles in <100> habit directions. A third set of needles are perpendicular to the foil [64].

Since crystallographic information cannot be inferred from atom-probe experiments, coherency loss of alloy carbides in the past has been determined from the morphological changes like aspect ratio [68]. Liddle et al.[68] used atom-probe to examine the morphology of the M_2C (M=Mo,Cr) carbides in AF1410 steel tempered at 510 ^oC for various aging times and observed the transformation of M_2C carbides from clusters to rods to spheroids and the larger irregular particles with increasing aging times. Davies et al.[69] observed in an Fe-Mo-C alloy that for small precipitate sizes, needles coexisted with spheres. The morphology according to them is influenced by composition, surface energy and strain energy.

Composition of M_2C carbides in Mo, Cr containing steels is usually mixed, consisting of both Mo and Cr. Substitution of Mo by Cr in M_2C carbides reduces its lattice parameter and is associated with the decrease in transformation strains [62, 70, 71]. Speich et al.[15] studied the effect of Cr on the tempering of a secondary hardening Mo containing steels and observed increased kinetics and hardening response of M_2C carbides with increasing Cr-additions of upto 2 wt. %, beyond

which the effect was saturated. Several researchers have modeled the strengthening from M_2C carbide precipitation in both the shearable and Orowan regime [72-74].

2.4 10 wt. % Ni steels

The development of 10 wt. % Ni steels has been accomplished by extensive composition, processing and mechanical property testing on low-carbon 2.5-10 wt. % Ni steels by Zhang [6]. To delay the onset of shear instability during high velocity fragment impact, the 10 wt. % Ni steels utilize the concept of transformation induced plasticity, as described in chapter 1. Since carbon is kept low (<0.1 wt. %) in these steels for weldability, Ni is used as a primary alloying element to stabilize austenite. Ni additions in steels are also believed to lower the ductile-to-brittle transition temperatures in steels due to its effect on cross-slip of dislocations [75] and/or on the cohesive energy of iron at low temperatures [76]. A common processing route to form Ni-enriched austenite in significant volume-fractions from the as-quenched microstructure is to employ intercritical heat-treatments in the ferrite (α) plus austenite (γ) two-phase field. Low-carbon (<0.1 wt.%) steels containing 5 to 9 wt. % Ni have been in use for several decades for cryogenic applications and are processed by single or multistep intercritical treatments [77-85]. Optimized QLT-treatment developed for 10 wt. % Ni steels consists of a water quench from the austenitizing temperature at ~ 800 ^{o}C (Q-step), followed by successive intercritical treatments at 630-660 ^{o}C (L-step) and 570-600 ^{o}C (T-step) with each step terminated by a water quench. These steps are schematically indicated on the Fe-Ni binary phase diagram by Goldstein and Ogilvie [86] in Figure 2.8. Significant additions of Mo, Cr, and V in the 10 wt. % Ni steels investigated here results in its very high hardenability; Fonda et al.[87] studied the transformation behavior for a similar 9 wt. % Ni-Cr-Mo-V steels containing 0.11 wt. % C and reported a predominantly martensitic microstructure

in the as-quenched condition for wide range of cooling rates (130 to 0.16 ^{o}C/s), Figure 2.9. Mechanical properties of 10 wt. % Ni steels and the role of austenite formed via QLT-treatment in influencing its ballistic resistance is described below using Figure 2.10 and Figure 2.11 [6].

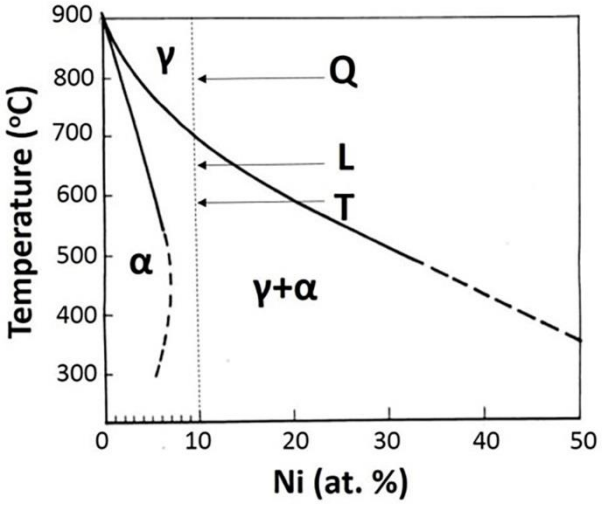

Figure 2.8- Fe-Ni phase diagram, determined by Goldstein and Ogilvie [86]. Q, L, and T-steps of the QLT-treatment are also indicated on the plot.

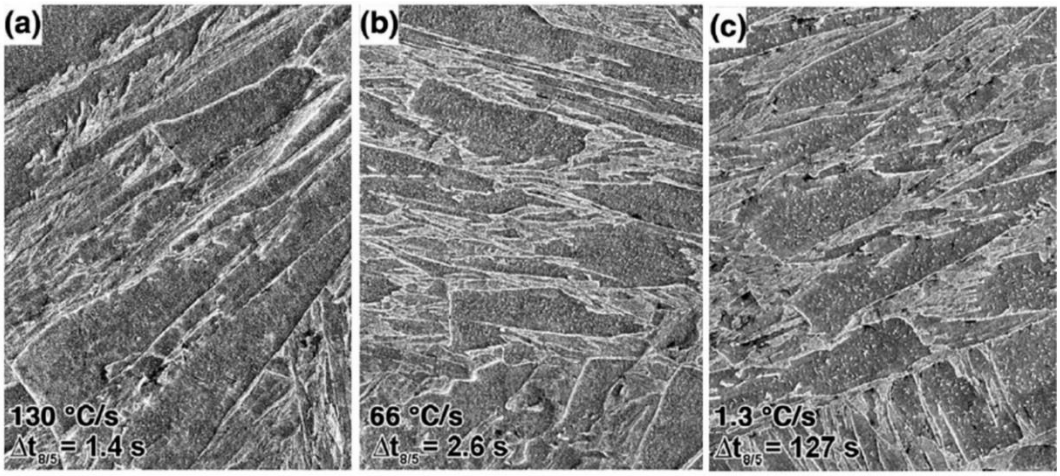

Figure 2.9- SEM images of the microstructure of a 0.11C-9Ni-Cr-Mo-V (wt. %) steel after heating to a temperature of 1200 ^{o}C (4 min hold) and subsequent cooling to room temperature at various cooling rates (a) 130 ^{o}C/s; (b) 66 ^{o}C/s; (c) 1.3 ^{o}C/s. Images display a fully martensitic microstructure characterized by coarse autotempered martensite and fine lath martensite [87].

Figure 2.10 displays the mechanical properties of the QLT-treated 10 wt. % Ni steels, QLT-treated 4.5-6.5 wt. % Ni steels, and non-QLT 2.5-10 wt. % Ni steels. Superior ballistic limit, V_{50} of the QLT-treated 10 wt. % Ni steels is evident along with an excellent combination of yield strength, ultimate tensile strength, impact toughness at -84.4 ^{o}C, and uniform elongation. The ballistic limit V_{50} is defined as an average velocity of an equal number of the highest partial penetration velocities and the lowest complete penetration velocities that occur within a specific velocity spread.

Microhardness maps of sectioned craters of ballistic samples coupled with austenite volume fraction measurements from the deformed regions indicated that dynamic deformation during the ballistic impact induced an austenite to martensite phase transformation. A higher volume fraction of austenite in the QLT-treated sample in comparison to QL-treated led to greater and more widespread strengthening in the former during dynamic deformation, Figure 2.11. This along with the greater reduction in thickness (an indicator of global dynamic deformation) of the QLT-treated crater was correlated with its superior ballistic limit, V_{50} and the phenomenon was referred to as 'ballistic induced plasticity (BIP)', to emphasize similarity with the TRIP-effect [6]. Role of dispersed austenite in other martensitic steels is described below.

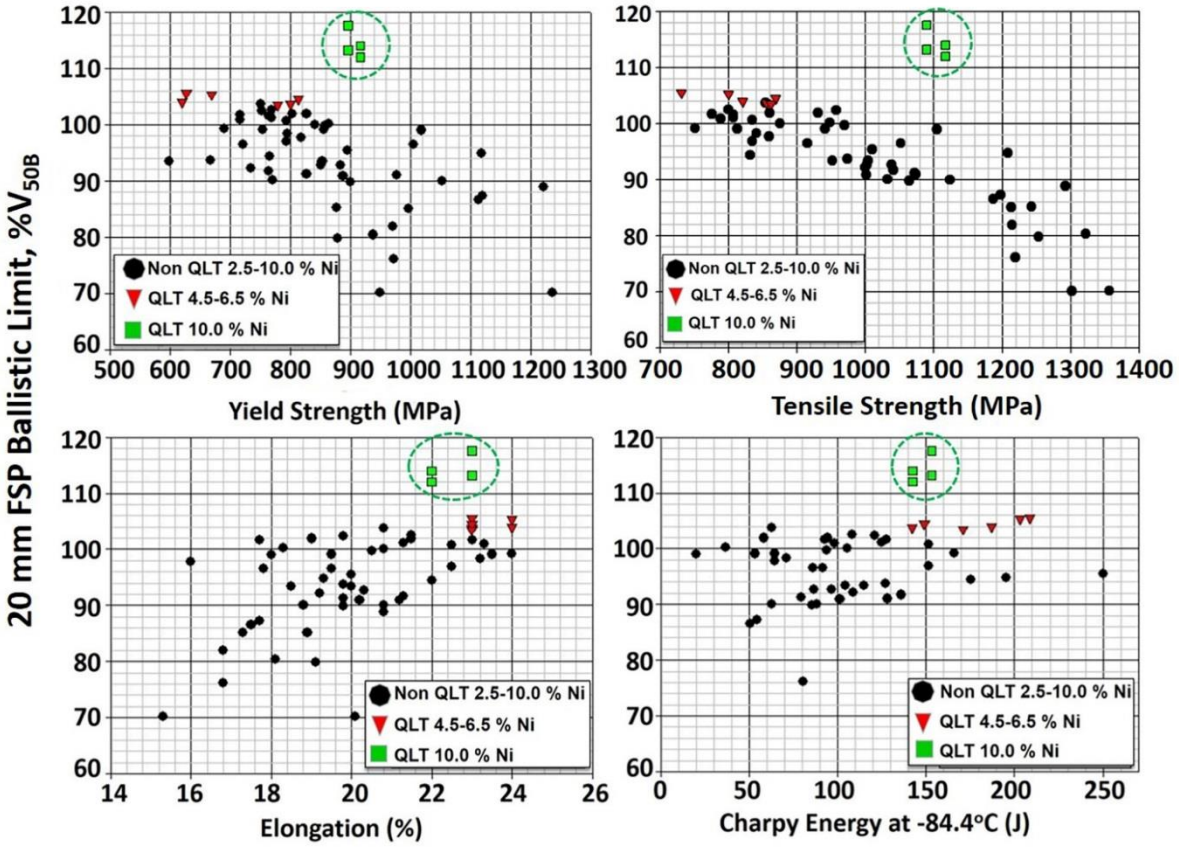

Figure 2.10- Comparison of 20 mm FSP ballistic limit V_{50} (normalized with respect to HSLA 100 steel) versus mechanical property plots for optimally QLT treated-10 wt.% Ni steel and various other steels illustrating the superiority of the former [6].

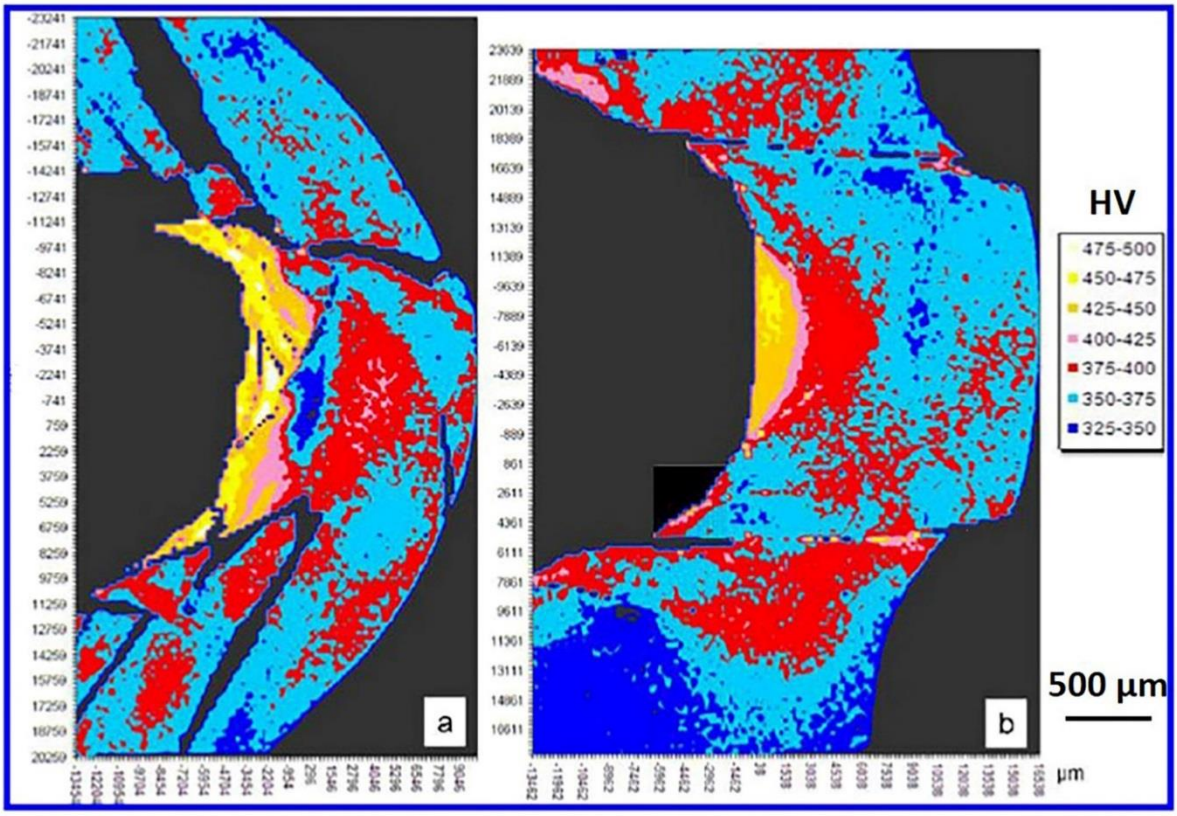

Figure 2.11- Microhardness maps of sectioned crater of (a) optimally QLT-treated 10 wt. % Ni steel; (b) QL-treated 10 wt. % Ni steel, created by respective V_{50} limits. The hardness map of QL-treated sample shows local adiabatic shear bands (ASBs) that caused a plugging failure. In comparison, no indication of the formation of ASB in QLT-treated sample, and the projectile was stopped by extensive plastic bulging of the strengthened target as it absorbed more energy [6].

2.5 Dispersed austenite in other martensitic steels

2.5.1 Intercritically formed austenite in 5.5 and 9 wt. % Ni cryogenic steels

Low-carbon 5.5 and 9 wt. % Ni steels used for cryogenic applications utilize single or multi-step QLT-type treatment to form Ni-rich austenite, which forms predominantly along the martensite lath boundaries, Figure 2.12 [77, 78, 88-90]. Austenite in these steels is associated with improving the upper shelf toughness by its scavenging action for carbon and other impurities [89, 91]. It also plays an indirect role in refining the martensite packet size, which lowers ductile-brittle transition

temperature. During plastic deformation, austenite along the martensite lath boundaries transforms to martensite, whose crystallographic variant is different from the surrounding packet. This interrupts the crystallographic alignment of laths within martensite packets, effectively refining the packet size [78, 90]. It is noted that unlike the 10 wt. % Ni steels investigated in the present research, these cryogenic 5.5 and 9 wt. % Ni steels did not have intentional additions of Mo and Cr that can form secondary hardening carbides.

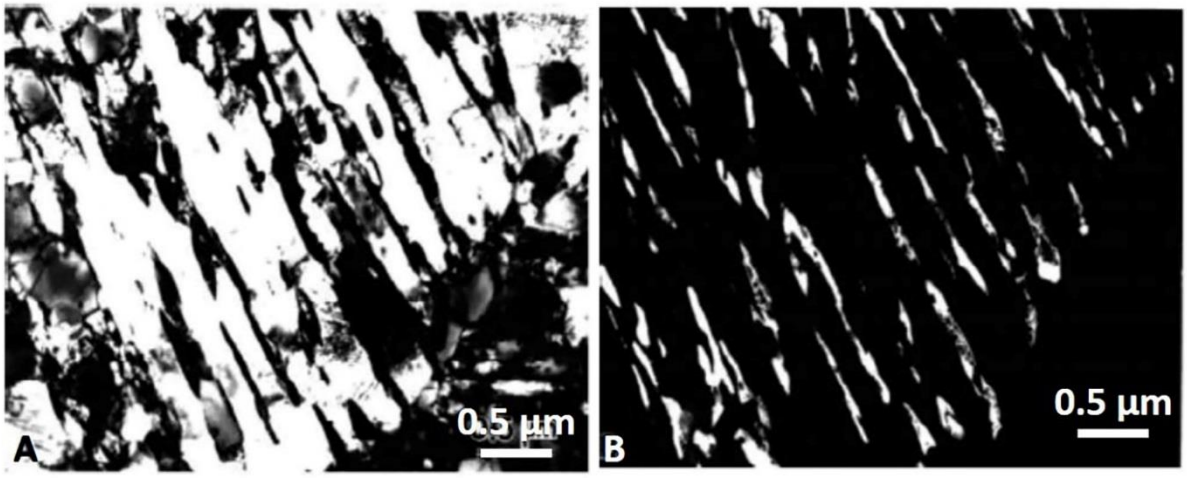

Figure 2.12- TEM micrographs (a) Bright Field; (b) Dark Field of QLT-treated 9 wt. % Ni steel showing austenite along lath boundaries [90].

2.5.2 Retained austenite in 4340 steels

Retained austenite refers to the austenite that remains untransformed after the austenitizing and quench treatment. In medium carbon low-alloy 4340 steels, 4 and 9 vol. % retained austenite was obtained following the austenitizing treatments at 870 and 1200 ºC respectively [92]. Microstructures with varied retained austenite contents following these treatments were obtained using cryogenic high magnetic field treatments. Thin-wall torsion experiments demonstrated that strain-induced transformation of retained austenite delayed shear instability. However, retained

austenite was unstable for the crack-tip stress state and thus did not affect K_{1C} fracture toughness [92]. 'Precipitated' austenite formed via high-temperature tempering or intercritical annealing provides a better opportunity to control the amount, size, composition, etc of dispersed austenite through specifically designed heat-treatments. Efforts were thus made to form dispersed austenite via single and multi-step tempering in high Ni-Co steels and utilize transformation-toughening effects [93]. These are described below in section 2.5.3.

2.5.3 Austenite formed via single and multi-step tempering in high Ni-Co steels

Haidemenopoulos explored different tempering treatments to form dispersed austenite and utilize transformation toughening in secondary hardened martensitic, 10 Ni-14 Co (wt. %) AF1410 steels [94]. A single step treatment at 510 ^{o}C resulted in the formation of interlath austenite, which was not stable enough for transformation toughening. Multistep tempering involving cementite formation during the first step at 420 ^{o}C/5h, followed by the nucleation of intralath austenite on alloyed cementite during the second step (510 ^{o}C/8 h) resulted in sufficient stabilization of austenite. However, undissolved cementite proved deleterious to the fracture toughness and negated the benefits from transformation toughening. The most optimized treatment for transformation toughening involved intercritical annealing step (600 ^{o}C/15 min), followed by 510 ^{o}C/8 h tempering step and resulted in uniformly dispersed intralath austenite (15 vol. %), stabilized by size refinement (10-20 nm) and Ni enrichment (30 wt. %). Nucleation energetics calculations using the driving forces estimated from ThermoCalc revealed that homogeneous nucleation of austenite, either coherent or semicoherent, was not feasible due to the large strain energy accompanying austenite nucleation. Nucleation of semicoherent austenite on dislocations and/or interaction of austenite nuclei with M_2C carbides were suggested as likely mechanisms for

austenite nucleation in these steels [95]. STEM-EDS analysis of a similar high Ni-Co secondary AerMet 100 martensitic steel after multi-step tempering (507 ^{o}C/15 min and 455 ^{o}C/7 h) revealed high Cr signals (4-5 at. %) in the matrix near the Ni-rich particle (Cr concentration in austenite is ~ 2 wt. %), indicating the nucleation of intralath austenite particle on M_2C carbides [96].

2.5.4 Austenite in BA-160 steels

In BA-160 steels containing 6.8 wt. % Ni, negligible austenite volume fraction was detected (< 1 %) for aging temperatures upto 600 ^{o}C and thus TRIP did not play any significant role at 160 ksi yield strength [3]. In the lower yield strength regime, higher fractions of upto 6.6 vol. % austenite were obtained after multi-step treatment (650 °C /2 h and 500 °C/4 h). Fraley explored the potential of BA-160 steel for passive damping applications requiring high uniform ductility. He reported that the austenite formed after the above multi-step treatment was highly unstable during tensile testing and transformed in the undesirable stress-assisted regime and did not affect the uniform ductility [97].

Chapter 3

Multicomponent High-Strength Low-Alloy Steel Precipitation-Strengthened by Sub-nanometric Cu precipitates and M_2C carbides

Abstract

HSLA-115 is a novel high-strength low-alloy structural steel derived from martensitic Cu-bearing HSLA-100. HSLA-100 is typically used in conditions with overaged Cu precipitates, to obtain acceptable impact toughness and ductility. Present work on HSLA-115 demonstrates that incorporating sub-nanometric sized M_2C carbides along with Cu precipitates produces higher strength steels that still meet impact toughness and ductility requirements. Isothermal aging at 823 K (550 ^{o}C) precipitates M_2C carbides co-located with the Cu precipitates and distributed heterogeneously at lath-boundaries and dislocations. 3-D atom-probe tomography is used to characterize the evolution of these precipitates at 823 K (550 ^{o}C) in terms of mean radii, number densities and volume fractions. These results are correlated with microhardness, impact toughness, and tensile strength. The optimum combination of mechanical properties, 972 MPa yield strength, 24.8 % elongation to failure, and 188.0 J impact toughness at 255 K (−18^{o}C), is attained after 3 h aging at 823 K (550 ^{o}C). Strengthening by M_2C precipitates offsets the softening due to overaging of Cu precipitates and tempering of martensitic matrix. It is shown that this extended yield strength plateau can be used as a design principle to optimize strength and toughness at the same time.

3.1 Introduction

High-strength high-toughness weldable steels are utilized as high performance structural materials for naval applications. More than two decades ago, the U.S. Navy replaced the higher carbon steels (0.14-0.20 wt.% C), designated as High Yield-Strength steels (HY-80 and HY-100) by lower carbon concentration (<0.06 wt.% C) steels: specifically, High Strength Low Alloy steels (HSLA-80 and HSLA-100) [1, 11]. The numerals 80 and 100 designate the minimum obtainable tensile yield strength (YS) in ksi (1 ksi = 6.9 MPa). The carbon concentration was reduced in HSLA steels to decrease the susceptibility of the heat-affected zone in welds to hydrogen cracking, simplifying welding procedures as is indicated by the Graville diagram [36]. Enhanced weldability reduces the preheating requirements and consequently the processing cost [37]. To compensate for the loss in strength due to the lower carbon concentration, Cu was added to utilize precipitation strengthening provided by the Cu precipitates [8-10]. Niobium was added in small amounts as it forms stable carbonitride precipitates, Nb(C,N), during the solutionizing and hot-rolling treatments. These precipitates impede austenite grain growth during austenitization at high temperatures, and thus refine grain size, benefitting both strength and toughness [40-42]. Conventional heat treatments of HSLA-100 steel involves austenitizing, water quenching and aging treatment, which results in a tempered martensitic-bainitic microstructure (depending on its hardenability) with overaged Cu precipitates [8, 11]. Detailed information concerning the development of the widely used Naval HSLA-100 steels can be found elsewhere [1, 4].

To reduce the weight of naval vessels, continuous efforts were made by the U.S. Navy to develop stronger steels having a similar composition as HSLA-100, while also meeting other performance requirements like low-temperature impact toughness and weldability. The idea behind the

development program was that the similar chemical composition of the new steel would shorten the qualification process, prevent expenses related to the approval of new welding processes and expedite the implementation process. The work of the project team led by the Navy Metalworking Center (NMC) resulted in the development of HSLA-115, whose composition is based on HSLA-100 composition 3, which is an HSLA-100 grade slightly richer in Cu, Mo and Ni than composition-2 [2]. HSLA-115 was approved for plate production by the Naval Sea Systems Command (NAVSEA) in January 2009 [2] and has been used for the construction of the flight deck of the CVN-78 aircraft carrier [7].

Efforts were also made in the past decade at Northwestern University to develop leaner chemistry Cu-precipitation strengthened ferritic steels as alternatives to HSLA-80 and HSLA-100 steels, specifically eliminating Mo and Cr [16, 17, 52, 53, 98-107]. These efforts led to the development of several alloys, which were designated as NUCu-X, where NUCu denotes the *Northwestern University Copper* alloyed steel and the numeral X stands for the obtainable tensile Y.S. in ksi. One of these alloys, NUCu-70 is now designated as ASTM A710-B and has been used for construction of a bridge in Illinois [17]. One of the higher strength grade steel in these series of alloys is NUCu-140. The chemical composition of the A710-B alloy was modified by additions of Al and Ni to utilize the strengthening provided by the intermetallic NiAl (B2 structure) phase. Work by Vaynman et al.[17] and Kolli et al.[103] revealed, however, that homogeneous precipitation of NiAl phase did not occur in the ferritic matrix and that the NiAl precipitates were mostly observed distributed heterogeneously at α-Fe/Cu-precipitate interfaces or at grain boundaries. Nevertheless, promising results were obtained for desirable combinations of strength and toughness properties in NUCu-140 steels at an aging temperature of 823 K (550 ^{o}C).

A major difference between HSLA-115 and NUCu-140 steels is the presence of Mo and Cr in HSLA-115. These were originally added in HSLA-100 steel to increase its hardenability to obtain a martensitic matrix on quenching [11]. These elements, if present in sufficient quantities can also form stable alloy carbides, such as M_2C (M = Mo, Cr, Fe) carbides, when the steel is tempered in a suitable temperature range of approximately 773-873 K (500-600 ^oC) [14]. Fine dispersions of these carbides are known to provide secondary hardening in tempered martensitic steels and are also considered beneficial for impact toughness as their precipitation can result in the dissolution of the brittle coarse cementite phase [14, 15]. Cementite, even though metastable, inevitably precipitates out prior to the precipitation of alloy carbides owing to the rapid diffusion of interstitial carbon, while the substitutional elements may remain immobile [108]. Suitable aging temperatures to utilize Cu precipitation strengthening range from 723 to 923 K (450 to 650 ^oC) [12, 16, 17] and thus it seems possible to co-precipitate M_2C carbides and Cu precipitates in HSLA-115. A steel that was first designed to utilize precipitation strengthening from both Cu precipitates and M_2C carbides was the low-carbon blast resistant steel, BA-160 [44]. In a subsequent experimental study, Mulholland et al.[18] utilized 3-D atom-probe tomography (3-D APT) to demonstrate that a suitable aging treatment can lead to the precipitation of both Cu precipitates and M_2C carbides in BA-160 steel. 3-D APT with its sub-nanometric scale resolution and excellent mass resolving power is a unique instrument to investigate microstructures in such precipitation-hardened alloys [20-23].

One of the key objectives of the present study is to explore the possibility of co-precipitating M_2C carbides with Cu precipitates in HSLA-115. Previous research on the as-received HSLA-115 steel

(which was aged at 933 K (660 ^{o}C) for 49 minutes after the solutionizing treatment) revealed overaged Cu precipitates and the rare occurrence of co-located precipitates of AlN, Cu, M_2C, and NbC [43]. A 3-D APT investigation performed in the present study reveals that aging at 823 K (550 ^{o}C) facilitates the co-precipitation of sub-nanometer sized Cu precipitates and M_2C carbides in HSLA-115. Additionally, bulk mechanical properties obtained for the isothermally aged HSLA-115 at 823 K (550 ^{o}C) are correlated with the temporal evolution of microstructure studied using 3-D APT. These results are compared with those obtained by Hunter [43] in his study of NUCu-140 steel, also aged at 823 K (550 ^{o}C). NUCu-140 steel does not form M_2C carbides and thus this comparison helps in understanding the effects that M_2C carbides have on the bulk-mechanical properties of HSLA-115 and on the evolution of Cu precipitates in it. A fundamental understanding of the various precipitating processes in these steels and their correlation with the obtained bulk-mechanical properties will help in optimizing the processing of these steels and in exploring their potential for U.S. Naval systems and other structural applications.

3.2 Experimental Methods

Chemical compositions of HSLA-115 and NUCu-140 [43] steels were measured using optical emission spectroscopy and are displayed in Table 3.1. HSLA-115 steel was subjected to two consecutive austenitization treatments for 35 min each at 1185 K (912 °C), and each treatment was followed by water quenching. This was followed by isothermal aging at 823 K (550 ^{o}C) for various aging times and water quenching. Multiple austenitizing treatments involving shorter holding times minimize the formation of large isolated austenite grains, which benefits both strength and impact toughness [11]. NUCu-140 steels were austenitized at 1173 K (900 ^{o}C) for 1 h followed by water quenching and were then aged at 823 K (550 ^{o}C) for different aging times and air cooled

[43]. HSLA-115 samples for metallography and microhardness measurements were prepared by standard mounting, grinding and polishing methods with a final polish with 0.06 μm colloidal silica. The samples were then etched with 2% nital prior to optical metallography examination and microhardness testing. Vickers microhardness testing was conducted using a Struers Duramin tester applying 500 g load for an indentation time of 15 s. Each reported microhardness value is an average of 15 measurements and the error given is the standard deviation of the average. HSLA-115 samples for tensile testing were machined in accordance with ASTM E8 standard and the tensile tests were performed at room temperature using an Instron type machine and a strain rate of 0.08/min. Two specimens for each aging condition were tested and the average value is reported. The error is determined by the standard deviation of the average. The Charpy V-notch (CVN) specimens were machined as per ASTM E23 standard and the tests were performed at sub-ambient temperatures of 255.2 K (-17.8^{o} C) and 188.6 K (-84.4 ^{o}C). The samples were cooled to 255.2 K (-17.8^{o} C) by immersing them in a bath of methanol and dry ice, while a mixture of liquid nitrogen and acetone was used to cool samples to 188.6 K (-84.4 ^{o}C). Three samples were tested for each aging condition and the average value is reported and the error is determined by the standard deviation of the average. Fractographs of the tested impact specimens were obtained using a field-emission gun scanning electron microscope (FEI Quanta 600F). Samples for APT experiments were prepared by first cutting blanks with dimensions of approximately 0.3x0.3x10 mm^{3}, which were then electropolished at room temperature using a two-step electropolishing procedure. Initial polishing was done with 10 vol.% perchloric acid in acetic acid solution using a direct current (DC) voltage of 15-20 V, while the final polishing was done with 2 vol.% perchloric acid in butoxyethanol solution at a reduced voltage of 8-12 Vdc. The samples were then rinsed in pure ethanol and placed under vacuum. APT experiments for HSLA-115 and the 3 and 16 h aged

NUCu-140 samples were performed using a Cameca local-electrode atom probe (LEAP) 4000X-Si tomograph, employing a ultraviolet (wavelength =355 nm) picosecond laser pulsing with an energy of 30 pJ per pulse, a pulse repetition rate of 500 kHz and an average evaporation rate (number of ions per pulse) of 2 %. The samples were analyzed at a specimen base temperature of 60 K in ultrahigh vacuum (< 10^{-8} Pa) and the data obtained was analyzed using the program IVAS 3.6 (Cameca, Madison, WI). Copper precipitates in both HSLA-115 and NUCu-140 steels were identified by the envelope method, which is based on the maximum separation distance alogorithm [109-112]. The envelope method is not directly applied to M_2C carbides as these carbides undergo severe local magnification effects in APT owing to their higher evaporation fields than the matrix Fe-atoms, which causes trajectory overlaps of the field-evaporated ions [56]. M_2C carbides are, therefore, first delineated using 5 at. % (C+Cr+Mo) isoconcentration surfaces and then the atomic contents interior to the isoconcentration surfaces are evaluated using the envelope method. This methodology follows from the research of Mulholland et al.[113], who in their work found that use of laser-pulsing instead of voltage pulsing can cause an increase in a specimen's apex temperature and can further exacerbate such artifacts as local magnification. The use of laser pulsing reduces, however, the failure rate of the specimens when compared to voltage-pulsing and this is particularly beneficial for carbide-containing steel specimens, which are prone to early fracture [114]. Additionally, for precipitation-hardened alloys, larger datasets enable the characterization of a large number of precipitates, which improves the counting statistics.

The radius of the precipitate, R_v is the radius of a volume equivalent sphere [107] and is given by,

$$R_v = \left(\frac{3N_{ppt}}{4\pi\rho_{th}\eta} \right)^{\frac{1}{3}} \qquad 3.1$$

where, N_{ppt} is the total number of detected atoms within the analyzed precipitate, ρ_{th} is the theoretical atomic density of the precipitate (taken to be same as that of b.c.c. α-Fe, 84.3 atom nm^{-3}), and η is the detection efficiency of our LEAP tomograph, taken to be 0.50. The value of the radius reported for a given aging condition is the mean value, $<R_v>$, for the precipitates obtained in that aging condition, while the error reported is the standard deviation of the distribution.

The volume fraction, ϕ_v of the precipitates is determined from,

$$\phi_v = \frac{N_{precip}}{N_{total}} \qquad 3.2$$

where, N_{precip} is the sum total number of atoms that are detected within all the precipitates in the reconstructed volume and N_{total} is the total number of atoms detected in the reconstructed volume.

The number density N_V of the precipitates is determined employing,

$$N_V = \frac{N\rho_{th}\eta}{N_{total}} \qquad 3.3$$

where, N is the total number of precipitates identified in the reconstructed volume. The errors for ϕ_v and N_V are determined from counting statistics and are given by $\frac{\phi_v}{\sqrt{N}}$ and $\frac{N_V}{\sqrt{N}}$ respectively.

Table 3.1- Chemical compositions of HSLA-115 and NUCu-140*, as measured by optical emission spectroscopy.

	Elements	**Fe**	**Cu**	**Ni**	**Mn**	**Si**	**Al**	**Mo**	**Cr**	**Nb**	**C**	**V**	**N**
HSLA-115	wt.%	Bal.	1.29	3.37	0.97	0.22	0.02	0.56	0.64	0.02	0.05	<0.01	0.016
	at.%	Bal.	1.13	3.21	0.99	0.44	0.04	0.33	0.69	0.012	0.23	<0.01	0.064
NuCu-140	wt.%	Bal.	1.64	2.77	0.48	0.50	0.59	-	0.02	0.065	0.05	-	<0.005
	at.%	Bal.	1.43	2.61	0.48	0.98	1.21	-	0.02	0.039	0.23	-	<0.02

*Chemical composition of NUCu-140 is taken from Hunter [43].

3.3 Results

3.3.1 Optical Microscopy

An optical-micrograph of the as-quenched HSLA-115 sample is shown in Figure 3.1(a). It reveals a predominantly lath-martensitic microstructure, as has been reported by other researchers [8, 11, 12, 115, 116] for the as-quenched HSLA-100 steels. Figure 3.1(b, c, d) display the optical-micrographs of the HSLA-115 samples aged at 823 K (550 ^{o}C) for 0.25, 3 and 64 h respectively. The transformation from lath morphology in the as-quenched sample to the polygonally shaped grains in the aged samples is evident. Prior austenite grain boundaries are clearly visible in the aged samples, probably due to the precipitation of secondary phases at these boundaries, which may cause the etchant to highlight these boundaries.

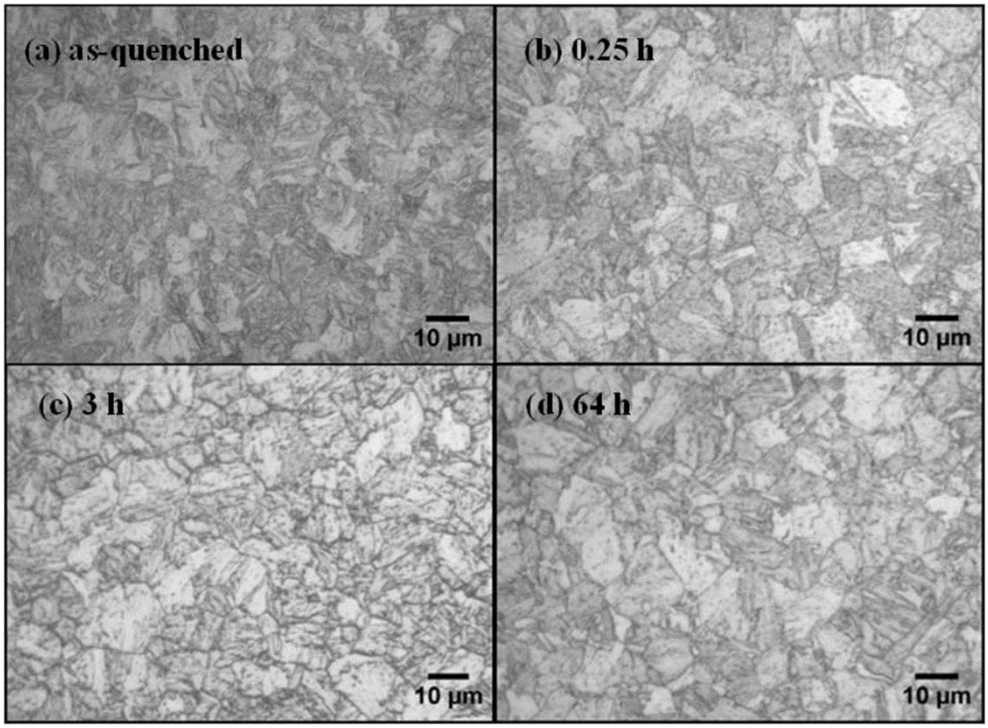

Figure 3.1- Optical micrographs of HSLA-115 after etching in 2% Nital, (a) As-quenched; (b) 0.25 h at 823 K (550 ^{o}C); (c) 3 h at 823 K (550 ^{o}C); and (d) 64 h at 823 K (550 ^{o}C).

3.3.2 Mechanical Properties

Figure 3.2 displays the microhardness evolution for HSLA-115 and NUCu-140 with aging at 823 K (550 ^{o}C). The as-quenched Vickers microhardness of HSLA-115, 343 kgf/mm^2 (3364 MPa) is significantly higher than that of NUCu-140, 273 kgf/mm^2 (2677 MPa); this is attributed to the predominantly lath-martensitic microstructure of HSLA-115, which has a high dislocation density [13, 115, 116]. In contrast, the microstructure of the as-quenched NUCu-140 is a mixture of equiaxed-ferrite and elongated acicular ferrite, which is comparatively softer [17, 43]. On aging, the microhardness in HSLA-115 first decreases and then increases and attains its peak aged value (still smaller than the as-quenched value) in the 0.25 h aged condition. This trend is primarily seen due to two competitive processes occurring during these aging times; the softening of the martensitic matrix due to recovery processes and the strengthening due to Cu precipitation. The microhardness in HSLA-115 decreases by only 3.3 % in the 3 h aged condition from its peak aged value; it then continues to decrease on further aging as is seen from the values for the 16 and 64 h aged conditions. Microhardness in NUCu-140 increases from its as-quenched value on aging and attains its peak aged value at 0.5 h. The microhardness then decreases monotonically on further aging. The decrease from the peak microhardness value on further aging of NUCu-140 is, however, much steeper; ~10.4 % decrease at 3 h of aging from its peak aged value as compared to the corresponding decrease of ~3.3 % for HSLA-115.

Strictly speaking, tempering refers to the heat treatment employed to improve the ductility and toughness of as-quenched martensitic steels and often results in the loss of strength, while aging refers to the heat treatment that precipitation-hardens the alloy. Due, however, to the simultaneous

occurrence of both these processes in HSLA-115 during the heat treatment at 823 K (550 ºC), these terms are used interchangeably in this study for convenience.

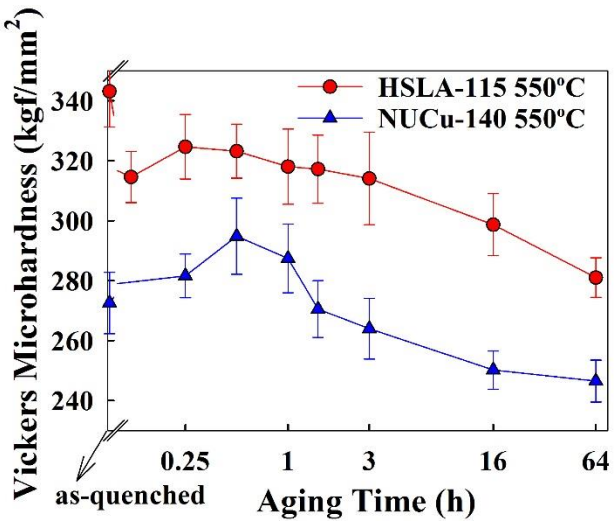

Figure. 3.2- Variation of the Vickers microhardness with aging time for HSLA-115 and NuCu-140 (both aged at 823 K (550 ºC)). Microhardness measurements for NUCu-140 for aging times of 3 h and less are from Hunter's PhD Thesis [43].

Variations of the ultimate tensile strength (UTS) and yield strength (YS) with aging time in HSLA-115 are shown in Figure 3.3(a). While the UTS varies similarly as microhardness with aging time, the YS increases from its as-quenched value and attains its maximum in the 0.25 h aged condition. On further aging, it varies similarly to the UTS, i.e., it attains a plateau until 3 h and then decreases on further aging. The low YS of the as-quenched sample is probably due to the presence of a large number of mobile dislocations in its microstructure [13, 115, 116], which promote easy slip. We also obtain from the ratio of the UTS to YS, Figure 3.3(b), that the as-quenched sample undergoes a significant amount of work hardening when compared to the aged samples, which show negligible work hardening. This results in the higher UTS of the as-quenched sample than the aged samples, despite having lower YS. The elongation to failure,

Figure 3.3(c), increases monotonically with aging time until 3 h, where it attains its maximum value and then decreases with subsequent aging.

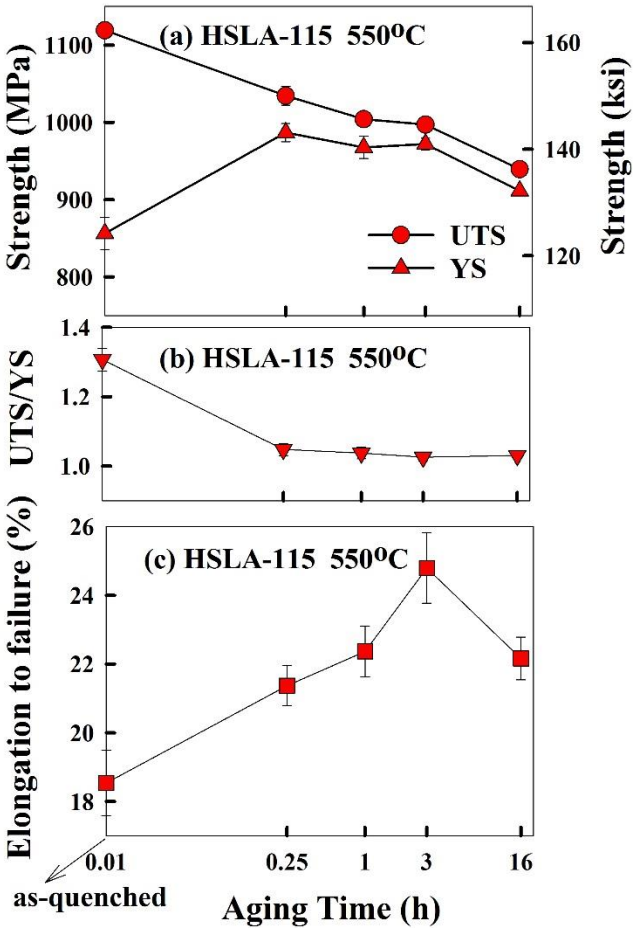

Figure 3.3- Variation of (a) Ultimate Tensile Strength (UTS) and Yield Strength (YS); (b) UTS to YS ratio; and (c) elongation to failure with aging time for HSLA-115 aged at 823 K (550 ^{o}C).

The variation in impact toughness of HSLA-115 and NUCu-140 with aging time at 823 K (550 ^{o}C) at the testing temperatures of 255.2 K (-17.8 ^{o}C) and 233 K (-40 ^{o}C) respectively is shown in Figure 3.4. The as-quenched HSLA-115's high impact toughness at 255.2 K (-17.8 ^{o}C), 118.3 ± 0.6 ft-lbs (160.4 ± 0.8 J) is attributed to its lath-martensitic microstructure, which consists of low-angle lath-boundaries and high-angle packet and block boundaries, which can act as obstacles to

prevent cleavage crack propagation [117-120]. Similarly, good impact toughness in the as-quenched condition was also obtained by Bhagat et al. [121] in two-variants of HSLA-100 steels. Upon aging at 823 K (550 ^{o}C), the impact toughness of HSLA-115 at 255.2 K (-17.8 ^{o}C) first decreases from its as-quenched value and then increases and attains its maximum value of 138.7 ± 8.4 ft-lbs (188.0 ± 11.4 J) at 3 h, which is 67% higher than the value obtained in the 0.25 h aged condition. The impact toughness then decreases monotonically on further aging. It is noted that the tensile test results showed that elongation to failure was a maximum (>24%) for the 3 h aged sample, which coincides with the maximum impact toughness obtained in this aging condition. Only the 3 h aged HSLA-115 samples were tested at 188.6 K (-84.4 ^{o}C) due to the limited availability of material and the impact toughness obtained was 74.0±5.6 ft-lbs (100.3±7.6 J). The impact toughness values obtained at 3 h of aging meet the minimum requirements as per the Navy specifications of 80 ft-lbs (108.5 J) at 255.2 K (-17.8 ^{o}C) and 60 ft-lbs (81.3 J) at 188.6 K (-84.4 ^{o}C) [122].

The high impact toughness of the as-quenched NUCu-140 at 233 K (-40 ^{o}C) is due to its acicular-ferritic microstructure [17, 43], which consists of fine-grained interlocking laths that are separated by high-angle boundaries [123, 124]. During aging at 823 K (550 ^{o}C), the impact toughness of NUCu-140 at 233 K (-40 ^{o}C) first decreases and then gradually increases to attain its maximum value at 3 h (impact toughness tests for longer aging times were not performed) [43]. Thus, NuCu-140 displays a similar trend in the variation of impact toughness with aging time (until 3 h of aging) at 823 K (550 ^{o}C) as HSLA-115.

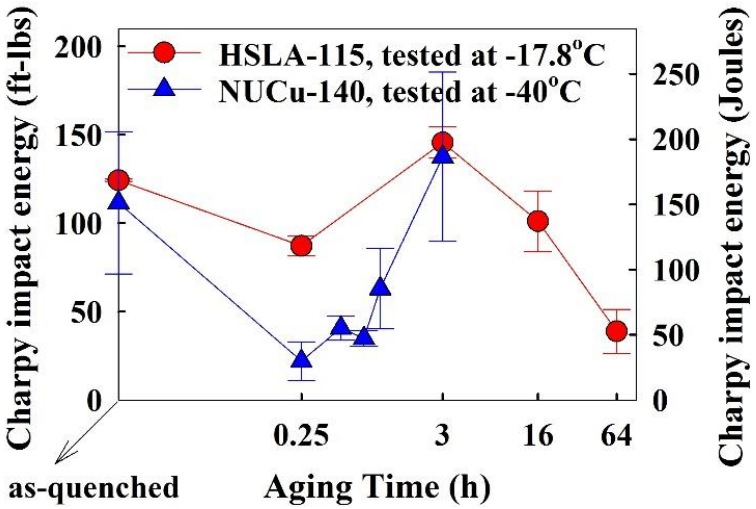

Figure 3.4- Variation of the impact toughness of HSLA-115 and NUCu-140 with time at 823 K (550 ºC) at testing temperatures of 255.2 K (-17.8 ºC) and 233 K (-40 ºC), respectively. Impact toughness tests for NUCu-140 are from Hunter's PhD Thesis [43].

3.3.3 SEM Fractography

SEM micrographs of the fractured surfaces of the Charpy impact specimens of HSLA-115 aged at 823 K (550 ºC) for the indicated times are displayed in Figure 3.5. Dimple-like features, characteristic of ductile failure are observed in the micrographs of the as-quenched, Figure 3.5(a) and the 3 h aged, Figure 3.5(c) samples (both tested at 255.2 K (-17.8 ºC)), while quasi-cleavage transgranular failure is observed for the 0.25 h (Figure 3.5(b)), 16 h (Figure 3.5(d)) and 64 h (Figure 3.5(e)) samples, tested at 255.2 K (-17.8 ºC) and for the 3 h (Figure 3.5(f)) sample tested at 233 K (-40 ºC). These results are in general qualitative agreement with the impact toughness obtained at these times, Figure 3.4.

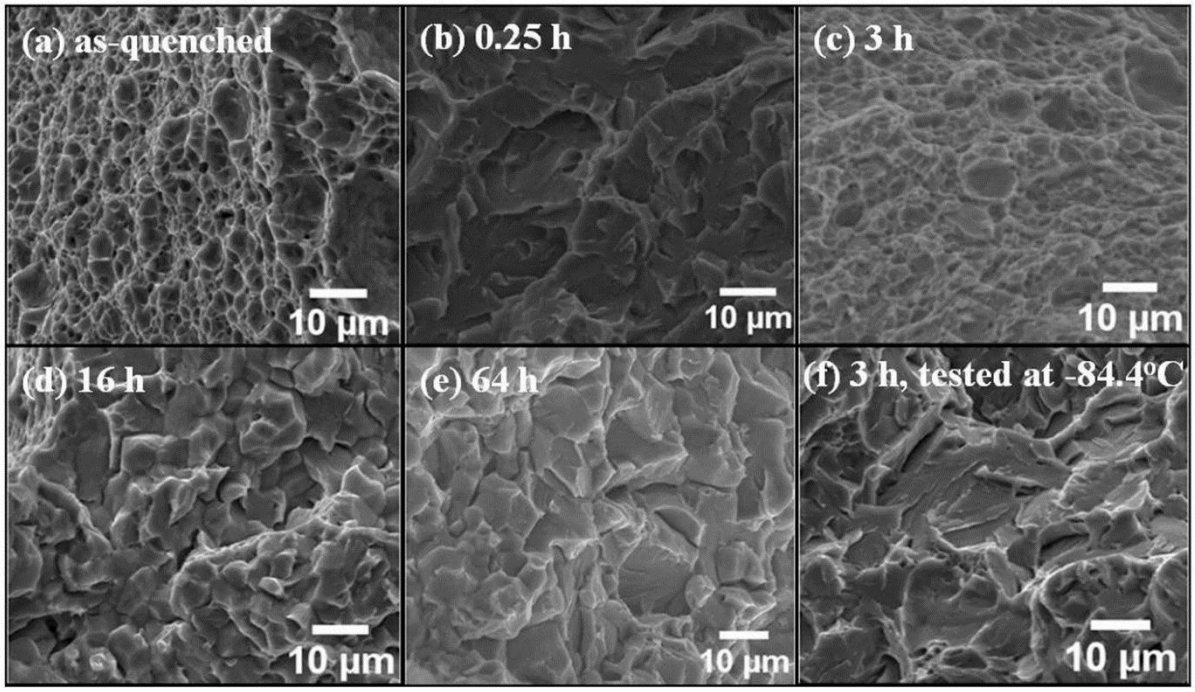

Figure 3.5- SEM fractographs of Charpy V-Notch impact tested samples of HSLA-115, (a) As-quenched, tested at 255.2 K (-17.8 ^{o}C); (b) 0.25 h at 823 K (550 ^{o}C), tested at 255.2 K (-17.8 ^{o}C); (c) 3 h at 823 K (550 ^{o}C), tested at 255.2 K (-17.8 ^{o}C); (d) 16 h at 823 K (550 ^{o}C), tested at 255.2 K (-17.8 ^{o}C); (e) 64 h at 823 K (550 ^{o}C), tested at 255.2 K (-17.8 ^{o}C); and (f) 3 h at 823 K (550 ^{o}C), tested at 188.6 K (-84.4 ^{o}C).

3.3.4 Atom-Probe Tomography

The temporal evolution of the mean radius $<R_v(t)>$, number density, $N_v(t)$, and volume fraction $\phi_v(t)$ of Cu precipitates in HSLA-115 with aging time at 823 K (550 ^{o}C) is displayed in Figure 3.6. Copper precipitates are not observed in the as-quenched sample but profuse Cu-precipitation ($N_v(t) \sim 7.2 * 10^{23}$ m^{-3}) is observed for the 7 min condition (shortest aging time studied). The $N_v(t)$ of Cu precipitates then decreases monotonically until 1 h, with a concomitant increase in $<R_v(t)>$ and $\phi_v(t)$, indicating their growth and coarsening. Interestingly, we observe a second burst of nucleation of Cu precipitates between 1 and 3 h. To check for consistency, we examined two APT nanotips for both aging times of 1 and 3 h and the results are consistent for both nanotips, i.e., the

$N_v(t)$ value was greater in the samples aged for 3 h. As we discuss below, the kinetics of Cu precipitation in HSLA-115 is complex and is affected by microstructural defects, such as lath-boundaries and dislocations, and the co-located M_2C carbides. On further aging, we obtain a decrease in the $N_v(t)$ of Cu precipitates in the 16 h condition with a concomitant increase in their $<R_v(t)>$, while the $\phi_v(t)$ is nearly the same as in the 3 h condition, indicating the occurrence of quasi-steady coarsening.

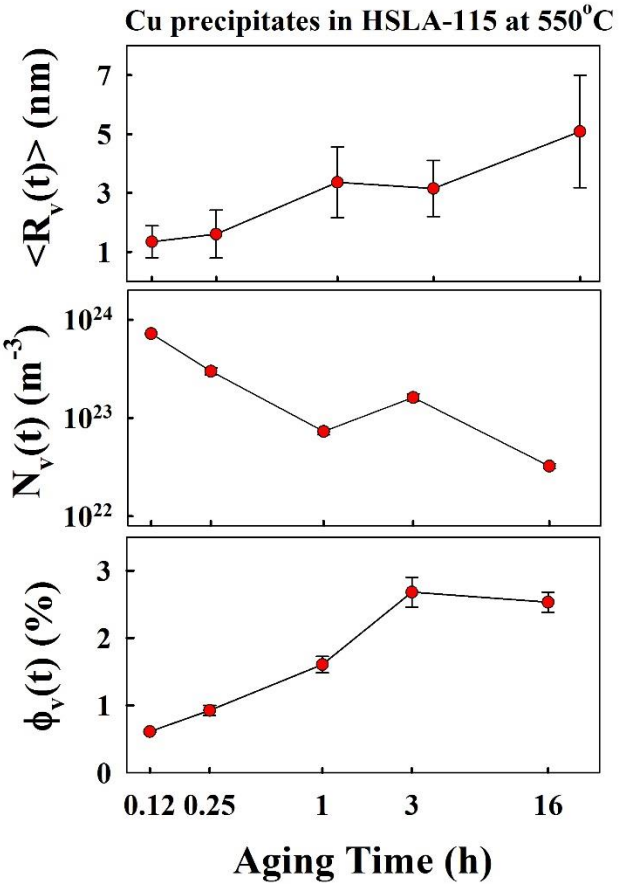

Figure 3.6- Temporal evolution of Cu precipitates in HSLA-115 aged at 823 K (550 ^oC).

The temporal evolution of $<R_v(t)>$, $N_v(t)$ and $\phi_v(t)$ of M_2C carbides in HSLA-115 with aging time at 823 K (550 ^oC) is displayed in Figure 3.7. M_2C alloy carbides are not observed in the as-

quenched state and the 7 min samples. The earliest aging time in which they are observed is in the 0.25 h condition, and thus, their nucleation is preceded by those of Cu precipitates. 3-D APT reconstruction of the 0.25 h sample with two orthogonal views is displayed in Figure 3.8. In this figure, Cu precipitates and M_2C carbides are delineated by 10 at.% Cu isoconcentration- (red) and by 5 at.% (C + Cr + Mo) isoconcentration-surfaces (dark-green) respectively. A coarse cementite precipitate, delineated by 5 at.% C isoconcentration surface (black) is also observed in this reconstruction. To the extreme left in this figure, the distribution of carbon atoms in and around the cementite particle is shown. Compositional analysis of this precipitate resulted in a composition of 72.0Fe-22.7C-0.9Mn-2.4Ni-0.7Cr-0.4Mo-0.3V-0.4Cu-0.2Si at.%, which is compatible with cementite, Fe_3C. We also observe heterogeneously distributed Cu precipitates at the α-Fe/cementite interface. A more detailed description of the partitioning behavior of various alloying elements across the α-Fe/cementite interface is beyond the scope of this work.

Similar to what we observed for the Cu precipitates, a second burst of nucleation of M_2C carbides occurs between 1 and 3 h with their $N_v(t)$ reaching its maximum value of $1.5x10^{23}$ m^{-3} at 3 h. The $N_v(t)$ of M_2C carbides was greater at 3 h in each of the two APT nanotips examined for these aging times. Secondary burst of nucleation of M_2C carbide precipitates was also observed by Allen et al.[125] in AF1410 steels between 1 and 2 h of aging at 510^{o}C. On further aging, we obtain a decrease in the $N_v(t)$ of the M_2C carbides in the 16 h condition, with a concomitant increase in their $<R_v(t)>$, while the $\phi_v(t)$ is nearly same as in the 3 h condition, indicating the onset of quasi-steady coarsening.

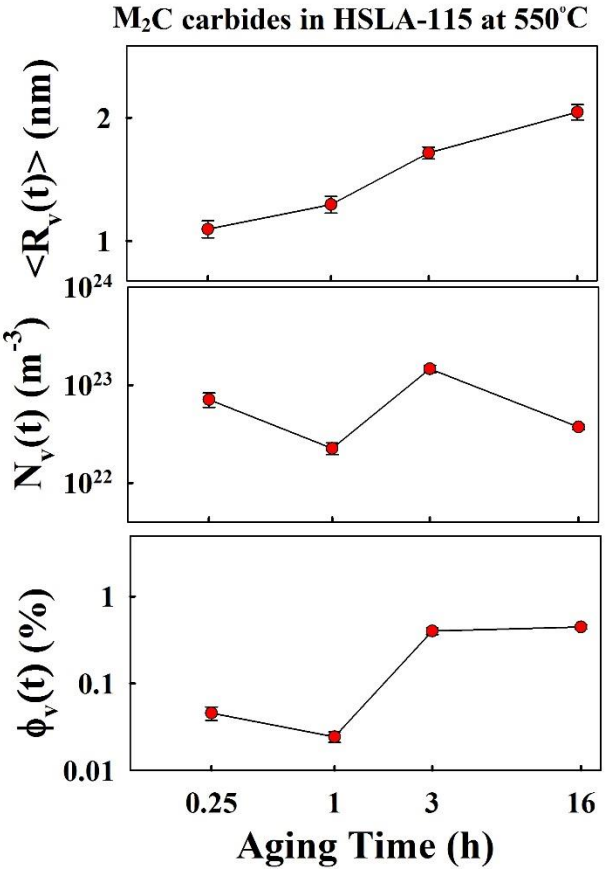

Figure 3.7- Temporal evolution of M_2C carbides in HSLA-115 aged at 823 K (550 ^oC).

It is noted that there could be slight deviations in the measured precipitates' statistics for both Cu precipitates and M_2C carbides due to experimental artifacts, such as trajectory overlap effects, as is described in the experimental section. Despite these limitations, the results described above reveal the co-existence of M_2C carbides and Cu precipitates in HSLA-115 aged at 823 K (550 ^oC) and enable us to follow the temporal evolution of its microstructure at sub-nanometric scale in great detail. Additionally, as we demonstrate next, these M_2C carbides are co-located with Cu precipitates at the aging times discussed and are distributed heterogeneously at lath-boundaries and dislocations.

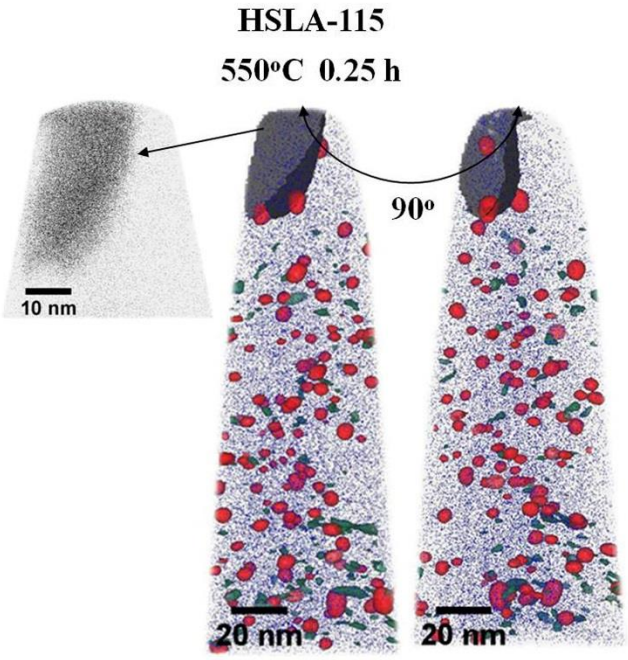

Figure 3.8- 3-D APT reconstruction of 0.25 h HSLA-115 specimen at 823 K (550 °C). Copper precipitates and M_2C carbides are delineated by 10 at.% Cu isoconcentration- (red) and by 5 at.% (C + Cr + Mo) isoconcentration-surfaces (dark-green), respectively. Iron atoms are displayed in blue: only a small fraction is shown for clarity. A coarse cementite precipitate is delineated by a 5 at.% C isoconcentration-surface (black). To the extreme left, the distribution of carbon atoms (black), in and around the cementite particle is displayed.

The 3-D APT reconstructions of the 3 and 16 h specimens with two orthogonal views are displayed in Figures 3.9 and 3.10, respectively. These figures reveal that M_2C carbides (dark-green) are co-located with Cu precipitates (red) and also evident in these figures is the association of these precipitates with dislocations and lath-boundaries: see encircled regions in the figures.

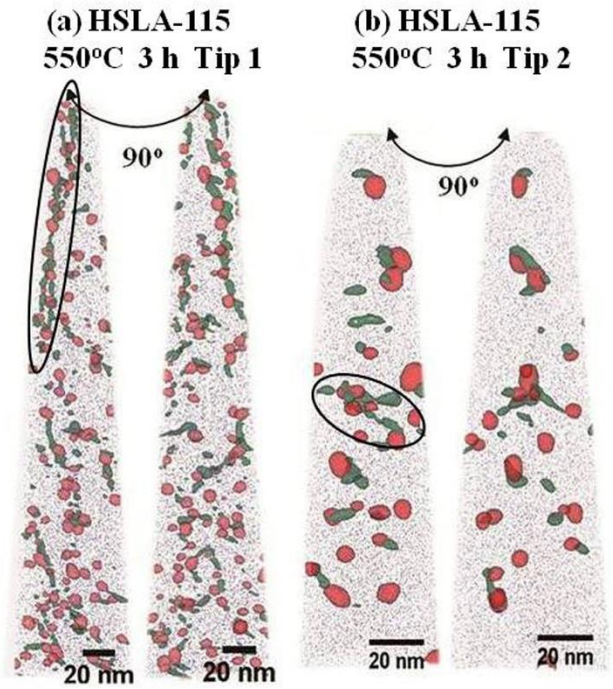

Figure 3.9- 3-D APT reconstructions of 3 h HSLA-115 specimen at 823 K (550 °C) C, (a) Nanotip 1; (b) Nanotip 2. Copper precipitates and M_2C carbides are delineated by 10 at.% Cu isoconcentration- (red) and by 5 at.% (C + Cr + Mo) isoconcentration-surfaces (dark-green), respectively. Iron atoms are shown in blue: only a small fraction is shown for clarity.

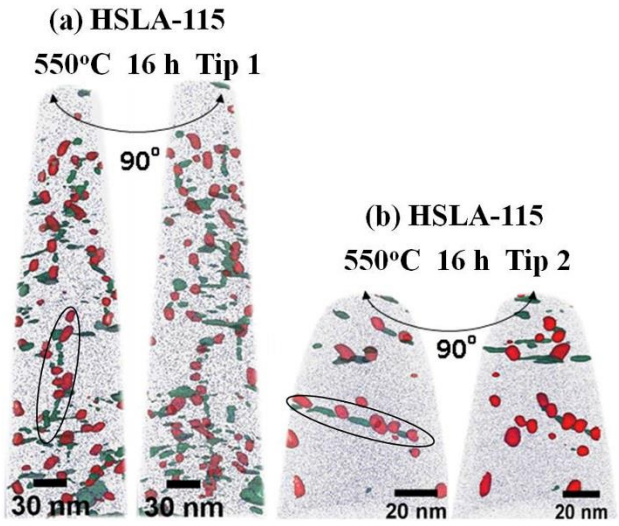

Figure 3.10- 3-D APT reconstructions of 16 h HSLA-115 specimen at 823 K (550 °C), (a) Nanotip 1; (b) Nanotip 2. Copper precipitates and M_2C carbides are delineated by 10 at.% Cu isoconcentration- (red) and by 5 at.% (C + Cr + Mo) isoconcentration-surfaces (dark-green), respectively. Iron atoms are displayed in blue: only a small fraction is shown for clarity.

The collocation of these precipitates is further demonstrated in Figure 3.11(a, b and c), which displays the proximity histogram (proxigram) [126] concentration profiles obtained from M_2C carbides in 1, 3 and 16 h samples, respectively. The apparent rise in the concentration profile of Cu at the α-Fe matrix side near the α-Fe/M_2C carbides interface indicates the geometrical proximity of Cu precipitates and M_2C carbides as the profile is based on the relative distance from the 5 at.% (C + Cr + Mo) isoconcentration surfaces used to delineate the M_2C carbides.

We also observe in Figures 3.9 and 3.10 that the M_2C carbides assume the morphology of rods/needles/laths, which is in agreement with earlier studies [15, 64, 65, 68, 127]. On further aging, we observe in the 64 h specimen that these carbides transform to coarse irregular spheroidal particles, indicating their loss of coherency. One of these carbides obtained in the 64 h sample is displayed in the inset towards the bottom left in Figure 3.11(d). This figure displays the proxigram concentration profiles obtained from this carbide. The composition of this precipitate, as determined from the proxigram, is 49.8Mo-13.3Cr-30.9C-2.1Fe-2.6Mn-0.3V-0.3Ni-0.1Cu-0.1Si at.%. We do not observe any increase in the concentration profile of Cu near the α-Fe/M_2C carbides interface in this proxigram, which indicates that they are no-longer co-located with Cu precipitates and is suggestive of their loss of coherency.

At early aging times, the carbon concentration in M_2C carbides is significantly less than its nominal stoichiometric concentration of 33.3 at.% (Figure (3.11(a,b,c)). A sub-stoichiometric carbon concentration during the initial stages of precipitation of M_2C carbides has been previously reported by Stiller et al.[128] and Carinci et al.[129] In these studies, the carbon concentration was observed to increase in M_2C carbides with increasing aging time and approach the

stoichiometric value, as is also the case in our study. The observed rod/needle/lath-like morphology of M_2C carbide precipitates at early aging times coupled with their composition obtained at 64 h is evidence of the fact that these alloy carbides are M_2C carbides. A more detailed description of the temporal evolution of the chemical composition of M_2C carbides and their morphologies is beyond the scope of this work.

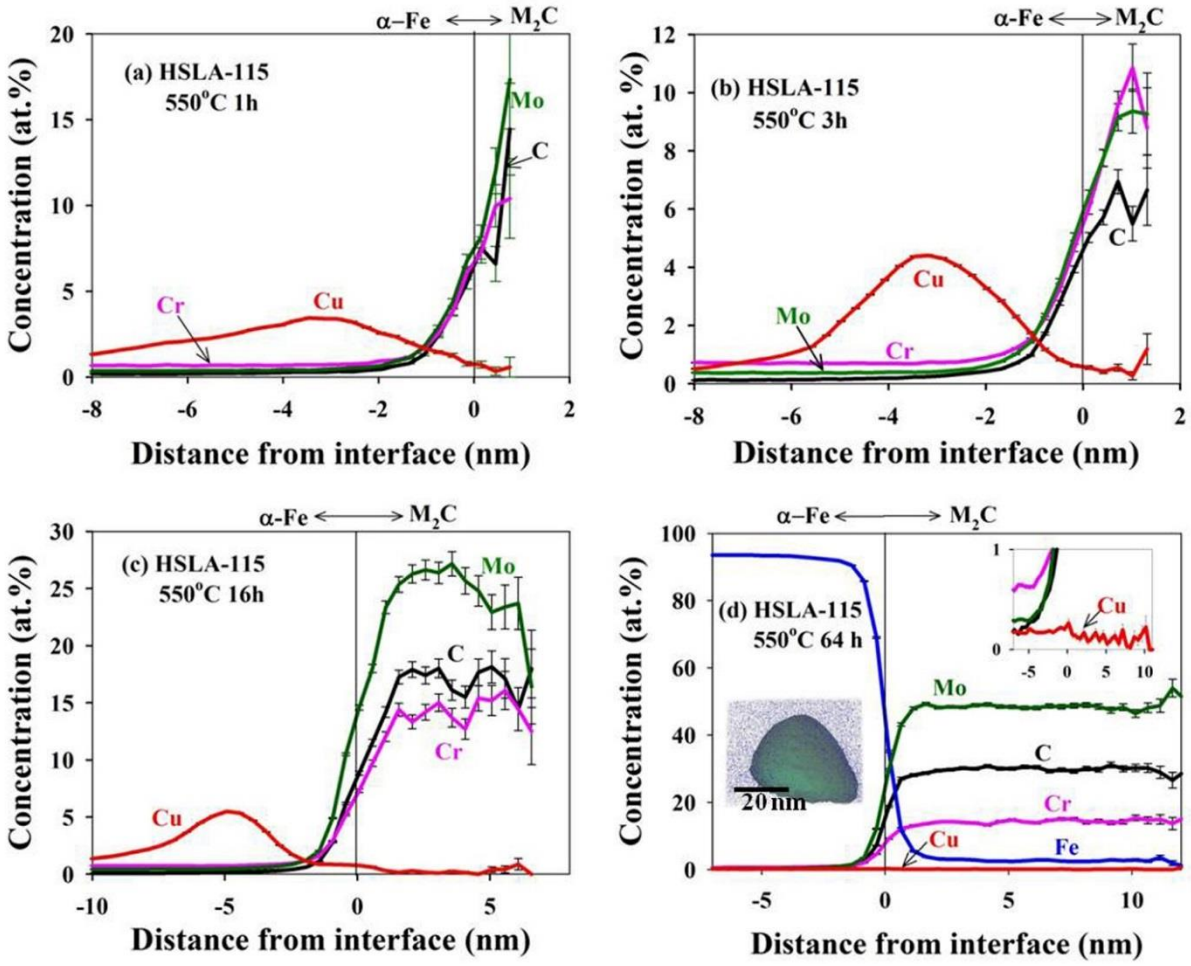

Figure 3.11- Proxigram concentration profiles (at.%) of C, Cr, Mo and Cu obtained from 5 at.% (C + Cr + Mo) isoconcentration-surfaces, which are used to delineate the M_2C carbides in HSLA-115 samples aged at 823 K (550 ^oC) for: (a) 1 h; (b) 3 h; (c) 16 h; and (d) 64 h. The Fe concentration profile is displayed in 11(d). Fiducial marker is placed vertically at the zero of the proxigrams, which is chosen as the inflection point of the Fe-concentration profile.

3.4 Discussion

3.4.1 Mechanical Properties

3-D APT results reveal that aging at 823 K (550 ^{o}C) facilitates the co-precipitation of Cu precipitates and M_2C carbides in HSLA-115. While we observe only Cu precipitates in the 7 min aged condition, both Cu precipitates and M_2C carbides are observed after 0.25 h aging at 823 K (550 ^{o}C), the aging time at which peak YS is attained. The YS of HSLA-115 decreases by only 1.5% at 3 h from its peak YS attained at 0.25 h, Figure 3.3, and the microhardness decreases by only 3.3% between these aging times, Figure 3.2. This is attributed to the strengthening provided by M_2C carbides, which attain their maximum $N_v(t)$ of $1.46\pm0.13 \times 10^{23}$ m^{-3} at 3 h, Figure 3.7. The precipitation strengthening provided by these sub-nanometer sized carbides offsets the softening due to the overaging of Cu precipitates and recovery of the martensitic dislocation substructure in HSLA-115. Mulholland et al.[18] in their 3-D APT study of BA-160 steel also observed co-precipitation of Cu precipitates and M_2C carbides and reported a decrease of only 7% in the YS after 320 h at 723 K (450 ^{o}C) from its peak condition, 5 h at 723 K (450 ^{o}C). Alternatively, in NUCu-140, which does not contain M_2C carbides, a decrease of more than 10% in microhardness occurs by 3 h from its peak microhardness at 0.5 h, Figure 3.2.

Figure 3.12 displays a log-log plot of the temporal evolution of $N_v(t)$ of Cu precipitates at 823 K (550 ^{o}C) in HSLA-115 and NUCu-140. It is noted that the nominal Cu-concentration in HSLA-115 is 1.13 at.%, which is similar to that in NUCu-140 (1.43 at.%), Table 3.1. While the $N_v(t)$ of Cu precipitates in NUCu-140 decreases monotonically with increasing aging times, a second burst of nucleation of Cu precipitates occurs between 1 and 3 h in HSLA-115, with their $N_v(t)$ exceeding 10^{23} m^{-3} in the 3 h condition. This is significantly greater than the $N_v(t)$ at 3 h for NUCu-140

($3.7\pm0.4x10^{22}$ m^{-3}). Thus, besides the additional strengthening contribution from M_2C carbides, the presence of Cu precipitates with a high $N_v(t)$ at 3 h for HSLA-115 also contributes to maintaining a high YS of 972.1 MPa (141 ksi) for this aging state.

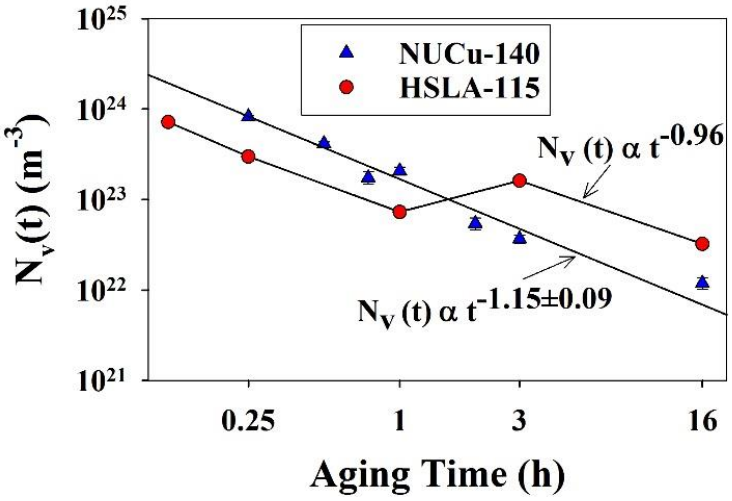

Figure 3.12- Evolution of the number density of Cu precipitates, $N_v(t)$, with aging time for HSLA-115 and NUCu-140 at 823 K (550 ^oC). The APT experiments for NUCu-140 steel for aging times < 3 h are from Hunter's PhD Thesis [43].

It is noted that although the temporal exponent in the $N_v(t)$ plot for HSLA-115, Figure 3.12, in the quasi-stationary coarsening regime is close to -1, as expected for stationary-state coarsening models [130-132], it need not follow these models, as these models are for a two-phase system, the matrix and a single precipitating phase. Precipitation kinetics of Cu precipitates in HSLA-115 is likely affected by high density of dislocations and lath-boundaries in its microstructure as well as the co-located M_2C carbides and is discussed in section 3.4.2.

The lower impact toughness obtained for the 0.25 h aged condition as compared to the as-quenched value for both HSLA-115 and NUCu-140, Figure 3.4, coincides with the attainment of the peak

YS in HSLA-115 and near peak microhardness in NUCu-140. In the fractographs of the HSLA-115 samples, we also observe a change from the ductile fracture mode in the as-quenched condition, Figure 3.5(a), to quasi-cleavage transgranular failure in the 0.25 h condition, Figure 3.5(b). Previous isochronal aging studies of HSLA-100 (aging time ~ 1 h) also reported the co-occurrence of the peak aged condition with low impact toughness at aging temperatures of 723 to 773 K (450 to 500 ^{o}C) [12, 13]. In these studies, improvement in the impact toughness at higher aging temperatures was observed, but with a significant decrease in YS. In the current study, however, for HSLA-115, we observe that the impact toughness does not simply vary inversely with the YS. The impact toughness increases significantly by 67% at 3 h from its low value at 0.25 h with a negligible decrease of only 1.5% in the YS. The interplay between impact toughness and YS is thus complex in HSLA-115 and the influence of secondary phases in its microstructure, such as Cu precipitates, cementite and M_2C carbides may be critical; this is discussed below.

A common microstructural feature in both HSLA-115 and NUCu-140 at 0.25 h is the presence of Cu precipitates, whose $<R(t)>$ is < 2 nm and they are, therefore, assumed to have a metastable b.c.c.-structure and be coherent with the α-Fe matrix [49, 50]. There exist contradictory view points in the literature on the effect of coherent Cu precipitates in α-Fe on impact toughness. Based on the suggestion of Weertman [133], Fine et al.[99, 134] attributed good impact toughness properties at cryogenic temperatures in NUCu-70 (A710-B) to the interaction of screw dislocations with the strain fields of slightly misfitting coherent Cu precipitates in the α-Fe matrix. This interaction was stated to reduce the Peierls stress locally and thus improve the dislocation mobility and therefore, the toughness. This interpretation is inconsistent with the low impact toughness and the quasi-cleavage transgranular failure mode that we observed; Figure 3.5(b) for HSLA-115 at 0.25 h. Low

impact toughness is also obtained at early aging times for NUCu-140 aged at 823 K (550 ^{o}C), Figure 3.4. Other research also has attributed the low impact toughness obtained in similar Cu precipitation strengthened HSLA steels to the presence of coherent Cu (b.c.c.) precipitates [121, 135, 136].

The precipitation of coherent Cu precipitates occurs at early aging times and coincides with the formation of metastable cementite in these steels, which is known to be deleterious to impact toughness [15]. In the present study, we observed a coarse cementite precipitate in the 0.25 h aged condition in HSLA-115 by APT, Figure 3.8. Formation of cementite in similar steels, such as HSLA-100, due to autotempering of martensite during the quenching treatment has been reported by other researchers [115, 137]. Cementite formation may also take place during early aging times due to the decomposition of retained austenite and tempering of martensite, as reported for NUCu-150 by Isheim et al.[16] and for BA-160 by Mulholland et al.[18]. The presence of cementite, therefore, makes it a challenging task to study in isolation the effect of coherent Cu precipitates on impact toughness.

We observe a change from quasi-cleavage transgranular failure for the 0.25 h condition, Figure 3.5(b), to the ductile mode of failure in the 3 h condition, Figure 3.5(c), in HSLA-115. This is also reflected in the significantly higher impact toughness (67% higher) and elongation to failure (16 % higher) obtained for the 3 h condition when compared to the 0.25 h aged condition. Improvement in the impact toughness of HSLA-115 at 3 h may be attributed to the combination of precipitation of fine M_2C carbides [15, 18], overaging of Cu precipitates, tempering of martensite, and possibly dissolution of cementite. On aging beyond 3 h, impact toughness in HSLA-115 monotonically

deteriorates with increasing aging times, despite the concomitant decrease in YS. The quasi-cleavage transgranular mode of failure, Figure 3.5(d and e), is observed at aging times of 16 and 64 h, respectively, as opposed to the ductile mode of failure observed in the 3 h condition. This trend is also observed in the elongation to failure values, which decrease monotonically after 3 h, Figure 3.3(c). The extremely low impact toughness at 64 h is attributed to the severe coarsening of the microstructure. While the coarse morphology of M_2C carbides and Cu precipitates at this aging time would aid in easy crack nucleation, the coarser-polygonal ferrite grains would provide less resistance to crack-propagation.

3.4.2 Temporal evolution of Cu precipitates and M_2C carbides in HSLA-115

At 823 K (550 ^oC), precipitation of Cu occurs first in HSLA-115 and is followed by nucleation of M_2C carbide precipitates, most of which are observed to be co-located with the Cu precipitates. This is consistent with Mulholland et al.'s [18] observations for BA-160 and of Tiemens et al.'s [19, 138] for ultrahigh-strength carburized steel and indicates that Cu precipitates may be acting as heterogeneous sites for M_2C carbide nucleation. Copper precipitates have been known to act as nucleation sites in other systems, such as for $Ni_3(Ti,Al)$ intermetallics in maraging steels [139] and the Laves phase in Cr-bearing ferritic steels [140] Additionally, we observed heterogeneous distributions of M_2C carbides at dislocations and lath-boundaries (see encircled regions in Figures 3.9 and 3.10). M_2C carbides are known to nucleate heterogeneously at dislocations and grain boundaries [62], and therefore, Cu precipitates may also indirectly favor the precipitation of M_2C carbides by pinning the dislocations and lath-boundaries, which would result in more heterogeneous nucleation sites for M_2C carbides [13, 141]. Cobalt has traditionally been used in secondary-hardening steels to facilitate M_2C carbide nucleation on dislocations. Cobalt inhibits

dislocation recovery during the tempering treatment of martensitic steels, which ultimately results in a finer dispersion of dislocation-nucleated M_2C carbides [15]. Tiemens et al.[19, 138] reported that Cu precipitates can assist M_2C carbide precipitation in ultrahigh-strength carburized steel, but to a lesser degree than Co. They suggested that alloying additions of Cu could be used as a lower cost substitute for Co, to facilitate M_2C carbide precipitation. The role of dislocations and lath-boundaries in the microstructure of HSLA-115, as well as the co-located M_2C carbides in influencing the precipitation kinetics of Cu precipitates is discussed below.

As described before, a significant fraction of the Cu precipitates in HSLA-115 are distributed heterogeneously at dislocations and lath-boundaries and are also co-located with M_2C carbides, Figures 3.9 and 3.10. The second burst of nucleation of Cu precipitates in HSLA-115 between 1 and 3 h, Figure 3.6, is likely the result of these interactions of Cu precipitates with dislocations, lath-boundaries and M_2C carbides. Other researchers have reported the influence of defects in the microstructure of similar low-carbon martensitic steels on the kinetics of Cu-precipitation. Bhagat et al.[121] measured electrical resistivity changes during isothermal aging of HSLA-100 and obtained a significantly smaller activation energy, 114-118 kJ/mol corresponding to the diffusion of Cu atoms in HSLA-100 than the activation energy associated with diffusion of Cu in α-Fe, ~284 kJ/mol [142]. They suggested that the high dislocation-density of the martensitic matrix in HSLA-100 influences Cu precipitation significantly by promoting short-circuit diffusion of Cu atoms. Yang et al.[143] developed a numerical model to simulate the competitive precipitation of Cu precipitates at lath-boundaries, dislocations and homogeneous nucleation in the matrix in a low-carbon martensitic steel. Their results for the steel containing 1.5 wt. % Cu and aged at 823 K (550 ^{o}C) indicated that nucleation of Cu precipitates occurred preferentially at lath-boundaries and

dislocations and that their precipitation kinetics was significantly different from that of the homogeneously distributed Cu precipitates in the matrix. The authors, however, ignored the influence of carbon on Cu precipitation in this model. Maruyama et al.[144] studied the influence of the matrix's microstructures on Cu precipitation in low alloy ferritic and martensitic steels. Their TEM investigation revealed that most of the Cu precipitated on internal dislocations in laths and on lath-boundaries in the martensitic steel, while the Cu precipitates in the ferritic steel were homogeneously distributed in the matrix.

In addition to the influence of microstructural defects, evolution of Cu precipitates is likely to be affected by the co-located M_2C carbides in HSLA-115. As is described above, precipitation of Cu precedes the precipitation of M_2C carbides in HSLA-115 at 823 K (550 ^oC). Nevertheless, M_2C carbides are observed as early as 0.25 h. Subsequently, M_2C carbide precipitates can play a role in influencing the second burst of nucleation of Cu precipitates that occurs between 1 and 3 h. They can act as nucleation sites for Cu precipitates and can inhibit the dislocation recovery by pinning dislocations and thus in process increase the density of heterogeneous sites for nucleation of Cu precipitates.

3.5 Summary and Conclusions

In this research, we demonstrated that aging at 823 K (550 ^oC) facilitates the co-precipitation of sub-nanometric sized Cu precipitates and M_2C carbides in a high-strength low-alloy structural steel, HSLA-115. We correlated the obtained mechanical properties for different aging times at 823 K (550 ^oC) with the temporal evolution of these precipitates, studied using 3-D APT. Precipitation strengthening provided by M_2C carbides offsets the softening due to the overaging

of Cu precipitates and tempering of the martensitic matrix. Therefore, HSLA-115 aged at 823 K (550 ^{o}C) maintains high YS even after prolonged aging, compared to alloys relying solely on Cu precipitation strengthening, such as NUCu-140 steels. Resistance to softening on prolonged aging is highly beneficial as it is generally observed that optimum impact toughness in Cu precipitation-strengthened steels is obtained only in a microstructure overaged with respect to Cu precipitates, as was the case in the present study. The extended yield strength plateau afforded by the M_2C carbide precipitates can be used as a design principle to optimize strength and toughness at the same time. Major findings of this work are summarized below:

1. Co-precipitation of Cu precipitates and M_2C carbides is shown for the first time in a U.S. Naval high-strength low-alloy structural steel, designated as HSLA-115, using 3-D APT. Precipitation of Cu occurs first during the isothermal aging at 823 K (550 ^{o}C) and is followed by nucleation of M_2C carbides, which are observed to be co-located with Cu precipitates. This suggests that Cu precipitates act as heterogeneous sites for M_2C carbides nucleation.

2. Following the precipitation of M_2C carbides, a second burst of nucleation occurs for both the Cu precipitates as well as M_2C carbides between 1 and 3 h at 823 K (550 ^{o}C), (Figures 3.6 and 3.7). 3-D APT reconstructions reveal that a significant proportion of these precipitates are distributed heterogeneously at dislocations and lath-boundaries and are also co-located with one another, (Figures 3.9 and 3.10). The interactions of these precipitates with each other and with different microstructural defects render their precipitation kinetics quite complex in HSLA-115, as can be inferred from the second burst of nucleation of these precipitates.

3. M_2C carbides assume the morphologies of rods/needles/laths as they grow and then transform to coarse irregular spheroidal particles with long-term aging. M_2C carbides with sub-stoichiometric carbon concentrations are observed during the initial stages of their precipitation, but the carbon concentration of these carbides approaches the stoichiometric value with increasing aging time at 823 K (550 ^oC).

4. During aging at 823 K (550 ^oC), the microhardness in HSLA-115 decreases by only 3.3 % at 3 h of aging from its peak-aged value at 0.25 h. In contrast, a decrease of more than 10 % in microhardness occurs at 3 h in NUCu-140 aged at 823 K (550 ^oC) from its peak-aged value at 0.5 h, Figure 3.2. This is primarily due to the precipitation strengthening provided by M_2C carbides, which offsets the softening due to the overaging of Cu precipitates and recovery of the martensitic dislocation substructure in HSLA-115. Additionally, the occurrence of a second burst of nucleation of Cu precipitates results in a significantly higher $N_v(t)$ (~$1.6x10^{23}$ m^{-3}) of Cu precipitates in HSLA-115 in the 3 h aged condition as compared to their $N_v(t)$ in the 3 h aged NUCu-140 (~$3.7x10^{22}$ m^{-3}), Figure 3.12; which also contributes to increased resistance to softening in HSLA-115 as compared to NUCu-140.

5. The impact toughness variation in HSLA-115 with aging time at 823 K (550 ^oC) is quite complicated and does not simply vary inversely with the yield strength (YS), Figure 3.4. Upon aging at 823 K (550 ^oC), the impact toughness at 255.2 K (-17.8 ^oC) first decreases at 0.25 h. It then increases significantly by 67 % to attain its maximum value in the 3 h aged condition, with a concomitant decrease of only 1.5 % in its YS. This trend is also depicted by fractographic surfaces, Figure 3.5, which show a ductile mode of failure for both the as-quenched and the 3 h aged sample, while transgranular quasi-cleavage failure occurs for the 0.25 h aged sample.

While the low impact toughness at 0.25 h of aging may be partially attributed to the cementite phase and the improved toughness at 3 h to the precipitation of fine M_2C carbides; the influence of Cu precipitates on impact toughness is unclear. A monotonic decrease in both impact toughness and YS occurs after 3 h, which can perhaps best be attributed to the coarsening of microstructure.

6. HSLA-115 aged at 823 K (550 ^oC) for 3 h maintains a YS of ~972 MPa (141 ksi) with an impact toughness of ~188.0 J at 255.2 K (-17.8 ^oC) and ~100 J at 188.6 K (-84.4 ^oC) and elongation to failure of ~24 %. These mechanical properties indicate that utilizing an aging treatment that leads to the precipitation of M_2C carbides with Cu precipitates provides an opportunity to design higher YS steels to further reduce the weight of structural components. Also, the extended YS plateau attained due to additional strengthening by M_2C carbides can be used as a design principle to optimize strength and toughness at the same time.

Chapter 4

Carbon Redistribution and Carbide Precipitation in a High-Strength Low-Carbon HSLA-115 Steel Studied on a Nanoscale by Atom-Probe Tomography

Abstract

HSLA-115 is a newly developed Cu-bearing high-strength low-carbon martensitic steel for use in Naval structural applications. This research provides, for the first time, a comprehensive compositional analysis of carbon redistribution and associated complex phase transformations in an isothermal aging study of HSLA-115 at 823 K (550 ^{o}C). Specifically, we characterize carbon segregation at lath-boundaries, grain-refining niobium carbonitrides, cementite, and secondary-hardening M_2C carbides, in addition to copper precipitation, by 3-D atom-probe tomography (APT). Segregation of carbon (3-6 at. % C) is observed at martensitic lath-boundaries in the as-quenched and 0.12 h aged microstructures. On further aging, carbon redistributes itself forming cementite and M_2C carbides. Niobium carbonitride precipitates do not dissolve during the austenitizing treatment and are inherited in the as-quenched and aged microstructures; these are characterized along with cementite by synchrotron X-ray diffraction and APT. Sub-nanometer sized M_2C carbide precipitates are observed after the formation of Cu precipitates, co-located with the latter, indicating heterogeneous nucleation of M_2C. The temporal evolution of the composition and morphology of M_2C carbides at 823 K (550 ^{o}C) is described using APT; their precipitation kinetics is intertwined with Cu precipitates, affecting the bulk mechanical properties of HSLA-115. Phase compositions determined by APT are compared with computed compositions at thermodynamic equilibrium using ThermoCalc.

4.1 Introduction

Low-carbon (<0.06 wt.%) martensitic *high-strength low-alloy* (HSLA) steels replaced the higher carbon containing *high-yield* (HY) steel grades as structural materials for Naval vessels during the 1980's [1, 11]. The low-carbon concentration of HSLA steels improves weldability, which reduces the preheating requirements and decreases considerably the processing cost [145]. To meet the strength requirements, Cu was added in HSLA-80 and HSLA-100 steels to utilize strengthening from Cu precipitates [10, 11, 146]. The numerals-80 and -100 denote the minimum obtainable tensile yield strength (YS) in ksi (1 ksi = 6.9 MPa). Since the approval of HSLA-100 for surface combatant ships in 1989, efforts were made by the US Navy to develop steels with similar compositions as HSLA-100 but with higher YS, while maintaining desirable impact toughness and weldability. These efforts led to the development of an HSLA-115 steel, whose composition is slightly richer in Cu, Ni, and Mo than HSLA-100 (composition-2) [2]. HSLA-115 was approved for plate production in 2009 [2] and has been used in the flight deck of the CVN-78 aircraft carrier [7] and is the focus of this chapter.

Traditionally, commercial processing practices of HSLA-100 steels have employed an austenitizing, water-quenching and an aging treatment at temperatures exceeding 873 K (600 ^{o}C), which results in a tempered-martensitic microstructure and over-aged Cu precipitates [8, 11]. However, Wilson et al. [11] reported rapid decrease in its YS for aging temperatures between 894 K (621 ^{o}C) and 950 K (677 ^{o} C), which limits its applications. In the previous chapter and associated article on HSLA-115 [147], it was demonstrated that sub-nanometer sized M_2C carbides (M is Mo, Cr, Fe) can be co-precipitated with Cu precipitates in high number density (~10^{23} m^{-3}) during isothermal aging at 823 K (550 ^{o}C). This results in an extended YS plateau during aging,

compared to alloys relying solely on Cu precipitation-strengthening and can be used as a design principle to simultaneously optimize strength and impact toughness and develop higher strength steels [147]. Besides the two precipitating phases described above, grain-refining niobium carbonitride precipitates, Nb(C,N), and the embrittling cementite phase are other important microstructural constituents of HSLA-115 and similar HSLA-100 steels, which influence phase transformations and overall mechanical properties [137]. Microalloying additions of Nb (0.02-0.06 wt. %) are added to HSLA steels to form Nb(C,N) precipitates, which pin austenite grain boundaries during hot-rolling and austenitizing treatments and thus prevent excessive grain growth [40-42]. The dissolution of these precipitates has been shown to cause severe grain coarsening, as seen for instance in simulated weld heat-affected zones of HSLA-100 steel [137, 148]. Thus, the stability of Nb(C,N) precipitates plays a key role in controlling grain size, which in turn affects hardenability, strength and toughness properties. Cementite, alternatively, is associated with poor impact toughness properties in steels [15]. It forms due to the decomposition of retained austenite and low-carbon martensite and/or at the expense of the transient primary carbides, such as epsilon carbide, $Fe_{2.4}C$ and the eta-carbide, Fe_2C [149].

In this chapter, we provide a systematic nanoscale analyses of carbon redistribution, segregation, and carbide precipitation for HSLA-115, isothermally aged at 823 K (550 ^{o}C) using 3-D atom-probe tomography (APT). 3-D APT is a unique technique that provides three-dimensional spatial information of atoms as well as their chemical identities (including that of the lighter elements, such as carbon) with a sub-nanoscale spatial resolution [20, 21, 23]. We first describe, the carbon redistribution that occurs during quenching after the austenitizing treatment, which in turn results in carbon-segregation at martensitic lath-boundaries. We then characterize niobium carbonitride

and cementite precipitates in terms of their composition, morphology, and the partitioning behavior of various alloying elements between the α-Fe (b.c.c.) matrix and these precipitates; the evolution of these carbides is also investigated by synchrotron X-ray diffraction experiments, performed at the Advanced Photon Source. Lastly, we describe in detail, the temporal evolution of the composition and morphology of M_2C carbides at 823 K (550 ^oC). Their evolution in terms of mean radii, number densities, and volume fractions was described in correlation with the mechanical properties in the previous chapter and in the associated article [147]. APT measured chemical compositions of the carbide precipitates- niobium carbonitride, cementite, and M_2C carbide (at long aging times) are also compared with the respective computed compositions at thermodynamic equilibrium using ThermoCalc.

In recent years, quantitative information from APT experiments combined with the theory-driven computational design-based approach have been used to design a blast-resistant BA-160 steel, which is a low-carbon martensitic steel, precipitation-strengthened by Cu precipitates and M_2C carbides [18, 44, 150]. Precipitate size distributions obtained in 3-D from APT can be used to develop models, predicting the YS of precipitation-hardened alloys [73]. APT with its sub-nanoscale spatial resolution allows one to determine the concentrations of alloying elements at the heterophase interfaces and at grain boundaries, which helps in understanding the kinetics of complex phase transformations, such as grain boundary precipitation [151], growth mode of cementite during tempering of steels [152], etc. Using APT, one can detect precipitates at early aging times and hence determine the temporal evolution of their compositions, which can provide deep insights into their nucleation kinetics [153] and has also been suggested to be useful in estimating the remnant lifetime of steel components in power plant steels [154].

4.2 Experimental methods

The overall chemical composition of HSLA-115 steel, as measured using optical emission spectroscopy is displayed in Table 4.1. HSLA-115 steel samples were subjected to two consecutive austenitizing treatments of 35 min each at 1185 K (912 °C), and each austenitizing treatment was followed by water-quenching to room temperature. Multiple austenitizing treatments with shorter holding times as compared to the single austenitization of the same total duration, reduce the formation of large isolated austenite grains [11]. The as-quenched samples were then isothermally aged at 823 K (550 ^{o}C) for aging times ranging from 0.12 to 256 h and were then water-quenched to room temperature. High intensity synchrotron X-ray diffraction (XRD) scans were performed on polished samples having a final polish of 0.06 μm colloidal silica at the 5-IDB beam line at the Advanced Photon Source (Argonne National Laboratory, Argonne, IL, USA). Scans were performed from 2θ ranging from 9.995° to 33.500° using a step size of 0.015°, a count time of 3 s per step, and a wavelength of 0.71 Å. At each step, the sample was rocked through 0.75^{o} in θ to reduce preferential orientation effects. Nanotips for APT experiments were prepared by first cutting blanks with dimensions of approximately 0.3x0.3x10 mm^3. These blanks were then electropolished at room temperature using a two-step electropolishing procedure, the details of which are provided elsewhere [147]. APT experiments were performed with a Cameca local-electrode atom probe (LEAP) 4000X-Si tomograph, using a pulsed ultraviolet (wavelength = 355 nm) picosecond laser, with energy of 30 pJ per pulse, a pulse repetition rate of 500 kHz, and an average evaporation rate (number of ions per pulse) of 2 %. The samples were analyzed at a specimen base temperature of 60 K (-213 ^{o}C) in ultrahigh vacuum (< 10^{-8} Pa) and the data obtained was analyzed using the program IVAS 3.6 (Cameca, Madison, WI). The chemical compositions of the different microstructural features, identified by APT, are obtained using the proximity

histogram (proxigram) concentration profile method [126] and the errors reported are ±2σ, where σ is obtained from counting statistics [53] and is given by,

$$\sigma = \sqrt{\frac{c_i\,(1-\,c_i)}{N}} \qquad 4.1$$

where c_i is the measured concentration of element i and N is the total number of atoms in the sampled volume. It is noted that the average composition of the different microstructural features is determined after taking the weighted average of their core concentrations (based on the total number of atoms). Since the analysed volume decreases significantly (smaller number of total atoms, N) toward the core of the microstructural features, the weighted average is a more accurate representation of their composition. The APT mass spectra of the carbide precipitates- Nb(C,N), cementite, and M_2C carbides are also presented here, since it is important to explain in detail how the compositions of these phases were obtained, which is not trivial due to critical isobaric peak overlaps and various complex-molecular ion peaks in these mass spectra. Thermodynamic calculations are performed using ThermoCalc, version S, and the thermodynamic data is obtained from the TCFE6 steel database (SGTE).

Table 4.1- Chemical composition of HSLA-115, as measured by optical emission spectroscopy

Elements	**Fe**	**Cu**	**Ni**	**Mn**	**Si**	**Al**	**Mo**	**Cr**	**Nb**	**C**	**V**	**N**
wt. %	Bal.	1.29	3.37	0.97	0.22	0.02	0.56	0.64	0.02	0.05	<0.01	0.016
at. %	Bal.	1.13	3.21	0.99	0.44	0.04	0.33	0.69	0.012	0.23	<0.01	0.064

4.3 Results and Discussion

4.3.1 Mechanical Properties

Tensile yield strength (YS), ultimate tensile strength (UTS), and elongation-to-failure for HSLA-115 (at room temperature) in the as-quenched condition and for samples aged at 823 K (550 ^{o}C) for different aging times are listed in Table 4.2. The YS values are also plotted with Charpy impact energy (measured at 255 K (-17.8 ^{o}C)) for these samples in Figure 4.1. These results reveal an increase of 67 % in impact toughness after 3 h aging from its value obtained in the 0.25 h aged condition, with a negligible decrease of 1.5% in YS. More detailed discussion on these mechanical properties is provided in previous chapter and in the associated article [147], where we correlated the co-precipitation of M_2C carbides with Cu precipitates in HSLA-115 to this extended YS plateau attained during aging at 823 K (550 ^{o}C).

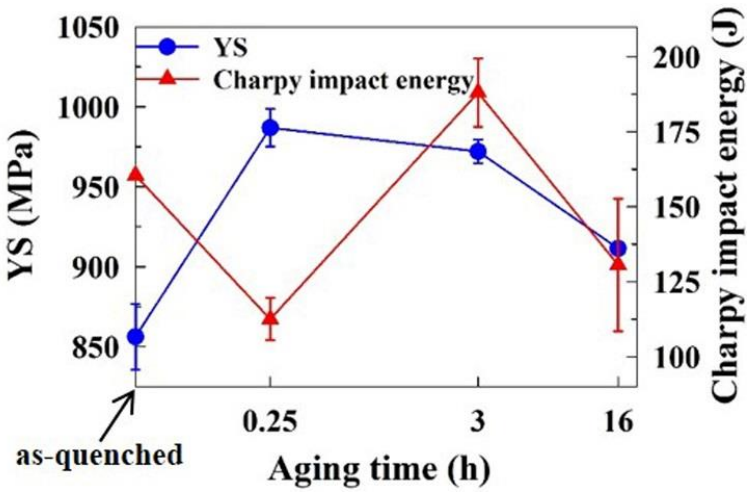

Figure 4.1- Yield Strength (YS) at room temperature and Charpy impact energy at 255 K (-17.8 ^{o}C) for HSLA-115 in the as-quenched condition and after aging at 823 K (550 ^{o}C) for 0.25, 3, and 16 h.

Table 4.2- Tensile test results at room-temperature for HSLA-115 in the as-quenched condition and after aging at 823 K (550 ^{o}C) for 0.25, 1, 3, and 16 h

Aging time (h)	YS (MPa)	UTS (MPa)	Elongation to failure (%)
as-quenched	856.3±20.6	1119.2±6.9	18.5±1.0
0.25	986.8±11.8	1034.5±12.2	21.4±0.6
1	967.6±14.3	1004.2±7.0	22.4±0.7
3	972.1±7.5	997.2±9.8	24.8±1.0
16	911.4±3.4	939.5±6.6	22.2±0.6

4.3.2 Synchrotron X-ray Diffraction (XRD)

Figure 4.2 shows the XRD scans for HSLA-115 in the as-quenched condition, and for samples aged at 823 K (550 ^{o}C) for 0.25, 3, and 16 h. We observe reflections corresponding to niobium carbide (NbC) in the as-quenched sample as well as in all the aged samples, Figure 4.2(a). Cementite (θ_{cem}) peaks are not observed in the as-quenched sample but are present in all the aged samples, Figure 4.2(a), confirming the formation of cementite during aging at 823 K (550 ^{o}C). It is noted that the low overall carbon concentration of HSLA-115 (0.23 at. % or 0.05 wt. %) limits the volume fraction of these carbides to less than 1 %. Additional difficulty arises in characterizing cementite due to the overlap of its largest intensity reflection with that of $(110)_{\alpha}$ reflection [18]. Volume fraction of austenite in the as-quenched sample, as calculated using the direct comparison method [155] is less than 1 %. Low volume fraction of retained austenite is anticipated in the as-quenched microstructure of such low-carbon low-alloy steels, and is in agreement with the findings for similar HSLA-100 steels [12]. Additionally, this retained austenite is unstable on aging, as is evident from the decrease in the intensity of the $(200)_{\gamma}$ reflection in the XRD scans of the aged samples, Figure 4.2(b).

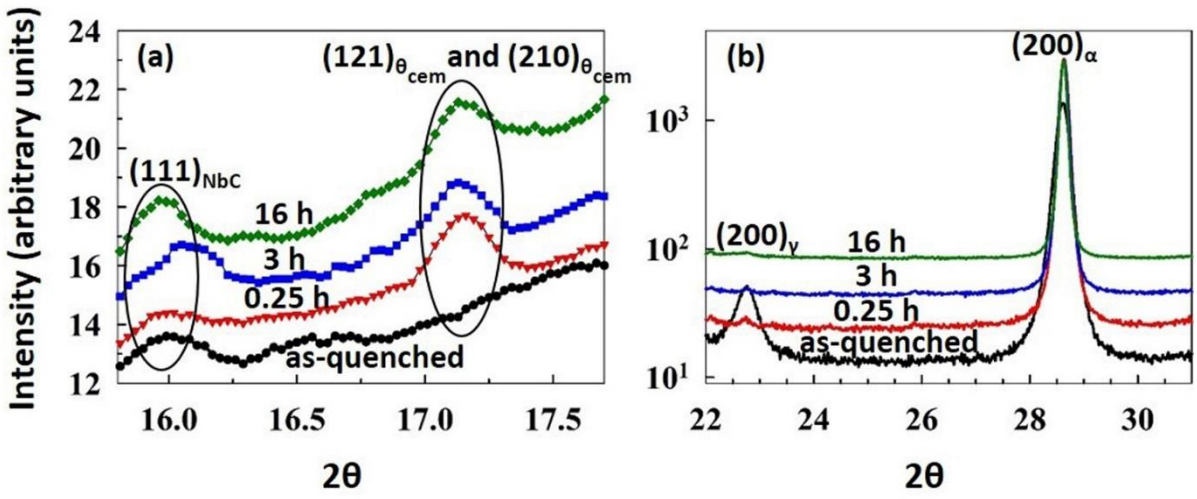

Figure 4.2- Synchrotron X-ray diffraction scans of the as-quenched HSLA-115 sample and those aged at 823 K (550 ^{o}C) for 0.25, 3, and 16 h. The subscripts, θ_{cem} and NbC on the reflection indices in (a) refer to niobium carbide and cementite respectively, while the subscripts, γ and α in (b) refer to austenite and ferrite respectively.

4.3.3 Atom-Probe Tomography

4.3.3.1 Carbon-segregation at martensitic lath-boundaries

We observe enrichment of carbon at several regions in the 3-D APT reconstruction of the as-quenched sample, Figure 4.3. These C-enriched regions are marked as 1, 2, and 3 in Figure 4.3 and are delineated by 1 at. % C isoconcentration surfaces. Proximity histogram (proxigram) concentration profiles with respect to distance from these isoconcentration surfaces are displayed in Figure 4.4 (a), (b), and (c) for regions 1, 2, and 3 respectively.

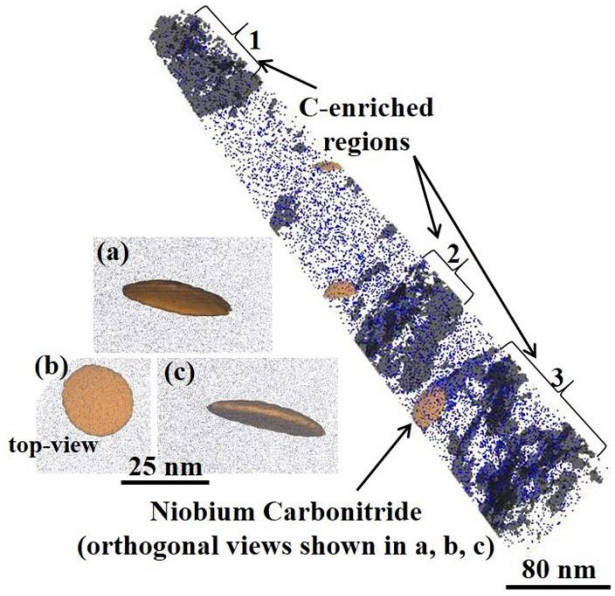

Figure 4.3- 3-D APT reconstruction of the as-quenched HSLA-115 sample. C-enriched regions are delineated by 1 at. % C isoconcentration surfaces (black). Niobium carbonitride precipitates are delineated by 15 at. % (Nb + C) isoconcentration surfaces (brown). Only a fraction of the Fe atoms is displayed (blue dots) and the other alloying element atoms are omitted for the sake of clarity.

Carbon concentrations in the core of the C-enriched regions (~2 nm region at the far right-hand side of the proximity histograms in Figure 4.4) are 3.6 ± 0.1, 6.2 ± 0.1, and 6.4 ± 0.1 at. % for regions 1, 2, and 3 respectively, while the average carbon concentration of the α-Fe matrix in proximity of these regions, as obtained from the 2.5 nm region at the far left-hand side of the proximity histograms in Figure 4.4 is 0.06 ± 0.01 at. %. It is noted that the methodology described by Geuser et al.[156] that uses the distribution of isolated atoms in atom-probe reconstructions provides an alternative method to determine the matrix concentrations of alloying elements. However, detailed analysis using this method is beyond the scope of this work since proximity histogram concentration profiles provide the C concentrations in the C-enriched regions as well as in the α-Fe matrix, as a function of distance from the interface between them.

Concentration profiles in Figure 4.4 also reveal that the enrichment of carbon results mainly in the depletion of Fe in these regions, while the alloying elements- Ni, Cu, Mn, Cr, and Mo exhibit negligible partitioning between the α-Fe matrix and C-enriched regions. Silicon, however, behaves differently as its concentration is enhanced near the interface with respect to its α-Fe matrix concentration (most prominent in Figure 4.4(c)), but decreases towards the inner-core of the C-enriched regions at the far right-hand side of the concentration profile. This is suggestive of Si being rejected from these C-enriched regions.

Several other studies have also reported similar C-enriched regions with varying carbon concentrations from 2-10 at. %, and have interpreted their results as carbon-segregation at martensitic lath-boundaries or as thin-austenitic films at these boundaries [157-161]. Carbon segregation in the as-quenched sample suggests that carbon diffusion occurs from the freshly formed martensite during quenching. This process is facilitated due to the extremely low solubility of carbon in lath-martensite [162], coupled with a high martensite-start temperature (M_s) of HSLA-115. The M_s temperature of HSLA-115, as calculated from Andrew's empirical formula, is 705 K (432 ^oC) [163], which is in good agreement with the measurements of the M_s temperature of ~ 693 K (420 ^oC) for similar HSLA-100 steels from dilatometry experiments [11, 137]. While APT provides direct evidence of carbon segregation, the same conclusion has been made based on electrical resistivity measurements by Speich [164], who suggested that most of the carbon segregates to dislocations and lath-boundaries in low-carbon as-quenched lath martensites (C < 0.2 wt.%). In the present study, we also measure much lower carbon concentration of 0.08 at. % in the α-Fe matrix (excluding the C-enriched regions), as compared to 0.21 at. % C measured for

the entire analyzed volume of the as-quenched APT sample, which is close to the alloy's overall carbon concentration, 0.23 at. %, Table 4.1.

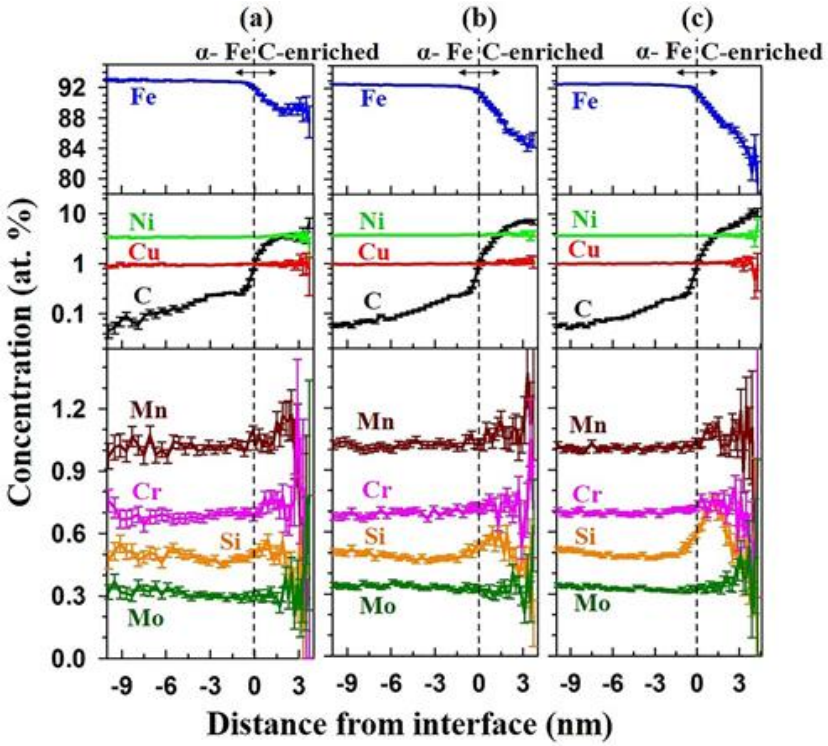

Figure 4.4- Proximity histogram concentration profiles (at. %) of Fe, C, Ni, Cu, Mn, Cr, Si, and Mo for C-enriched regions-1, 2, and 3 in Figure 4.3 and their vicinity are displayed in (a), (b), and (c) respectively. These C-enriched regions are delineated by 1 at. % C isoconcentration surfaces in Figure 3, which is the 3-D APT reconstruction of the as-quenched HSLA-115 sample. Ordinate axis of the plots displaying C, Ni, and Cu concentration profiles is drawn on a log-scale for clear visualization of the C concentrations in α-Fe matrix in vicinity of C-enriched regions.

A similar C-enriched region is also observed in the HSLA-115 sample aged at 823 K (550 ºC) for 0.12 h. This is evident from the distribution of carbon atoms shown in the two orthogonal views of the 3-D APT reconstruction of this sample, Figure 4.5(a). Copper precipitates are also observed at this aging time and are delineated by 7 at. % Cu isoconcentration surfaces. Proximity histogram concentration profiles with respect to distance from 1 at. % C isoconcentration surfaces are displayed in Figure 4.5(b). We obtain a carbon concentration of 2.7 ± 0.1 at. % in the core of the

C-enriched region (~1 nm region at the far right-hand side of the proxigram), which is comparatively less than the carbon concentrations measured in similar regions in the as-quenched sample. Additionally, we observe enrichment of Mn, Cr, and Mo in the C-enriched region in this 0.12 h aged sample, Figure 4.5(b), which is in contrast to the homogeneous distributions of these elements observed across the α-Fe matrix and the C-enriched regions in the as-quenched sample, Figure 4.4.

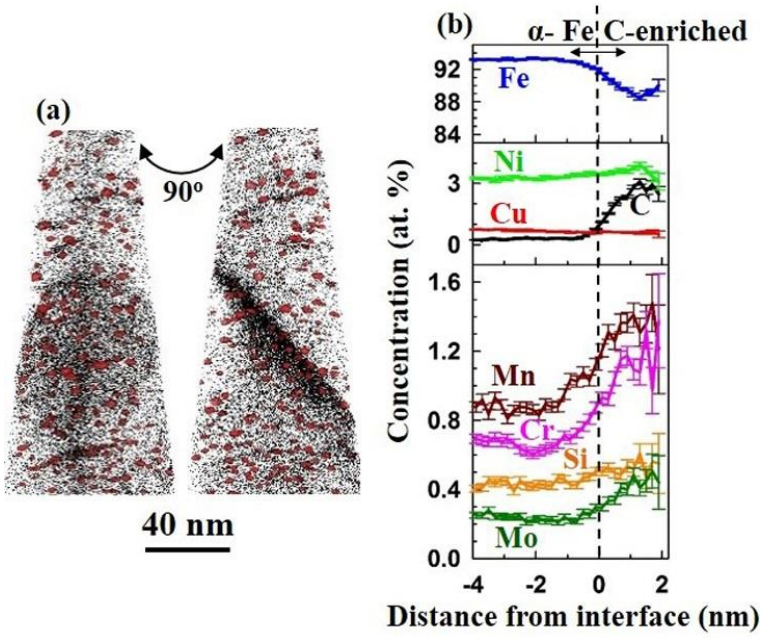

Figure 4.5- (a) 3-D APT reconstruction (two orthogonal views) of the HSLA-115 sample aged at 823 K (550°C) for 0.12 h. Carbon atoms are displayed as black dots, Cu precipitates are delineated by 7 at. % Cu isoconcentration surfaces (red) and the other alloying element atoms are omitted for the sake of clarity; (b) Proximity histogram concentration profiles (at. %) of Fe, C, Ni, Cu, Mn, Cr, Si, and Mo for C-enriched region in (a) and its vicinity (excluding the Cu precipitates, which were removed from the dataset before the proxigram analysis using the IVAS program).

4.3.3.2 Niobium Carbonitride precipitates

Three niobium carbonitride precipitates are observed in the 3-D APT reconstruction of the as-quenched sample and are delineated by 15 at. % (Nb + C) isoconcentration surfaces (brown),

Figure 4.3. Two of the niobium carbonitride precipitates are dissected in the 3-D reconstruction, while the third one lies completely inside it and is indicated by an arrow, Figure 4.3. Three orthogonal views of this precipitate are also displayed in this figure; the precipitate appears to have a a thin platelet-like morphology, which has been reported earlier in other APT [165-167] and TEM [168] studies of Nb-containing steels. The APT mass spectrum of this precipitate is displayed in Figure 4.6(a). Carbon peaks are obtained corresponding to C^{2+}, C^{+}, C_3^{2+}, and C_2^{+} ions, while niobium is detected as Nb^{4+}, Nb^{3+}, and Nb^{2+} and as molecular ions- $(NbN)^{3+}$and $(NbN)^{2+}$ along with nitrogen. The peak at 14 amu contributes 3.7 at. % of the total number of atoms associated with this precipitate and is taken as $^{14}N^{+}$, although there may be some contribution from $^{28}Si^{2+}$. We note that a number of molecular ion peaks, identified herein, may easily be overlooked and/or the ionic peaks may be wrongly assigned in the bulk mass spectrum of the sample due to the extremely low overall Nb concentration (0.012 at. %) in this alloy. For instance, the peak at 31 amu can be incorrectly assumed to be $^{62}Ni^{2+}$, if we analyse the precipitate using the mass spectrum of the bulk sample. For an accurate analysis, Nb(C,N) precipitates should first be isolated from the rest of the matrix and then the analysis of the spatially segmented mass spectrum should be performed separately to ensure correct identification of all mass peaks.

Thermodynamic equilibrium calculations for HSLA-115 predict that Nb(C,N) precipitates dissolve above 1408 K (1135 ^{o}C) but are stable at the austenitizing temperature of 1185 K (912 ^{o}C) and are thus effective in inhibiting grain growth during the austenitizing treatment. Thus, the precipitates obtained in the as-quenched sample are likely inherited from the austenitizing treatment. Proximity histogram displaying concentration profiles of Fe, Nb, C, and N across the

hetero-interface between α-Fe matrix and the Nb(C,N) precipitate are displayed in Figure 4.6(b). Table 4.3 lists the composition of the Nb(C,N) precipitate obtained from this proximity histogram along with its computed composition at thermodynamic equilibrium at 1185 K (912 ^{o}C). From APT analysis, we obtain a combined contribution of 51.4 at. % from C and N, while the metal composition is primarily Nb with some Mo, Cr, V, and Fe. While the Nb concentration in the precipitate, as measured by APT (43.2 at. %) is in reasonably good agreement with the predicted concentration from thermodynamic equilibrium calculations (40.7 at. %), the concentrations of the interstitial solute elements, C and N, differ significantly between the two methods.

Thermodynamic equilibrium calculations at the austenitizing temperature of 1185 K (912 ^{o}C) reveal that the C concentration in Nb(C,N) precipitates increases at the expense of N if the available concentration of N decreases from its overall bulk concentration of 0.016 wt. %; this trend holds even for lower bulk C concentrations than the 0.05 wt. % in this steel. For instance, for bulk C concentration of 0.04 wt. %, and N bulk concentrations of 0.012, 0.008, and 0.004 wt. %, equilibrium calculations predict 26.9, 20.1, and 15.7 at. % N and 22.9, 29.7, and 33.9 at. % C respectively in Nb(C,N) precipitates. Thus, we infer that less than 0.016 wt. % N is available during the austenitizing treatment as it may have combined with pre-existing Nb(C,N) precipitates formed during prior processing treatment steps and this likely is the reason that we obtain higher C concentration than N in the Nb(C, N) precipitates analysed by APT.

Additionally, the predicted equilibrium composition overestimates V and to a smaller extent Cr in the precipitate and underestimates the Mo and Fe concentrations. It also predicts negligible

solubility of Si in niobium carbonitride, which makes it reasonable to assign the peak at 14 amu in the APT mass spectrum to $^{14}N^{+}$.

In the present study, we also observe a Nb(C,N) precipitate in the APT reconstruction of the 16 h aged sample. XRD results described earlier revealed the presence of niobium carbide in the as-quenched sample and in the samples aged at 823 K (550 ^{o}C) for 0.25, 3 and 16 h, Figure 4.2(a). These precipitates are, however, only observed in the 3-D APT reconstructions of the as-quenched and the 16 h aged samples due to their low number densities.

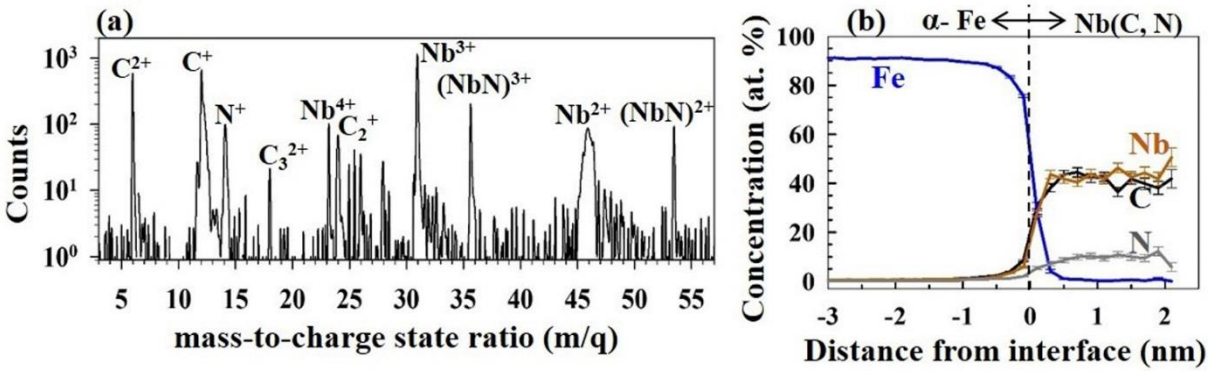

Figure 4.6- (a) Atom-probe tomographic mass spectrum of the niobium carbonitride precipitate, observed in the as-quenched HSLA-115 sample and is indicated by an arrow in Figure 4.3. Mass peaks associated with Nb, C, and N are labelled in the mass spectrum, while those of other minor elements in the precipitate, such as Fe, Mo, Cr, and V are not labelled for the sake of clarity; (b) Proximity histogram concentration profiles (at. %) of Fe, Nb, C, and N for the niobium carbonitride precipitate and its vicinity. A fiducial marker is placed vertically at the origin (0) of the proxigram, which is chosen as the inflection point of the Fe-concentration profile.

Table 4.3- Chemical composition (at. %) of the niobium carbonitride precipitate observed in the as-quenched HSLA-115 sample, as obtained from APT measurements. Equilibrium composition of niobium carbonitride from thermodynamic computations at 1185 K (912 ^{o}C) is also displayed.

Element	Nb	C	N	Fe	Mo	Cr	V
APT measured composition	43.2±1.4	41.6±1.4	9.8±0.8	0.5±0.2	2.7±0.4	1.1±0.3	0.5±0.20
Computed composition, ThermoCalc	40.7	15.4	34.5	0.02	0.05	2.1	7.2

4.3.3.3 Cementite precipitate

A cementite (θ_{cem}) precipitate is observed in the 3-D APT reconstruction of the 0.25 h aged sample at 823 K (550 ^{o}C) and is delineated by a 5 at. % C isoconcentration surface, Figure 4.7(a). Also, displayed in this APT reconstruction are the Cu precipitates (red) and M_2C carbides (dark-green). C-enriched regions observed in the as-quenched and 0.12 h aged samples, Figures 4.3 and 4.5(a), respectively, and/or the decomposition of the retained austenite and lath-martensite in the as-quenched microstructure are the likely sources of carbon for cementite formation during aging at 823 K (550 ^{o}C). The cementite precipitate's coarser morphology relative to the M_2C carbides is evident in Figure 4.7(a) and is usually associated with poor impact toughness [15]. In the previous chapter and associated article [147], we discussed the possible role of the cementite phase in the poor impact toughness that results after 0.25 h aging as compared to the as-quenched sample: Figure 4.1 in this chapter. Here, we focus on the concentrations and the partitioning behavior of alloying elements across the α-Fe/θ_{cem} hetero-interface, obtained using the proximity histogram displayed in Figure 4.7(b).

Analysis of the mass spectrum of the cementite precipitate revealed carbon peaks at 6, 12, 18, 24, 36, and 48 amu, that correspond to C^{2+}, C^{+}, C_3^{2+}, C_2^{+}or C_4^{2+}, C_3^{+}, and C_4^{+} ions, respectively, Figure

4.8. These include overlaps of $C_2^+$and C_4^{2+} at 24 amu and of C_4^+ and Mo^{2+} at 48 amu. Contribution of C_4^{2+} to the counts at 24 amu is inferred by the mass peak at 24.5 amu, which corresponds to $(^{12}C_3{}^{13}C)^{2+}$. We also observe that counts at 48 amu exceed the counts at 49 amu, which contradicts the relative natural isotopic abundances for Mo^{2+}. This indicates additional contributions from other ions at 48 amu, which is most likely C_4^+. The individual contributions of the overlapping ions at 24 and 48 amu were determined following the methodology of relative isotopic abundances, described by Sha et al. [169] for a binary Fe-C alloy.

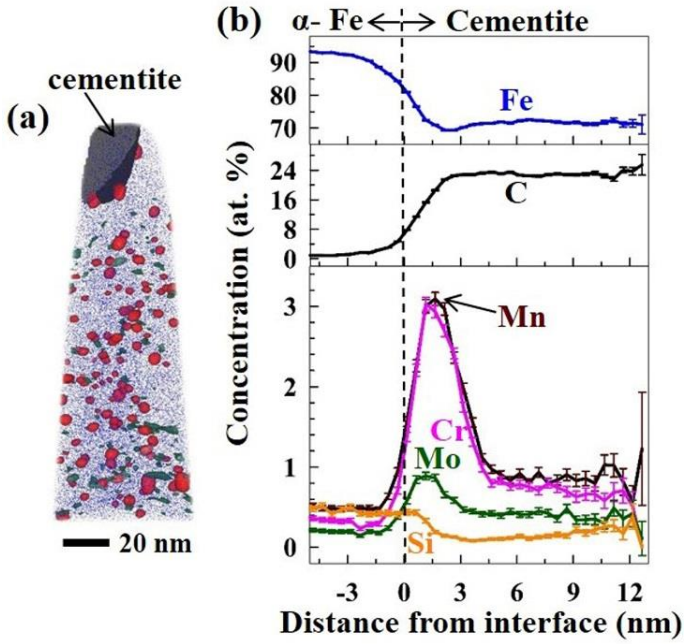

Figure 4.7- (a) 3-D APT reconstruction of the HSLA-115 sample aged at 823 K (550°C) for 0.25 h. The cementite precipitate is delineated by a 5 at. % C isoconcentration surface (black). Copper precipitates and M_2C carbides are delineated by 10 at. % Cu isoconcentration surfaces (red) and 5 at. % (C + Cr + Mo) isoconcentration surfaces (dark-green) respectively. Only a fraction of the Fe atoms is shown (blue dots) and the other alloying element atoms are omitted for the sake of clarity; (b) Proximity histogram concentration profiles (at. %) of Fe, C, Mn, Cr, Mo, and Si for the cementite precipitate and its vicinity. A fiducial marker is placed vertically at the origin (0) of the proxigram, which is chosen as the inflection point of the Fe-concentration profile.

In the proximity histogram, Figure 4.7(b), we obtain localized concentration peaks of Mn, Cr, and Mo having a width of a few nm near the θ_{cem}/α-Fe interface, with their peak concentrations of 3.0 ± 0.2, 3.0 ± 0.2 and 0.9 ± 0.1. at. %, respectively. The diffusion distances of Mn, Cr, Mo, and Si for 0.25 h at 823 K (550 ^{o}C), estimated by one-dimensional root-mean-squared distance, $\sqrt{2Dt}$ are 20, 14, 5, and 38 nm respectively and are three-to-four orders of magnitude smaller than that of carbon. Diffusion constants (D) of these elements in α-Fe at 823 K (550 ^{o}C) are listed in Table 4.4 along with the corresponding references [170-174]. These diffusion distances, particularly of Mn, Cr, and Mo reveal the sluggish diffusion kinetics of these elements, which results in their localized concentrations peaks observed near the θ_{cem}/α-Fe interface. We note, however, that even the peak concentrations of Mn and Cr (~ 3 at. % each) obtained from the APT analysis are significantly less than their respective concentrations of 9.1 and 23.9 at. % in cementite, computed by considering thermodynamic metastable equilibrium between ferrite and cementite at 823 K (550 ^{o}C), Table 4.5. However, these locally enriched concentrations do indicate that growth of cementite precipitate is in an intermediate stage between paraequilibrium (partitioning of only interstitial species (carbon) occurs as per equilibrium thermodynamics) and orthoequilbrium (partitioning of all elements including substitutional ones occurs).[108] A similar growth mode of cementite was also reported in an atom-probe study of an Fe-1.0C-0.30Si-0.2Mn-1.4Cr (wt.%) steel, aged isothermally at 773 K (500 ^{o}C) [175].

In the core of the cementite precipitate (6 nm region at the far right-hand side of the proxigram in Figure 4.7(b)), we observe nearly homogeneous distribution of all elements and the average composition of this region is displayed in Table 4.5. We note that the carbon concentration in the

core of the cementite precipitate is 22.7 ± 0.2 at. %, as opposed to the stoichiometric value of 25.0 at. %. Similar and much lower levels of carbon in cementite have been reported in other atom-probe studies [176-178]. Carbon concentrations can be underestimated during APT analysis due to the losses that can occur due to multiple detection events, and in particularly, if field-evaporation leads to the formation of molecular species and potentially their dissociation [179, 180]. Partitioning ratios of elements, defined as the ratio of their concentration in the core of the cementite precipitate to their concentrations in α-Fe matrix [107] are also listed in Table 4.5. Partitioning ratios for each of Mn, Cr, and Mo are greater than 1.5, indicating their enrichment in the cementite precipitate. Alternatively, Si partitions away from the cementite and has a partitioning ratio of 0.3. It is noted that its minimum concentration in the cementite precipitate is 0.08 ± 0.02 at. % (at ~ 3.6 nm from the origin of the abscissa), which gradually increases to 0.16 at. % in the core of the precipitate. Silicon is known to suppress the formation of cementite during tempering in steels [177, 181, 182]. It is believed that the rejection of Si from cementite results in the increase in the activity of carbon in Si-rich regions (in proximity of cementite), which reduces the carbon flux towards cementite and restricts its further growth [181, 182]. In general, the partitioning behavior of alloying elements, observed herein, in terms of their enrichment/depletion is consistent with other studies, which have also reported enrichment of Mn [152, 166, 176, 178, 183, 184], Cr [152, 178, 184], and Mo [152] and depletion of Si [152, 166, 176-178, 183, 184] in cementite with respect to their respective concentrations in the α-Fe matrix.

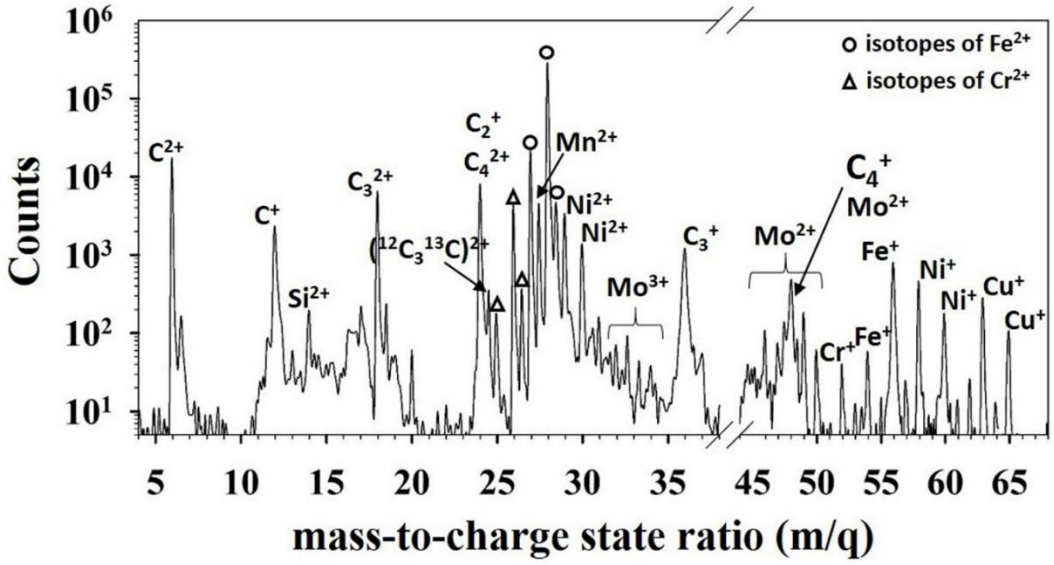

Figure 4.8- Atom-probe tomographic mass spectrum of the cementite precipitate observed in the HSLA-115 sample aged at 823 K (550^{o}C) for 0.25 h

Table 4.4- Diffusion coefficients of different elements in α-Fe at 823 K (550 ^{o}C)

Element	Diffusion coefficient ($cm^2 s^{-1}$)	Ref.
C	$1.26x10^{-7}$	[170]
Mo	$1.54x10^{-16}$	[171]
Mn	$2.26x10^{-15}$	[172]
Cr	$1.06x10^{-15}$	[173]
Si	$7.93x10^{-15}$	[174]

Table 4.5- Chemical composition (at. %) of the core of the cementite precipitate observed in HSLA-115 aged at 823 K (550 ^{o}C) for 0.25 h and the partitioning ratios of elements, as obtained from APT measurements. Metastable equilibrium composition of cementite from thermodynamic computations at 823 K (550 ^{o}C) is also displayed.

Element	Fe	C	Mn	Cr	Cu	Ni	Mo	Si
APT	72.18±0.22	22.71±0.21	0.86±0.05	0.71±0.04	0.37±0.03	2.24±0.08	0.40±0.03	0.16±0.02
Partitioning ratio (APT)	0.77±0.002	34.56±1.74	1.78±0.14	1.63±0.14	0.73±0.07	0.78±0.03	1.87±0.22	0.31±0.04
ThermoCalc	40.59	25.0	9.08	23.89	-	0.31	0.76	-

4.3.3.4 Temporal evolution of Cu precipitates and M_2C carbides at 823 K (550 ^oC)

The precipitation kinetics of Cu precipitates and M_2C carbides in HSLA-115 aged at 823 K (550 ^oC) are closely inter-linked with one another. Nucleation of Cu precipitates occurs first, Figure 4.9(a), and is followed by the precipitation of M_2C carbides with longer aging times, most of which are co-located with Cu precipitates, Figure 4.9(b, c, d, and e). This indicates that Cu precipitates act as heterogeneous nucleation sites for M_2C carbides; similar observations for Cu precipitates and M_2C carbides have been reported for a BA-160 steel [18] and a ultrahigh-strength carburized steel [19]. We also observe a second burst of nucleation of both Cu precipitates and M_2C carbides between 1 and 3 h aging at 823 K (550 ^oC); see Table 4.6 and 4.7 respectively, for the temporal evolution of their mean radii, number densities and volume fractions. The complex kinetics of these precipitates, as observed herein, is likely affected by the interactions of these precipitates with each other and with dislocations and lath-boundaries in the microstructure. This was discussed in correlation with the mechanical properties of HSLA-115 in the previous chapter and the associated article [147]. Herein, we describe the temporal evolution of the morphologies and compositions of Cu precipitates and M_2C carbides at 823 K (550 ^oC). As the main focus of this chapter is carbon redistribution and carbide precipitates, the temporal evolution of Cu precipitates is only briefly described.

Table 4.6- Temporal evolution of mean radius, <R(t)>, number density, $N_v(t)$, and volume fraction, Φ(%), of Cu precipitates in HSLA-115 aged at 823 K (550 °C)

Aging time (h)	<R(t)> nm	$N_v(t)$ (m^{-3})	Φ(%)
0.12	1.34±0.54	$(7.22\pm0.14)\times10^{23}$	0.61±0.01
0.25	1.60±0.81	$(2.99\pm0.24)\times10^{23}$	0.93±0.07
1	3.36±1.20	$(7.30\pm0.55)\times10^{22}$	1.61±0.12
3	3.15±0.95	$(1.62\pm0.13)\times10^{23}$	2.68±0.22
16	5.09±1.91	$(3.24\pm0.19)\times10^{22}$	2.53±0.15

Table 4.7- Temporal evolution of mean radius, <R(t)>, number density, $N_v(t)$, and volume fraction, Φ(%), of M_2C carbide precipitates in HSLA-115 aged at 823 K (550 °C)

Aging time (h)	<R(t)> nm	$N_v(t)$ (m^{-3})	Φ(%)
0.25	1.07±0.30	$(7.10\pm1.17)\times10^{22}$	0.05±0.01
1	1.22±0.42	$(2.25\pm0.31)\times10^{22}$	0.02±0.003
3	1.64±0.63	$(1.46\pm0.13)\times10^{23}$	0.40±0.03
16	2.06±1.62	$(3.72\pm0.20)\times10^{22}$	0.45±0.02

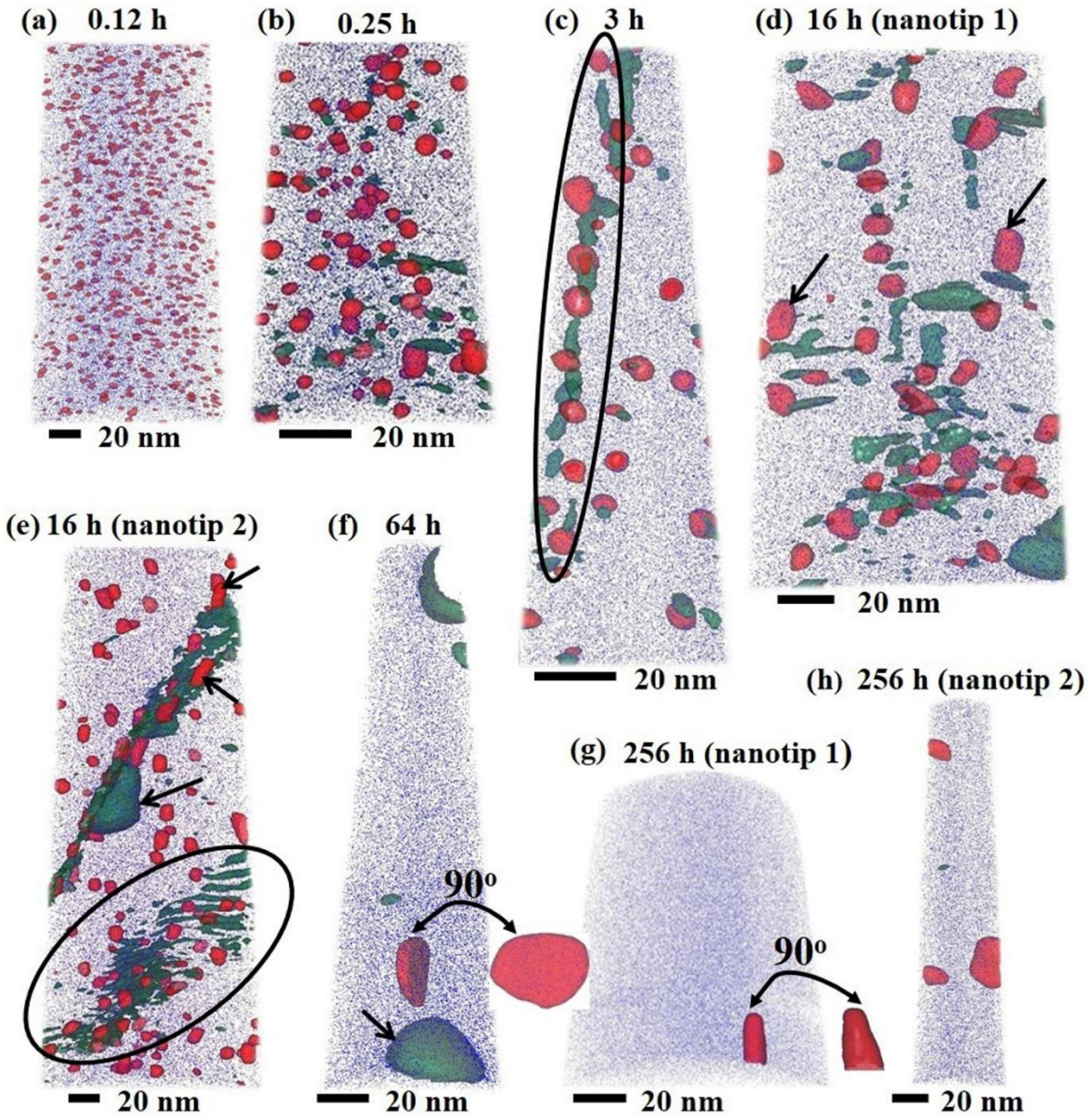

Figure 4.9- 3-D APT reconstructions of HSLA-115 samples aged at 823 K (550 ^{o}C) for: (a) 0.12 h; (b) 0.25 h; (c) 3 h; (d) 16 h (nanotip 1); (e) 16 h (nanotip 2); (f) 64 h; (g) 256 h (nanotip 1); and (h) 256 h (nanotip 2). Only a fraction of the Fe atoms is shown (blue dots) and the other alloying element atoms are omitted for the sake of clarity. Copper precipitates are delineated by 10 at. % Cu isoconcentration surfaces (red). M_2C carbides are delineated by 5 at. % (C + Cr + Mo) isoconcentration surfaces (dark-green) in all reconstructions except in (e), where 7 at. % (C + Cr + Mo) isoconcentration surfaces are used to delineate M_2C carbides.

It is known that Cu nucleates as coherent (b.c.c.) spheroidal precipitates in α-Fe [45-47]. As Cu precipitates grow and coarsen upon aging, they undergo shear transformations to 9R and 3R structures and finally transform to the equilibrium f.c.c. structure [49, 50]. As their size increases, they also acquire ellipsoidal and more elongated rod-like morphologies [45, 48, 50, 53]; some of these elongated precipitates after 16 and 256 h aging, are marked by arrows in Figure 4.9(d, e, and g). The elongated morphology of Cu precipitates is attributed to a large anisotropy in the α-Fe/Cu-precipitate interfacial energy [48] and/or the shear associated with partial dislocations resulting in transformation to the 3R structure [50]. In the 64 h aged sample, Figure 4.9(f), the observed platelet/disk-like morphology of the Cu precipitate is attributed to the additional consideration of elastic strain energy [185].

M_2C carbides are first observed in the 0.25 h aged sample, Figure 4.9(b). In the 3-D APT reconstructions of the 3 and 16 h aged samples, elongated rod-like carbides are observed to be distributed heterogeneously along a dislocation line and at a martensitic lath-boundary, see encircled regions in Figure 4.9(c) and Figure 4.9(e)**,** respectively. M_2C carbides are known to assume an elongated needle/rod-like morphology in α-Fe [15, 19, 62, 64, 65, 68, 127, 186, 187] and grow along $<100>_{\alpha\text{-Fe}}$ directions due to good lattice match along this direction [62, 64]. As the carbide precipitates coarsen further, they assume irregular spheroidal morphologies, which is indicative of a loss of coherency with the matrix; two such carbides are indicated by arrows in Figure 4.9(e and f). The temporal evolution of the morphology of M_2C carbides, as described above, is consistent with the findings of Liddle et al.[68], who reported the transition of M_2C carbides (in AF1410 steel) from small clusters to rods to larger irregular spheroidal particles with

increasing aging times at 783 K (510 ^{o}C). We next describe the compositional evolution of Cu precipitates and M_2C carbides at 823 K (550 ^{o}C).

Copper precipitates observed in the 0.12 h aged sample (shortest aging time studied) contain ~ 50.0 at. % Fe, which is consistent with the composition of Cu (b.c.c.) precipitates reported at early aging times in several other atom-probe studies [16, 51-53]. In contrast, negligible Fe concentrations have been reported in Cu precipitates from small-angle neutron scattering (SANS) studies [54, 55]. While the composition of Cu precipitates at early aging times, as determined by APT, may be affected by the artificial inclusion of matrix-Fe atoms due to ion-trajectory overlaps [56], the SANS based analysis assumes the Cu precipitates in α-Fe to be non-ferromagnetic, which is highly questionable in light of the significant Fe concentrations reported from atom-probe studies. This remains an unresolved issue and has been discussed in detail elsewhere [188]. Cu precipitates observed at longer aging times have much higher Cu concentrations, which is consistent with other atom-probe studies [18, 53, 189]. The average core composition of Cu precipitates in the 256 h aged condition, Figure 4.9(h), is 91.4Cu-3.3Ni-4.2Mn-1.0Fe (at. %). For all aging times studied, we observe segregation of Ni and Mn at the α-Fe/Cu-precipitate interface, which has been reported and is attributed to the reduction in the interfacial energy of the heterophase interface [52, 53]. We note that the Cu concentration measured in the α-Fe matrix (excluding the Cu precipitates) after 256 h aging is ~ 0.20 at. % (0.23 wt. %), which is in excellent agreement with the experimentally determined Cu solubility of 0.21 wt. % in α-Fe at 823 K (550 ^{o}C) [39]. We now discuss in detail the compositional evolution of M_2C carbides by APT.

Proximity histogram concentration profiles of C, Mo, and Cr obtained for the respective ten largest M_2C carbide precipitates in the 0.25, 1, 3, and 16 h (nanotip 1) aged samples are displayed in Figure 4.10, which reveal the enrichment of these elements in the carbide precipitates. The coarser blocky carbide precipitate observed to the bottom right in Figure 4.9(d) has been excluded from this analysis to obtain a well-defined analysis of the smaller carbide precipitates and to distinguish precipitates at different stages of their growth.

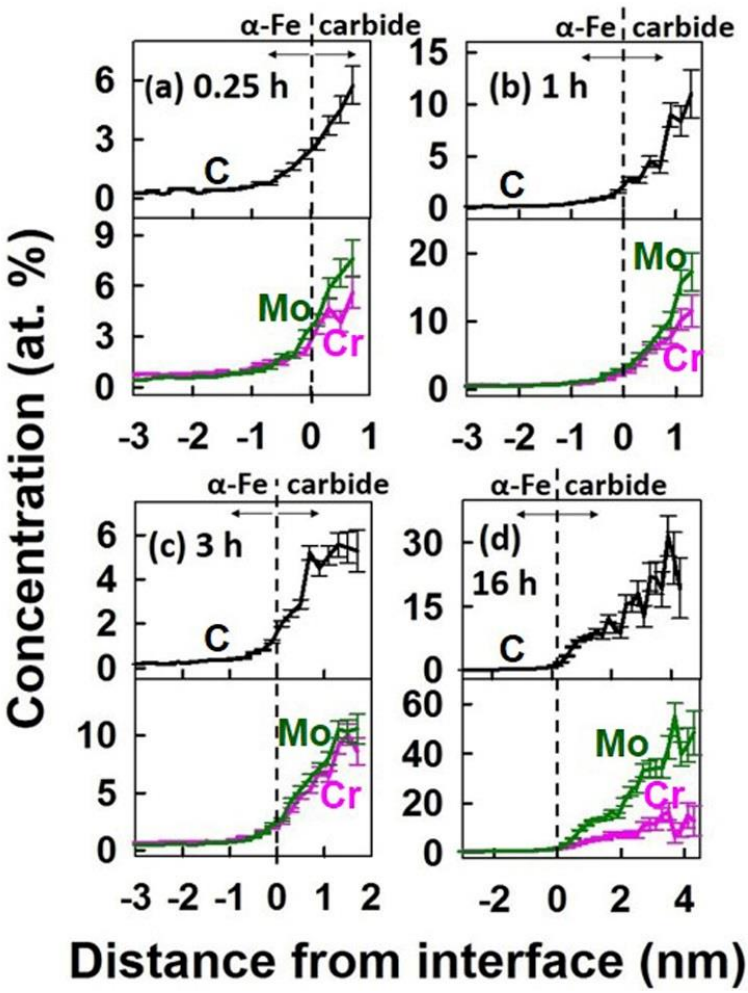

Figure 4.10- Proximity histogram concentration profiles (at. %) of C, Mo, and Cr for the ten largest M_2C carbide precipitates and their vicinity in HSLA-115 samples aged at 823 K (550 ^{o}C) for: (a) 0.25; (b) 1; (c) 3; and (d) 16 h (nanotip 1).

It is important to mention that in the 3-D APT reconstruction, M_2C carbide precipitates suffer from local magnification artifacts owing to their higher field-evaporation strength than the matrix Fe-atoms [56]. This leads to ion-trajectory overlaps and results in artificial inclusion of matrix atoms in M_2C carbides, which can complicate the evaluation of their compositions, particularly during early aging times. Additionally, carbon concentrations measured by APT can be influenced by the experimental variables, that is, specimen temperature [184] and laser pulse energy [190], as has also been shown specifically for M_2C carbides [113, 129]. Working within these limitations, we focus on the temporal evolution of the atomic ratios, (Mo + Cr)/C and Mo/Cr in the M_2C carbide precipitates at 823 K (550 ^oC), rather than their absolute compositions.

However, compositions of coarser M_2C carbide precipitates such as those indicated by arrows in Figure 4.9(e and f) can be determined with much greater accuracy and are described first. Their compositions, as determined using proximity histograms (displayed in Figure 4.11) are listed in Table 4.8 along with the computed composition of M_2C carbide at thermodynamic equilibrium at 823 K (550 ^oC). The measured carbon concentrations of these two carbides are similar (30-31 at. %) and in close agreement with the expected stoichiometric carbon concentration of 33.3 at. % in M_2C carbides. Mass spectrum of the M_2C carbide precipitate, which is indicated by an arrow in Figure 4.9(f) is displayed in Figure 4.12. Carbon mass peaks are obtained corresponding to C^{2+}, C^+, C_3^{2+}, C_2^+, and C_3^+ ions, Mo is observed in charge states 2+ and 3+, while Cr field-evaporates primarily in charge state 2+. It is noted that C and Mo are also obtained as combined molecular species in the form of $(MoC)^{2+}$. We now describe the temporal evolution of the atomic ratios, (Mo + Cr)/C and Mo/Cr in the M_2C carbide precipitates at 823 K (550 ^oC).

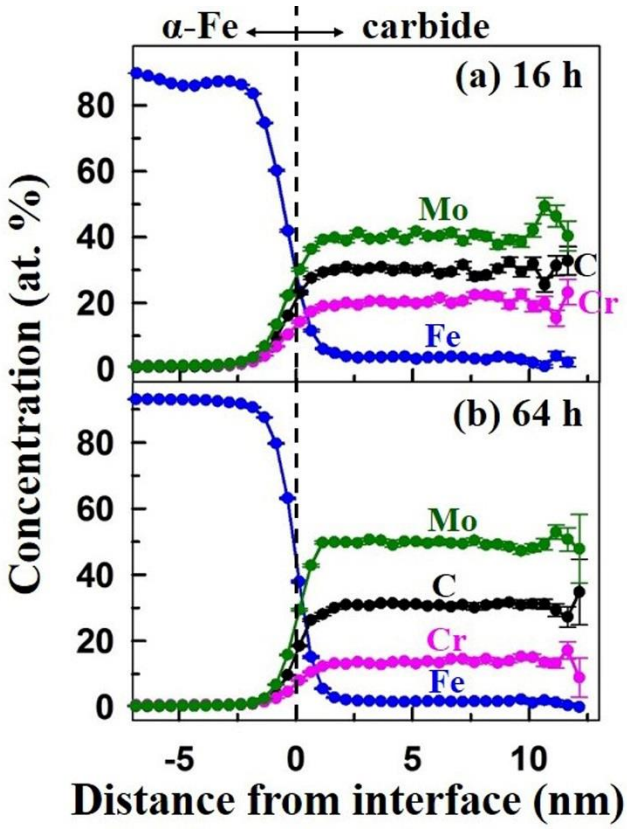

Figure 4.11- Proximity histogram concentration profiles (at. %) of Fe, Mo, C, and Cr for: (a) M_2C carbide (indicated by an arrow in Figure 4.9(e)) and its vicinity; (b) M_2C carbide (indicated by an arrow in Figure 4.9(f)) and its vicinity. Figure 4.9(e and f) are the 3-D APT reconstructions of HSLA-115 samples aged at 823 K (550 ^{o}C) for 16 and 64 h respectively. A fiducial marker is placed vertically at the origin (0) of the proximity histograms, which is chosen as the inflection point of the Fe-concentration profile.

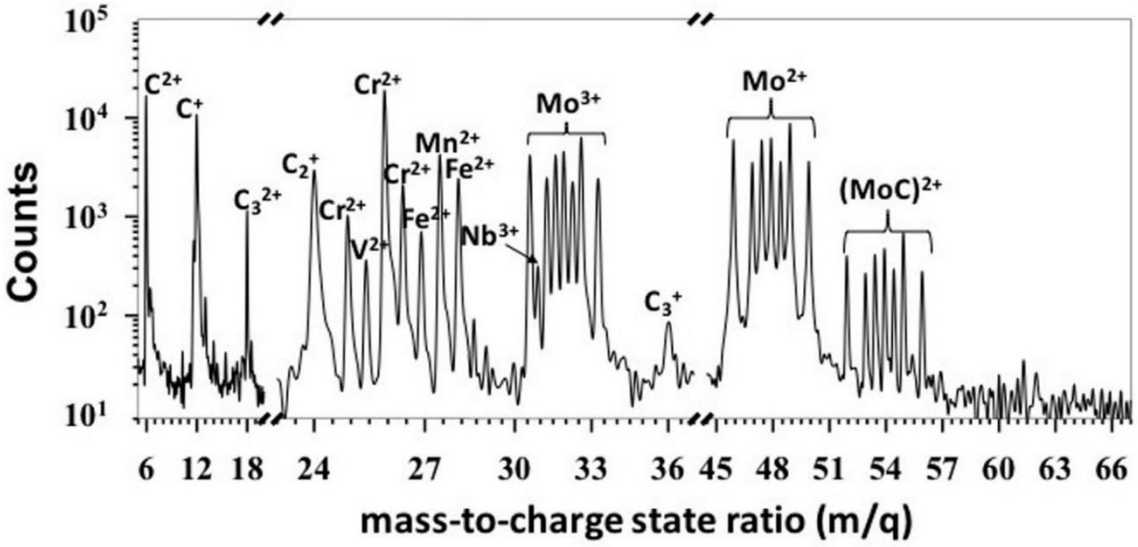

Figure 4.12- Atom-probe tomographic mass spectrum of the M_2C carbide precipitate observed in the HSLA-115 sample aged at 823 K (550 ^oC) for 64 h, which is indicated by an arrow in Figure 4.9(f). It is noted that the abscissa scale chosen is not linear to enlarge portions of the mass spectrum for clarity.

Table 4.8- Compositions (at. %) of M_2C carbide precipitates, which are indicated by arrows in Figure 4.9(e and f) in HSLA-115 samples aged at 823 K (550 ^oC) for 16 and 64 h respectively, as obtained from APT measurements and equilibrium composition of M_2C carbide from thermodynamic computations at 823 K (550 ^oC)

Element	Mo	Cr	C	Fe	Mn	V	Ni	Cu
APT, 16 h	40.35±0.43	20.49±0.36	30.12±0.40	3.43±0.16	3.63±0.16	0.20±0.06	0.48±0.06	0.30±0.05
APT, 64 h	49.76±0.28	13.63±0.19	30.91±0.26	1.81±0.07	2.62±0.09	0.29±0.03	0.26±0.03	0.10±0.02
ThermoCalc, 550 ^oC	58.3	5.6	33.3	0.5	1.1	1.1	-	0.1

Figure 4.13 displays plots of the atomic ratios, (Mo + Cr)/C and Mo/Cr for the ten largest M_2C carbide precipitates and their vicinity in the 0.25, 1, 3, and 16 h (nanotip 1) aged samples; proximity histogram concentration profiles in Figure 4.10 were also obtained from these carbides. Since the matrix is mainly Fe, any contribution of Mo, Cr, and C from ion-trajectory effects is not anticipated to affect the ratios of (Mo + Cr)/C and Mo/Cr significantly. Thus, these plots are helpful for discriminating the carbide precipitates from the matrix and in calibrating the potential compositional influence from ion-trajectory effects. In Figure 4.13, we observe a gradual decrease in the (Mo + Cr)/C atomic ratio from its value in the α-Fe matrix (left-hand side of the plots) toward the carbide precipitates (far right-hand side of the plots), where it approaches a plateau. This plateau region to the right-hand side of the vertical fiducial marker in Figure 4.13 is identified as the core of the M_2C carbide precipitates and the mean values of atomic ratios, (Mo + Cr)/C and Mo/Cr obtained from these plateau regions for different aging times are displayed in Figure 4.14.

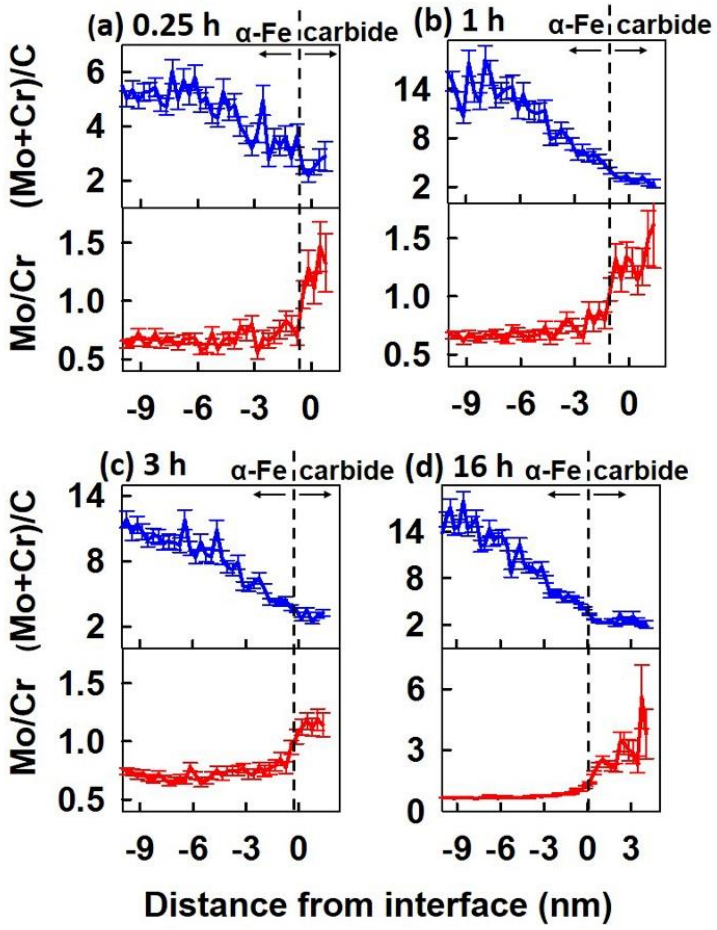

Figure 4.13- Atomic ratios, (Mo + Cr)/C and Mo/Cr for the ten largest M_2C carbides and their vicinity in HSLA-115 samples aged at 823 K (550 ^oC) for: (a) 0.25 h; (b) 1 h; (c) 3 h; and (d) 16 h (nanotip 1). The portions of the diagrams on the right-hand side of the vertical fiducial markers in these plots represent the core of the M_2C carbide precipitates with nearly constant (Mo + Cr)/C values.

At early aging times of 0.25, 1, and 3 h, M_2C carbide precipitates are significantly sub-stoichiometric in carbon and have a (Mo + Cr)/C atomic ratio of 2.5, 2.8, and 3.0 respectively, Figure 4.14(a). This ratio decreases to 2.2 for carbides in the 16 h aged sample, thereby approaching the ideal value for M_2C carbide stoichiometry. Sub-stoichiometric carbon concentrations in the M_2C carbide precipitates have been previously reported[19, 68, 127, 153,

191, 192]. Olson et al. [153] performed thermodynamic calculations to understand compositional trajectory of M_2C carbides in AF1410 steels, aged isothermally at 783 K (510 ^oC) and attributed lower carbon in the carbides at shorter aging times to the reduction in the interfacial energy of precipitating nuclei. For the coarser carbides, whose proximity histogram analyses is displayed in Figure 4.11, the (Mo + Cr)/C atomic ratio decreases to 2.0. It is noted that while metal content of these M_2C carbide precipitates consists primarily of Mo and Cr, they also contain some Mn, Fe, and very little V, Ni, and Cu, Table 4.8. However, since their carbon concentrations measured by APT (30-31 at. %) are less than the ideal 33.3 at. %, the (Mo+Cr)/C ratio of 2.0 in these carbides is slightly higher than the 1.9 obtained by equilibrium thermodynamic calculations, which also predict some Mn, V, and Fe in the M_2C carbide, Table 4.8.

The Mo/Cr atomic ratio in the M_2C carbide precipitates at early aging times of 0.25, 1, and 3 h is nearly constant at ~1.3, but increases to 2.4 for carbides in the 16 h aged sample, Figure 4.14(b). Substitution of Mo by Cr in M_2C carbide reduces its lattice parameter and is associated with the decrease in transformation strains [62, 70, 71]. Heterogeneous nucleation of M_2C carbides at Cu precipitates coupled with their sub-stoichiometric carbon composition, observed herein, further reduces the nucleation barrier for M_2C carbide precipitation. The Mo/Cr ratio increases further to 3.7 in the M_2C carbide precipitate analyzed in the 64 h aged sample, while this ratio is 7.8 for the computed composition of M_2C at thermodynamic equilibrium, Table 4.8. Thus, at early aging times, when M_2C carbide precipitates are presumably coherent, they have a smaller Mo/Cr ratio and sub-stoichiometric carbon concentrations. At longer aging times, the Mo/Cr ratio and the overall composition tends to approach the predicted composition at thermodynamic equilibrium.

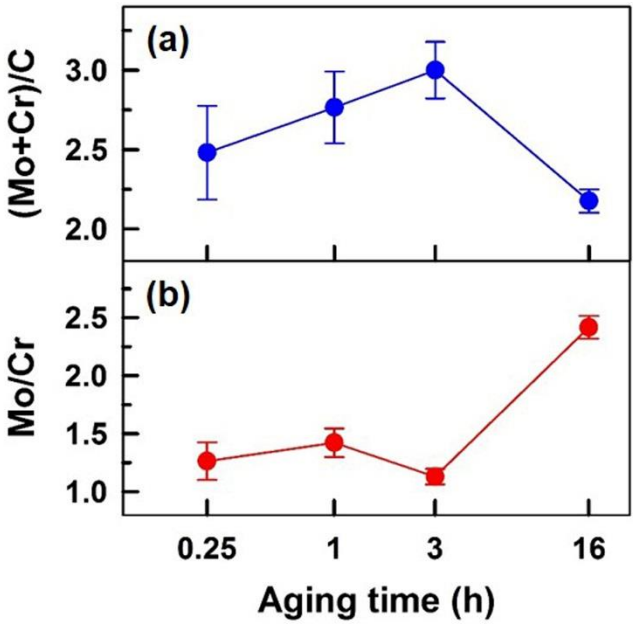

Figure 4.14- Temporal evolution of atomic ratios: (a) (Mo + Cr)/C; and (b) Mo/Cr in the M_2C carbide precipitates for HSLA-115 aged at 823 K (550 ºC). For aging times of 1, 3, and 16 h, these values are the mean values obtained from the analysis of the two APT nanotips for each of these aging times. Coarser blocky carbide precipitates observed to the bottom right in Figure 4.9(d) and the one indicated by an arrow in Figure 4.9(e) have been excluded from this analysis to obtain a clearer analysis of the smaller carbide precipitates and to distinguish precipitates at different stages of their growth.

4.4 Summary and Conclusions

For the first time, detailed compositional analysis of carbon redistribution and associated complex phase transformations are provided for an HSLA-115 steel, isothermally aged at 823 K (550 ºC), which includes carbon segregation at lath-boundaries, niobium carbonitride precipitates, cementite, M_2C carbide precipitates, and the synergetic interactions with Cu precipitation that happens simultaneously. The results are summarized in the conclusions below:

1. Segregation of carbon (3-6 at. % C) is observed by 3-D APT at martensitic lath-boundaries in the as-quenched, Figure 4.3, and 0.12 h aged samples, Figure 4.5(a), indicating that diffusion of carbon occurs from the freshly formed martensite during quenching, following the

austenitizing treatment. While Mn, Cr, and Mo are homogeneously distributed between the α-Fe matrix and the C-enriched regions in the as-quenched sample, Figure 4.4, their enrichment is observed in the C-enriched region in the 0.12 h aged sample, Figure 4.5(b). On further aging, carbon is redistributed, forming cementite and M_2C carbide precipitates.

2. Some carbon in the as-quenched microstructure is also associated with niobium carbonitride precipitates, as they do not dissolve during the austenitizing treatment. Composition of one such precipitate observed in the 3-D APT reconstruction of the as-quenched sample, Figure 4.3, having a thin platelet-like morphology, is 43.2Nb-41.6C-9.8N-2.7Mo-1.1Cr-0.5V-0.5Fe (at. %) or 79.9Nb-10.0C-2.7N-5.2Mo-1.1Cr-0.5V-0.6Fe (wt. %). These precipitates are also present in the microstructure after aging at 823 K (550 ^{o}C) for 0.25, 3, and 16 h, as confirmed by synchrotron XRD, Figure 4.2(a).

3. Cementite formation occurs during aging at 823 K (550 ^{o}C), Figure 4.2(a). Carbon-enriched regions at lath-boundaries, Figures 4.3 and 4.5(a), and the decomposition of retained austenite and lath-martensite in the as-quenched microstructure are the likely sources of carbon for cementite formation. Core composition of the cementite precipitate observed in the 3-D APT reconstruction of the 0.25 h aged sample, Figure 4.7, is 72.0Fe-22.7C-2.5Ni-0.9Mn-0.7Cr-0.4Mo-0.4Cu-0.2Si (at. %) or 87.5Fe-5.9C-3.2Ni-1.1Mn-0.8Cr-0.8Mo-0.6Cu-0.1Si (wt. %). Mn, Cr, and Mo partition to the cementite precipitate, while Si is rejected from it. A much higher degree of enrichment of Mn, Cr, and Mo is observed near the cementite/α-Fe interface than in the core of the cementite precipitate, which is attributed to their sluggish diffusion kinetics.

4. The precipitation kinetics of M_2C carbides and Cu precipitates are closely intertwined at 823 K (550 ^oC). Their precipitation sequence coupled with co-located nature suggest that Cu precipitates catalyze the nucleation of M_2C carbides, Figure 4.9(a, b, and c). M_2C carbides assume elongated rod-like morphologies as they grow and coarsen; a significant fraction of these are observed to be distributed heterogeneously along a dislocation line and at a martensitic lath-boundary, Figure 4.9 (c and e) respectively. On further aging and consequent coarsening, they acquire irregular spheroidal morphology, Figure 4.9(f).

5. The compositional evolution of M_2C carbide precipitates during aging at 823 K (550 ^oC) is described by measuring the atomic ratios, (Mo+Cr)/C and Mo/Cr in the core of the carbide precipitates using 3-D APT. At early aging times of 0.25, 1, and 3 h, M_2C carbides are significantly sub-stoichiometric in carbon with the (Mo+Cr)/C atomic ratio varying from 2.5 to 3 and they have a nearly constant Mo/Cr atomic ratio of ~1.3, Figure 4.14. On further aging, their composition tends to approach the computed composition at thermodynamic equilibrium at 823 K (550 ^oC), with a nearly stoichiometric carbon concentration and a higher Mo/Cr atomic ratio. Composition of one such M_2C carbide precipitate observed in the 64 h aged sample is 49.8Mo-13.3Cr-30.9C-2.1Fe-2.6Mn-0.3V-0.3Ni-0.1Cu (at. %) or 77.8Mo-11.3Cr-6.0C-1.9Fe-2.3Mn-0.2V-0.3Ni-0.1Cu (wt. %).

Chapter 5

Thermally Stable Ni-rich Austenite Formed Utilizing Multistep Intercritical Heat-Treatment in a Low-Carbon 10 wt. % Ni Martensitic Steel

Abstract

Austenite reversion and its thermal stability attained during the transformation is key to enhanced toughness and blast resistance in transformation-induced-plasticity (TRIP) martensitic steels. We demonstrate that the thermal stability of Ni-stabilized austenite and kinetics of the transformation can be controlled by forming Ni-rich regions in proximity of pre-existing (retained) austenite. Atom-probe tomography (APT) in conjunction with thermodynamic and kinetic modeling elucidate the role of Ni-rich regions in enhancing growth kinetics of thermally stable austenite, formed utilizing a multistep intercritical (*Quench-Lamellarization-Tempering* (QLT)-type) heat treatment for a low-carbon 10 wt. % Ni steel. Direct evidence of austenite formation is provided by dilatometry and the volume fraction is quantified by synchrotron X-ray diffraction. The results indicate the growth of nm-thick austenite layers during the second intercritical tempering treatment (T-step) at 863 K (590 ^{o}C), with austenite retained from first intercritical treatment (L-step) at 923 K (650 ^{o}C) acting as a nucleation template. For the first time, the thermal stability of austenite is quantified with respect to its compositional evolution during the multi-step intercritical treatment of these steels. Austenite compositions measured by APT are used in combination with the thermodynamic and kinetic approach formulated by Ghosh and Olson to assess thermal stability and predict the martensite-start temperature. This approach is particularly useful as empirical relations cannot be extrapolated for the highly Ni-enriched austenite investigated here.

5.1 Introduction

High performance structural materials are needed for U. S. Naval applications, such as ship hulls and decks, which require an excellent combination of strength, low-temperature impact toughness, ductility, blast and fragment (ballistic)-resistance and weldability[1-4]. In recent years, several research efforts have been performed, to develop alternatives to the widely used Naval HSLA-100 steels with a superior yield strength, blast and ballistic-resistance to reduce the weight of structural components and pre-empt increasing terrorist threats[3, 5, 6, 33, 34, 43, 106, 147]. Optimizing the overall mechanical properties for such applications entails several design challenges; most importantly, increasing the strength invariably leads to concomitant deterioration in toughness and ductility. The concept of transformation-induced-plasticity (TRIP) has been commonly utilized to combine high-strength in martensitic steels with good toughness [44, 94, 193] and to enhance ductility in automotive steels [194-196]. TRIP utilizes deformation-induced martensitic transformations to enhance plasticity of alloys [30-32]. The benefits of transformation toughening and enhanced ductility from such martensitic transformations rely on the volume fraction and relative stability of austenite, which can be tailored by optimizing the chemical compositions and heat treatments of steels.

Low-carbon steels (<0.1 wt. % C) are preferred for Naval structural applications for good weldability and low-processing costs [36, 37]. Thus, unlike the advanced high-strength quench and partitioning steels, which rely on carbon partitioning for stabilizing austenite [197, 198], the steel investigated in the present study is a low-carbon (0.09 wt. %) 10 wt. % Ni-Cr-Mo-V steel, which utilizes Ni as the primary austenite stabilizer. Additionally, Ni additions in steels are also believed to lower the ductile-to-brittle transition temperatures in steels due to its effect on cross-slip of dislocations [75] and/or on the cohesive energy of iron at low temperatures [76]. Recent

dilatometry and microhardness characterization of a similar steel containing 9 wt. % Ni reported martensitic microstructures after solutionizing and quenching treatment (for a wide range of cooling rates) [87]. A common processing route to form Ni-rich austenite in significant volume-fractions from the as-quenched microstructure is to employ intercritical heat-treatments in the ferrite (α) plus austenite (γ) two-phase field. Low-carbon (<0.1 wt.%) steels containing 5 to 9 wt. % Ni have been in use for several decades for cryogenic applications and are processed by similar single or multistep intercritical treatments [77-85].

In the present study, we utilize a *Quench-Lamellarization-Tempering* (QLT) heat-treatment, where 'L' and 'T' refer to the intercritical isothermal treatments in the upper and lower range of the α plus γ dual-phase field, employed after the solutionizing and quenching step (Q). Detailed evaluation of the mechanical properties of this steel after the optimal QLT-treatment revealed an excellent combination of yield strength,130 ksi (896.3 MPa), ultimate tensile strength, 158 ksi (1089.4 MPa), an elongation to failure of 23%, a Charpy impact toughness of 153 J at 188.7 K (-84.4 ^{0}C), and a 18 % higher ballistic limit, V_{50} than the widely used HSLA-100 steels for Naval structural applications [6]. Its superior ballistic resistance is attributed to its enhanced dynamic plasticity, due to the deformation-induced martensitic transformation of the dispersed austenitic phase [6]. Here, we elucidate the basic physical principles behind the multistep intercritical treatment; specifically, the thermal stability and formation kinetics of reverted austenite using dilatometry, synchrotron X-ray diffraction, ultraviolet (wavelength = 355 nm) laser assisted 3-D atom-probe tomography (APT), and computational modeling tools, ThermoCalc [199, 200] and DICTRA [200, 201].

APT is a unique analytical technique that provides 3-D spatial information of atoms and concurrently their chemical identities with sub-nanometer spatial resolution [20, 21, 23].

Investigating the microstructure at the sub-nanometer scale is crucial as the very small diffusivity of substitutional austenite stabilizers (for example Ni or Mn) in austenite at the intercritical temperatures leads to local chemical concentration gradients, which are directly related to austenite reversion and its stability [84, 202, 203]. The composition of intercritically formed austenite measured employing 3-D APT is used to predict the martensite-start (M_s) temperature. The M_s temperature is an important design parameter to estimate the thermodynamic stability of austenite, which is primarily dependent on the composition of austenite [204-207]. We utilize the Ghosh-Olson thermodynamic and kinetic approach [208-210], which integrates computational thermodynamics and the Olson-Cohen barrierless martensite nucleation model [211] to predict the M_s temperature. It is also demonstrated that commonly used empirical relations are unable to predict the M_s temperature of the Ni-rich austenite phase formed after the QLT heat-treatment. 3-D APT results in conjunction with DICTRA simulations are used to study the kinetics of austenite formation during the T-step.

5.2 Experimental Methods

The overall chemical composition of the steel, as measured by optical emission spectroscopy (for metallic elements) and combustion infrared detection analyser (for carbon) is given in Table 5.1. The steel was processed by vacuum induction melting (VIM) and cast into an ingot, which was heated to 1533 K (1260 ^{o}C), and then held for 7 h in a gas-fired furnace with a flow of protective nitrogen gas. Then it was hot rolled to 20.3 cm x 2.5 cm (8” x 1”) plates with a finishing temperature of 1116 K (843 ^{o}C). The final QLT heat-treatment employed consists of an austenitizing treatment at 1073 K (800 ^{o}C) for ~1 h and water quenching to room temperature (Q), followed by the first intercritical heat treatment (L) at 923 K (650 ^{o}C) for 20 to 30 min and a second

intercritical heat treatment (T) at 863 K (590 ^{o}C) for 1 h. Each intercritical heating step is terminated by water quenching the specimen to room temperature. To follow the evolution of the microstructure at different stages of the QLT-treatment, we also examined the samples in the as-quenched (Q), quenched-and-L-step (QL), and quenched-and-T-step (QT) conditions.

Samples for metallography were prepared by standard mounting, grinding and polishing methods with a final polish using 0.06 μm diameter colloidal silica, followed by etching with a 2% Nital solution. The dilatometric tests were performed using a Gleeble 3500 thermal system employing 9.5 mm diameter cylindrical specimens. High-intensity synchrotron X-ray diffraction (XRD) scans were performed on polished samples at the 5-IDB beam line at the Advanced Photon Source (Argonne National Laboratory, Argonne, IL, USA). Scans were performed from 2θ ranging from 9.995° to 33.500°; employing a step size of 0.015°, a count time of 3 s per step, and a wavelength of 0.71 Å. At each step, the sample was rocked through 0.75^{o} in θ to reduce preferential orientation effects. A NIST standard sample containing 5.8 vol. % austenite was also analysed under identical conditions for calibration purposes. The data analysis involving peak positions, integrated intensities and background removal was performed utilizing MDI JADE 2010 software (Materials Data Inc.). The volume-fractions of austenite were calculated employing the direct comparison method [155], which involves comparing the integrated intensities of the $(111)_{\gamma}$, $(110)_{\alpha,}$ $(200)_{\gamma,}$ $(200)_{\alpha}$, and $(220)_{\gamma}$ reflections, and the error is determined based on counting statistics [212].

Figure 5.1 shows SEM micrographs of QL, QT and QLT-treated 10 wt. % Ni samples. In the QL and QLT-treated samples, the brighter phase protruding from the surface is a mixture of reverted austenite (formed during the intercritical treatment) and fresh-martensite, which resulted from the transformation of some of the reverted austenite during quenching [6]. During intercritical heating, a portion of the parent as-quenched martensite does not transform to austenite and is referred to as

tempered martensite. The intercritically formed austenite (or fresh-martensite) phase protrudes from the surface as the tempered martensitic matrix is preferentially removed during etching [202]. We did not observe such dispersions of austenite (or fresh-martensite) in the QT-treated sample, Figure 5.1(b), as the microstructure consists predominantly of tempered martensite. Nanotips for 3-D APT investigations were prepared by a standard dual-beam focused-ion beam (FIB) microscopy lift-out preparation technique [213], targeting the austenite (fresh-martensite) phase. Details of this method are provided in a prior article on 4.5 and 10 wt. % Ni steels [202]. 3-D APT experiments were performed with a Cameca local-electrode atom probe (LEAP) 4000X-Si tomograph, using ultraviolet (wavelength =355 nm) picosecond laser pulsing with an energy of 30 pJ per pulse, a pulse repetition rate of 500 kHz and an average evaporation rate (number of ions per pulse) of 2 %. The samples were analysed at a specimen base temperature of 60 K (-213 ^{o}C) in ultrahigh vacuum (< 10^{-8} Pa) and the data obtained were analysed using the program IVAS 3.6 (Cameca, Madison, WI).

Table 5.1- Chemical composition of 10 wt. % Ni steel, as measured by optical emission spectroscopy

Elements	**Fe**	**Ni**	**Mn**	**C**	**Si**	**Cr**	**Mo**	**Cu**	**V**
wt.%	87.11	9.85	0.60	0.09	0.21	0.60	1.23	0.15	0.08
at.%	87.43	9.41	0.61	0.42	0.42	0.65	0.72	0.13	0.09

5.3 Martensite-start (M_s) temperature calculations and DICTRA simulations

M_s temperature calculations corresponding to the austenite compositions obtained in the QL- and QLT- treated samples were performed using the Ghosh-Olson thermodynamic and kinetic

approach [208-210], based on the Olson-Cohen model [211], in which the critical driving force for martensite nucleation, $\Delta G_{ch\text{-}crit}$, is expressed as

$$\Delta G_{ch-crit} = -[K + w_{\mu} + w_{th}] \quad 5.1$$

where K is evaluated as 1010 J/mol and includes the strain and interfacial energies associated with semicoherent nucleation of martensite, and w_{μ} and w_{th} are the athermal and thermal interfacial frictional work respectively, required for the motion of dislocations [208]. The interfacial work terms are modeled based on the theory of solid-solution strengthening [214, 215] and are given by equations 5.2 and 5.3 below:

$$w_{\mu} = \sqrt{\sum_i (k_{\mu}^i X_i^{0.5})^2} + \sqrt{\sum_j (k_{\mu}^j X_j^{0.5})^2} \quad 5.2$$

where X is the concentration (mole-fraction) of the solute elements, i = C, Cr, Mn, Mo, Si, and V and j = Cu, Ni [210] and the coefficients, k_{μ} for these elements are listed in Table 5.2.

$$w_{th}(T) = w_o[1 - (T/T_{\mu})^{1/q}]^{1/p} \quad 5.3$$

where p = 0.5, q = 1.5, and $T_{\mu} \approx 500$ (in Kelvin) [209] and,

$$w_o = w_o^{Fe} + \sqrt{\sum_i (k_o^i X_i^{0.5})^2} + \sqrt{\sum_j (k_o^j X_j^{0.5})^2} \quad 5.3\ (a)$$

where i = C, Cr, Mn, Mo, Si, and V and j = Cu, Ni [210] and w_o^{Fe} is the value of w_o for pure Fe and is evaluated as 836 J/mol [209] and the coefficients, k_o for these elements are listed in Table 5.2.

For a given austenite composition, X and temperature, T, the volume free energy change associated with compositionally invariant martensitic transformation, $\Delta G_{ch}(T, X)$ is calculated using ThermoCalc; version S employing the *kMART thermodynamic database* [210, 216]. M_s temperature is then calculated to be the temperature at which,

$$\Delta G_{ch}(T, X) = \Delta G_{ch-crit} \qquad 5.4$$

Kinetic simulations using DICTRA were performed for Fe-Ni system using the *mobFe1 mobility database* and the *TCFe6 thermodynamic database*. A linear cell geometry is chosen with fixed dimensions, which is commonly used to study austenite/ferrite diffusional transformations in steels [201, 217, 218]. The DICTRA cell consists of different regions, which represent different phases and are separated by mobile planar boundaries [201, 218]. Simulations are performed assuming local equilibrium conditions at these heterophase boundaries, which implies infinite interface mobility and results in the transformation kinetics being controlled by the diffusion of Ni.

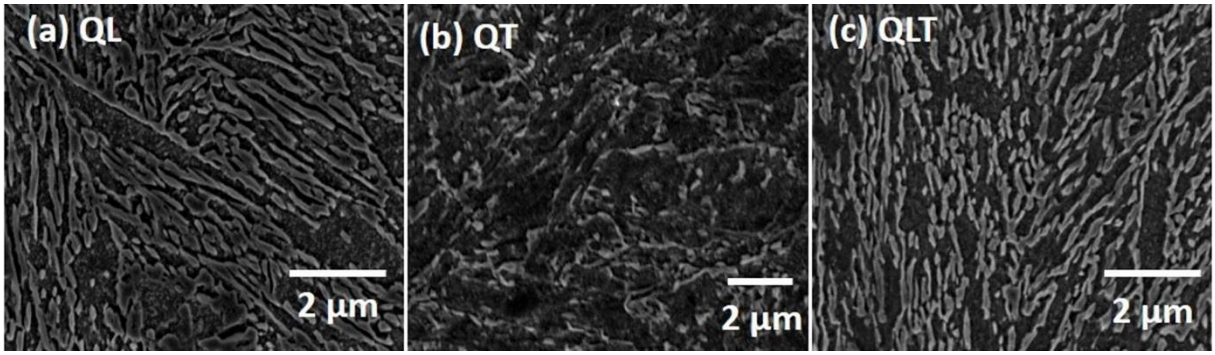

Figure 5.1- SEM micrographs of: (a) QL; (b) QT; and (c) QLT-treated 10 wt. % Ni steel etched with a 2% Nital solution.

Table 5.2- Values of coefficients, k_μ and k_o, used in martensite-start temperature calculations

Element	k_μ (J/mol)	k_o (J/mol)
C	3807	21,216
Mn	1980	4107
Si	1879	3867
Cr	1868	3923
V	1618	3330
Mo	1418	2918
Cu	752	1548
Ni	172	345

5.4 Results

5.4.1 Dilatometry

Figure 5.2 shows the dilatometric response of the QLT-treated 10 wt. % Ni steel during intercritical treatments. The observed contraction during the isothermal steps at 923 K (650 ^{o}C) and 863 K (590 ^{o}C) indicates the formation of austenite during these L and T-steps, respectively. During quenching, following the isothermal step at 923 K (650 ^{o}C), we observe that the sample begins to expand at ~ 461 K (188 ^{o}C), indicating the onset of a martensitic transformation. This temperature is thus the M_s temperature for the austenite formed during the L-step. The sample does not expand during quenching following the T-step, indicating that the austenite after tempering at 863 K (590 ^{o}C) has a greater thermal stability than the austenite formed during the L-step.

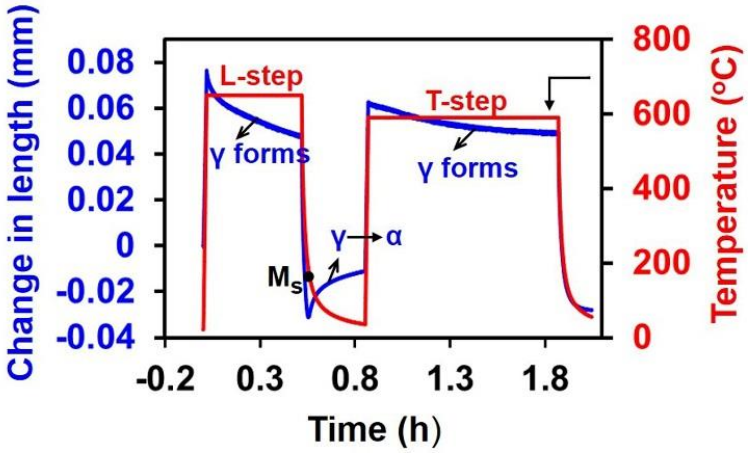

Figure 5.2- Dilatometric responses of the 10 wt. % Ni steel (in blue) exhibiting austenite formation during intercritical isothermal steps at 923 K (650 ^{o}C) and 863 K (590 ^{o}C). Some of the austenite transforms to martensite during quenching, after isothermal aging at 923 K (650 ^{o}C). This transformation commences at 461 K (188 ^{o}C), the martensite-start (M_s) temperature. Dilatometry performed by Dr. Zhang, NSWCCD.

5.4.2 Synchrotron X-ray Diffraction (XRD)

High intensity synchrotron X-ray diffraction (XRD) scans of the 10 wt. % Ni steel samples after different stages of the QLT-treatment are displayed in Figure 5.3. The volume-fraction of austenite measured in the NIST standard is 5.4±0.1%, while the calibrated standard value is 5.8 %. The volume-fractions of austenite after calibration for the as-quenched, QT, QL and QLT-treated samples are 1.5, 2.9, 8.1 and 18.5 vol. %, respectively, Table 5.3. We also obtained a volume-fraction of ~ 18% for the QLT-treated sample that was subsequently quenched to 188.7 K (-84.4 ^{o}C), prior to the XRD investigation. This indicates that austenite after the T-step is thermally stable and its Ms temperature is less than 188.7 K (-84.4 ^{o}C).

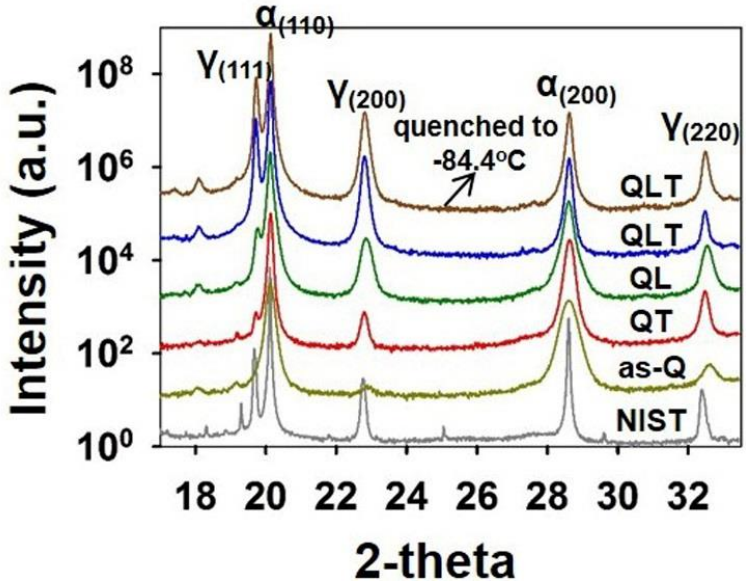

Figure 5.3- Synchrotron X-ray diffraction scans of the 10 wt. % Ni steel after different stages of the QLT-treatment, including the QLT-treated sample that was subsequently quenched to 188.7 K (-84.4 ^{o}C), prior to the X-ray diffraction analysis. The NIST standard sample is also analysed for calibration purposes.

Table 5.3- Volume percent of austenite in 10 wt. % Ni steel samples after different stages of the QLT-treatment, as obtained by synchrotron X-ray diffraction (XRD) experiments performed at the Advanced Photon Source at Argonne National Laboratory.

	as-quenched	QT	QL	QLT	QLT (quenched to 188.7 K (-84.4ºC), prior to XRD)
Vol. %	1.5±0.5	2.9±0.2	8.1±0.3	18.5±0.2	18.0±0.2

5.4.3 3-D Atom-Probe Tomography (APT)

5.4.3.1 APT analyses of the QL-treated samples

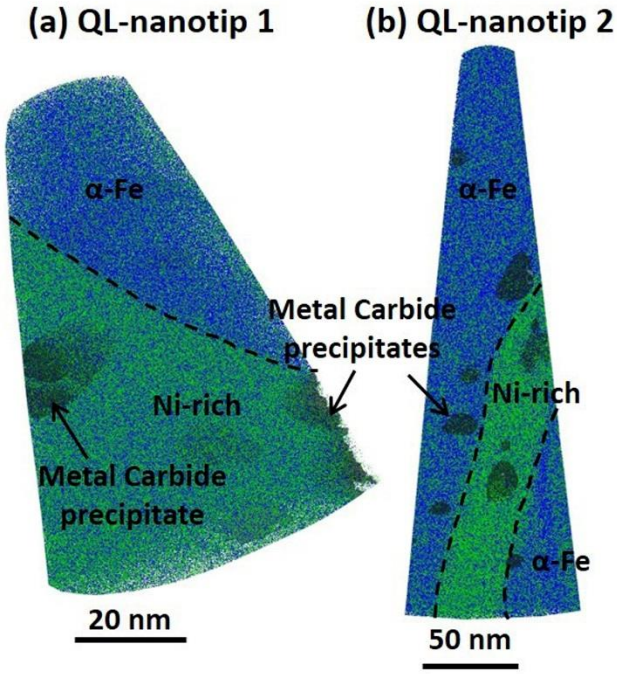

Figure 5.4- 3-D APT reconstructions of the QL-treated 10 wt. % Ni steel: (a) QL-1 sample, Fe atoms (10 %) are displayed as blue dots, Ni atoms (100%) are displayed in green; (b) QL-2 sample, Fe atoms (3 %) are displayed as blue dots, Ni atoms (30%) are displayed in green. The heterophase interface (indicated by a dashed curve) between the tempered martensite matrix, α-Fe, and the Ni-rich region is delineated by 9 and 11 at. % Ni isoconcentration surfaces in (a) and (b), respectively. Metal carbides are delineated by a 10 at. % (C plus Cr plus Mo plus V) isoconcentration surfaces (black) in both reconstructions.

Figure 5.4(a) and Figure 5.4(b) display the 3-D APT reconstructions of the QL-treated steel, in which Fe atoms are displayed in blue and Ni atoms are in green. We also observe mixed metal carbides of MC and M_2C-type in both APT reconstructions; these carbides are displayed in black, and are rich in Mo, Cr, and V. During the austenite formation at 923 K (650 ^oC), Ni partitions to austenite and it is depleted in the tempered martensite matrix, α-Fe, which is richer in Fe and thus appears in blue in Figure 5.4. We note that some of the austenite formed during the L-step transforms to martensite during quenching, as is revealed by dilatometry (Figure 5.2). We refer to this martensite as fresh-martensite, whose composition is assumed to be the composition of the reverted austenite formed at 923 K (650 ^oC). This assumption is reasonable as the martensitic transformation is compositionally invariant and commences at a relatively low temperature in the QL-treated sample, 461 K (188 ^oC), below which the diffusion of solute elements (especially substitutional) in austenite or martensite during quenching is negligible. Kim et al.[85] also obtained similar composition of fresh-martensite as reverted austenite in a 5.5 wt. % Ni steel (intercritically annealed at 943 K (670 ^oC)) using energy-dispersive X-ray spectroscopy (EDS) in a scanning transmission electron microscope (STEM). Thus, the composition of the Ni-rich region in the APT reconstructions in Figure 5.4 represents the composition of austenite formed at 923 K (650 ^oC) and is obtained using a proximity histogram (or proxigram for short)[126], which measures the concentrations of each element as a function of distance from a specified isoconcentration surface. Since we want to determine the concentration profiles of elements only in the α-Fe matrix and the Ni-rich region, the metal carbides observed in the 3-D reconstructions were excluded from the dataset, using the IVAS code before obtaining the proximity histograms. The resulting proximity histogram concentration profiles for the QL-1 and QL-2 samples, obtained from 9 and 11 at. % Ni isoconcentration surfaces, Figure 5.4, are displayed in Figure 5.5(a) and

Figure 5.5(b), respectively and they reveal enrichment of Ni, Mn, C, Cr and Cu in austenite (toward the right-hand side of the vertical fiducial marker). While Ni, Mn, C and Cu are well known austenite stabilizers [219], the partitioning of Cr in austenite is noteworthy, which has been observed in an APT investigation of 4.5 and 10 wt. % Ni steels, and was attributed to metastable equilibrium between austenite and martensite in the absence of the ferrite phase [202].

The average compositions obtained for the α-Fe matrix and austenite from these proximity histograms are listed in Table 5.4 and the error reported is $\pm\sigma$, where σ is obtained from counting statistics [53], and is expressed as

$$\sigma = \sqrt{\frac{c_i\,(1-c_i)}{N}} \qquad 5.5$$

where c_i is the measured concentration of element i in a sampled volume containing N total number of atoms. The compositions of α-Fe matrix and austenite from equilibrium thermodynamic calculations at 923 K (650 ^{o}C) using ThermoCalc are also presented in Table 5.4. Austenite in the QL-treated samples is primarily enriched in Ni (12.5-16.7 at. %) and contains much smaller concentrations of the other solute elements, ~ 0.4C-1.1Mn-0.8Cr-0.3Si-0.6Mo-0.2Cu at. %, Table 5.4. The enrichment of C (strong austenite stabilizer) in austenite is small (0.4 at. %) due to its overall small concentration in steel (0.4 at. %), coupled with the simultaneous precipitation of metal carbides during the intercritical treatment. Here, we discuss in detail, the partitioning behaviour of Ni across the austenite and α-Fe matrix interface during the QLT-treatment.

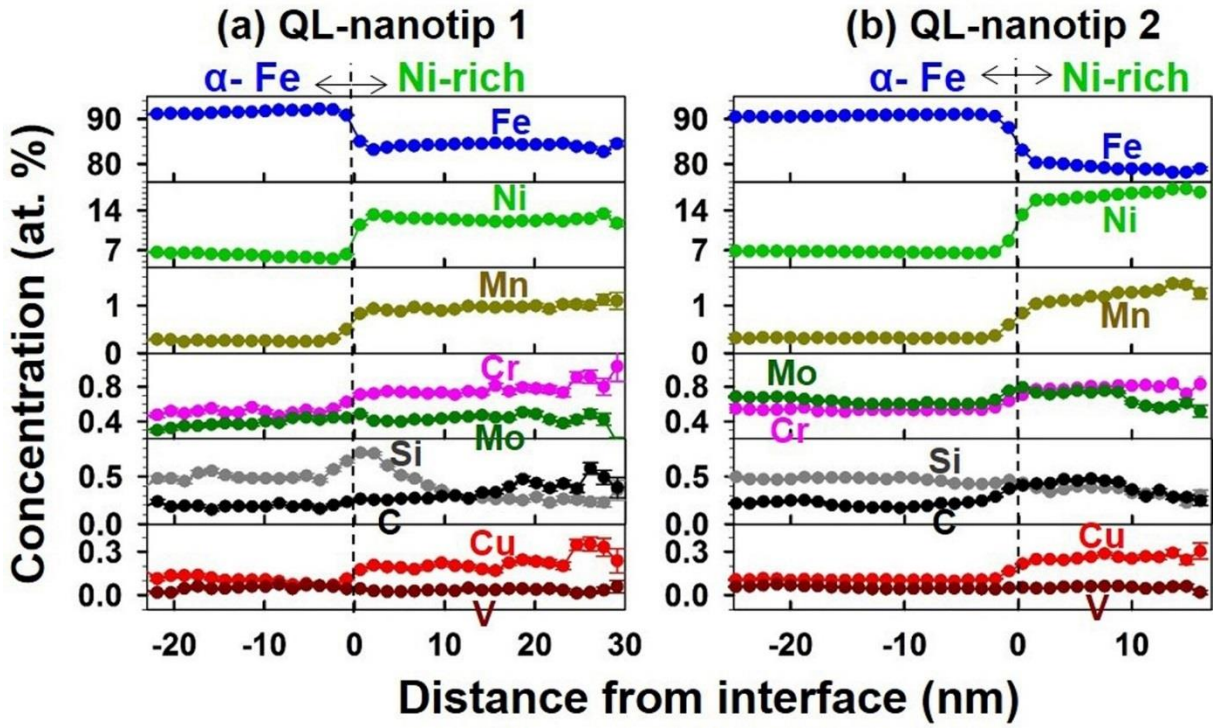

Figure 5.5- Proximity histogram concentration profiles obtained from 9 and 11 at. % Ni isoconcentration surfaces in: (a) QL-1; and (b) QL-2 10 wt. % Ni steel samples, respectively, displaying the concentration profiles of Fe, Ni, Mn, Cr, Mo, Si, C, Cu, and V across the α-Fe matrix and Ni-rich region. Metal carbides were excluded from the datasets before obtaining the proximity histograms.

Table 5.4- Chemical compositions (at. %) of Ni-rich region (austenite formed during L-step at 923 K (650 ^{o}C)) and the tempered martensite matrix, α-Fe in the QL-treated 10 wt. % Ni steel, as measured by APT. Martensite-start (M_s) temperatures, as calculated using the Ghosh-Olson thermodynamic and kinetic approach are also shown. Compositions of austenite and α-Fe, obtained from equilibrium thermodynamic calculations at 923 K (650 ^{o}C) using ThermoCalc are also listed.

Nanotip 1	**Fe**	**Ni**	**Mn**	**C**	**Si**	**Cr**	**Mo**	**Cu**	**V**	**M_s K(^{o}C)**
Austenite at L-step	84.06 ±0.26	12.50 ±0.23	0.96 ±0.07	0.36 ±0.04	0.35 ±0.04	0.77 ±0.06	0.43 ±0.05	0.23 ±0.04	0.04 ±0.01	459.6 (186.5)
α-Fe	90.98 ±0.22	6.73 ±0.19	0.26 ±0.04	0.21 ±0.04	0.46 ±0.05	0.50 ±0.05	0.34 ±0.04	0.14 ±0.03	0.03 ±0.01	
Nanotip 2	**Fe**	**Ni**	**Mn**	**C**	**Si**	**Cr**	**Mo**	**Cu**	**V**	**M_s K(^{o}C)**
Austenite at L-step	79.22 ±0.16	16.68 ±0.15	1.23 ±0.04	0.39 ±0.02	0.34 ±0.02	0.79 ±0.03	0.67 ±0.03	0.26 ±0.02	0.06 ±0.01	345 (71.9)
α-Fe	90.54 ±0.05	6.83 ±0.05	0.32 ±0.01	0.23 ±0.01	0.48 ±0.01	0.53 ±0.01	0.66 ±0.01	0.11 ±0.01	0.06 ±0.004	
ThermoCalc 923 K (650 ^{o}C)	**Fe**	**Ni**	**Mn**	**C**	**Si**	**Cr**	**Mo**	**Cu**	**V**	
Austenite	85.53	11.80	0.80	0.18	0.48	0.68	0.31	0.17	0.006	
α-Fe	95.47	3.23	0.09	0.003	0.28	0.51	0.27	0.03	0.016	

5.4.3.2 APT analyses of the QLT-treated samples

3-D APT reconstructions of the QLT-1 and QLT-2 samples are displayed in Figure 5.6(a) and Figure 5.6(b), respectively. The heterophase interface between α-Fe and the Ni-rich region (indicated by a dashed curve) in these APT reconstructions is delineated by 11 at. % Ni isoconcentration surfaces. As in the QL-treated samples, we observe mixed metal-carbides enriched in Mo, Cr, and V of MC- and M_2C-types in both QLT-treated samples. Proximity histogram concentration profiles obtained from the 11 at. % Ni isoconcentration surfaces in QLT-1 and QLT-2 samples (after excluding the metal carbides from the dataset) are displayed in Figure 5.7(a) and Figure 5.7(b), respectively.

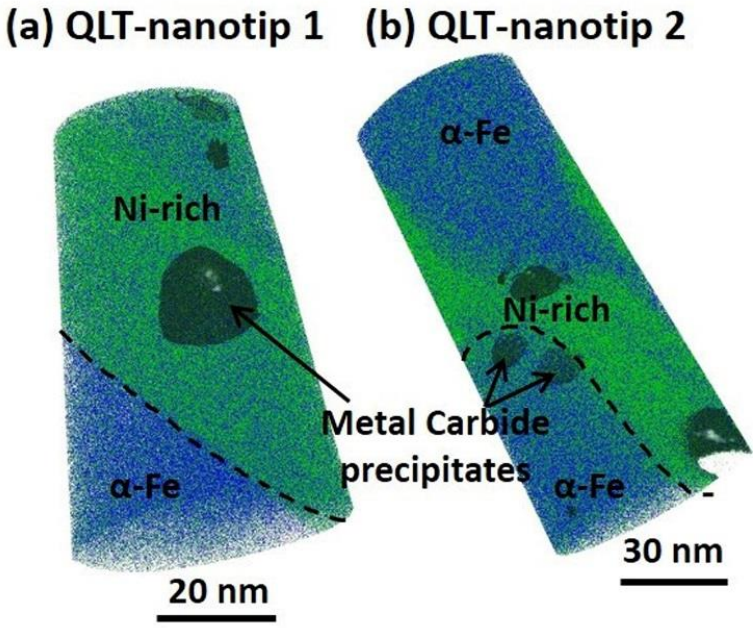

Figure 5.6- 3-D APT reconstructions of the QLT-treated 10 wt. % Ni steel: (a) QLT-1 sample, Fe atoms (10 %) are displayed as blue dots, Ni atoms (80%) are displayed in green; (b) QLT-2 sample, Fe atoms (5 %) are displayed as blue dots, Ni atoms (50%) are displayed in green. The heterophase interface (indicated by a dashed curve) between the tempered martensite matrix, α-Fe, and the Ni-rich region is delineated by 11 at. % Ni isoconcentration surface in both (a) and (b). Metal carbides are delineated by a 10 at. % (C plus Cr plus Mo plus V) isoconcentration surfaces (black) in both reconstructions.

In Figure 5.7(a), we observe significant inhomogeneities in the Ni concentrations within the Ni-rich region (right-hand side of the vertical fiducial marker in the proximity histogram). Ni-rich region in this proximity histogram is, therefore, divided into three regions having different Ni concentrations; the region with the highest Ni concentration is shaded in the proximity histogram and has an average Ni concentration of 21.7 at. %, and the two regions to the left-and right-hand sides of this shaded region have average Ni concentrations of 17.7 and 14.6 at. %, respectively. Table 5.5 lists the overall compositions of these Ni-rich regions along with the composition of α-Fe and the error reported is ±σ, where σ is determined from equation 5.5. The inhomogeneous distribution of Ni is also observed in the Ni-rich region in the proximity histogram corresponding to the QLT-2 sample, Figure 5.7(b). The shaded regions in the proximity histogram have an average Ni concentration of 21.9 at. %, while the average Ni concentration in the plateau region between these shaded regions is 15.9 at. %. Table 5.5 lists the overall compositions of these regions along with the composition of α-Fe. Similar trends as described for Ni is also observed for the Mn and Cu concentration profiles in both the proximity histograms in Figure 5.7. Compositions of austenite and α-Fe from equilibrium thermodynamic calculations at 863 K (590 ^{o}C) using ThermoCalc are also presented in Table 5.5. The inhomogeneous distributions of these elements is a result of the austenite forming with different compositions during intercritical treatments at 923 K (650 ^{o}C) and 863 K (590 ^{o}C), coupled with sluggish diffusion of these elements in austenite, which is discussed in more detail in Section 5.5.1.

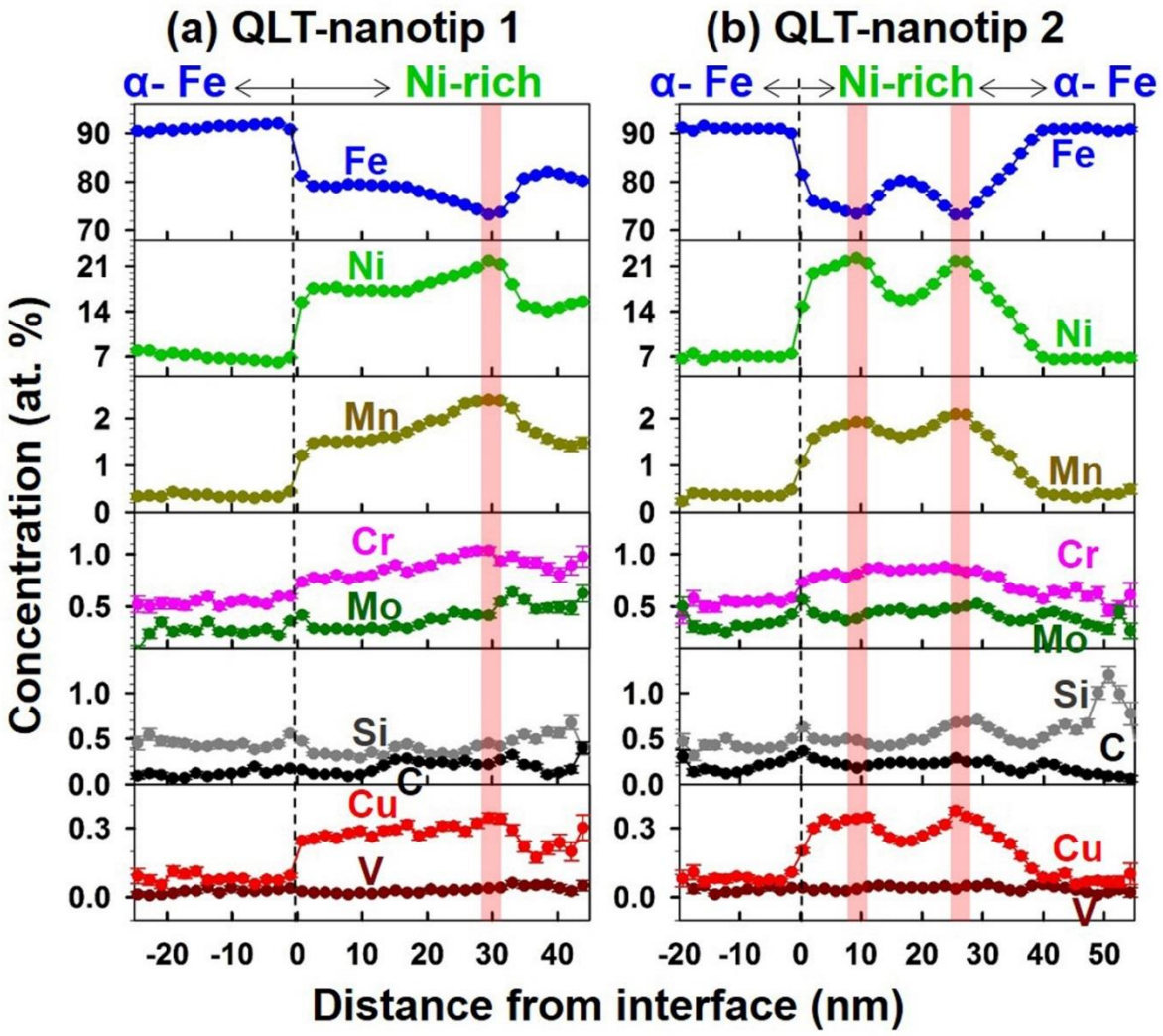

Figure 5.7- Proximity histogram concentration profiles obtained from 11 at. % Ni isoconcentration surfaces in: (a) QLT-1; and (b) QLT-2 10 wt. % Ni steel samples, displaying the concentration profiles of Fe, Ni, Mn, Cr, Mo, Si, C, Cu, and V across the α-Fe matrix and Ni-rich region. Metal carbides were excluded from the dataset before obtaining the proximity histograms. Shaded regions on the Ni-rich side in (a) and (b) represent the composition of austenite formed during the T-step tempering at 863 K **(**590 ^{o}C).

Table 5.5- Chemical compositions (at. %) of Ni-rich regions (austenite formed during T-step at 863 K (590 ºC) and retained austenite from L-step at 923 K (650 ºC)) and the tempered martensite matrix, α-Fe in the QLT-treated 10 wt. % Ni steel samples, as measured by APT. Martensite-start (M_s) temperatures, as calculated using the Ghosh-Olson thermodynamic and kinetic approach are also shown. Compositions of austenite and α-Fe, obtained from equilibrium thermodynamic calculations at 863 K (590 ºC) using ThermoCalc are also listed.

Nanotip 1	**Fe**	**Ni**	**Mn**	**C**	**Si**	**Cr**	**Mo**	**Cu**	**V**	**M_s K (ºC)**
Austenite at T-step, nanotip 1	73.37 ±0.31	21.73 ±0.29	2.40 ±0.11	0.20 ±0.03	0.45 ±0.05	0.99 ±0.07	0.43 ±0.05	0.33 ±0.04	0.04 ±0.01	125.7 (-147.4)
Austenite from L-step (left of shaded region, Figure 5.7(a))	79.15 ±0.24	17.34 ±0.22	1.55 ±0.07	0.16 ±0.02	0.35 ±0.03	0.80 ±0.05	0.29 ±0.03	0.28 ±0.03	0.02 ±0.01	332.8 (59.7)
Austenite from L-step (right of shaded region, Figure 5.7(a))	81.40 ±0.52	14.62 ±0.48	1.58 ±0.17	0.15 ±0.05	0.57 ±0.10	0.88 ±0.13	0.48 ±0.09	0.23 ±0.06	0.05 ±0.03	390.8 (117.7)
α-Fe	90.65 ±0.41	7.52 ±0.37	0.37 ±0.08	0.08 ±0.03	0.46 ±0.09	0.52 ±0.10	0.25 ±0.07	0.09 ±0.04	0.02 ±0.01	
Nanotip 2	**Fe**	**Ni**	**Mn**	**C**	**Si**	**Cr**	**Mo**	**Cu**	**V**	**M_s K (ºC)**
Austenite at T-step,	73.43 ±0.16	21.89 ±0.15	2.00 ±0.05	0.23 ±0.02	0.58 ±0.03	0.83 ±0.03	0.44 ±0.02	0.36 ±0.02	0.04 ±0.01	153.2 (-119.9)
Austenite from L-step	80.05 ±0.15	15.87 ±0.13	1.64± 0.05	0.23± 0.02	0.46± 0.02	0.85± 0.03	0.46± 0.02	0.25± 0.02	0.04± 0.01	351.4 (78.3)
α-Fe	90.89 ±0.32	6.82 ±0.28	0.36 ±0.07	0.15 ±0.04	0.62 ±0.09	0.56 ±0.08	0.34 ±0.06	0.03 ±0.02	0.08 ±0.03	
ThermoCalc 863 K (590ºC)	**Fe**	**Ni**	**Mn**	**C**	**Si**	**Cr**	**Mo**	**Cu**	**V**	
Austenite	78.49	18.09	1.39	0.1	0.68	0.71	0.2	0.29	0.002	
α-Fe	95.18	3.72	0.074	0.001	0.25	0.53	0.13	0.024	0.006	

5.5 Discussion

5.5.1 3-D Atom-Probe Tomography (APT)

5.5.1.1 APT analyses of the QL-treated samples

Nickel concentration in austenite in QL-1 sample, as obtained from the proximity histogram in Figure 5.5(a) is 12.5 at. %, which is in reasonable agreement with 11.8 at. % Ni, predicted by thermodynamic equilibrium calculations at 923 K (650 ^{o}C), Table 5.4. The austenite in the QL-2 sample has, however, a significantly higher Ni concentration, which increases gradually from 15.3 at. % near the α-Fe/austenite heterophase interface to 17.9 at. % toward the inner core of austenite, Figure 5.5(b). We note that the right-hand side of the proximity histogram in Figure 5.5(b) represents the concentration of the inner core of the austenite region, Figure 5.4(b). A similar trend as for Ni is also observed for the Mn concentration profile, Figure 5.5(b). Due to the limited holding time of 30 minutes at 923 K (650 ^{o}C), composition of austenite can deviate from the equilibrium calculated values. Higher average Ni concentration in austenite, as observed in the QL-2 sample, could be facilitated by short-circuit diffusion of Ni along lath-boundaries and dislocations. In comparison to QL-2 sample, there is little variation in the Ni concentration within the austenite in QL-1 sample, Figure 5.5(a). It is slightly lesser near the center of the austenitic region, ~12 at. % than at the α-Fe/austenite heterophase interface and toward the extreme right-hand side of the proximity histogram, ~ 13 at. %. Fultz et al.[84] observed a higher Ni concentration toward the surfaces of austenite particles as compared to their inner regions in their STEM-EDS study of a 9 wt. % Ni steel, intercritically tempered at 863 K (590 ^{o}C). They suggested that with increasing aging time, the available carbon concentration in martensite decreases and therefore, continued growth of austenitic particles required a higher Ni-concentration. They, however, could not measure the carbon concentration in austenite due to limitation of the EDS

technique. In the present study, we do not observe this trend in the QL-2 sample, as the Ni concentration near the center of the austenitic region is greater than at the α-Fe/austenite heterophase interface. Additionally, unlike the 9 wt. % Ni steels analysed by Fultz et al.[84], the steel investigated in the present study also contains significant additions of strong carbide forming elements, specifically Mo, Cr and V. The presence of the metal carbides in the microstructure increases the complexity of analysing small variations in the C and Ni concentrations in austenite. Linear concentration profiles of Ni, C, Mo, Cr and V across a M_2C-type carbide observed in austenite in the QL-2 sample are displayed in Figure 5.8, which reveal strong partitioning of C and Ni toward and away from the carbide phase, respectively. Thus, even though the metal carbides were excluded before obtaining the proximity histograms displayed in Figure 5.5, concentrations of C and Ni in austenite in proximity to the carbides can be affected.

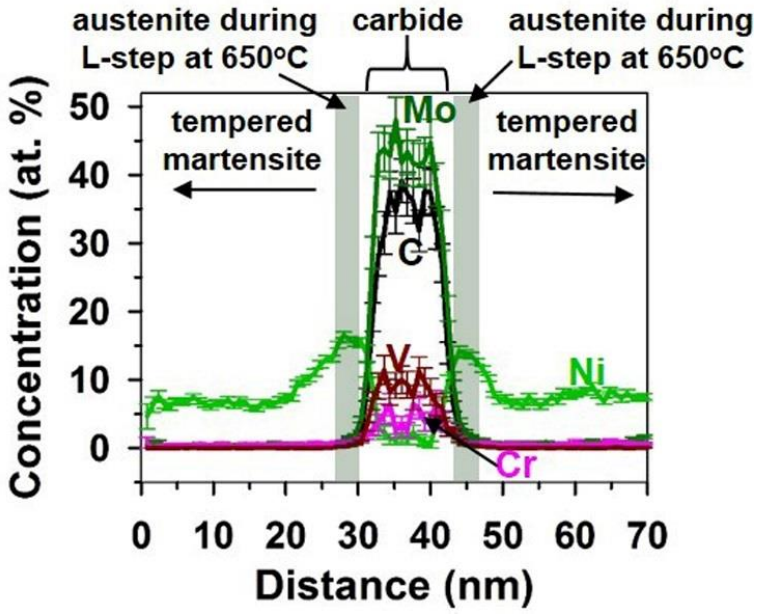

Figure 5.8- Linear concentration profiles of Mo, C, V, Cr, and Ni across the tempered martensite (α-Fe), Ni-rich region (austenite), and an M_2C-type carbide precipitate in the QL-2 10 wt. % Ni steel sample exhibiting strong partitioning of C and Ni toward and away from the carbide phase, respectively.

5.5.1.2 APT analyses of the QLT-treated samples

Shaded regions in the proximity histogram, Figure 5.7, represent the nanolayers of austenite that form during the T-step tempering treatment at 863 K (590 ^{o}C). The new austenite formed has a higher Ni concentration (~22 at. %) than the austenite formed during the L-step (~12-17 at. %). This result is in general agreement with the thermodynamic equilibrium calculations, which predict a higher Ni concentration in austenite at 863 K (590 ^{o}C) than at 923 K (650 ^{o}C), Table 5.4 and 5.5. We emphasize that the Ni diffusivity, *D* in austenite at 863 K (590 ^{o}C) is extremely small, therefore, its estimated root-mean-squared diffusion distance, $\sqrt{2Dt}$ in austenite for 1 h is only ~1 nm [220, 221]. As a result, the Ni concentration in austenite does not homogenize and we are able to differentiate the austenitic Ni compositions formed during the L- and T-steps in the proximity histograms, Figure 5.7. Therefore, the Ni-rich regions lying in the vicinity of the shaded regions in the proximity histograms represent austenite that is retained from the L-step and contains ~ 14.5-17.0 at. % Ni. Diffusivity of Ni in ferrite at 863 K (590 ^{o}C) is more than three orders of magnitude greater than in austenite and its estimated root-mean-squared diffusion distance, $\sqrt{2Dt}$ in ferrite for 1 h is 37 nm [220]. Thus, during the T-step tempering, Ni diffuses from the martensitic matrix toward retained austenite (as dictated by thermodynamics), but due to its negligible diffusion in austenite, gets accumulated at its surface. This leads to the growth of austenite (with a higher Ni concentration) on top of the retained austenite from the L-step.

A previous APT investigation of a similar 10 wt. % Ni steel also indicated a similar growth mode of a thin layer of austenite with a higher Ni concentration at a tempering temperature of 811 K (538 ^{o}C) over the austenite inherited from prior annealing at 894 K (621 ^{o}C) [202]. Austenite reversion via growth at martensite-austenite interface has also been reported in Fe-12 wt. % Mn

steel [151, 218]. Using APT, the authors showed that retained austenite (from as-quenched condition) acted as a template for the growth of austenite during aging at 723 K (450 ^{o}C).

5.5.2 Martensite-start (M_s) temperature calculations

Using the Ghosh-Olson thermodynamic and kinetic approach [208-210], and the composition of austenite measured utilizing APT, the predicted M_s temperatures for austenite in the QL-1 and QL-2 samples are 459.6 K (186.5 ^{o}C) and 345 K (71.9 ^{o}C), respectively, Table 5.4. The calculated M_s temperature for the QL-1 sample is in excellent agreement with the dilatometric results, which indicated that the M_s temperature for the austenite formed during the L-step is 461 K (188 ^{o}C), Figure 5.2. Austenite in the QL-2 sample is richer in Ni and thus has a lower M_s temperature. Nevertheless, it is certain that the austenite formed after the L-step is too lean in its solute content to be stable at sub-ambient temperatures. We emphasize that the martensitic transformation commences at M_s and continues to occur on further cooling and is complete at the martensite-finish (M_f) temperature [222]. Thus, depending on the final temperature reached on cooling, some of the austenite can be retained below the M_s temperature, as is the case for the QL-treated sample in which 8.1 vol. % austenite is retained at room temperature, Table 5.3. It has been observed in 9 wt. % Ni steels that individual austenite particles may undergo only a partial martensitic transformation [77, 84]. Regions within the austenite particles with leaner Ni concentrations were found to be less stable and transformed to martensite, while other regions remained untransformed [84].

For the austenite formed during the T-step in the fully QLT-treated samples (shaded regions in the proximity histograms in Figure 5.7, compositions in Table 5.5), M_s temperature is calculated to be 126 K (-147 ^{o}C) and 153 K (-120 ^{o}C) for the austenite in QLT-1 and QLT-2 samples, respectively.

These predictions are in agreement with the X-ray diffraction results, which revealed that the austenite after the T-step remains thermally stable even at 188.7 K (-84.4ºC). In contrast, commonly used linear empirical relations in the archival literature [163, 204, 223-226] are unable to predict accurately, the M_s temperatures for the austenite formed during the T-step, Table 5.6. In general, the applicability of these empirical relations is restricted to leaner solute compositions of austenite [163] and thus, they are not meaningful for the highly Ni-rich austenite obtained in the present study after the T-step.

Table 5.6- Comparison of M_s temperature predictions for austenite obtained after the T-step at 863 K (590 ºC) in the QLT-treated 10 wt. % Ni steel samples using the Ghosh-Olson approach and empirical relations.

	M_s K (ºC) QLT- 1	**M_s K (ºC) QLT- 2**
Present (Ghosh-Olson approach)[208-210]	126(-147)	153(-120)
Payson et al. [223]	267(-6)	278(5)
Grange et al.[224]	210 (-63)	224(-49)
Nehrenberg[225]	273 (0)	283(10)
Steven et al.[226]	328(55)	337(64)
Andrews[163]	306(33)	313(40)

5.5.3 DICTRA simulations

To simulate austenite formation during the T-step, the DICTRA cell at t = 0 s is constructed to represent the microstructure of the QL-treated sample, Figure 5.9(a). It consists of tempered martensite, fresh-martensite and retained austenite with Ni concentrations of 7, 15 and 15 at. %, respectively, as approximated from the APT analyses of the QL-treated samples, Table 5.4. The dimension of the retained austenitic region in the DICTRA cell, Figure 5.9(a), is fixed at 10 nm,

similar to regions representing retained austenite from the L-step in the proximity histograms, Figure 5.7. The extent of the fresh martensitic region is kept to 20 nm and the total length of tempered martensitic region, 70 nm is obtained after fixing the overall Ni concentration at 9.4 at. % in the alloy. Following the discussion in Section 5.5.1.2, we use the retained austenite from the L-step as a template for austenite growth during the T-step.

DICTRA simulations after 1 h at 863 K (590 ^{o}C) indicate that austenite grows predominantly into the Ni-rich fresh-martensitic region, Figure 5.9(b), and contains 18 at. % Ni. In Figure 5.9(b), we also observe that the Ni concentration of the newly formed austenite (18 at. %) during the 1 h simulation at 863 K (590 ^{o}C) does not homogenize with the Ni concentration of the austenite inherited from the L-step (15 at. %). We also similarly interpret the APT proximity histograms of the QLT-treated samples, Figure 5.7. DICTRA simulation after 100 h exhibit, however, a more homogeneous Ni concentration in the austenitic phase, Figure 5.9(c).

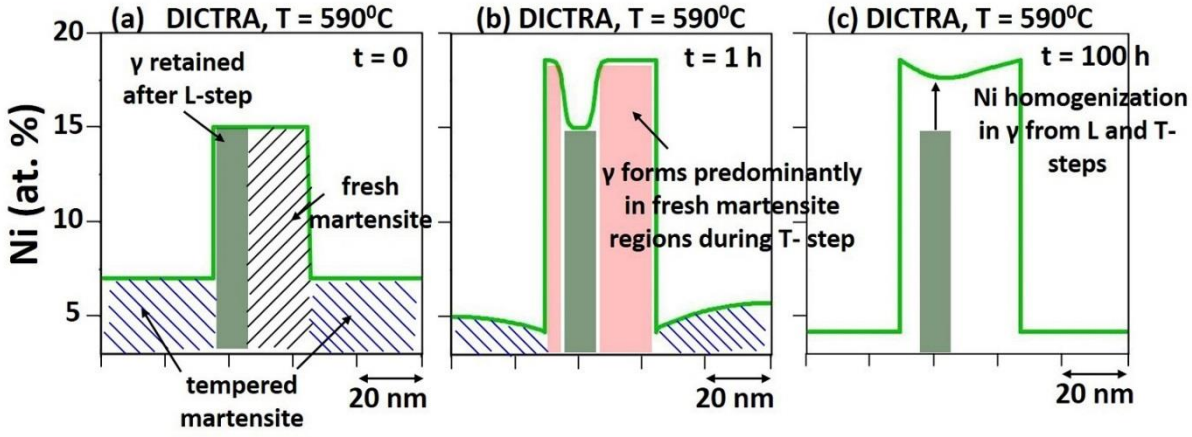

Figure 5.9- DICTRA simulations during T-step tempering at 863 K **(**590 ^{o}C) displaying a Ni concentration profile after: (a) 0 s; (b) 1 h; and (c) 100 h. A DICTRA simulation after 1 h in (b) indicates that austenite grows predominantly into the fresh-martensitic region.

5.5.4 Austenite formation during the T-step

Austenite formation is significantly more profuse during isothermal treatment at higher intercritical temperatures, due to the higher predicted equilibrium volume-fraction of austenite coupled with the faster diffusion kinetics of Ni. Thus, even though some of the austenite formed is not thermally stable after the L-step, densely distributed Ni-rich regions are created, Figure 5.1(a), in the form of fresh-martensite or retained austenite. The presence of Ni-rich martensitic regions in proximity of retained austenite reduces the root-mean-squared diffusion distance for Ni toward retained austenite, which enhances the growth kinetics of austenite during the T-step. Thus, significant austenite growth occurs within 1 h as the austenite volume-fraction increases from 8.1 % in the QL-treated sample to 18.5 % in the QLT-treated sample. In contrast, we obtain only 2.9 vol. % austenite in the QT-treated sample, tempered at 863 K (590 ^{o}C) for 1 h without a prior intercritical step at a higher temperature. Thus, a multistep intercritical treatment facilitates the formation of a significant volume-fraction of thermally stable austenite in relatively short holding times, which are of great practical relevance. Similar multistep intercritical treatments have also been employed for 5.5 wt. % Ni ferritic steels [78, 83, 85] and ultrahigh strength AF1410 martensitic steels [94] to form finely dispersed austenite, enriched with stabilizing solutes.

Additionally, if the T-step treatment is done without an intermediate quench to the room temperature after the L-step (no fresh-martensite formation occurs), we obtain only 6 vol. % austenite after the QLT-treatment, Figure 5.10(b). In contrast, the optimal QLT-treatment (involving an intermediate quench to the room temperature after the L-step) results in 18 vol. % austenite, Figure 5.10(a). This provides direct evidence of the role of fresh martensite in austenite formation during T-step tempering.

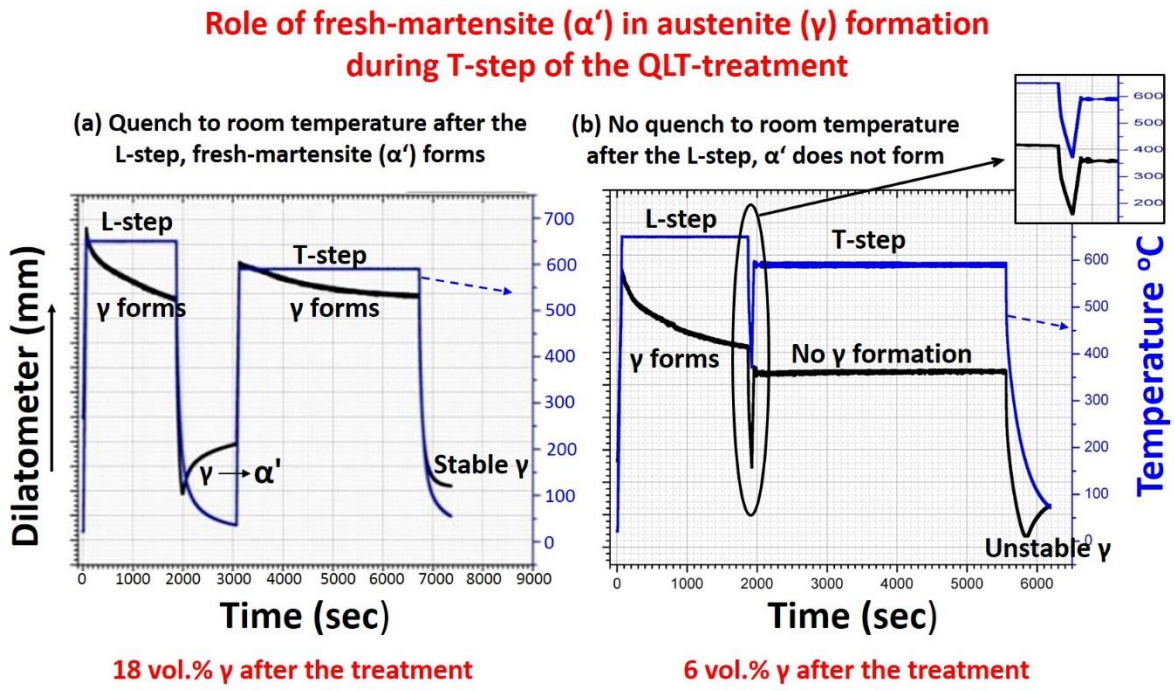

Figure 5.10- Dilatometric responses of the 10 wt. % Ni steel (in blue) for, (a) optimal QLT-treatment involving a quench to room temperature following the L-step (isothermal heating at 923 K (650 ^{o}C)). Some of the austenite transforms to martensite during quenching; this transformation commences at 461 K (188 ^{o}C), the martensite-start (Ms) temperature; (b) QLT-treatment without the quench to room temperature after the L-step. No austenite formation occurs during the T-step (isothermal heating at 863 K (590 ^{o}C)). Dilatometry performed by Dr. Zhang, NSWCCD.

It can now be inferred that the growth of the austenitic layer during the T-step, Figure 5.7(a), occurred at the expense of the fresh-martensitic region, which was sandwiched between the retained austenite regions, inherited from the L-step. Alternatively, if the retained austenite region is placed between the fresh-martensitic regions (as in the DICTRA cell, Figure 5.11(a)), the austenitic layers grow on both sides of the retained austenite during the T-step, Figure 5.11(b). The DICTRA simulated Ni concentration profile, Figure 5.11(b), is qualitatively similar to the Ni concentration profile obtained in the proximity histogram of the QLT-2 sample, Figure 5.7(b), and is reproduced herein, Figure 5.11(c), for comparative purposes. The Ni concentration of the newly

formed austenite layer is, however, higher in the APT profile (~22 at. %) than that obtained by DICTRA simulations, 18 at. %. These differences can arise as the DICTRA simulations are performed on a simpler Fe-Ni system, assume an infinite mobility of the heterophase interface and neglect effects from curved interfaces [201, 218].

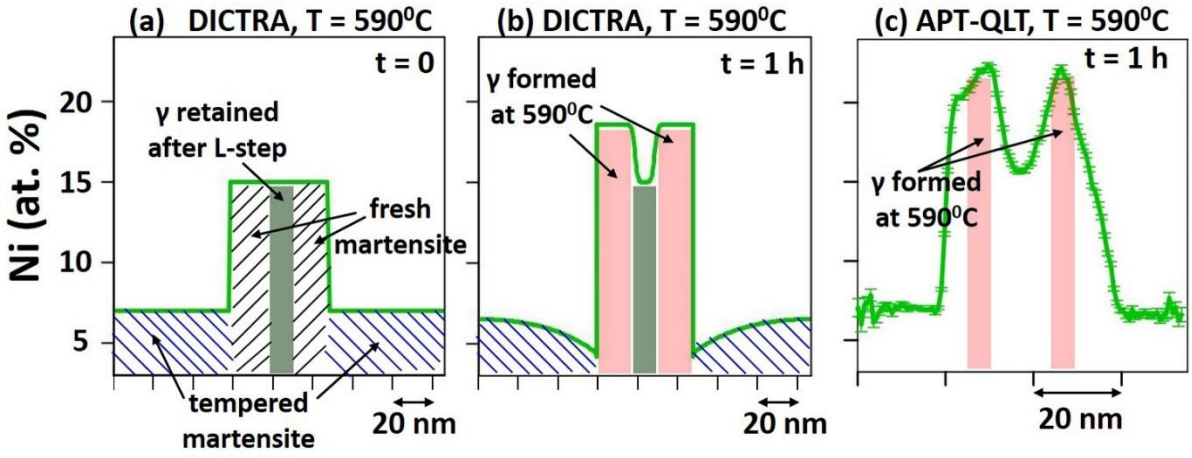

Figure 5.11- DICTRA simulations during T-step tempering at 863 K (590 ^{o}C) displaying a Ni concentration profile after: (a) 0 s; (b) 1 h; and (c) Ni concentration profile obtained from an APT investigation of the QLT-treated 10 wt. % Ni steel (QLT-2 sample, Figure 5.7(b)). Nickel concentration profiles obtained from both APT and DICTRA simulations indicate the formation of nanolayers of austenite with a higher Ni concentration on top of the retained austenite from the L-step containing lower Ni concentration.

5.6 Summary and Conclusions

In this research, the role of Ni-rich, austenite and fresh martensitic regions, inherited from the L-step at 923 K (650 ^{o}C), in forming thermally stable austenite during the T-step tempering at 863 K (590 ^{o}C) is highlighted. The major findings are as follows:

1. Austenite formed during the first intercritical treatment (L-step) at 923 K (650 ^{o}C) starts transforming to martensite at 461 K (188 ^{o}C), Figure 5.2. A significant volume fraction of

austenite (8.1 %) is, however, retained and still present after quenching the sample to room temperature, as determined by synchrotron X-ray diffraction experiments performed at the Advanced Photon Source at Argonne National Laboratory.

2. The volume-fraction of austenite in the QLT-treated sample at room temperature is 18.5 %; 18 vol. % austenite is also obtained in the QLT-treated sample that was quenched to 188.7 K (-84.4 ^{o}C), prior to the X-ray diffraction experiment at the Advanced Photon Source, Table 5.3. This indicates that austenite after the T-step is thermally stable and its M_s is below 188.7 K (-84.4 ^{o}C).

3. The composition of austenite formed during the L-step intercritical treatment at 923 K (650 ^{o}C), as obtained by atom-probe tomography is 84.1Fe-12.5Ni-1.0Mn-0.36C-0.35Si-0.77Cr-0.43Mo-0.23Cu-0.04V (at. %) for the QL-1 sample, and 79.2Fe-16.7Ni-1.2Mn-0.39C-0.34Si-0.79Cr-0.67Mo-0.26Cu-0.06V (at. %) for the QL-2 sample, Table 5.4. The corresponding M_s temperatures, as calculated using the Ghosh-Olson thermodynamic and kinetic approach are 459.6 K (186.5 ^{o}C) and 345 K (71.9 ^{o}C) for austenite in the QL-1 and QL-2 samples, respectively.

4. Atom-probe tomographic concentration profiles obtained for the QLT-treated samples indicate that nanolayers of austenite, with a higher Ni concentration grow during the T-step at 863 K (590 ^{o}C), on top of the retained austenite from the L-step, Figure 5.7. The composition of austenite formed during the T-step, as obtained by atom-probe tomography is 73.4Fe-21.7Ni-2.4Mn-0.2C-0.45Si-0.99Cr-0.43Mo-0.33Cu-0.04V (at. %) for QLT-1 sample, and 73.4Fe-

21.9Ni-2.0Mn-0.23C-0.58Si-0.83Cr-0.44Mo-0.36Cu-0.04V (at. %) for the QLT-2 sample, Table 5.5.

5. The M_s temperature for the austenite formed during the T-step in the QLT-treated samples, as calculated using the Ghosh-Olson thermodynamic and kinetic approach is less than 173 K (-100 ^{o}C), which is in an excellent agreement with our experimental results. Alternatively, linear empirical relations in the archival literature are not meaningful for estimating M_s temperatures for the austenite with such high Ni concentrations, Table 5.6.

6. DICTRA simulations in conjunction with atom-probe tomography experiments reveal that austenite growth during the T-step tempering at 863 K (590 ^{o}C) occurs predominantly in the Ni-rich fresh-martensitic regions, Figure 5.9. The presence of Ni-rich fresh-martensitic regions in vicinity of retained austenite enhances growth kinetics of thermally stable austenite formed during the T-step, and results in the significant increase of austenite volume fraction from 8.1 to 18. 5 % in a relatively short holding time of 1 h at 863 K (590 ^{o}C). In contrast, only 2.9 vol. % austenite is obtained in the sample tempered at 863 K (590 ^{o}C), without a prior L-step treatment.

Chapter 6

Atom-Probe Tomographic Investigation of Austenite Stability and Carbide Precipitation in a TRIP-assisted 10 wt. % Ni Steel and its Weld Heat-Affected Zones

Abstract

Newly developed low-carbon 10 wt. % Ni-Mo-Cr-V martensitic steels rely on the Ni-enriched, thermally stable austenite (formed via multistep intercritical QLT-type treatment) for their superior mechanical properties, specifically ballistic resistance. Critical to the thermal stability of austenite is its composition, which can be severely affected in the weld heat-affected-zones (HAZs) and thus needs to be investigated. This article represents the first study of the nanoscale redistribution of C, Ni, and Mn in the single-pass HAZ microstructures of QLT-treated 10 wt. % Ni steels. Local compositions of Ni-rich regions (representative of austenite compositions) in the HAZs are determined using site-specific 3-D atom-probe tomography (APT). Martensite-start temperatures are then calculated corresponding to these compositions, employing the Ghosh-Olson thermodynamic and kinetic approach. These calculations predict that austenite (present at high temperatures) in the HAZs is susceptible to martensitic transformation upon cooling to room temperature, unlike the austenite in the QLT-treated base metal. While C in the QLT-treated base metal is consumed primarily in MC and M_2C-type carbides (M is Mo, Cr, V), its higher concentration in the Ni-rich regions in the HAZs indicates the dissolution of carbides, particularly M_2C carbides. The role of M_2C carbides and austenite stability is discussed in relation to the increase in microhardness observed in the HAZs, relative to the QLT-treated base metal. Insights

gained from this research on austenite stability and carbide precipitation in the single-pass HAZ microstructures will assist in designing multiple-weld cycles and *Gleeble*-weld simulations for these novel 10 wt. % Ni steels.

6.1 Introduction

The need to develop higher strength steels with superior blast and fragment protection for Naval applications than existing HSLA-100 steels [1, 11] has attracted a lot of attention in recent years [5, 6, 17, 18, 106, 150, 227]. Deformation due to the impact of high velocity fragments from a blast can cause shear localization, which then leads to plastic shear instability and flow localization within thin adiabatic shear bands [24-26]. This results in the shear plugging failure, in which material ahead of the projectile is ejected as one solid piece with little energy absorption [25-27]. To delay the onset of shear localization, the phenomenon of transformation-induced-plasticity (TRIP) [30-32] is utilized in the newly developed low-carbon 10 wt. % Ni-Mo-Cr-V martensitic steels, referred to as 10 wt. % Ni steels herein [6, 228]. Carbon concentration in these steels is kept low (~0.1 wt. %) to lower the susceptibility of weld heat-affected-zones (HAZs) to hydrogen cracking [36, 37]. Ni is used as a primary austenite stabilizer, as has been in the low-carbon 5.5 and 9 wt. % Ni steels, which have been in use for several decades for cryogenic applications [77, 78, 83-85, 88-91, 229]. Significant additions of Mo, Cr, and V in the 10 wt. % Ni steels results in the formation of alloy carbides [202, 228], which are not present in 5.5 and 9 wt. % Ni cryogenic steels. Additions of these elements also results in very high hardenability of 10 wt. % Ni steels; Fonda et al.[87] studied the transformation behavior for a similar 9 wt. % Ni-Cr-Mo-V steel containing 0.11 wt. % C and reported a predominantly martensitic microstructure in the as-quenched condition for a wide range of cooling rates (130 to 0.16 ^{o}C/s).

10 wt. % Ni steels are optimally processed via a multi-step *Quench Lamellarizing Tempering* (QLT)-treatment to form a fine dispersion of thermally stable Ni-enriched austenite (18-19 vol. %) in a tempered martensitic matrix [6, 228]. In our companion paper [228], we elucidated the need to use a multi-step QLT-treatment and described the factors controlling the thermal stability and kinetics of formation of Ni-stabilized austenite. It was established that the austenite formed after the T-step tempering remains thermally stable even at sub-zero temperatures. Zhang demonstrated that the austenite thus formed via QLT-treatment transforms to martensite during ballistic deformation [6]. Deformation-induced martensitic transformation of austenite leads to increased dynamic plasticity and an increment of 18 % in the ballistic-limit (characterized by the parameter V_{50}) over HSLA-100 [6]. QLT-treated 10 wt. % Ni steels also possess an excellent combination of yield strength 130 ksi (~ 896 MPa), elongation to failure 23%, and Charpy impact toughness 153 J at 188.8 K (-84.4 ^{0}C) [6].

Microstructure after the QLT-treatment can be severely affected by the thermal cycles during welding and the resulting complex phase transformations. Redistribution of alloying elements due to the heating involved during welding can lead to significant changes in austenite composition and thereby, affect its thermal stability. This research focuses on investigating the local redistribution of elements (particularly, the austenite stabilizers-Ni, Mn, and C) in the HAZ regions of the QLT-treated 10 wt. % Ni steel, after a single pass autogenous weld cycle. Compositions of Ni-rich regions (representative of austenite compositions) in the HAZs are determined by site-specific 3-D atom-probe tomography (APT). The corresponding martensite-start (M_s) temperatures are then calculated using the Ghosh-Olson thermodynamic and kinetic approach [208-210] to assess the thermal stability of austenite in HAZs and compare it with the QLT-treated base metal. Additionally, (Mo, Cr, V)-rich MC and M_2C-type carbides in 10 wt. % Ni steels are

characterized using APT. High temperatures reached during the weld cycle can affect the stability of carbides, which in turn affects C partitioning to austenite. The role of austenite stability and M_2C-type carbides is also described in relation to the increase in microhardness observed in the HAZs, relative to the QLT-treated base metal. Since the 10 wt. % Ni steels are relatively newly developed, there does not exist a prior welding study on these alloys. Investigation of austenite stability and carbide precipitation in the HAZs will help in optimizing the welding parameters and in designing multiple weld cycles. It will also ensure that the *Gleeble*-weld simulations accurately represent, the microstructures of the actual HAZs for the 10 wt. % Ni steel.

6.2 Experimental Methods

The chemical compositions of 10 wt. % Ni steels, investigated in this article, as measured by optical emission spectroscopy, are given in Table 6.1. These steels are referred to as steel-1 and steel-2 for clarity and have similar compositions. Optimal heat-treatment for these steels, referred to as a *Quench-Lamellarization-Tempering* (QLT) treatment consists of an austenitizing step at 1053-1073 K (780-800 ^{o}C) for ~1 h, followed by water quenching to room temperature (Q); subsequent steps involve intercritical (dual α plus γ phase field) isothermal heating at 923 K (650 ^{o}C) for 20 to 30 min (L-step) and at 863 K (590 ^{o}C) for 1 h (T-step). Isothermal heating during each of L and T-steps is terminated by water quenching the specimen to room temperature.

QLT-treated steel-1 plate (12 mm thickness) was subjected to an autogenous single-pass, gas tungsten arc weld (GTAW) cycle. The welding parameters used were 150 A, 10 V, and a travel speed of 2 mm/s. Cross-section of the weld was prepared by standard metallographic technique through a final polish of 0.05 μm colloidal silica followed by etching with 2% Nital for 10-15 s. Microhardness across the weld was measured using a Leco LM-248 hardness tester with a 100 g

load on a Vickers indenter. SEM micrographs of the base metal and HAZs were obtained using a field-emission gun scanning electron microscope (FEI Quanta 600F). SEM micrograph of the QLT-treated steel-1 is shown in Figure 6.1. The etchant preferentially removes the tempered martensitic matrix and the phase protruding from the matrix is the Ni-rich austenite and/or Ni-rich martensite [6, 202]. As previously described [6, 228], austenite forms as lamellae/rods during the L-step, some of which transforms to martensite during the subsequent quenching to room temperature. During the second intercritical T-step, a fraction of these lamellae/rods decompose into finer austenite particles. Site-specific 3-D APT nanotips were prepared (targeting the Ni-rich phase) by a standard lift-out preparation technique using dual-beam focused-ion beam (FIB) microscopy [213]. Specific details of the lift-out process are provided elsewhere [202].

To investigate MC/M_2C carbides at different stages of the QLT-treatment, samples in the as-quenched (Q), quenched-and-L-step (QL), quenched-and-T-step (QT) conditions were also analysed by APT. QL and QT refer to the samples, which were isothermally tempered at 923 K (650 ^oC) for 30 min and at 823 K (590 ^oC) for 1 h respectively, following the austenitizing and quenching treatment. Quenched and isothermally tempered sample at 811 K (538 ^oC) for 1 h was also analysed. Each isothermal tempering treatment was terminated by water quenching to room temperature. APT nanotips for these samples were prepared by a 2-step electropolishing process, whose details are provided elsewhere [147]. Vickers microhardness for these samples was measured using a Struers Duramin tester, applying 500 g load for an indentation time of 15 s. Each reported microhardness value is an average of 15 measurements and the error reported is the standard deviation of the average. 3-D APT experiments were performed with a Cameca local-electrode atom probe (LEAP) 4000X-Si tomograph, using ultraviolet (wavelength =355 nm) picosecond laser pulsing with an energy of 30 pJ per pulse, a pulse repetition rate of 500 kHz, and

an average evaporation rate (number of ions per pulse) of 2 %. The samples were analysed at a specimen base temperature of 60 K in ultrahigh vacuum (< 10^{-8} Pa) and the data obtained were analysed using the program IVAS 3.6 (Cameca, Madison, WI). As described previously [228], highly Ni-enriched composition of austenite (formed during the T-step) lies outside the compositional domain of empirical relations, commonly used to calculate M_s temperatures [163, 204, 223-226]. Therefore, Ghosh-Olson approach [208-210], which integrates computational thermodynamics and the Olson-Cohen barrierless martensite nucleation model [211] is applied to predict the M_s temperatures. Gibbs free energy change, associated with compositionally invariant martensitic transformation, is calculated using ThermoCalc (version S), employing the *kMART thermodynamic database* [210]. A more detailed description of this approach is provided in the companion paper [228]. Phase fractions at equilibrium were calculated using *TCFE6* steel database.

Table 6.1. Chemical compositions of 10 wt. % Ni steels (steel-1 and steel-2), as measured from optical emission spectroscopy.

Steel		**Fe**	**Ni**	**Mn**	**C**	**Si**	**Cr**	**Mo**	**Cu**	**V**
Steel-1	(wt. %)	Bal.	9.64	0.64	0.10	0.18	0.65	1.53	0.16	0.06
	(at. %)	Bal.	9.22	0.65	0.47	0.36	0.70	0.90	0.14	0.07
Steel-2	(wt. %)	Bal.	9.85	0.60	0.09	0.21	0.60	1.23	0.15	0.08
	(at. %)	Bal.	9.41	0.61	0.42	0.42	0.65	0.72	0.13	0.09

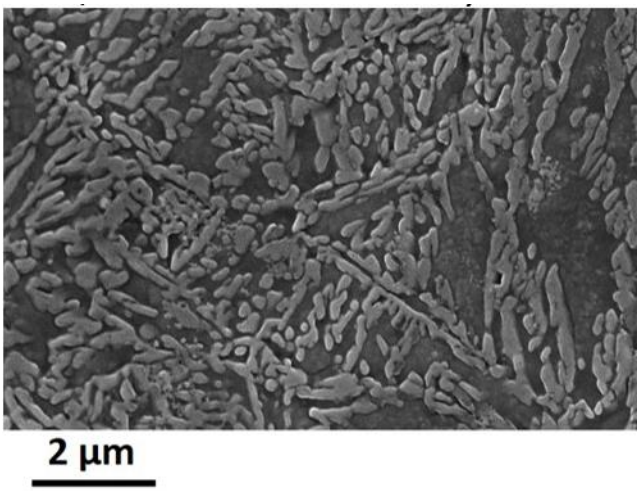

Figure 6.1- SEM micrograph of the QLT-treated 10 wt. % Ni steel-1 (base metal). Brighter appearing phase, dispersed in the matrix is the Ni-rich constituent, consisting of austenite and martensite, with the latter formed during the quenching following the L-step [6, 228].

6.3 Results

6.3.1 Scanning Electron Microscopy (SEM)

SEM micrographs of the QLT-treated base metal (BM), HAZ-1, and HAZ-2 regions in steel-1 are shown in Figure 6.2 (a, b, c) respectively. The relative positions of HAZ-1 and HAZ-2 regions with respect to BM are shown in Figure 6.3. From the SEM micrographs, we observe a much denser and coarser distribution of the brighter Ni-rich phase (protruding from the matrix) on moving from base metal (BM) toward fusion zone (FZ), with its coalescence observed at several regions in HAZ-2 microstructure (see encircled region in Figure 6.2 (c)). According to equilibrium thermodynamic calculations, the Ac_3 temperature for steel-1 is 951 K (678 ^{o}C), while equilibrium austenite volume fractions at 923 K (650 ^{o}C) and 823 K (590 ^{o}C) are 72 and 39 % respectively. Thus, high temperatures reached during the heating portion of the weld cycle would facilitate the formation of new austenite and/or drive the growth and coarsening of the existing austenite in the QLT-treated BM. However, as discussed later in section 6.4, some of the austenite present at high

temperatures in HAZs, may transform back to martensite during cooling due to insufficient enrichment of Ni. Hence, the Ni-rich constituent in these SEM micrographs is referred to as a mixture of martensite and austenite. Since martensitic transformations are diffusionless [219], it is assumed that the composition of this Ni-rich martensite-austenite mixture, represents the composition of parent austenite, present at high temperatures. It is noted that description of the FZ microstructure and properties is beyond the scope of this article and we will limit our discussion to regions experiencing solid state phase transformations only.

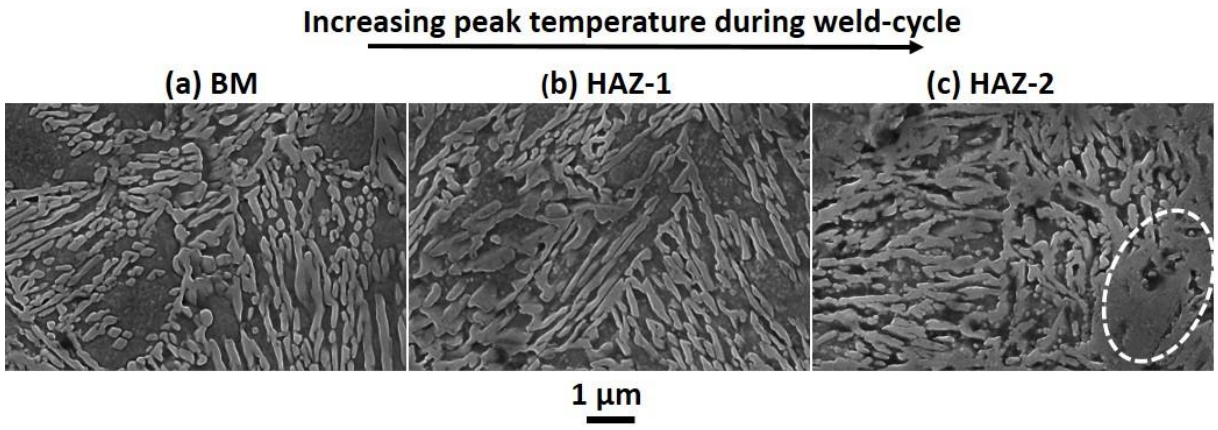

Figure 6.2- SEM micrographs of QLT-treated 10 wt. % Ni steel-1, (a) Base Metal (BM); (b) HAZ-1 region; (c) HAZ-2 region. The relative positions of HAZ-1 and HAZ-2 regions with respect to BM are indicated in Figure 3, with HAZ-2 region lying in closer proximity to the fusion zone.

6.3.2 Vickers Microhardness

The microhardness trace across the weld traversing fusion zone (FZ), heat-affected-zone (HAZ), and base metal (BM) for steel-1 is shown in Figure 6.3. As compared to the BM microhardness of 335 HV, significant increase in hardness occurs in the FZ and HAZ regions. While the hardness within the BM and FZ regions is nearly constant, it varies significantly within the HAZ

region on traversing from BM toward FZ. For instance, hardness is 420 HV for the location in HAZ, marked as HAZ-1, while the peak hardness of 469 HV is attained in the HAZ-2 location. Hardness within the HAZ then decreases on moving from HAZ-2 toward the FZ. Similar trend in microhardness variation was observed for the autogenous gas tungsten arc welds of quench and tempered 0.05C-9Ni wt.% steel with BM hardness of 256 HV; maximum hardness of 381 HV was observed at 1.3 mm from the fusion line, while the hardness at distances of 0.2 and 0.7 mm were measured to be 347 and 367 HV respectively [230]. Below, the local distribution of Ni, Mn, and C in the microstructures of the QLT-treated BM and HAZs is described, which is used to assess austenite stability and to gain insights into these microhardness trends.

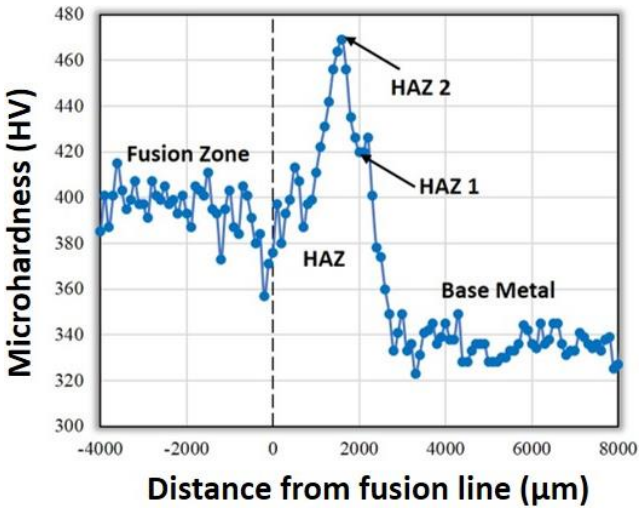

Figure 6.3- Microhardness trace across the autogenous Gas Tungsten Arc Weld (GTAW) of QLT-treated 10 wt. % Ni steel-1.

6.3.3 3-D Atom-Probe Tomography (APT)

6.3.3.1 Ni-rich regions in QLT-treated BM and HAZs

Figure 6.4(a) shows the 3-D APT reconstruction of the QLT-treated steel-2 sample, in which Fe atoms are displayed in blue, Ni atoms are in green, and the metal carbides rich in Mo, Cr, and V are delineated by 10 at. % (C plus Mo plus Cr plus V) isoconcentration surfaces (black). During intercritical L and T-steps, Ni partitions to austenite and gets depleted in the parent martensite, referred to as tempered martensite, α-Fe. Figure 6.4(b) displays the proximity histogram (proxigram) concentration profiles of Fe, Ni, Mn, and C across the α-Fe and Ni-rich region, obtained with respect to the distance from 11 at. % Ni isoconcentration surface (indicated by a dashed curve in Figure 6.4(a)). It is noted that the metal carbides were first removed from the dataset using the IVAS software so that the partitioning behavior of these elements can be studied without interference from carbides. The same methodology is followed for all other proxigram analyses. Partitioning of alloying elements across α-Fe and Ni-rich regions in the QLT-treated steel-2 sample was discussed in our companion paper [228]. The results are briefly summarized here, as these are critical to understanding austenite formation and associated Ni-enrichment during the QLT-treatment. In the proxigram in Figure 6.4(b), shaded regions with higher Ni concentration (~21.9 at. %) within the Ni-rich region represent the composition of austenite formed during the T-step, while the sandwiched plateau region (containing 15.9 at. % Ni) between these shaded regions represents the composition of austenite formed during the L-step. This can be understood from equilibrium thermodynamic calculations, which predict increasing Ni concentrations in austenite with decreasing intercritical temperatures [202, 228]. Since Ni diffusion in austenite is extremely sluggish (its estimated root-mean-squared diffusion distance, $\sqrt{2Dt}$ in austenite for 1 h at 863 K (590 ^{o}C) is only ~1 nm) [220, 221], its concentrations in austenite formed during the L and T-steps do not homogenize. APT analyses of the two QL-treated

steel-2 samples revealed Ni-rich regions with average Ni concentrations of 12.5 and 16.7 at. % [228]. Ni concentration of the sandwiched plateau region (15.9 at. %) in Figure 6.4(b) lies within this range, which is in good agreement with our interpretation described above.

Since steel-1 and steel-2 have similar overall compositions, comparable results were obtained for the QLT-treated BM of steel-1. This is evident from Figure 6.6(a), in which shaded regions with higher Ni concentrations contain 19.0 to 21.0 at. % Ni, while the plateau region near the centre of the proxigram within the Ni-rich region contains 16.6 at. % Ni. Similar behavior, as described for Ni, is also observed for Mn in the Ni-rich regions in QLT-treated BM. The overall chemical compositions of α-Fe and Ni-rich regions for QLT-treated base metal for steel-1 and steel-2 are provided in Table 6.2. The error (± σ) for each concentration c_i is obtained from counting statistics [53] and is given by,

$$\sigma = \sqrt{\frac{c_i\,(1-c_i)}{N}} \qquad (6.1)$$

where *N* is the total number of detected atoms. It is noted that during the QLT-treatment, C gets preferentially combined with (Mo, Cr, V)-rich metal carbides, such as those observed in Figure 6.4(a), which limits its concentration in austenite (0.2-0.6 at. %), Table 6.2. Due to the small number density of the metal carbides (~ $2x10^{22}$ m^{-3}) in the QLT-treated BM, relative to the analyzed volume from APT, we may not always observe these carbides in the APT reconstruction, as is the case with the QLT-treated steel-1 sample, Figure 6.5(a).

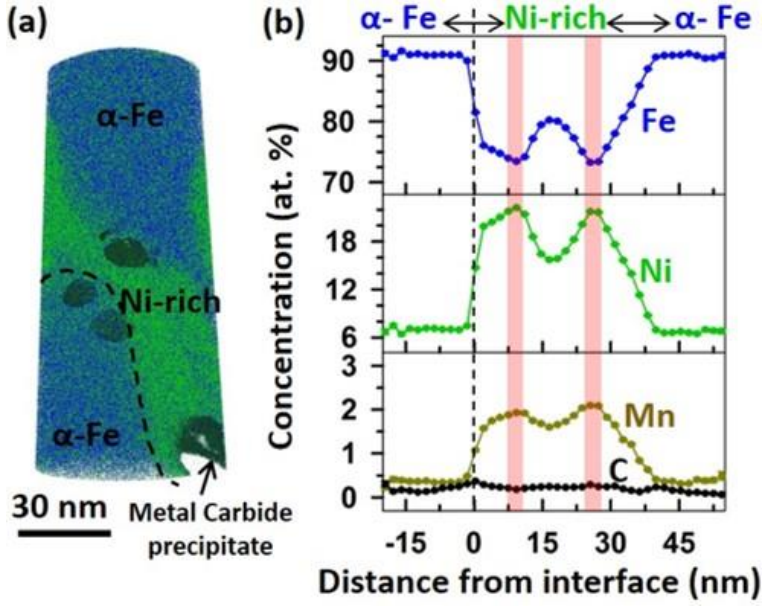

Figure 6.4- (a) 3-D APT reconstruction of the QLT-treated 10 wt. % Ni steel-2. Fe (5 %) and Ni (50%) atoms are displayed in blue and green respectively. The heterophase interface between the tempered martensite matrix, α-Fe, and the Ni-rich region is delineated by 11 at. % Ni isoconcentration surface (shown schematically by a dashed curve). Metal carbides are delineated by 10 at. % (C plus Mo plus Cr plus V) isoconcentration surfaces (black); (b) Proximity histogram concentration profiles of Fe, Ni, Mn, and C across the α-Fe matrix and the Ni-rich region. Shaded regions on the Ni-rich side represent the composition of austenite formed during the T-step tempering at 863 K (590 ^{o}C).

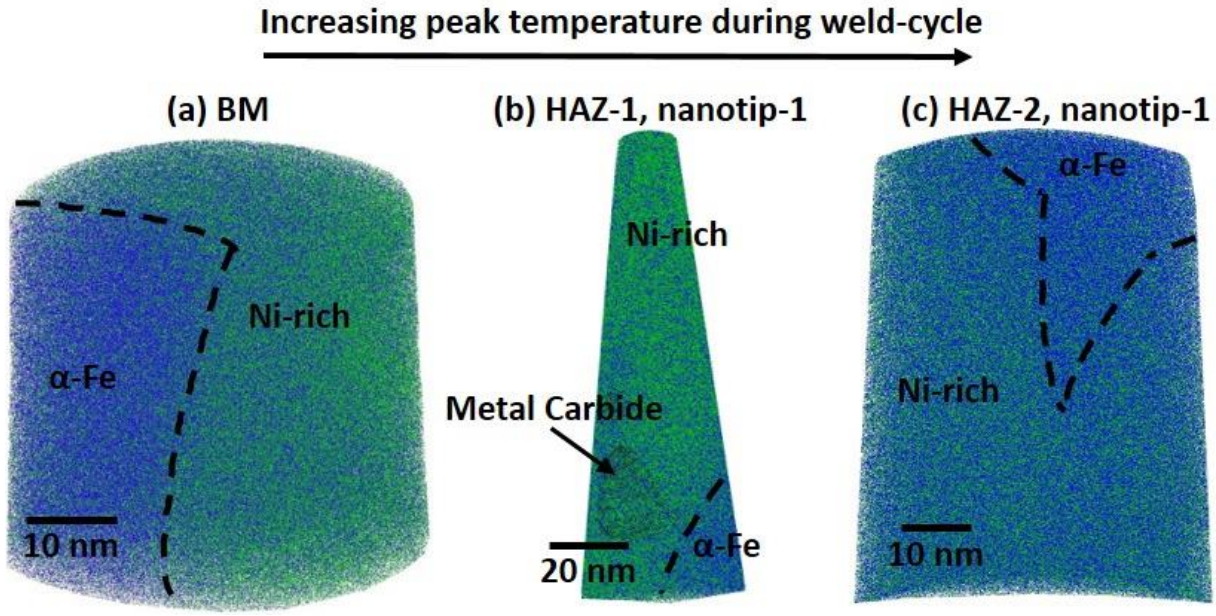

Figure 6.5- 3-D APT reconstructions of QLT-treated 10 wt. % Ni steel-1, (a) Base Metal (BM), Fe (20 %) and Ni (100%) atoms are displayed in blue and green respectively; (b) HAZ-1 (nanotip-1), Fe (10 %) and Ni (80%) atoms are displayed in blue and green respectively, metal carbides are delineated by 10 at. % (C plus Mo plus Cr plus V) isoconcentration surfaces (black); (c) HAZ-2 (nanotip-1), Fe (20 %) and Ni (100%) atoms are displayed in blue and green respectively. The heterophase interface between the tempered martensite matrix, α-Fe, and the Ni-rich region is delineated by 13, 11, and 11 at. % Ni isoconcentration surfaces in a, b, and c respectively (shown schematically by dashed curves).

Table 6.2. Compositions (at. %) of Ni-rich regions and tempered martensite, α-Fe for QLT-treated base metal for steel-1 and steel-2.

QLT-treated Steel-2	**Fe**	**Ni**	**Mn**	**C**	**Si**	**Cr**	**Mo**	**Cu**	**V**
Austenite at T-step	73.43 ±0.16	21.89 ±0.15	2.00 ±0.05	0.23 ±0.02	0.58 ±0.03	0.83 ±0.03	0.44 ±0.02	0.36 ±0.02	0.04 ±0.01
Austenite from L-step	80.05 ±0.15	15.87 ±0.13	1.64 ±0.05	0.23 ±0.02	0.46 ±0.02	0.85 ±0.03	0.46 ±0.02	0.25 ±0.02	0.04 ±0.01
Tempered Martensite, α-Fe	90.89 ±0.32	6.82 ±0.28	0.36 ±0.07	0.15 ±0.04	0.62 ±0.09	0.56 ±0.08	0.34 ±0.06	0.03 ±0.02	0.08 ±0.03
QLT-treated Steel-1	**Fe**	**Ni**	**Mn**	**C**	**Si**	**Cr**	**Mo**	**Cu**	**V**
Austenite at T-step (19.2 at. % Ni)	75.75 ±0.16	19.22 ±0.15	1.75 ±0.05	0.60 ±0.03	0.55 ±0.03	0.91 ±0.04	0.65 ±0.03	0.32 ±0.02	0.02 ±0.01
Austenite at T-step (21.2 at. % Ni)	74.08 ±0.21	21.22 ±0.20	2.06 ±0.07	0.29 ±0.03	0.38 ±0.03	0.85 ±0.04	0.60 ±0.04	0.28 ±0.03	0.03 ±0.01
Austenite from L-step	79.08 ±0.15	16.62 ±0.14	1.57 ±0.05	0.41 ±0.02	0.55 ±0.03	0.80 ±0.03	0.46 ±0.02	0.24 ±0.02	0.03 ±0.01
Tempered Martensite, α-Fe	90.9 ±0.17	7.0 ±0.15	0.43 ±0.04	0.37 ±0.04	0.25 ±0.03	0.51 ±0.04	0.31 ±0.03	0.08 ±0.02	0.02 ±0.01

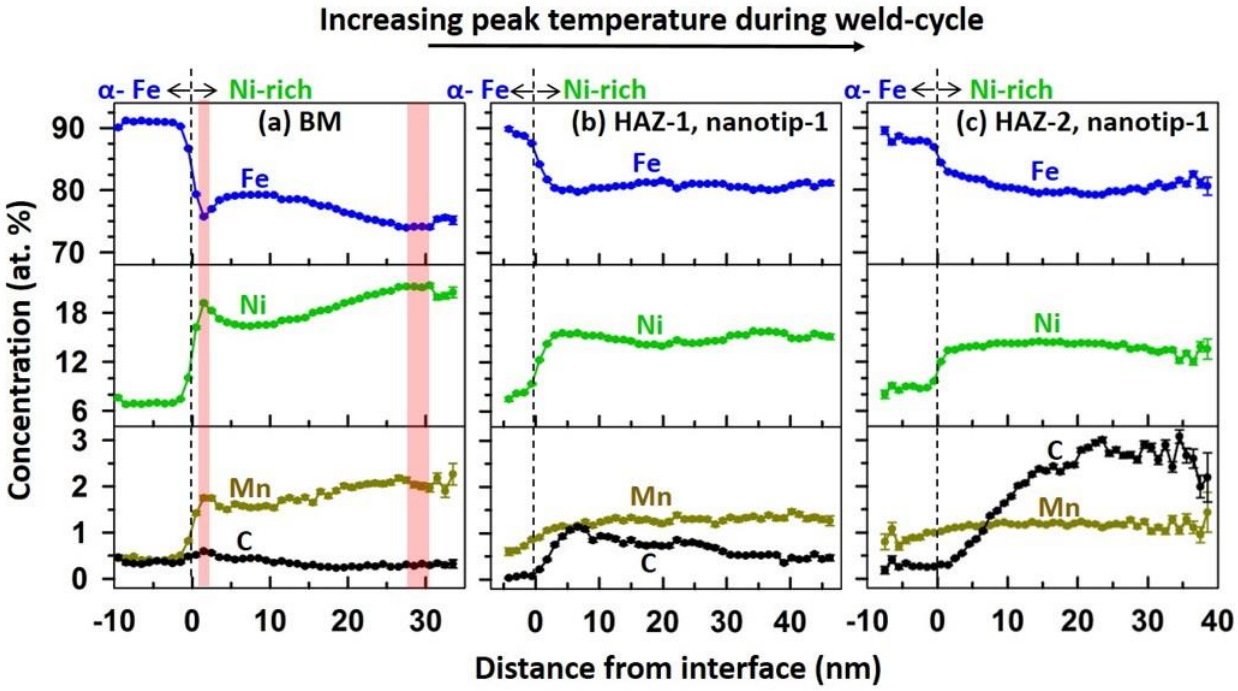

Figure 6.6- Proximity histogram concentration profiles of Fe, Ni, Mn, and C across the α-Fe matrix and the Ni-rich region for the QLT-treated 10 wt. % Ni steel-1, (a) Base metal (BM); (b) HAZ-1 (nanotip-1); (c) HAZ-2 (nanotip-1).

3-D APT reconstructions of the HAZ-1 (nanotip-1) and HAZ-2 (nanotip-1) regions of the QLT-treated steel-1 are shown in Figure 6.5 (b, c) respectively. Interface between the α-Fe matrix and the Ni-rich regions in these APT reconstructions is delineated by 11 at. % Ni isoconcentration surfaces, shown schematically by dashed curves, and the corresponding proxigrams are shown in Figure 6.6 (b, c). In the Ni-rich region corresponding to HAZ-1 (nanotip-1), Figure 6.6(b), Ni concentration is slightly higher near the interface and at the extreme right-hand side of the proxigram (15.4 at. %) as compared to at the centre (14.4 at. %). Mn is nearly homogeneously distributed within the Ni-rich region and has a concentration of 1.3 at. %. Concentrations of Ni and Mn in α-Fe matrix are 8.0 and 0.7 at. % respectively. The carbon concentration is 1 at. % near the interface and then gradually decreases to 0.5 at. % toward the extreme right-hand side of the

proxigram, while its concentration in α-Fe matrix (excluding the metal carbides) is 0.06 at. %, Figure 6.6(b). In HAZ-2 (nanotip-1), homogeneous distributions of both Ni and Mn are observed in the Ni-rich region, with average concentrations of 13.6 and 1.2 at. % respectively, Figure 6.6(c). Ni and Mn concentrations in α-Fe matrix are 8.8 and 0.9 at. % respectively. Significant enrichment of C is observed in the Ni-rich region, Figure 6.6(c); its concentration in the plateau region toward the extreme right-hand side of the proxigram is 2.8 at. %, while its concentration in α-Fe matrix is 0.3 at. %.

A second APT nanotip was analyzed for each of the HAZ-1 and HAZ-2 regions. 3-D APT reconstructions and the corresponding proxigram concentration profiles for Ni, Mn, and C across the α-Fe and the Ni-rich region are shown in Figure 6.7. In the Ni-rich region corresponding to HAZ-1 (nanotip-2), average Ni concentration is 16.9 at. % in the 10-nm wide region near the interface, while it is 18.9 at. % in the 24-nm wide region toward the centre, Figure 6.7(a2). Inhomogeneities in the distribution of Ni within the Ni-rich region, as observed here, are reminiscent of its distribution in the BM. Mn concentration within the Ni-rich region increases gradually from 1.4 at. % near the interface to 1.7 at. % toward the centre of the proxigram. Ni and Mn concentrations in α-Fe matrix (left-hand side of the proxigram) are 5.6 and 0.3 at. % respectively. The carbon concentration in the Ni-rich region is nearly constant (0.4-0.6 at. %), while its concentration in α-Fe matrix is 0.06 at. %, Figure 6.7(a2). In the Ni-rich region corresponding to HAZ-2 (nanotip-2), we observe homogeneous distributions of Ni, Mn, and C with respective concentrations of 14.6, 1.0, and 0.6 at. %, while their concentrations in the α-Fe matrix are 8.7, 0.6, and 0.1 at. % respectively, Figure 6.7(b2).

Based on the above results, the following differences are observed in the distributions of Ni, Mn, and C within the Ni-rich regions in the BM, HAZ-1, and HAZ-2 regions. Firstly, concentrations of Ni and Mn decrease on moving from BM toward the fusion zone, while higher C concentrations are obtained within the Ni-rich regions in the HAZs as compared to the BM. Additionally, except for HAZ-1 (nanotip-2), we observe that Ni and Mn are nearly homogeneously distributed within the Ni-rich regions in the HAZs. In contrast, distinct regions with higher concentrations of Ni and Mn are observed in the QLT-treated BM, that correspond to the austenite formed during the T-step (see shaded regions in Figures 6.4(b) and 6.6(a)). The effect of these changes in the local compositions of the Ni-rich regions on austenite stability is described in section 6.4.1. Below, we characterize alloy carbides observed in the as-quenched and isothermally tempered 10 wt. % Ni steels using APT.

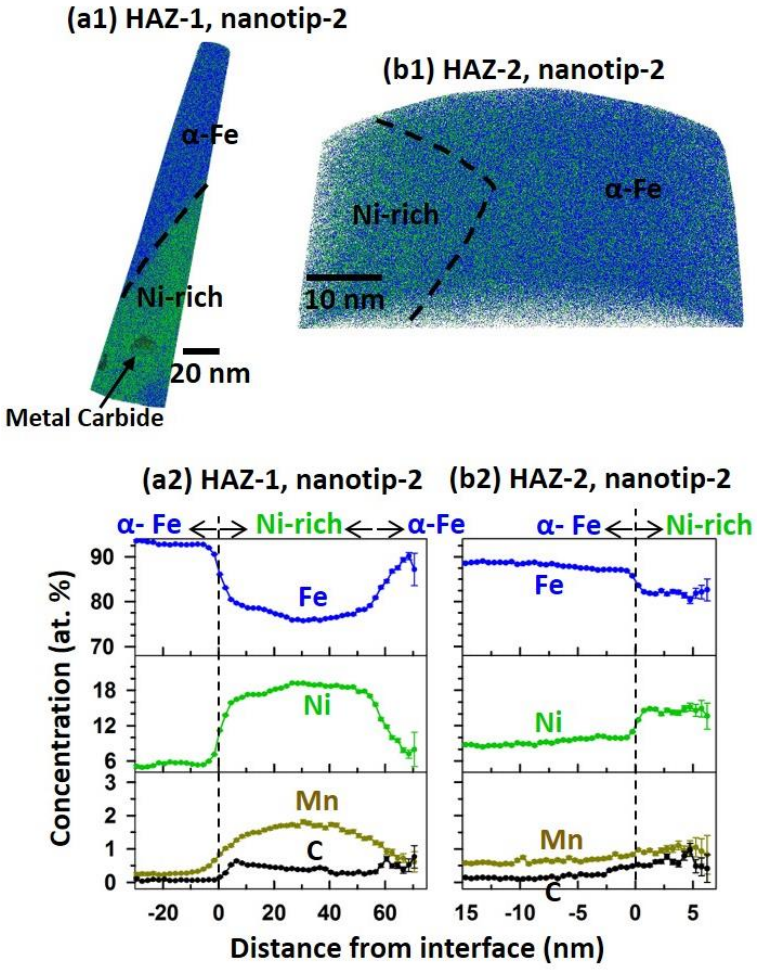

Figure 6.7- 3-D APT reconstructions of QLT-treated 10 wt. % Ni steel-1, (a1) HAZ-1 (nanotip-2), Fe (10 %) and Ni atoms (80 %) are displayed in blue and green respectively, metal carbides are delineated by 10 at. % (C plus Mo plus Cr plus V) isoconcentration surfaces (black); (b1) HAZ-2 (nanotip-2), Fe (15 %) and Ni atoms (100 %) are displayed in blue and green respectively. The heterophase interface between the tempered martensite matrix, α-Fe, and the Ni-rich region is identified by 9 and 12 at. % Ni isoconcentration surfaces in (a1) and (b1) respectively (shown schematically by dashed curves). Proximity histogram concentration profiles of Fe, Ni, Mn, and C across the α-Fe matrix and the Ni-rich region for, (a2) HAZ-1 (nanotip-2); (b2) HAZ-2 (nanotip-2).

6.3.3.2 MC/M_2C-type Carbides (M is Mo, Cr, V) in 10 wt. % Ni steels

3-D APT reconstruction of the as-quenched steel-2 is shown in Figure 6.8(a). Several MC-type carbides, having platelet-like morphology are observed in the reconstruction and are delineated by

7 at. % (C plus Mo plus V) isoconcentration surfaces. Average composition of the 5 largest carbides, as obtained from the proximity histogram analysis, Figure 6.8(c) is 30.8Mo-11.1V-3.5Cr-6.8Fe-1.8Ni-0.6Mn-43.8C (at. %). Similar and even higher Mo concentrations in V-containing MC carbides with NaCl-type B1 crystal structure have been reported in other steels [168, 231-236]. Sub-stoichiometric C concentrations in (Mo,V)-rich MC carbides have also been reported in other atom-probe studies [236, 237]. First-principle calculations performed by Jang et al. [238] for MC carbides with B1 crystal structure showed that substitution by vacancies at C interstitial sites of upto 50 % increases the stability of MoC, while vacancies at the interstitial sites are not preferred for VC. MC carbides are stable at high temperatures reached during hot-rolling and austenitizing steps and prevent excessive grain growth by pinning austenite grain boundaries during these treatments [40-42]. They can, however, dissolve in the HAZs close to the FZ, which can cause severe grain coarsening, as had been observed in the weld simulated HAZs of HSLA-100 steels [137, 239].

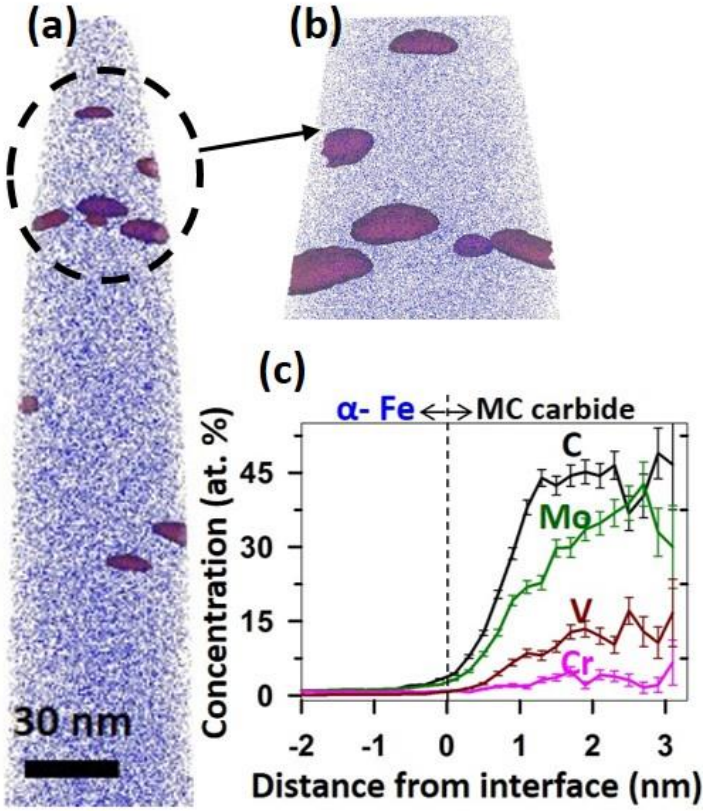

Figure 6.8- (a) 3-D APT reconstruction of the as-quenched 10 wt. % Ni steel-2. Fe atoms (0.2 %) are displayed in blue and MC-type carbides are delineated by 7 at. % (C plus Mo plus V) isoconcentration surfaces (dark-red); (b) Magnified view of the encircled region in (a); (c) Proxigram concentration profiles of C, Mo, V, and Cr across the α-Fe matrix and MC carbides.

3-D APT reconstructions of the isothermally tempered samples at 811 K (538 ^{o}C)/1 h, 863 K (590 ^{o}C)/1 h, and 923 K (650 ^{o}C)/0.5 h are shown in Figure 6.9 (a, b, & c) respectively. APT reconstruction of the QLT-treated sample is also shown in Figure 6.9(d). Metal carbides enriched in Mo, Cr, and V are observed in all the reconstructions and are delineated by 10 at. % (C plus Mo plus Cr plus V) isoconcentration surfaces.

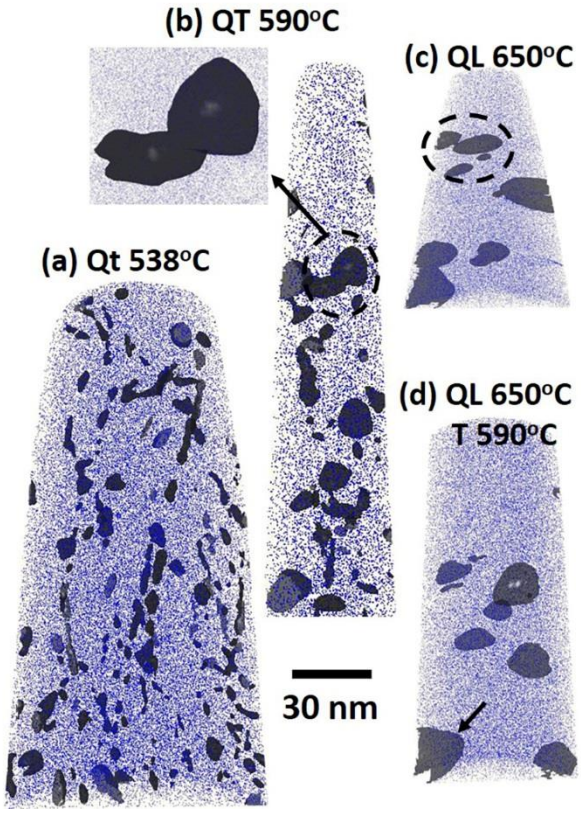

Figure 6.9- 3-D APT reconstructions of quenched and isothermally tempered 10 wt. % Ni steel samples at, (a) 811 K (538 °C) for 1 h; (b) 863 K (590 °C) for 1 h; (c) 923 K (650 °C) for 0.5 h; (d) 923 K (650 °C) for 0.5 h and 863 K (590 °C) for 1 h. Fe atoms are displayed in blue (only a fraction is shown for clarity). Metal carbides are delineated by 10 at. % (C plus Mo plus Cr plus V) isoconcentration surfaces (black). It is noted that all samples are from steel-2, except (a), which is obtained from a 10 wt. % Ni steel, whose overall composition is 0.07C-10.31Ni-1.12Mo-0.07V-0.61Mn-0.60Cr-0.22Si (wt. %).

In the sample tempered at 811 K (538 °C), profuse precipitation of M_2C-type carbides (M is Mo, V, and Cr) is observed, Figure 6.9(a). The number density of the carbides is 1.3×10^{23} m^{-3}, while the metal-to-carbon atomic ratio, as obtained from the proximity histogram analysis of the 20 largest carbides is 2.3. Cr/Mo and V/Cr atomic ratios are 0.5 and 1.2 respectively. The elongated morphology of some of these carbides, as observed here, is characteristic of the well-known rod/needle-like morphology for M_2C carbides in α-Fe [64, 65, 68]. Sub-stoichiometric C

concentration in the M_2C carbide precipitates has been previously reported in several steels [68, 192, 232, 240, 241] and is attributed to the reduction in the interfacial energy of the precipitating nuclei [240].

At higher tempering temperatures of 863 K (590 ^oC) and 923 K (650 ^oC), much coarser distribution of carbides is observed, Figure 6.9(b, c, d). We also observe several mixed/complex and co-located MC/M_2C-type carbides in these APT reconstructions; one such carbide is indicated by an arrow in Figure 6.9(d). The distribution of V and C inside this carbide is shown in Figure 6.10 (a) and the linear concentration profiles in the direction indicated in Figure 6.10(a) are shown in Figure 6.10 (b). Sub-nm resolution of APT [20] allows us to resolve the composition of these mixed carbides into M_2C carbide (outer shell) and MC carbide (inner core). Their compositions are 41Mo-7.9V-6.3Cr-7.5Fe-1.3Ni-0.9Mn-33.4C (at. %) and 29.4Mo-14.2V-3.8Cr-1.7Fe-0.3Ni-0.8Mn-47.1C (at. %) respectively. V/Cr atomic ratios are 1.3 and 3.7 for the M_2C and MC-type carbides respectively. Co-located MC/M_2C-type carbides, observed in the sample tempered at 863 K (590 ^oC) are encircled in Figure 6.9(b). A magnified view of this encircled region shows a spheroidal M_2C carbide (39.6Mo-7.1V-8.2Cr-4.1Fe-1.2Ni-1.8Mn-34.9C at. %) that grows on a platelet-like MC carbide (32.0Mo-8.0V-5.3Cr-1.6Fe-1.5Ni-0.8Mn-48.4C at. %). V/Cr atomic ratios are 0.9 and 1.5 for the M_2C and MC-type carbides respectively. Several MC-type carbides, which are not associated with M_2C-carbide are observed in the sample tempered at 923 K (650 ^oC), see encircled region in Figure 6.9(c).

Mixed carbides having a H-shaped morphology, comprising of V-enriched MC carbide at the center and elongated Mo_2C carbides at the sides have been observed in Cr-Mo-V power plant steels

[231, 242, 243]. Based on the observations that Mo concentration increases at the expense of V with increasing size of MC carbides, it was inferred that the nucleation of Mo_2C carbides occurs on pre-existing V-enriched MC carbides [235, 242]. In the present study, we obtain high concentration of Mo (~ 30 at. %) in the MC carbides in the as-quenched sample, Figure 6.8(c). We also observe mixed and co-located M_2C and MC-type carbides after isothermal tempering at 923 K (650 ^oC) and/or 863 K (590 ^oC). These findings are suggestive of a similar mechanism of heterogeneous nucleation of M_2C carbides on MC carbides during isothermal tempering at 923 K (650 ^oC) and 863 K (590 ^oC).

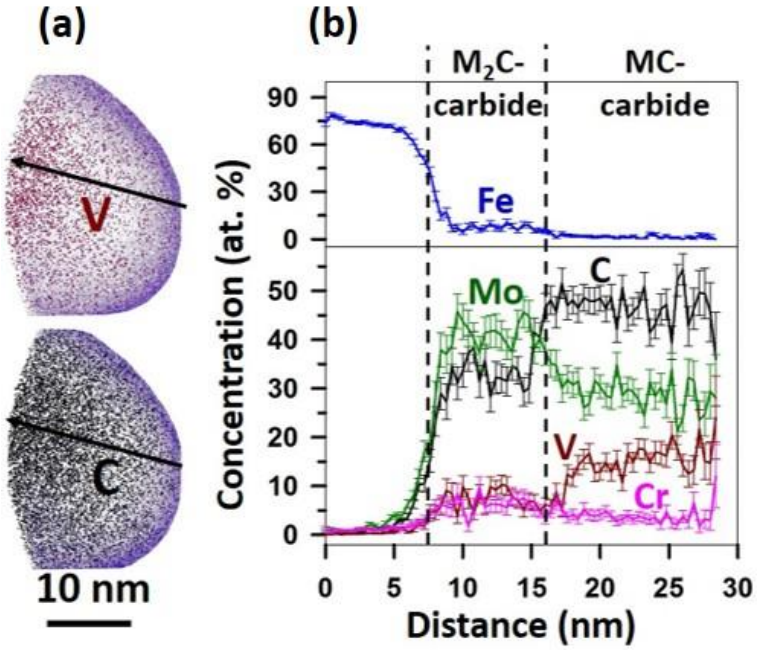

Figure 6.10- (a) Distribution of V (dark-red), C (black), and Fe (blue) atoms in a mixed MC/M_2C-type carbide, observed in the 10 wt. % Ni QLT-treated steel-2 sample; (b) Linear concentration profiles of Fe, C, Mo, V, and Cr, obtained from the selected region of interest, in the direction of the arrow in (a). These profiles reveal the mixed nature of the carbide, consisting of M_2C carbide in the outer shell and MC carbide in the inner core.

6.4 Discussion

6.4.1 Austenite stability in HAZs: Prediction of M_s temperatures

The distributions of Ni, Mn, and C in Ni-rich regions in the HAZs are affected due to the weld cycle. Ni concentrations in the Ni-rich regions in HAZ-2 (closer to the FZ) are 13.6 at. % (nanotip-1, Figure 6.6(c)) and 14.6 at. % (nanotip-2, Figure 6.7(b2)). These are lower than its concentrations in the Ni-rich regions in HAZ-1 (closer to the BM), which are ~14.9 at. % (nanotip-1, Figure 6.6(b)) and vary from 17 to 18.9 at. % in nanotip-2, Figure 6.7(a2). In contrast, distinct regions of significantly higher Ni concentrations (19.2-21.2 at. %, Figure 6.6(a)) and (21.9 at. %, Figure 6.4(b)) are observed in the QLT-treated BM, which correspond to the austenite formed during the T-step. Similarly, Mn concentrations in the Ni-rich regions decrease on moving from BM toward FZ.

Chemical compositions of the Ni-rich regions (representative of the austenite compositions) are used to calculate the M_s temperatures, employing the `Ghosh-Olson' approach, referred to in the experimental section. The M_s temperatures thus obtained are displayed in Table 6.3 for specific Ni-rich regions observed in QLT-treated BM and HAZs of steel-1. M_s temperatures for the QL and QLT-treated steel-2 samples, as described in the companion paper are also listed [228]. These calculations reveal that the austenite (present at high temperatures) in the HAZs (except HAZ-1 (nanotip-2) containing 18.9 at. % Ni) is susceptible to martensitic transformation during the cooling of the weld to room temperature, as is the case for the austenite in the two QL-treated samples containing 12.5 and 16.7 at. % Ni.

It is noted that C concentrations in the Ni-rich regions in the HAZs are comparatively higher than in the QLT-treated BM. Carbon concentration in the Ni-rich regions varies from 0.5 to 1 at. % in HAZ-1 (nanotip-1, Figure 6.6(b)) and is 0.5 at. % in HAZ-1 (nanotip-2, Figure 6.7(a2)). In the Ni-

rich regions in HAZ-2, we obtain 2.8 at. % C (nanotip-1, Figure 6.6(c)) and 0.6 at. % C (nanotip-2, Figure 6.7(b2)). In comparison, C concentration within the Ni-rich regions in QLT-treated BM varies from 0.2-0.6 at. %, Table 6.2. Although, it cannot be stated with certainty that M_2C carbides in the HAZ-2 region have dissolved partially or completely, significant increase in the C concentration in the Ni-rich regions in HAZ-2, Figure 6.6(c), as compared to the BM provides an indirect evidence of their dissolution. The dissolution of carbides will free up some C, which will then partition to austenite. However, M_s temperature calculations predict that C-enrichment is not sufficient to stabilize austenite in HAZ-2 at room temperature and below. Additionally, Ni-rich phase observed in HAZs is much coarser than that observed in the BM, Figure 6.2. According to the Olson-Cohen heterogeneous martensitic nucleation model [211], this will adversely affect the stability of austenite as more sites will be available for martensitic nucleation to occur. Experimental results from welding studies of 9 wt. % Ni cryogenic steels have reported significant decrease in austenite volume fractions in HAZs relative to the BM [230, 244, 245]. This is in general agreement with our present findings that indicate that austenite (present at high temperatures) in the HAZs is likely to transform to martensite during the cooling to room temperature, unlike the austenite in the BM. Austenite volume fraction measurements from the *Gleeble* simulated HAZ microstructures will provide further insights into these predictions. This research is being performed at Lehigh University.

Table 6.3. M_s temperature calculations for the Ni-rich regions observed from APT, using the Ghosh-Olson approach [208-210].

Steel composition	Ni-rich region observed from APT	M_s K (°C)
Steel-1	QLT base metal (austenite during T-step)	< 273 (<0)
	HAZ-1 (nanotip-1)	359 (86)
	HAZ-1 (nanotip-2, 16.9 at. % Ni)	327 (54)
	HAZ-1 (nanotip-2, 18.9 at. % Ni)	< 273 (<0)
	HAZ-2 (nanotip-1)	318 (45)
	HAZ-2 (nanotip-2)	394 (121)
Steel-2	QL (nanotip-1, 12.5 at. % Ni)	460 (187)
	QL ((nanotip-2, 16.7 at. % Ni)	345 (72)
	QLT base metal (austenite during T-step)	< 273 (<0)

6.4.2 Microhardness increase in HAZs: Role of M_2C-type carbides and austenite stability

The average number density of the M_2C-type carbides in the QLT-treated steel-2 samples is $2.2x10^{22}$ m^{-3}, Figure 6.11(a); number density of the order of 10^{22} m^{-3} is quite small and is associated with the coarsening regime of M_2C carbides in BA-160 steels [18], AF1410 steels [240], and HSLA-115 steels [147, 241]. Similar coarse distribution of these carbides with average number density of $2.5x10^{22}$ m^{-3} is observed in the APT reconstructions of the HAZ-1 region, Figure 6.11(b), while no carbides are observed in the APT reconstructions of the HAZ-2 region, Figure 6.11(c). Thus, even if carbides might have dissolved in the HAZ-2 region due to the high temperatures experienced during the weld cycle, their re-precipitation does not occur during the cooling of the weld. Hence, precipitation-strengthening from M_2C carbides is not responsible for the significant increase in the microhardness observed in the HAZ-1 and HAZ-2 regions, Figure

6.3. The role of other microstructural variables in influencing the microhardness in the HAZ is described below in the context of the present findings.

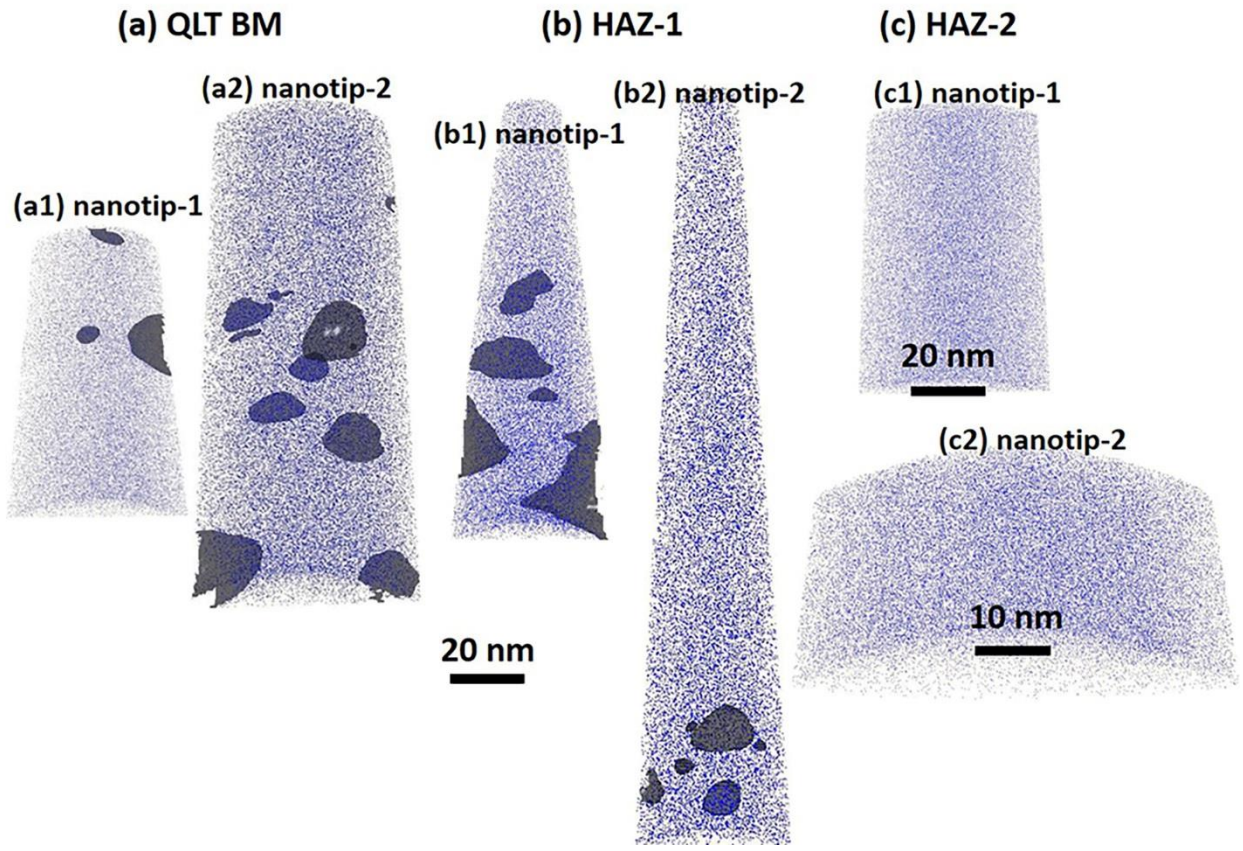

Figure 6.11- 3-D APT reconstructions of QLT-treated 10 wt. % Ni steel, (a) base metal (steel-2): (a1) nanotip-1, (a2) nanotip-2; (b) HAZ-1 (steel-1): (b1) nanotip-1, (b2) nanotip-2; (c) HAZ-2 (steel-1): (c1) nanotip-1, (c2) nanotip-2. Fe atoms are displayed in blue (only a fraction is shown for clarity) and metal carbides are delineated by 10 at. % (C plus Mo plus Cr plus V) isoconcentration surfaces (black).

As described in section 6.4.1, M_s temperature calculations coupled with the coarser distribution of Ni-rich phase in the HAZs, indicate, the susceptibility of austenite (present at high temperatures) in the HAZ microstructure to martensitic transformation during cooling of the weld. The untampered, fresh-martensite in the HAZ microstructures will increase the hardness of these

regions as compared to the BM, which consists of relatively softer phases, austenite (~18-19 vol. %) and tempered martensite [162]. To further emphasize the role of fresh-martensite, a comparison of the microhardness of the as-quenched steel-2 sample with the QLT, QL, and QT steel-2 samples is provided. The microhardness of the as-quenched steel-2 sample, which consists of predominantly fresh-martensite is 443 HV. This is significantly higher than the corresponding values for the QLT (337 HV), QL (364 HV), and QT (384 HV)-treated steel-2 samples, but lies within the range of microhardness of HAZ-1 (420 HV) and HAZ-2 (469 HV) regions of steel-1. Microhardness within the HAZ then decreases on moving from HAZ-2 toward the FZ, but is still significantly higher than the BM. Microhardness within the HAZ region can be affected by the fraction of fresh-martensite and/or M-A constituent and its composition (in particularly, its carbon content) [245, 246], prior austenite grain size in the HAZs, which in turn controls the size of martensite sub-grain boundaries [247]. In the present study, we obtained significant variations in the C content of the Ni-rich regions analysed in the HAZs. In the Ni-rich regions in HAZ-2, we obtain 2.8 and 0.6 at. % C for nanotip-1 and nanotip-2 respectively. For HAZ-1, we obtained Ni-rich regions with C varying from 0.5-1 at. %. In 9 wt. % Ni cryogenic steels, Nippes et al.[230] reported refinement of grain size for the weld simulated sample to 1273 K (1000 ^{o}C) peak temperature, while severe grain coarsening was observed for the sample simulated to 1573 K (1300 ^{o}C) peak temperature. Thus, within the HAZ microstructures, there are significant variations in the C content of the M-A constituents and possibly in grain size, which can lead to the variations observed in the microhardness. *Gleeble* simulated HAZ microstructures, representative of actual HAZs are being investigated at Lehigh University, and will provide further insights into the role of above described microstructural variables.

6.5 Conclusions

1. Local chemical compositions of Ni-rich regions in the HAZ microstructures (representative of austenite compositions) are measured by site-specific APT, Figures 6.6 and 6.7. Martensite-start temperature calculations corresponding to these compositions predict that austenite (present at high temperatures) in the HAZs is susceptible to martensitic transformation upon cooling to room temperature, Table 6.3. Formation of fresh-martensite is the likely source of increase in microhardness in HAZ regions, Figure 6.3.

2. Co-located and mixed MC/M_2C-type carbides (M is Mo, Cr, V) are observed in the QT, QL and QLT-treated samples, where T and L refer to isothermal treatments at 863 K (590 ^oC) and 923 K (650 ^oC) respectively. Mixed carbides comprise of a M_2C carbide shell, while the core is the MC carbide, Figure 6.10. Since MC carbides are inherited from the as-quenched condition, Figure 6.8, it is inferred that nucleation of M_2C-type carbides is assisted by the MC carbides during tempering at these temperatures.

3. Significant increase in C concentration in the Ni-rich region in HAZ-2 as compared to the QLT-treated BM, Figure 6.6, provides an indirect evidence of the dissolution of M_2C-type carbides. However, re-precipitation of M_2C carbides is not observed in the APT reconstructions of the HAZ-2 region, Figure 6.11(c). Hence, increase in the microhardness in HAZs is not due to precipitation-strengthening from M_2C carbides.

Chapter 7

Suggestions for Future Work

Low-carbon 10 wt. % Ni steels have emerged as very promising alternatives to the widely used Naval HSLA-100 steels. Their composition and processing can be further optimized and their potential explored for various other applications. Several suggestions can be made based on this research on 10 wt. % Ni steels and are listed below.

1. If the intermediate quench between the L and T-steps of the QLT-treatment is eliminated, only 6 vol. % austenite results in the final microstructure, as opposed to the 18 vol. % austenite obtained for the optimally treated QLT sample (with an intermediate quenching step). This highlights the importance of fresh-martensite in austenite formation during the T-step. However, longer tempering times during the T-step (than 1 h) should be explored for the samples without an intermediate quench. Dilatometry, X-ray diffraction, and APT investigations of these samples (without the intermediate quench) will provide for interesting comparison with the optimally treated QLT sample and will be useful to gain further insights into the mechanism of austenite formation during the T-step.

2. In the QL-treated sample, we obtain 8 vol. % austenite at room temperature, which can be varied by the application of high-magnetic field cryogenic treatments, as had been illustrated previously for 4340 steels [92]. Investigating these samples after the T-step treatment will help to clarify the role of retained austenite from the L-step, in austenite formation during the T-step.

Present research indicated that austenite from L-step, serves as a nucleation template for austenite growth during the T-step.

3. Determination of M_s^{σ} temperature for QL and QLT-treated 10 wt. % Ni steels- M_s^{σ} temperature is an important parameter to determine austenite stability with respect to mechanically-induced martensitic transformation and is dependent on the stress-state [92]. Experimentally, M_s^{σ} temperature can be obtained for tension and compression using the single-specimen technique developed by Richman and Bolling [248], and can then be estimated for pure shear and crack-tip stress states [92]. Determination of stress-state dependence of the M_s^{σ} temperature will help in exploring and optimizing the use of 10 wt. % Ni steels for several other applications.

4. Experimental data obtained in the present study for the QL and QLT-treated 10 wt. % Ni steels (austenite composition, volume fraction, kinetics of formation), available mechanical testing data from the work of Zhang [6] in conjunction with future experimental determination of M_s^{σ} temperature and estimates of austenite size will provide a strong basis for future modeling to predict austenite stability during deformation, which is a function of composition, size, and stress state [94]. Computational tools can then be used to design variants of these steels for defined performance objectives.

5. Previous research on 9 wt. % Ni cryogenic steels and results from the present research indicate that martensite lath boundaries play an important role in austenite formation during intercritical treatments. It is not well understood whether M_2C carbides observed in the QL and QLT-treated samples play any significant role in austenite formation. Their number density ($\sim 2x10^{22}$ m^{-3})

and distribution, as observed from APT indicates that the L-step treatment at 650 ^{o}C for 20-30 min leads to the significant coarsening of these precipitates, which also suggests that QLT-treatment is not designed to utilize precipitation strengthening from these carbides. A multi-step heat treatment involving a first tempering step at ~ 500-550 ^{o}C for ~ 1 h followed by a second tempering step (without an intermediate quench) at ~ 620-650 ^{o}C for different aging times can be explored to investigate the potential of carbides as heterogeneous nucleation sites for intralath austenite precipitation [96].

6. Significant increase in carbon in the Ni-rich region in heat-affected-zone (HAZ)-2 was observed as compared to QLT-treated base metal, Figure 6.6, which provided an indirect evidence of dissolution of the M_2C-type carbides in these regions. Post weld tempering treatment at 500-550 ^{o}C for ~ 1 h and subsequent site-specific APT investigation of the HAZ-2 region (indicated in Figure 6.3) will provide a direct evidence of whether the dissolution of M_2C-type carbides occurred in the HAZ-2 region.

7. Distribution of Ni and Mn in the Ni-rich regions observed in the HAZs, Figure 6.6 (b, c) is similar to that observed in the QL-treated sample, Figure 5.5. The corresponding martensite-start temperature calculations revealed that austenite in these HAZ regions is not stable at room temperature, as is the case for the QL-treated samples. A post-weld heat treatment, like the T-step tempering (570-600 ^{o}C) step of the QLT-treatment can stabilize the austenite in the HAZs and should be investigated. Formation of thermally stable austenite at the expense of Ni-rich fresh martensite may also decrease the microhardness in the HAZs (after the single-pass weld cycle) and bring it closer to the base metal hardness, Figure 6.3.

References

[1] E.J. Czyryca, R.E. Link, R.J. Wong, D.A. Aylor, T.W. Montemarano, J.P. Gudas, "Development and Certification of HSLA-100 Steel for Naval Ship Construction", *Nav. Eng. J.* 102(3) (1990) 63-82.

[2] P.J. Konkol, K.M. Stefanick, G.S. Pike, "New Steel Shows Promise for Navy Ships", *Weld. J.* 90(2) (2011) 34-41.

[3] M.D. Mulholland, "Co-precipitation Kinetic Pathways in a Blast Resistant Steel for Naval Applications ", Ph.D. Thesis, Northwestern University, Evanston, IL, 2011.

[4] T.W. Montemarano, B.P. Sack, J.P. Gudas, "High strength low alloy steels in naval construction", *J. Ship Prod.* 2(3) (1986) 145-62.

[5] N.J. Wengrenovich, G.B. Olson, "Optimization of a TRIP Steel for Adiabatic Fragment Protection", *Materials Today: Proceedings* 2 (2015) S639-42.

[6] X.J. Zhang, "Microhardness characterisation in developing high strength, high toughness and superior ballistic resistance low carbon Ni steel", *Mater. Sci. Technol.* 28(7) (2013) 818-22.

[7] C. Revising, "Ford-Class Aircraft Carrier", Report No. GAO-15-22, United States Government Accountability Office, Washington, DC,, November 2014, pp. 45-46.

[8] R.P. Foley, M.E. Fine, "Microstructure and Property Investigation of Quenched and Tempered HSLA-100 Steel", *International Conference on Processing, Microstructure and Properties of Microalloyed and Other Modern High Strength Low Alloy Steels*, Warrendale, PA, 1991, pp. 315-330.

[9] E. Hornbogen, "Aging and plastic deformation of an Fe-0.9% Cu alloy", *Trans. ASM* 57 (1964) 120-32.

[10] C.S. Smith, E.W. Palmer, "The Precipitation Hardening of Copper Steels", *Trans. AIME* 104 (1933) 133-168.

[11] A.D. Wilson, E.G. Hamburg, D.J. Colvin, S.W. Thompson, G. Krauss, "Properties and microstructures of copper precipitation aged plate steels", *Microalloyed HSLA Steels*, ASM International, Metals Park, OH, 1988, pp. 259-75.

[12] S.K. Dhua, D. Mukerjee, D.S. Sarma, "Influence of tempering on the microstructure and mechanical properties of HSLA-100 steel plates", *Metall. Mater. Trans. A* 32(9) (2001) 2259-2270.

[13] M. Mujahid, A.K. Lis, C.I. Garcia, A.J. DeArdo, "HSLA-100 steels: influence of aging heat treatment on microstructure and properties", *Journal of materials Engineering and Performance* 7(2) (1998) 247-257.

[14] G.R. Speich, "Secondary Hardening Ultrahigh Strength Steels", in: G.B. Olson, M. Azrin, E.S. Wright (Eds.) *Innovations in Ultrahigh Strength Steel Technology*, Proc. 34th Sagamore Army Materials Research Conf., US Army Materials Technology Laboratory, Watertown, MA, 1990, pp. 89-110.

[15] G.R. Speich, D.S. Dabkowski, L.F. Porter, "Strength and toughness of Fe-10Ni alloys containing C, Cr, Mo, and Co", *Metall. Trans.* 4(1) (1973) 303-15.

[16] D. Isheim, R.P. Kolli, M.E. Fine, D.N. Seidman, "An atom-probe tomographic study of the temporal evolution of the nanostructure of Fe–Cu based high-strength low-carbon steels", *Scripta materialia* 55(1) (2006) 35-40.

[17] S. Vaynman, D. Isheim, R.P. Kolli, S.P. Bhat, D.N. Seidman, M.E. Fine, "High-strength low-carbon ferritic steel containing Cu-Fe-Ni-Al-Mn precipitates", *Metall. Mater. Trans. A* 39(2) (2008) 363-73.

[18] M.D. Mulholland, D.N. Seidman, "Nanoscale co-precipitation and mechanical properties of a high-strength low-carbon steel", *Acta Mater.* 59(5) (2011) 1881-97.

[19] B.L. Tiemens, A.K. Sachdev, R.K. Mishra, G.B. Olson, "Three-Dimensional (3-D) Atom Probe Tomography of a Cu-Precipitation-Strengthened, Ultrahigh-Strength Carburized Steel", *Metall. Mater. Trans. A* 43(10) (2012) 3626-3635.

[20] B. Gault, M.P. Moody, J.M. Cairney, S.P. Ringer, "Atom Probe Microscopy", Springer, NewYork, NY, 2012.

[21] T.F. Kelly, M.K. Miller, "Atom probe tomography", *Rev. Sci. Instrum.* 78(3) (2007) 031101.

[22] M.K. Miller, "Atom probe tomography-Analysis at the atomic level", Kluwer Academic/Plenum Publishers, New York, NY, 2000.

[23] D.N. Seidman, "Three-dimensional atom-probe tomography: advances and applications", *Annu. Rev. Mater. Res.* 37 (2007) 127-158.

[24] G.B. Olson, J.F. Mescall, M. Azrin, "Adiabatic deformation and strain localization", in: M.A. Meyers, L.E. Murr (Eds.), Shock waves and high-strain-rate phenomena in metals, Prenum Press, New York, 1981, pp. 221-47.

[25] J.F. Mescall, H. Rogers, "The role of Shear Instability in Ballistic Penetration", in: G.B. Olson, M. Azrin, E.S. Wright (Eds.) *Proc. 34th Sagamore Army Materials Research Conf.*, US Army Materials Technology Laboratory, Watertown, MA, 1990, pp. 287–313.

[26] J. Mescall, R. Papirno, "Spallation in cylinder-plate impact", *Experimental Mechanics* 14(7) (1974) 257-266.

[27] M.E. Backman, W. Goldsmith, "The mechanics of penetration of projectiles into targets", *Int. J. Eng. Sci.* 16(1) (1978) 1-99.

[28] C. Zener, J.H. Hollomon, "Effect of strain rate upon plastic flow of steel", *Journal of Applied physics* 15(1) (1944) 22-32.

[29] J.G. Cowie, M. Azrin, G.B. Olson, "Microvoid formation during shear deformation of ultrahigh strength steels", *Metallurgical and Materials Transactions A* 20(1) (1989) 143-153.

[30] V.F. Zackay, E.R. Parker, D. Fahr, R. Busch, "The enhancement of ductility in high-strength steels", *ASM Trans Quart* 60(2) (1967) 252-59.

[31] G.B. Olson, M. Azrin, "Transformation behavior of TRIP steels", *Metall. Trans. A* 9(5) (1978) 713-21.

[32] J.R. Patel, M. Cohen, "Criterion for the action of applied stress in the martensitic transformation", *Acta Metall.* 1(5) (1953) 531-38.

[33] P. Sadhukhan, "Computational design and analysis of high strength austenitic TRIP steels for blast protection applications ", Ph.D. Thesis, Northwestern University, Evanston, IL, 2008.

[34] Z.D. Feinberg, "Design and Optimization of an Austenitic TRIP Steel for Blast and Fragment Protection", Ph.D. Thesis, Northwestern University, Evanston, IL, 2012.

[35] A. Saha, "Systems Design of Ultra-tough High Strength Steels for blast-Resistant Naval Hull Application ", Ph.D. Thesis, Northwestern University, Evanston, Il, 2004.

[36] B.A. Graville, "Cold cracking in welds in HSLA steels", in: A.B. Rothwell, J.M. Gray (Eds.) *Proc. Int. Conf. on Welding of HSLA(Microalloyed) Structural Steels,*, ASM International, Metals Park, OH, 1978, pp. 85-101.

[37] T.L. Anderson, J.A. Hyatt, J.C. West, "The benefits of new high-strength low-alloy (HSLA) steels", *Weld. J.* 66(9) (1987) 21-26.

[38] L. Darken, H. Wriedt, "The solubility of copper in ferrite", *Trans Metall Soc AIME* 218(1) (1960) 30-36.

[39] M. Perez, F. Perrard, V. Massardier, X. Kleber, A. Deschamps, H. De Monestrol, P. Pareige, G. Covarel, "Low-temperature solubility of copper in iron: experimental study using

thermoelectric power, small angle X-ray scattering and tomographic atom probe", *Philosophical Magazine* 85(20) (2005) 2197-2210.

[40] C.S. Zener, "quoted by CS Smith", *Trans. AIME* 175 (1948) 15.

[41] T. Gladman, "On the theory of the effect of precipitate particles on grain growth in metals", *Proc. R. Soc. A* 294(1438) (1966) 298-309.

[42] L.J. Cuddy, J.C. Raley, "Austenite grain coarsening in microalloyed steels", *Metall. Trans. A* 14A(10) (1983) 1989-1995.

[43] A.H. Hunter, "An Atom Probe Tomographic Investigation of High-Strength, High-Toughness Precipitation Strengthened Steels for Naval Applications ", Ph.D. Thesis, Northwestern University, Evanston, IL, 2012.

[44] A. Saha, G.B. Olson, "Computer-aided design of transformation toughened blast resistant naval hull steels: Part I", *J. Comput. Aided Mater. Des.* 14(2) (2007) 177-200.

[45] R.C. Glenn, E. Hornbogen, "A metallographic study of precipitation of copper from alpha iron", *Trans. Metall. Soc. AIME* 218(6) (1960) 1064-70.

[46] S.R. Goodman, S.S. Brenner, J.R. Low, "An FIM-atom probe study of the precipitation of copper from lron-1.4 at. pct copper. Part I: Field-ion microscopy", *Metall. Trans.* 4(10) (1973) 2363-69.

[47] S. Pizzini, K.J. Roberts, W.J. Phythian, C.A. English, G.N. Greaves, "A fluorescence EXAFS study of the structure of copper-rich precipitates in Fe–Cu and Fe–Cu–Ni alloys", *Philos. Magn. Lett.* 61(4) (1990) 223-29.

[48] G.R. Speich, R.A. Oriani, "Rate of Coarsening of Copper Precipitate in an Alpha-Iron matrix", *Trans. Met. Soc. AIME* 233(4) (1965) 623-631.

[49] P. Othen, M. Jenkins, G. Smith, W. Phythian, "Transmission electron microscope investigations of the structure of copper precipitates in thermally-aged Fe—Cu and Fe—Cu—Ni", *Philosophical Magazine Letters* 64(6) (1991) 383-391.

[50] P. Othen, M. Jenkins, G. Smith, "High-resolution electron microscopy studies of the structure of Cu precipitates in α-Fe", *Philosophical magazine A* 70(1) (1994) 1-24.

[51] S.R. Goodman, S.S. Brenner, J.R. Low, "An FIM-atom probe study of the precipitation of copper from lron-1.4 at. pct copper. Part II: Atom probe analyses", *Metall. Trans.* 4(10) (1973) 2371-78.

[52] D. Isheim, M.S. Gagliano, M.E. Fine, D.N. Seidman, "Interfacial segregation at Cu-rich precipitates in a high-strength low-carbon steel studied on a sub-nanometer scale", *Acta Materialia* 54(3) (2006) 841-849.

[53] R.P. Kolli, D.N. Seidman, "The temporal evolution of the decomposition of a concentrated multicomponent Fe–Cu-based steel", *Acta Mater.* 56(9) (2008) 2073-88.

[54] F. Maury, N. Lorenzelli, C.H. De Novion, "Influence of Mn and Ni on Cu precipitation in dilute iron alloys during electron irradiation: A small-angle neutron scattering study", *J. Nucl. Mater.* 183(3) (1991) 217-20.

[55] K. Osamura, H. Okuda, K. Asano, M. Furusaka, K. Kishida, F. Kurosawa, R. Uemori, "SANS Study of Phase Decomposition in Fe-Cu Alloy with Ni and Mn Addition", *ISIJ Int.* 34(4) (1994) 346-54.

[56] F. Vurpillot, A. Bostel, D. Blavette, "Trajectory overlaps and local magnification in three-dimensional atom probe", *Appl. Phys. Lett.* 76(21) (2000) 3127-3129.

[57] F. Soisson, A. Barbu, G. Martin, "Monte Carlo simulations of copper precipitation in dilute iron-copper alloys during thermal ageing and under electron irradiation", *Acta Materialia* 44(9) (1996) 3789-3800.

[58] J.Z. Liu, A. Van De Walle, G. Ghosh, M. Asta, "Structure, energetics, and mechanical stability of Fe-Cu bcc alloys from first-principles calculations", *Physical Review B* 72(14) (2005) 144109.

[59] K.C. Russell, L. Brown, "A dispersion strengthening model based on differing elastic moduli applied to the iron-copper system", *Acta Metallurgica* 20(7) (1972) 969-974.

[60] T. Harry, D.J. Bacon, "Computer simulation of the core structure of the< 111> screw dislocation in α-iron containing copper precipitates:: I. structure in the matrix and a precipitate", *Acta materialia* 50(1) (2002) 195-208.

[61] T. Harry, D.J. Bacon, "Computer simulation of the core structure of the< 111> screw dislocation in α-iron containing copper precipitates: II. dislocation–precipitate interaction and the strengthening effect", *Acta materialia* 50(1) (2002) 209-222.

[62] J.S. Montgomery, G.B. Olson, "Kinematics of M_2C Carbide Precipitation", in: G.B. Olson, M. Azrin, E.S. Wright (Eds.) *Innovations in Ultrahigh Strength Steel Technology*, Proc. 34th Sagamore Army Materials Research Conf., US Army Materials Technology Laboratory, Watertown, MA, 1990, pp. 147-78.

[63] J.W. Cahn, "Nucleation on dislocations", *Acta Metallurgica* 5(3) (1957) 169-172.

[64] D.J. Dyson, S.R. Keown, D. Raynor, J.A. Whiteman, "The orientation relationship and growth direction of Mo< sub> 2</sub> C in ferrite", *Acta Metall.* 14(7) (1966) 867-875.

[65] D. Raynor, J.A. Whiteman, R.W.K. Honeycombe, "In-Situ Transformation of Fe3C to Mo2C in Iron-Molybdenum-Carbon Alloys", *J. Iron Steel Inst.* 204 (1966) 1114-1116.

[66] M. Tanino, T. Nishida, K. Aoki, "Orientation Relationship and Coherency between Mo2C and the Ferrite Matrix", *Iron Steel Inst J* 205(8) (1967).

[67] Y. Nagataki, J. Cohen, G. Olson, "X-ray line broadening analysis of coherent M {sub 2} C precipitation in Ni-Co secondary hardening steels", *In Advanced Materials for the 21 st Century: The 1999 Julia R. Weertman Symposium*, 1999, pp. 241-250.

[68] J.A. Liddle, G.D.W. Smith, G.B. Olson, "Alloy carbide precipitation in a high cobalt-nickel secondary hardening steel", *Le Journal de Physique Colloques* 47(C7) (1986) C7-223-C7-231.

[69] D.M. Davies, B. Ralph, "Field-ion microscopic study of quenched and tempered Fe-Mo-C", *J Iron Steel Inst.* 210(4) (1972) 262-66.

[70] R. Ayer, P.M. Machmeier, "Microstructural basis for the effect of chromium on the strength and toughness of AF1410-based high performance steels", *Metall. Mater. Trans. A* 27(9) (1996) 2510-2517.

[71] H. Morikawa, H. Komatsu, M. Tanino, "Effect of Chromium upon Coherency between M2C Precipitates and α-Iron Matrix in 0.1 C-10Ni-8Co-1Mo-Cr Steels", *J. Electron Microsc.* 22(1) (1973) 99-101.

[72] C. Campbell, G. Olson, "Systems design of high performance stainless steels I. Conceptual and computational design", *Journal of Computer-Aided Materials Design* 7(3) (2000) 145-170.

[73] J.S. Wang, M.D. Mulholland, G.B. Olson, D.N. Seidman, "Prediction of the yield strength of a secondary-hardening steel", *Acta Mater.* 61(13) (2013) 4939-52.

[74] J.P. Wise, "Systems design of advanced gear steels", Ph.D. Thesis, Northwestern University, Evanston, IL, 1998.

[75] W. Jolley, "Effect of manganese and nickel on impact properties of iron and iron-carbon alloys", *J. Iron Steel Inst.* 206(2) (1968) 170-73.

[76] W.C. Leslie, R.J. Sober, S.G. Babcock, S.J. Green, "Plastic Flow in Binary Substitutional Alloys of BCC Iron-Effects of Strain Rate, Temperature and Alloy Content", *ASM Trans Quart* 62(3) (1969) 690-710.

[77] B. Fultz, J.I. Kim, Y.H. Kim, H.J. Kim, G.O. Fior, J.W. Morris, "The stability of precipitated austenite and the toughness of 9Ni steel", *Metall. Trans. A* 16(12) (1985) 2237-49.

[78] J.I. Kim, C.K. Syn, J.W. Morris, "Microstructural sources of toughness in QLT-treated 5.5 Ni cryogenic steel", *Metall. Trans. A* 14(1) (1983) 93-103.

[79] C.K. Syn, B. Fultz, J.W. Morris, "Mechanical stability of retained austenite in tempered 9Ni steel", *Metallurgical Transactions A* 9(11) (1978) 1635-40.

[80] C.K. Syn, J.W. Morris, S. Jin, "Cryogenic fracture toughness of 9Ni steel enhanced through grain refinement", *Metallurgical Transactions A* 7(12) (1976) 1827-32.

[81] J.R. Strife, D.E. Passoja, "The effect of heat treatment on microstructure and cryogenic fracture properties in 5Ni and 9Ni steel", *Metallurgical Transactions A* 11(8) (1980) 1341-50.

[82] K.J. Kim, L.H. Schwartz, "On the effects of intercritical tempering on the impact energy of Fe-9Ni-0.1 C", *Mater. Sci. Eng.* 33(1) (1978) 5-20.

[83] J.I. Kim, H.J. Kim, J.W. Morris, "The role of the constituent phases in determining the low temperature toughness of 5.5 Ni cryogenic steel", *Metall. Trans. A* 15(12) (1984) 2213-19.

[84] B. Fultz, J.I. Kim, Y.H. Kim, J.W. Morris, "The chemical composition of precipitated austenite in 9Ni steel", *Metall. Trans. A* 17(6) (1986) 967-72.

[85] J.I. Kim, J.W. Morris, "The composition of precipitated austenite in 5.5 ni steel", *Metall. Trans. A* 12(11) (1981) 1957-63.

[86] J. Goldstein, R. Ogilvie, "A re-evaluation of the iron-rich portion of the Fe-Ni system(Alpha and gamma solubility limits in Fe-Ni phase diagram at temperatures above 500 degrees C, using quench-and-anneal and diffusion-couple techniques and electron probe microanalyzer)", *AIME, Transactions* 233 (1965) 2083-2087.

[87] R.W. Fonda, G. Spanos, "Effects of Cooling Rate on Transformations in a Fe-9 Pct Ni Steel", *Metall. Mater. Trans. A* 45(13) (2014) 5982-89.

[88] H.J. Kim, Y.H. Kim, J.W. Morris Jr, "Thermal Mechanisms of Grain and Packet Refinement in a Lath Martensitic Steel", *ISIJ international* 38(11) (1998) 1277-85.

[89] C. Marshall, R. Hehemann, A. Troiano, "The characteristics of 9% nickel low carbon steels", *Trans. ASM* 55 (1962) 135.

[90] J.W. Morris Jr, "On the ductile-brittle transition in lath martensitic steel", *ISIJ international* 51(10) (2011) 1569-1575.

[91] J.I. Kim, J.W. Morris, "On the scavenging effect of precipitated austenite in a low carbon Fe-5.5 Ni alloy", *Metall. Trans. A* 11(8) (1980) 1401-06.

[92] G.N. Haidemenopoulos, G.B. Olson, M. Cohen, K. Tsuzaki, "Transformation plasticity of retained austenite in stage-I tempered martensitic steels", *Scr. Metall.* 23(2) (1989) 207-212.

[93] G. Haidemenopoulos, M. Grujicic, G. Olson, M. Cohen, "Thermodynamics-based alloy design criteria for austenite stabilization and transformation toughening in the Fe-Ni-Co system", *Journal of Alloys and compounds* 220(1) (1995) 142-147.

[94] G.N. Haidemenopoulos, G.B. Olson, M. Cohen, "Dispersed-Phase Transformation Toughening in UltraHigh Strength Steels", in: G.B. Olson, M. Azrin, E.S. Wright (Eds.) *Innovations in Ultra-high Strength Steel Technology*,, Proc. 34th Sagamore Army Materials Research Conf., US Army Materials Technology Laboratory, Watertown, MA, 1990, pp. 549-93.

[95] G.N. Haidemenopoulos, "Dispersed-phase transformation toughening in ultrahigh-strength steels", Ph.D. Thesis, MIT, Cambridge, MA, 1988.

[96] H.E. Lippard, "Microanalytical investigations of transformation toughened Co-Ni steels", Ph.D. Thesis, MIT, Cambridge, MA, 1999.

[97] G.J. Fraley, "Principles of TRIP Steel Optimization for Passive Damping Applications", Ph.D. Thesis, Northwestern University, Evanston, IL, 2013.

[98] J.D. Farren, A.H. Hunter, J.N. Dupont, D.N. Seidman, C.V. Robino, E. Kozeschnik, "Microstructural Evolution and Mechanical Properties of Fusion Welds in an Iron-Copper-Based Multicomponent Steel", *Metall. Mater. Trans. A* 43(11) (2012) 4155-4170.

[99] M.E. Fine, S. Vaynman, D. Isheim, Y.W. Chung, S.P. Bhat, C.H. Hahin, "A New Paradigm for Designing High-Fracture-Energy Steels", *Metallurgical and Materials Transactions A* 41(13) (2010) 3318-3325.

[100] M.S. Gagliano, M.E. Fine, "Precipitation kinetics of niobium carbide and copper in a low carbon, chromium-free steel", *Calphad* 25(2) (2001) 207-216.

[101] M.S. Gagliano, M.E. Fine, "Characterization of the nucleation and growth behavior of copper precipitates in low-carbon steels", *Metallurgical and Materials Transactions A* 35(8) (2004) 2323-2329.

[102] A.H. Hunter, J.D. Farren, J.N. DuPont, D.N. Seidman, "An Atom-Probe Tomographic Study of Arc Welds in a Multi-Component High-Strength Low-Alloy Steel", *Metallurgical and Materials Transactions A* 44(4) (2013) 1741-1759.

[103] R.P. Kolli, Z. Mao, D.N. Seidman, D.T. Keane, "Identification of a $Ni_{0.5}(Al_{0.5-x}Mn_x)$ B2 phase at the heterophase interfaces of Cu-rich precipitates in an α-Fe matrix", *Applied Physics Letters* 91(24) (2007) 241903.

[104] R.P. Kolli, R.M. Wojes, S. Zaucha, D.N. Seidman, "A subnanoscale study of the nucleation, growth, and coarsening kinetics of Cu-rich precipitates in a multicomponent Fe–Cu based steel", *Int. J. Mater. Res.* 99(5) (2008) 513-527.

[105] S. Vaynman, M.E. Fine, S. Lee, H.D. Espinosa, "Effect of strain rate and temperature on mechanical properties and fracture mode of high strength precipitation hardened ferritic steels", *Scripta materialia* 55(4) (2006) 351-354.

[106] J.T. Bono, J.N. DuPont, D. Jain, S. Baik, D.N. Seidman, "Investigation of Strength Recovery in Welds of NUCu-140 Steel Through Multipass Welding and Isothermal Post-Weld Heat Treatments", *Metall. Mater. Trans. A* 46(11) (2015) 5158-5170.

[107] R.P. Kolli, D.N. Seidman, "Comparison of compositional and morphological atom-probe tomography analyses for a multicomponent Fe-Cu steel", *Microsc. Microanal.* 13(4) (2007) 272-284.

[108] G. Ghosh, G.B. Olson, "Precipitation of paraequilibrium cementite: Experiments, and thermodynamic and kinetic modeling", *Acta materialia* 50(8) (2002) 2099-2119.

[109] J.M. Hyde, "Computer modelling and analysis of microscale phase transformations", Ph.D. Thesis, University of Oxford, Oxford, UK, 1993.

[110] M.K. Miller, "Characterization of the early stages of phase separation by atom probe tomography", *MRS Proceedings* 580 (1999) 35-40.

[111] M.K. Miller, E.A. Kenik, "Atom probe tomography: A technique for nanoscale characterization", *Microscopy and Microanalysis* 10(03) (2004) 336-341.

[112] D. Vaumousse, A. Cerezo, P.J. Warren, "A procedure for quantification of precipitate microstructures from three-dimensional atom probe data", *Ultramicroscopy* 95 (2003) 215-221.

[113] M.D. Mulholland, D.N. Seidman, "Voltage-Pulsed and Laser-Pulsed Atom Probe Tomography of a Multiphase High-Strength Low-Carbon Steel", *Microscopy and Microanalysis* 17(06) (2011) 950-962.

[114] T.T. Tsong, "Field ion image formation", *Surface Science* 70(1) (1978) 211-233.

[115] S.W. Thompson, "Microstructural characterization of an as-quenched HSLA-100 plate steel via transmission electron microscopy", *Materials Characterization* 77 (2013) 89-98.

[116] R. Varughese, P.R. Howell, "The application of metallographic techniques to the study of the tempering of HSLA-100 steel", *Materials characterization* 30(4) (1993) 261-267.

[117] T. Inoue, S. Matsuda, Y. Okamura, K. Aoki, "The fracture of a low carbon tempered martensite", *Transactions of JIM* 11(1) (1970) 36-43.

[118] S. Morito, H. Tanaka, R. Konishi, T. Furuhara, T. Maki, "The morphology and crystallography of lath martensite in Fe-C alloys", *Acta Materialia* 51(6) (2003) 1789-1799.

[119] C. Wang, M. Wang, J. Shi, W. Hui, H. Dong, "Effect of microstructural refinement on the toughness of low carbon martensitic steel", *Scripta Materialia* 58(6) (2008) 492-495.

[120] J.P. Naylor, "The influence of the lath morphology on the yield stress and transition temperature of martensitic-bainitic steels", *Metallurgical Transactions A* 10(7) (1979) 861-873.

[121] A.N. Bhagat, S.K. Pabi, S. Ranganathan, O.N. Mohanty, "Aging behaviour in copper bearing high strength low alloy steels", *ISIJ international* 44(1) (2004) 115-122.

[122] U.S. Navy, "Base Materials for Critical Applications-Requirements for Low Alloy Steel Plate, Forgings, Castings, shapes,Bars and Heads of HY 80/100/130 and HSLA-80/100", in: N.S.S. Command (Ed.) NAVSEA Technical Publication T9074-BD-GIB-010/0300, 2002, p. 22.

[123] R.A. Farrar, P.L. Harrison, "Acicular ferrite in carbon-manganese weld metals: an overview", *Journal of materials science* 22(11) (1987) 3812-3820.

[124] D.J. Abson, R.J. Pargeter, "Factors influencing as-deposited strength, microstructure, and toughness of manual metal arc welds suitable for C-Mn steel fabrications", *International Metals Reviews* 31(1) (1986) 141-196.

[125] A.J. Allen, D. Gavillet, J.R. Weertman, "SANS and TEM studies of isothermal M< sub> 2</sub> C carbide precipitation in ultrahigh strength AF1410 steels", *Acta metallurgica et materialia* 41(6) (1993) 1869-1884.

[126] O.C. Hellman, J.A. Vandenbroucke, J. Rüsing, D. Isheim, D.N. Seidman, "Analysis of three-dimensional atom-probe data by the proximity histogram", *Microsc. Microanal.* 6(05) (2000) 437-44.

[127] J. Akré, F. Danoix, H. Leitner, P. Auger, "The morphology of secondary-hardening carbides in a martensitic steel at the peak hardness by 3DFIM", *Ultramicroscopy* 109(5) (2009) 518-523.

[128] K. Stiller, L.E. Svensson, P.R. Howell, W. Rong, H.O. Andren, G.L. Dunlop, "High resolution microanalytical study of precipitation in a powder metallurgical high speed steel", *Acta Metallurgica* 32(9) (1984) 1457-1467.

[129] G.M. Carinci, M.G. Hetherington, G.B. Olson, "M2C carbide precipitation in AF1410 steel", *Le Journal de Physique Colloques* 49(C6) (1988) C6-311-C6-316.

[130] I.M. Lifshitz, V.V. Slyozov, "The kinetics of precipitation from supersaturated solid solutions", *Journal of Physics and Chemistry of Solids* 19(1) (1961) 35-50.

[131] C. Wagner, "Theory of precipitate change by redissolution", *Z. Elektrochem* 65 (1961) 581-591.

[132] A. Umantsev, G.B. Olson, "Ostwald ripening in multicomponent alloys", *Scripta metallurgica et materialia* 29(8) (1993) 1135-1140.

[133] J. Weertman, "Dislocation Model of Low-Temperature Creep", *Journal of Applied Physics* 29(12) (1958) 1685-1689.

[134] M.E. Fine, A. Tongen, M.S. Gagliano, "Interaction of coherent nanoscale precipitates with screw dislocations to lower the Peierls stress in low carbon steels", *Electron Microscopy: Its Role in Materials Science*, The Mike Meshii Symp., J.R. Weertman, M.E. Fine, K. Faber, W. King, and P. Liaw, eds., TMS, Warrendale, PA, 2003, pp. 229-234.

[135] S.K. Das, S. Sivaprasad, S. Das, S. Chatterjee, S. Tarafder, "The effect of variation of microstructure on fracture mechanics parameters of HSLA-100 steel", *Materials Science and Engineering: A* 431(1) (2006) 68-79.

[136] L. Skoufari-Themistou, D.N. Crowther, B. Mintz, "Strength and impact behaviour of age hardenable copper containing steels", *Materials science and technology* 15(9) (1999) 1069-1079.

[137] G. Spanos, R.W. Fonda, R.A. Vandermeer, A. Matuszeski, "Microstructural changes in HSLA-100 steel thermally cycled to simulate the heat-affected zone during welding", *Metall. Mater. Trans. A* 26(12) (1995) 3277-93.

[138] B.L. Tiemens, A.K. Sachdev, G.B. Olson, "Cu-Precipitation Strengthening in Ultrahigh-Strength Carburizing Steels", *Metallurgical and Materials Transactions A* 43(10) (2012) 3615-3625.

[139] K. Stiller, M. Hättestrand, F. Danoix, "Precipitation in 9Ni–12Cr–2Cu maraging steels", *Acta materialia* 46(17) (1998) 6063-6073.

[140] B.S. Ku, J. Yu, "Effects of Cu addition on the creep rupture properties of a 12% Cr steel", *Scripta materialia* 45(2) (2001) 205-211.

[141] G.C. Hwang, S. Lee, J.Y. Yoo, W.Y. Choo, "Effect of direct quenching on microstructure and mechanical properties of copper-bearing high-strength alloy steels", *Materials Science and Engineering: A* 252(2) (1998) 256-268.

[142] E.A. Brandes, G.B. Brook, *Smithells metals reference book, 7th edn* (Butterworth-Heinemann Ltd., Oxford, 1992, Ch 13.).

[143] J.B. Yang, M. Enomoto, C. Zhang, "Modeling Cu precipitation in tempered martensitic steels", *Materials Science and Engineering: A* 422(1) (2006) 232-240.

[144] N. Maruyama, M. Sugiyama, T. Hara, H. Tamehiro, "Precipitation and phase transformation of copper particles in low alloy ferritic and martensitic steels", *Materials transactions-JIM* 40 (1999) 268-277.

[145] L.G. Kvidahl, "An improved high yield strength steel for shipbuilding", *Welding journal* 64 (1985) 42-48.

[146] E.J. Czyryca, "Advances in high strength steel technology for naval hull construction", *Key Eng. Mater.* 84 (1993) 491-520.

[147] D. Jain, D. Isheim, A.H. Hunter, D.N. Seidman, "Multicomponent High-Strength Low-Alloy Steel precipitation-strengthened by sub-nanometric Cu precipitates and M2C carbides", *Metall. Mater. Trans. A* 47(8) (2016) 3860-72.

[148] M. Shome, D.S. Sarma, O.P. Gupta, O.N. Mohanty, "Precipitate dissolution and grain growth in the heat affected zone of HSLA-100 steel", *ISIJ international* 43(9) (2003) 1431-37.

[149] G. Krauss, "Steels: processing, structure, and performance", ASM International, Metals Park, OH, 2005, 338-39.

[150] A. Saha, J. Jung, G.B. Olson, "Prototype evaluation of transformation toughened blast resistant naval hull steels: Part II", *J. Comput. Aided Mater. Des.* 14(2) (2007) 201-33.

[151] D. Raabe, S. Sandlöbes, J. Millán, D. Ponge, H. Assadi, M. Herbig, P.P. Choi, "Segregation engineering enables nanoscale martensite to austenite phase transformation at grain boundaries: A pathway to ductile martensite", *Acta Mater.* 61(16) (2013) 6132-52.

[152] R.C. Thomson, M.K. Miller, "Carbide precipitation in martensite during the early stages of tempering Cr-and Mo-containing low alloy steels", *Acta Mater.* 46(6) (1998) 2203-13.

[153] G.B. Olson, T.J. Kinkus, J.S. Montgomery, "APFIM study of multicomponent M2C carbide precipitation in AF1410 steel", *Surf Sci.* 246(1) (1991) 238-45.

[154] A. Afrouz, M.J. Collins, R. Pilkington, "Microstructural examination of 1Cr-0.5Mo steel during creep", *Metals Technology* 10(1) (1983) 461-63.

[155] B.D. Cullity, S.R. Stock, "Elements of X-ray Diffraction", 3rd ed., Prentice Hall, New Jersey, 2001.

[156] F.D. Geuser, W. Lefebvre, "Determination of matrix composition based on solute-solute nearest-neighbor distances in atom probe tomography", *Microsc. Res. Tech.* 74(3) (2011) 257-263.

[157] S. Morito, K. Oh-ishi, K. Hono, T. Ohba, "Carbon enrichment in retained austenite films in low carbon lath martensite steel", *ISIJ Int.* 51(7) (2011) 1200-02.

[158] L. Morsdorf, C.C. Tasan, D. Ponge, D. Raabe, "3D structural and atomic-scale analysis of lath martensite: Effect of the transformation sequence", *Acta Materialia* 95 (2015) 366-377.

[159] M.K. Miller, P.A. Beaven, G.D.W. Smith, "A study of the early stages of tempering of iron-carbon martensites by atom probe field ion microscopy", *Metall. Trans. A* 12(7) (1981) 1197-1204.

[160] C. Lerchbacher, S. Zinner, H. Leitner, "Atom probe study of the carbon distribution in a hardened martensitic hot-work tool steel X38CrMoV5-1", *Micron* 43(7) (2012) 818-26.

[161] B. Hutchinson, J. Hagström, O. Karlsson, D. Lindell, M. Tornberg, F. Lindberg, M. Thuvander, "Microstructures and hardness of as-quenched martensites (0.1–0.5% C)", *Acta Mater.* 59(14) (2011) 5845-58.

[162] G. Krauss, "Martensite in steel: strength and structure", *Mater. Sci. Eng. A* 273 (1999) 40-57.

[163] K.W. Andrews, "Empirical formulae for the calculation of some transformation temperatures", *J. Iron Steel Inst.* 203(7) (1965) 721-27.

[164] G.R. Speich, "Tempering of low-carbon martensite", *Trans. Met. Soc. AIME* 245(12) (1969) 2553-64.

[165] E. Bemont, E. Cadel, P. Maugis, D. Blavette, "Precipitation of niobium carbides in Fe–C–Nb steel", *Surf. Interface Anal.* 36(5-6) (2004) 585-88.

[166] R.P. Kolli, D.N. Seidman, "Co-precipitated and collocated carbides and Cu-rich precipitates in a Fe-Cu steel characterized by atom-probe tomography", *Microsc. Microanal.* 20(6) (2014) 1727-39.

[167] A.J. Breen, K.Y. Xie, M.P. Moody, B. Gault, H.W. Yen, C.C. Wong, J.M. Cairney, S.P. Ringer, "Resolving the Morphology of Niobium Carbonitride Nano-Precipitates in Steel Using Atom Probe Tomography", *Microsc. Microanal.* 20 (2014) 1100-10.

[168] K. Miyata, T. Kushida, T. Omura, Y. Komizo, "Coarsening kinetics of multicomponent MC-type carbides in high-strength low-alloy steels", *Metall. Mater. Trans. A* 34(8) (2003) 1565-1573.

[169] W. Sha, L. Chang, G.D.W. Smith, L. Cheng, E.J. Mittemeijer, "Some aspects of atom-probe analysis of Fe-C and Fe-N systems", *Surf. Sci.* 266(1) (1992) 416-23.

[170] J.K. Stanley, "The diffusion and solubility of carbon in alpha-iron", *Trans. AIME* 185(10) (1949) 752-61.

[171] V.T. Borisov, V.M. Golikov, G.V. Sherbedinskiy, "Diffusion of Molybdenum in Iron and an Iron-Molybedenum Alloy", *Phys. Met. Metallogr* 22 (1966) 175-76.

[172] C.J. Smithells, E.A. Brandes, G.B. Brook, "Smithells metals reference book", Butterworth-Heinemann, Oxford, 1992.

[173] A.W. Bowen, G.M. Leak, "Solute diffusion in alpha-and gamma-iron", *Metall.Trans.* 1(6) (1970) 1695-1700.

[174] R.J. Borg, D.Y.F. Lai, "Diffusion in α-Fe–Si Alloys", *J. Appl. Phys.* 41(13) (1970) 5193-5200.

[175] W. Song, J. von Appen, P. Choi, R. Dronskowski, D. Raabe, W. Bleck, "Atomic-scale investigation of ε and θ precipitates in bainite in 100Cr6 bearing steel by atom probe tomography and ab initio calculations", *Acta Mater.* 61(20) (2013) 7582-90.

[176] S.S. Babu, K. Hono, T. Sakurai, "Atom probe field ion microscopy study of the partitioning of substitutional elements during tempering of a low-alloy steel martensite", *Metall. Mater. Trans. A* 25(3) (1994) 499-508.

[177] L. Chang, G.D.W. Smith, "The silicon effect in the tempering of martensite in steels", *Le Journal de Physique Colloques* 45(C9) (1984) C9-397-C9-401.

[178] C. Zhu, X.Y. Xiong, A. Cerezo, R. Hardwicke, G. Krauss, G.D.W. Smith, "Three-dimensional atom probe characterization of alloy element partitioning in cementite during tempering of alloy steel", *Ultramicroscopy* 107(9) (2007) 808-12.

[179] M. Thuvander, J. Weidow, J. Angseryd, L.K.L. Falk, F. Liu, M. Sonestedt, K. Stiller, H.O. Andrén, "Quantitative atom probe analysis of carbides", *Ultramicroscopy* 111(6) (2011) 604-608.

[180] D.W. Saxey, "Correlated ion analysis and the interpretation of atom probe mass spectra", *Ultramicroscopy* 111(6) (2011) 473-479.

[181] W.S. Owen, "The effect of silicon on the kinetics of tempering", *Trans. ASM* 46 (1954) 812-29.

[182] H.K.D.H. Bhadeshia, D.V. Edmonds, "The bainite transformation in a silicon steel", *Metall. Trans. A* 10(7) (1979) 895-907.

[183] G. Miyamoto, J.C. Oh, K. Hono, T. Furuhara, T. Maki, "Effect of partitioning of Mn and Si on the growth kinetics of cementite in tempered Fe–0.6 mass% C martensite", *Acta Mater.* 55(15) (2007) 5027-38.

[184] J. Takahashi, K. Kawakami, Y. Kobayashi, "Quantitative analysis of carbon content in cementite in steel by atom probe tomography", *Ultramicroscopy* 111(8) (2011) 1233-38.

[185] F.R.N. Nabarro, "The strains produced by precipitation in alloys", *Proc. R. Soc. A* 175(963) (1940) 519-38.

[186] W. Rong, G.L. Dunlop, "The crystallography of secondary carbide precipitation in high speed steel", *Acta Metall.* 32(10) (1984) 1591-99.

[187] Y.N. Shi, P.M. Kelly, "The crystallography and morphology of Mo2C in ferrite", *J. Materi. Sci.* 37(10) (2002) 2077-85.

[188] M.E. Fine, J.Z. Liu, M.D. Asta, "An unsolved mystery: The composition of bcc Cu alloy precipitates in bcc Fe and steels", *Mater. Sci. Eng. A* 463(1) (2007) 271-74.

[189] M. Kapoor, D. Isheim, G. Ghosh, S. Vaynman, M.E. Fine, Y.W. Chung, "Aging characteristics and mechanical properties of 1600MPa body-centered cubic Cu and B2-NiAl precipitation-strengthened ferritic steel", *Acta Mater.* 73 (2014) 56-74.

[190] F. Liu, H.O. Andrén, "Effects of laser pulsing on analysis of steels by atom probe tomography", *Ultramicroscopy* 111(6) (2011) 633-41.

[191] H.F. Fischmeister, S. Karagöz, H.O. Andren, "An atom probe study of secondary hardening in high speed steels", *Acta Metall.* 36(4) (1988) 817-825.

[192] K. Stiller, L.E. Svensson, P.R. Howell, W. Rong, H.O. Andren, G.L. Dunlop, "High resolution microanalytical study of precipitation in a powder metallurgical high speed steel", *Acta Metall.* 32(9) (1984) 1457-67.

[193] M. Grujicic, "Design of precipitated austenite for dispersed-phase transformation toughening in high strength Co-Ni steels", *Mater. Sci. Eng. A* 128(2) (1990) 201-07.

[194] B.C. De Cooman, "Structure–properties relationship in TRIP steels containing carbide-free bainite", *Curr. Opin. Solid State Mater. Sci.* 8(3) (2004) 285-303.

[195] R. Kuziak, R. Kawalla, S. Waengler, "Advanced high strength steels for automotive industry", *Arch. Civ. Mech. Eng.* 8(2) (2008) 103-17.

[196] O. Matsumura, Y. Sakuma, H. Takechi, "Enhancement of elongation by retained austenite in intercritical annealed 0.4 C-1.5 Si-0.8 Mn steel", *Transactions of the Iron and Steel Institute of Japan* 27(7) (1987) 570-79.

[197] D.V. Edmonds, K. He, F.C. Rizzo, B.C. De Cooman, D.K. Matlock, J.G. Speer, "Quenching and partitioning martensite-A novel steel heat treatment", *Materials Science and Engineering: A* 438 (2006) 25-34.

[198] J. Speer, D.K. Matlock, B.C. De Cooman, J.G. Schroth, "Carbon partitioning into austenite after martensite transformation", *Acta materialia* 51(9) (2003) 2611-22.

[199] B. Sundman, B. Jansson, J.O. Andersson, "The thermo-calc databank system", *Calphad* 9(2) (1985) 153-90.

[200] J.O. Andersson, T. Helander, L. Höglund, P. Shi, B. Sundman, "Thermo-Calc & DICTRA, computational tools for materials science", *Calphad* 26(2) (2002) 273-312.

[201] A. Borgenstam, A. Engstrom, L. Hoglund, J. Agren, "DICTRA, a tool for simulation of diffusional transformations in alloys", *J Phase Equilib* 21(3) (2000) 269-80.

[202] D. Isheim, A.H. Hunter, X.J. Zhang, D.N. Seidman, "Nanoscale Analyses of High-Nickel Concentration Martensitic High-Strength Steels", *Metall. Mater. Trans. A* 44(7) (2013) 3046-59.

[203] S. Lee, S. Shin, M. Kwon, K. Lee, B.C. De Cooman, "Tensile Properties of Medium Mn Steel with a Bimodal UFG α+ γ and Coarse δ-Ferrite Microstructure", *Metall. Mater. Trans. A* 48(4) (2017) 1678-1700.

[204] C. Capdevila, F.G. Caballero, C.G.D. Andrés, "Determination of Ms temperature in steels: A Bayesian neural network model", *ISIJ international* 42(8) (2002) 894-902.

[205] M. Palumbo, "Thermodynamics of martensitic transformations in the framework of the CALPHAD approach", *Calphad* 32(4) (2008) 693-708.

[206] K. Ishida, "Calculation of the effect of alloying elements on the Ms temperature in steels", *J. Alloys Comp.* 220(1) (1995) 126-31.

[207] T. Sourmail, C. Garcia-Mateo, "Critical assessment of models for predicting the Ms temperature of steels", *Comput. Mater. Sci.* 34(4) (2005) 323-34.

[208] G. Ghosh, G.B. Olson, "Kinetics of FCC→ BCC heterogeneous martensitic nucleation—I. The critical driving force for athermal nucleation", *Acta Metall. Mater.* 42(10) (1994) 3361-70.

[209] G. Ghosh, G.B. Olson, "Kinetics of Fcc→ bcc heterogeneous martensitic nucleation—II. Thermal activation", *Acta Metall. Mater.* 42(10) (1994) 3371-79.

[210] G. Ghosh, G.B. Olson, "Computational thermodynamics and the kinetics of martensitic transformation", *J Phase Equilib* 22(3) (2001) 199-207.

[211] G.B. Olson, M. Cohen, "A general mechanism of martensitic nucleation: Part II. FCC→ BCC and other martensitic transformations", *Metall. Trans. A* 7(12) (1976) 1905-14.

[212] H.P. Klug, L.E. Alexander, "X-ray diffraction procedures", 2nd ed., John Wiley and Sons, New York, NY, 1974, 540.

[213] M.K. Miller, K.F. Russell, G.B. Thompson, "Strategies for fabricating atom probe specimens with a dual beam FIB", *Ultramicroscopy* 102(4) (2005) 287-98.

[214] R.L. Fleischer, "Substitutional solution hardening", *Acta metallurgica* 11(3) (1963) 203-09.

[215] R.L. Fleischer, "The strengthening of metals", Reinhold Publishing Corp., New York, NY, 1964.

[216] G. Ghosh, "kMART Database and its predecessors named MART, MART1, MART2, MART3, MART4, MART5", unpublished, Northwestern University, Evanston, IL, 2000.

[217] J. Ågren, "Computer simulations of the austenite/ferrite diffusional transformations in low alloyed steels", *Acta Metallurgica* 30(4) (1982) 841-51.

[218] O. Dmitrieva, D. Ponge, G. Inden, J. Millán, P. Choi, J. Sietsma, D. Raabe, "Chemical gradients across phase boundaries between martensite and austenite in steel studied by atom probe tomography and simulation", *Acta Mater.* 59(1) (2011) 364-74.

[219] H.K.D.H. Bhadeshia, R.W.K. Honeycombe, "Steels: Microstructure and Properties", Steels: Microstructure and Properties, Elsevier, Amsterdam, 2006, p. 96.

[220] K. Hirano, M. Cohen, B.L. Averbach, "Diffusion of nickel into iron", *Acta Metall.* 9(5) (1961) 440-45.

[221] S.J. Rothman, L.J. Nowicki, G.E. Murch, "Self-diffusion in austenitic Fe-Cr-Ni alloys", *J. Phys. F* 10(3) (1980) 383-98.

[222] G. Krauss, "Steels: processing, structure, and performance", ASM International, Materials Park, OH, 2005, 63.

[223] P. Payson, C.H. Savage, "Martensite reactions in alloy steels", *Trans. ASM* 33 (1944) 261-80.

[224] R.A. Grange, H.M. Stewart, "The temperature range of martensite formation", *Trans. AIME* 167 (1946) 467-501.

[225] A.E. Nehrenberg, "Phosphorus segregation in austenite in Ni–Cr steels", *Trans. AIME* 167 (1946) 494.

[226] W. Steven, A.G. Haynes, "The temperature of formation of martensite and bainite in low-alloy steels", *J. Iron Steel Inst.* 183(8) (1956) 349-59.

[227] F. Latourte, Z. Feinberg, L.F. Mori, G.B. Olson, H.D. Espinosa, "Shear and tensile plastic behavior of austenitic steel TRIP-120 compared with martensitic steel HSLA-100", *Int. J. Fract* 162(1) (2010) 187-204.

[228] D. Jain, D. Isheim, X.J. Zhang, G. Ghosh, D.N. Seidman, "Thermally Stable Ni-rich Austenite Formed Utilizing Multistep Intercritical Heat Treatment in a Low-Carbon 10 Wt Pct Ni Martensitic Steel", *Metall. Mater. Trans. A* (2017) 1-13.

[229] B. Fultz, J.W. Morris, "The mechanical stability of precipitated austenite in 9Ni steel", *Metall. Trans. A* 16(12) (1985) 2251-56.

[230] E.F. Nippes, J.P. Balaguer, "A study of the weld heat-affected zone toughness of 9% nickel steel", *Weld. J.* 65(9) (1986) 237.

[231] B. Senior, "A critical review of precipitation behaviour in 1Cr・ Mo・ V rotor steels", *Mater. Sci. Eng. A* 103(2) (1988) 263-271.

[232] H. Fischmeister, S. Karagöz, H. Andren, "An atom probe study of secondary hardening in high speed steels", *Acta Metall.* 36(4) (1988) 817-825.

[233] E. Cabrol, C. Bellot, P. Lamesle, D. Delagnes, E. Povoden-Karadeniz, "Experimental investigation and thermodynamic modeling of molybdenum and vanadium-containing carbide hardened iron-based alloys", *J. Alloys Compd.* 556 (2013) 203-209.

[234] M. Serna, J. Rossi, "MC complex carbide in AISI M2 high-speed steel", *Materials Letters* 63(8) (2009) 691-693.

[235] J. Janovec, A. Vyrostkova, M. Svoboda, "Influence of tempering temperature on stability of carbide phases in 2.6 Cr-0.7 Mo-0.3 V steel with various carbon content", *Metall. Mater. Trans. A* 25(2) (1994) 267-275.

[236] S. Karagöz, H. Fischmeister, H.-O. Andrén, C. Guang-Jun, "Microstructural changes during overtempering of high-speed steels", *Metall. Mater. Trans. A* 23(6) (1992) 1631-1640.

[237] W. Rong, H.-O. Andrén, H. Wisell, G. Dunlop, "The role of alloy composition in the precipitation behaviour of high speed steels", *Acta Metall. Mater.* 40(7) (1992) 1727-1738.

[238] J.H. Jang, C.H. Lee, Y.U. Heo, D.W. Suh, "Stability of (Ti, M) C (M= Nb, V, Mo and W) carbide in steels using first-principles calculations", *Acta Mater.* 60(1) (2012) 208-217.

[239] M. Shome, D. Sarma, O. Gupta, O. Mohanty, "Precipitate dissolution and grain growth in the heat affected zone of HSLA-100 steel", *ISIJ Int.* 43(9) (2003) 1431-1437.

[240] G. Olson, T. Kinkus, J. Montgomery, "APFIM study of multicomponent M 2 C carbide precipitation in AF1410 steel", *Surf. Sci.* 246(1) (1991) 238-245.

[241] D. Jain, D. Isheim, D.N. Seidman, "Carbon Redistribution and Carbide Precipitation in a High-Strength Low-Carbon HSLA-115 Steel Studied on a Nanoscale by Atom Probe Tomography", *Metall. Mater. Trans. A* 48(7) (2017) 3205–19.

[242] K. Williams, B. Wilshire, "Microstructural instability of 0.5 Cr・ 0.5 Mo・ 0.25 V creep-resistant steel during service at elevated temperatures", *Mater. Sci. Eng.* 47(2) (1981) 151-160.

[243] M.C. Murphy, G.D. Branch, "Microstructure, Creep, and Creep-Rupture Properties of Cr-Mo-V Steam-Turbine Casing Castings", *J. Iron Steel Inst.* 207(10) (1969) 1347-1364.

[244] J.I. Jang, Y. Yang, W. Kim, D. Kwon, "A study of fracture toughness and microstructures in the weld heat-affected zone of QLT-processed 9% Ni steel", Advances in Cryogenic Engineering Materials, Springer US, NewYork, 1998, pp. 41-48.

[245] J.I. Jang, J.B. Ju, B.W. Lee, D. Kwon, W.S. Kim, "Effects of microstructural change on fracture characteristics in coarse-grained heat-affected zones of QLT-processed 9% Ni steel", *Mater. Sci. Eng. A* 340(1) (2003) 68-79.

[246] J. Chen, Y. Kikuta, T. Araki, M. Yoneda, Y. Matsuda, "Micro-fracture behaviour induced by MA constituent (Island Martensite) in simulated welding heat affected zone of HT80 high strength low alloyed steel", *Acta Metall.* 32(10) (1984) 1779-1788.

[247] X. Yu, J.L. Caron, S. Babu, J.C. Lippold, D. Isheim, D.N. Seidman, "Characterization of microstructural strengthening in the heat-affected zone of a blast-resistant naval steel", *Acta Mater.* 58(17) (2010) 5596-5609.

[248] G. Bolling, R. Richman, "The plastic deformation-transformation of paramagnetic fcc Fe-Ni-C alloys", *Acta Metallurgica* 18(6) (1970) 673-681.

Appendix A

Investigation of Strength Recovery in Welds of NUCu-140 Steel Through Multipass Welding and Isothermal Post-Weld Heat Treatments

Abstract

NUCu-140 is a ferritic copper precipitation strengthened steel that is a candidate material for use in many naval and structural applications. Previous work has shown that the heat-affected zone (HAZ) and fusion zone (FZ) of NUCu-140 exhibit softening that is due to dissolution of the copper-rich precipitates. This study aims to recover the FZ and HAZ strength by re-precipitation of the copper-rich precipitates through either multiple weld passes or an isothermal post-weld heat treatment (PWHT). The potential use of multiple thermal cycles was investigated with HAZ simulations using a Gleeble thermo-mechanical simulator. The HAZ simulations represented two weld thermal cycles with different combinations of peak temperatures during the initial and secondary weld passes. To investigate the potential for a PWHT for strength recovery, gas tungsten arc weld (GTAW) samples were isothermally heated for various times and temperatures. Microhardness measurements revealed no strength recovery in the multipass HAZ samples. The time dependent precipitate characteristics were modeled under the HAZ thermal cycle conditions, and the results showed that the lack of strength recovery could be attributed to insufficient time for re-precipitation during the secondary weld pass. Conversely, full strength recovery in the HAZ was observed in the isothermally heat treated samples. Atom-probe tomography (APT) analysis correlated this strength recovery to re-precipitation of the copper-rich precipitates during the isothermal PWHT.

This study was performed in collaboration with Prof. John N. DuPont, Lehigh University. Details of the multipass weld cycles and MatCalc simulations are not described here and can be found in the associated article [1]. Below, a summary of this research with focus on atom-probe tomography (APT), performed at Northwestern University is provided. The composition of NuCu-140 steel investigated in this study is given in Table 1.

Table 1- Overall Composition of NUCu-140 Steel (wt. %), as measured by optical emission spectroscopy

Fe	**Al**	**C**	**Cu**	**Mn**	**Nb**	**Ni**	**Si**
Bal.	0.65	0.04	1.35	0.47	0.07	2.75	0.47

Figure 1 shows the microhardness traverse across a Gas Tungsten Arc weld sample in the as welded condition and spans the FZ, HAZ, and base metal. Local softening in the HAZ is observed as a result of the weld thermal cycle, which is consistent with previous work [2], where it was attributed to the dissolution of the copper-rich precipitates. The base metal has an average hardness of approximately 285 HV, while the HAZ exhibits a minimum in hardness of 215 HV. There is an increase in hardness closer to the fusion zone to levels approaching that of the base metal (270 HV). However, another drop in the microhardness is observed in the fusion zone to a level significantly below that of the base metal (240 HV). To better understand the microhardness trends, several regions were examined using light optical microscopy; these are indicated in Figure 1 (regions labeled FZ, HAZ 1, HAZ 2, HAZ 3, and base metal - BM). Figure 2 displays optical micrographs for each of the five regions. The BM and HAZ 1 region, each exhibit an equiaxed ferritic microstructure and there appears to be a slight increase in grain size in the HAZ 1 region.

The HAZ 2 region also appears to have an equiaxed ferritic structure, but with noticeably larger grains than the BM. This indicates that some grain coarsening has occurred. The HAZ 3 and FZ regions show a predominately acicular ferrite microstructure which forms from a combination of coarse prior austenite grains and high cooling rate in these regions as described in Farren et al. [2]. The grains in these regions also appear to be much larger than the other regions, which indicate significant grain coarsening.

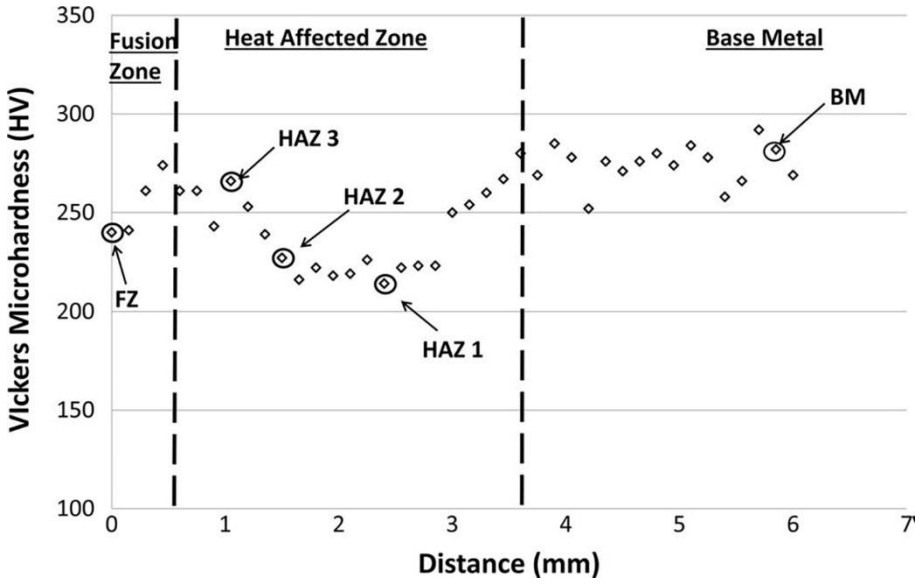

Figure 1- Vickers Microhardness traverse for the as-welded NUCu-140 Gas Tungsten Arc (GTA) weld sample [1].

Previous work has shown that the softening in the HAZ and FZ of NUCu-140 is due to dissolution of the copper-rich precipitates [2]. Dissolved precipitates can be re-precipitated with direct aging treatment after welding. This study explored if the strength in FZ and HAZ can be recovered by re-precipitation of the copper-rich precipitates through either multiple weld passes or an isothermal post-weld heat treatment (PWHT) without the need of a prior solutionizing treatment.

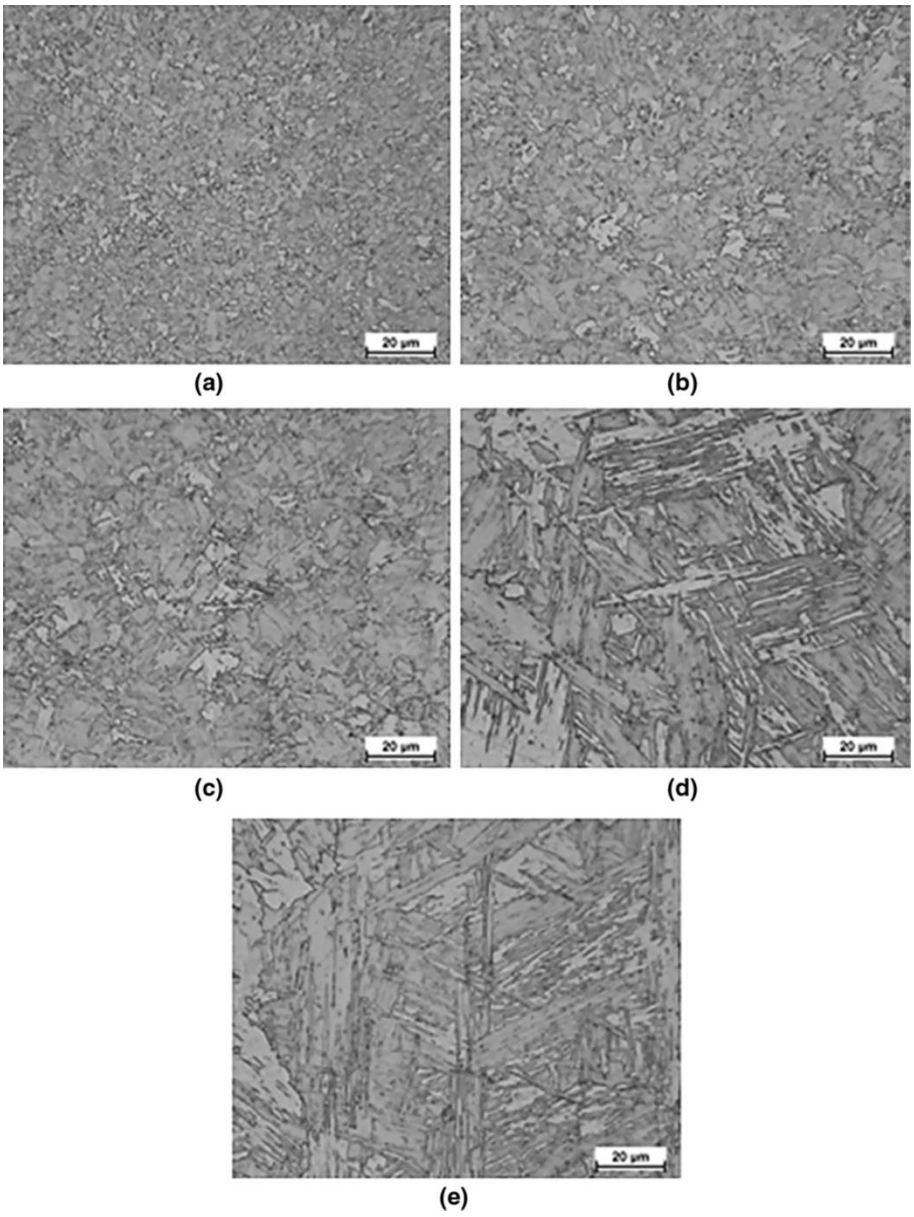

Figure 2- Optical micrographs showing the (a) BM; (b) HAZ 1; (c) HAZ 2; (d) HAZ 3; and (e) FZ regions in the as-welded NUCu-140 GTA weld sample at the locations marked in Figure 1 [1].

Multiple weld passes were not sufficient to reverse softening in the HAZ of NUCu-140 welds, where precipitation hardening is the primary source of strengthening [1]. This was attributed to the insufficient time during the second weld thermal cycle for re-precipitation.

PWHT at 773 K (500°C) for 1, 4, 10, and 16 h resulted in the increase in hardness in the HAZ to levels higher than that of the base metal and as-welded HAZ for all aging times, Figure 3(a). Also, there is no decrease in the base metal hardness after aging at 773 K (500°C) for up to 16 hours. These observations are significant because they indicate that aging at 773 K (500°C) for 1 h, or even possibly less time, is adequate for increasing the hardness of the HAZ without incurring any loss of hardness in the base metal. Figure 3(b) displays the microhardness curves for the samples aged at 823 K (550°C) for various times. The hardness in the HAZ increased after aging at 823 K (550°C) for the samples aged for 0.25 and 1 h. The increase in hardness in the HAZ is not as large compared to the samples aged at 823 K (500°C). The hardness in both the HAZ and the base metal decreases for the samples aged for longer than 1 h relative to the 0.25 and 1 h heat treatments.

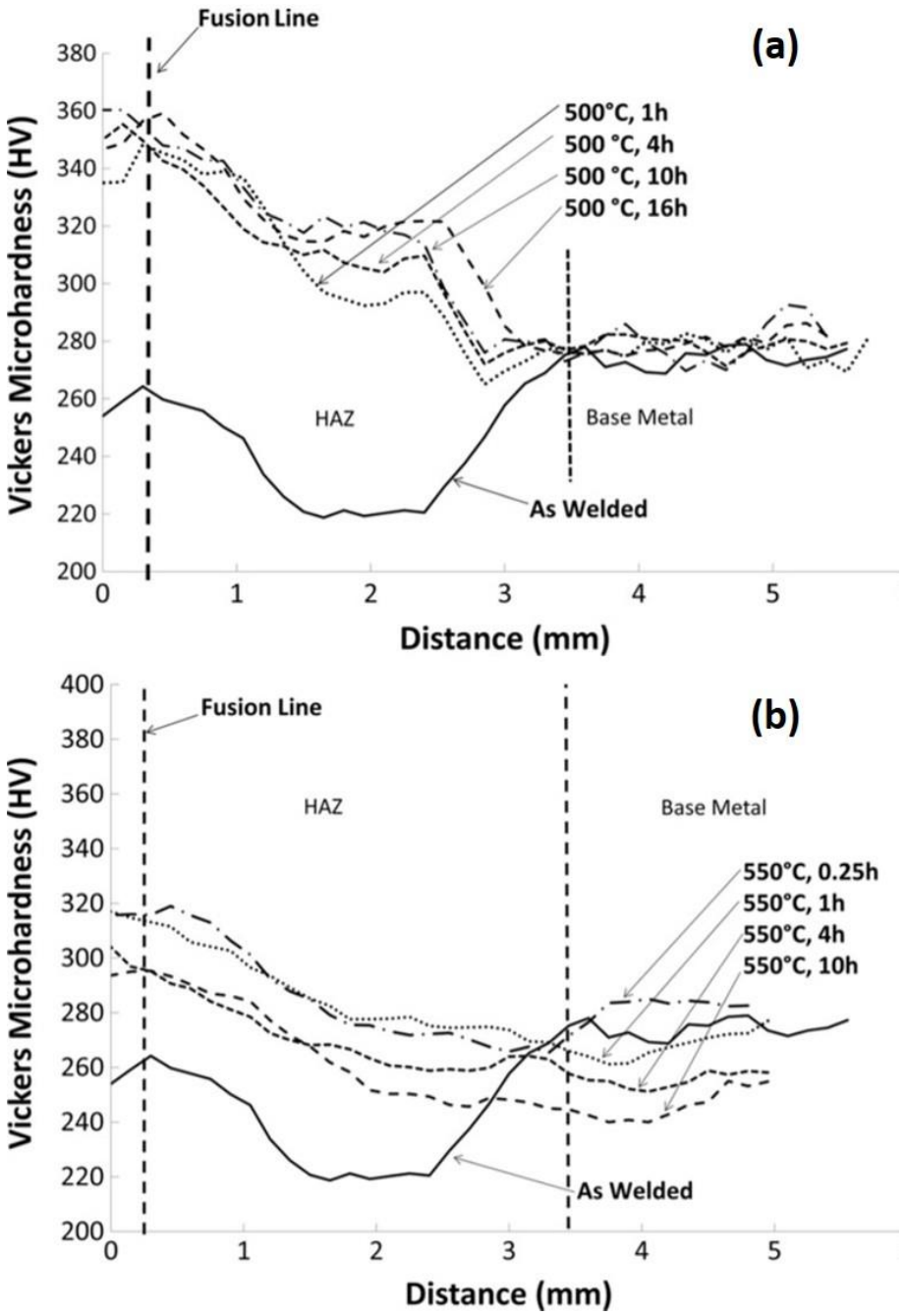

Figure 3- Microhardness traverses for the as-welded NUCu-140 GTA weld sample and for the NUCu-140 GTA weld sample aged at (a) 500°C for various aging times; (b) 550°C for various aging times [1].

3-D APT was utilized to study the evolution of Cu precipitates in the HAZ, FZ, and BM regions of the GTA welded sample and in the directly-aged sample, isothermally aged at 773 K (500°C) for 10 hours. Atom probe tips were prepared from the regions adjacent to the hardness indents indicated in Figure 4 for the as-welded sample and the directly aged sample. 3-D APT reconstructions for samples representing these regions are shown in Figure 5. Cu precipitates were not detected in the HAZ and FZ regions of the as welded sample, either by using envelope methodology or using isoconcentration surfaces. Re-precipitation of the Cu-precipitates occurred in the FZ and HAZ regions in the directly-aged sample, which was isothermally aged at 773 K (500°C) for 10 hours. These regions are represented as FZ 500 and HAZ 500 in Figure 4. A summary of Cu precipitates' statistics obtained in each region examined is displayed in Table 2. Note that the mean radius, $<R_v>$ is smaller and number density, N_V larger for Cu precipitates obtained in the directly aged samples in both regions, FZ 500 and HAZ 500 than the corresponding values in the as-welded base metal. This confirms that the local softening observed after the welding cycle in HAZ and FZ was predominantly due to the dissolution of Cu precipitates and not due to their coarsening. Further, we conclude that increase in hardness in regions closer to the fusion zone (for example, HAZ 3) as compared to HAZ 1, Figure 1 is due to the formation of acicular ferritic microstructure and not due to strengthening from Cu precipitates.

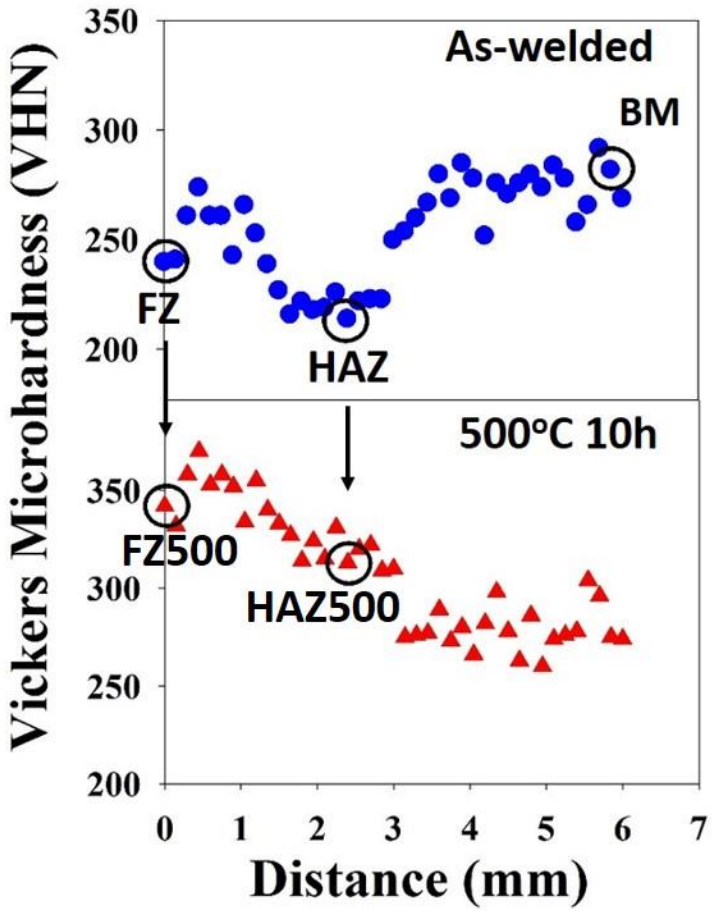

Figure 4- Vickers Microhardness traverse for the (a) as-welded NUCu-140 Gas Tungsten Arc (GTA) weld sample; (b) post weld sample aged for 10 h at 500 ºC. Nanotips for atom-probe tomography (APT) were prepared by extracting the lift-outs from regions adjacent to the microhardness indents encircled in the figure [1].

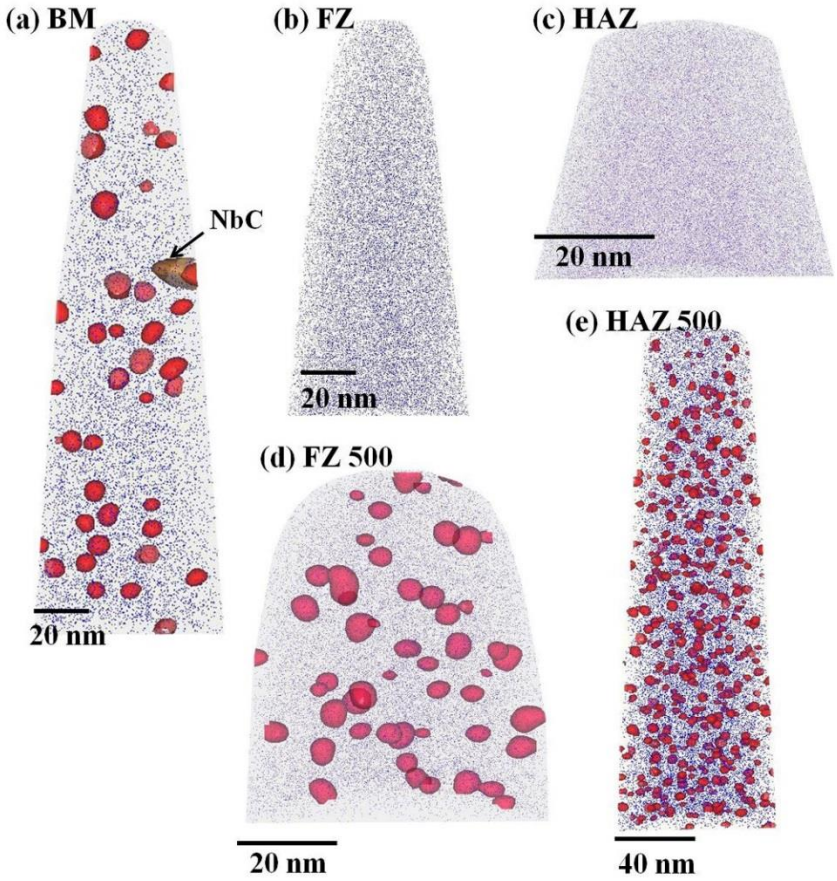

Figure 5- 3-D APT reconstructions of the NUCu-140 steel corresponding to the regions that represent (a) Base Metal (BM); (b) Fusion Zone (FZ); (c) Heat-Affected-Zone (HAZ); (d) FZ 500; and (e) HAZ 500. These regions are encircled in the microhardness traverses in Figure 4. NbC precipitate observed in the base metal is delineated by 3 at. % Nb isoconcentration surface (in brown). Cu precipitates are delineated by 10 at. % Cu isoconcentration surfaces (red). Fe atoms are shown in blue.

Table 2- Summary of Cu-precipitates' statistics obtained from APT for NUCu-140 in the as-welded condition and after directly aging at 500°C for 10 hours

Aging time (h)	$<R_v>$ nm	N_v (m^{-3})	Φ_v(%)
BM	3.39±1.13	$(9.62\pm1.47)*10^{22}$	2.04±0.31
HAZ	No precipitates observed		
FZ	No precipitates observed		
HAZ 500	2.40±0.68	$(4.62\pm0.16)*10^{23}$	3.32±0.12
FZ 500	2.26±0.78	$(3.68\pm0.34)*10^{23}$	2.39±0.22

The composition of the Cu-rich precipitates, their interfaces, and the surrounding matrix was obtained using proxigrams, which are obtained from 10 at. % Cu isoconcentration surfaces. Figure 6 shows the proxigram obtained from Cu precipitates in the as-welded BM, while Figure 7(a) and Figure 7(b) are obtained from Cu precipitates in the FZ 500 and HAZ 500 regions of the directly-aged samples respectively. Figure 6 reveals that segregation of Ni, Al, and Mn occurs at the precipitate/matrix interface of the Cu precipitates in the as-welded BM. The concentrations of these elements decrease significantly in the precipitate core, relative to their enriched concentrations at the interface. Figure 7 reveals that Cu precipitates in the directly aged samples in regions FZ 500 and HAZ 500 show similar degree of enrichment of these elements, both at the precipitate/matrix interface and in the precipitate core as compared to their concentrations in the Fe-matrix. The Cu precipitates in these regions contain significantly more Fe than the precipitates obtained in the as-welded BM. Silicon is observed to monotonically partition away from the Cu precipitates in both the BM and the directly-aged samples.

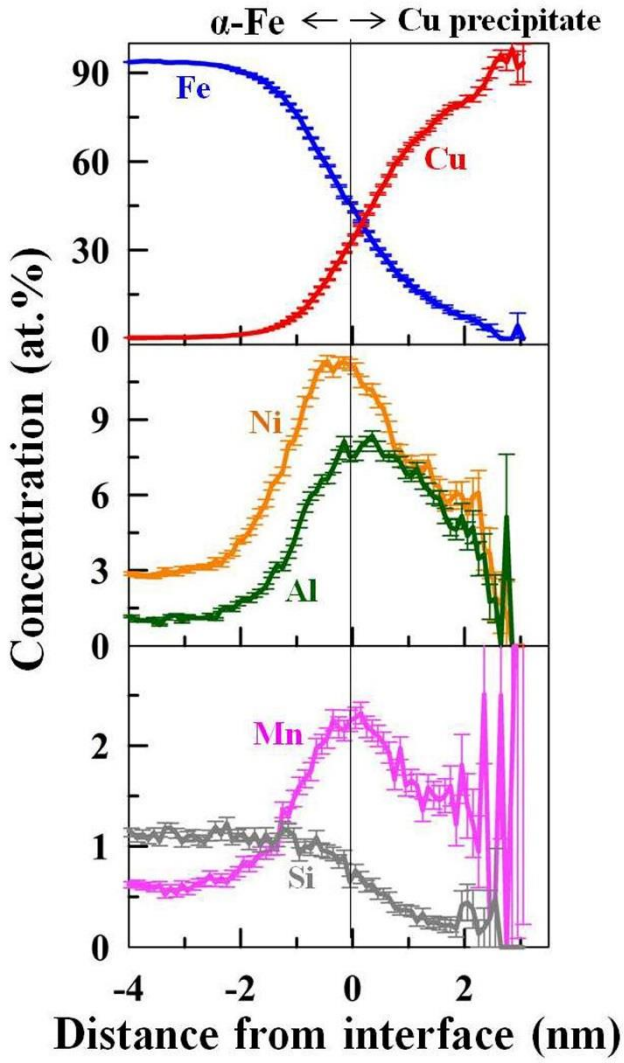

Figure 6- Proximity histogram concentration profiles of Fe, Cu, Ni, Al, Mn, and Si across the α-Fe/Cu precipitate interface, obtained from the Cu precipitates in the BM of the as-welded NUCu-140 GTA weld sample. The origin of the proxigram is taken as the inflection point of the Fe concentration profile.

The partitioning behavior of Ni, Al, and Mn between the Cu precipitates and the α-Fe matrix has been studied by several researchers using APT [3-6]. These studies have reported that small b.c.c. Cu precipitates contain significant amounts of Fe, Al, Mn, and Ni in their core and develop segregation of Ni, Al, and Mn at the precipitate/matrix interface, which lowers the interfacial

energy and hence the coarsening rate of the Cu precipitates. As the Cu precipitates increase in size, the precipitate core becomes richer in Cu, while the other elements, in particularly Fe and Al are rejected from the precipitate core. These findings are consistent with the results described above as Cu precipitates in the directly-aged sample in both HAZ 500 and FZ 500 regions are smaller in size than the Cu precipitates in the as-welded BM. It has also been established from previous research studies that the interfacial segregation of Ni, Al, and Mn eventually leads to the formation of an ordered B2 Ni(Al, Mn) phase at the Cu precipitate and Fe-matrix interface [7]. Wen et al. [6] reported that the coarsening rate of Cu precipitates in a Fe-Cu-Ni-Al alloy was two orders of magnitude lower as compared to in binary Fe-Cu alloys or ternary Fe-Cu-Ni alloys. They attributed slower coarsening of Cu precipitates in the Fe-Cu-Ni-Al alloy to the formation of thermally stable B2 NiAl shells around the Cu-rich core and the lower diffusivity of Cu in the intermetallic ordered-phase, which would inhibit its growth and coarsening. These shells are further reinforced with the addition of Mn and serve as an effective barrier to Cu diffusion. It is to be noted that the segregation of Ni, Al, and Mn at the interface of Cu rich precipitates in NuCu-140 steels is not uniform and that the Ni(Al, Mn) precipitates that form do not envelope the Cu rich precipitates completely [3]. Nevertheless, the reduction in interfacial energy caused by the segregation of these elements at the precipitate-matrix interface and the co-located Ni(Al,Mn) precipitates will likely impede the coarsening kinetics of Cu rich precipitates in NuCu-140. As a result, BM strength is not affected due to the PWHT at 773 K (500°C).

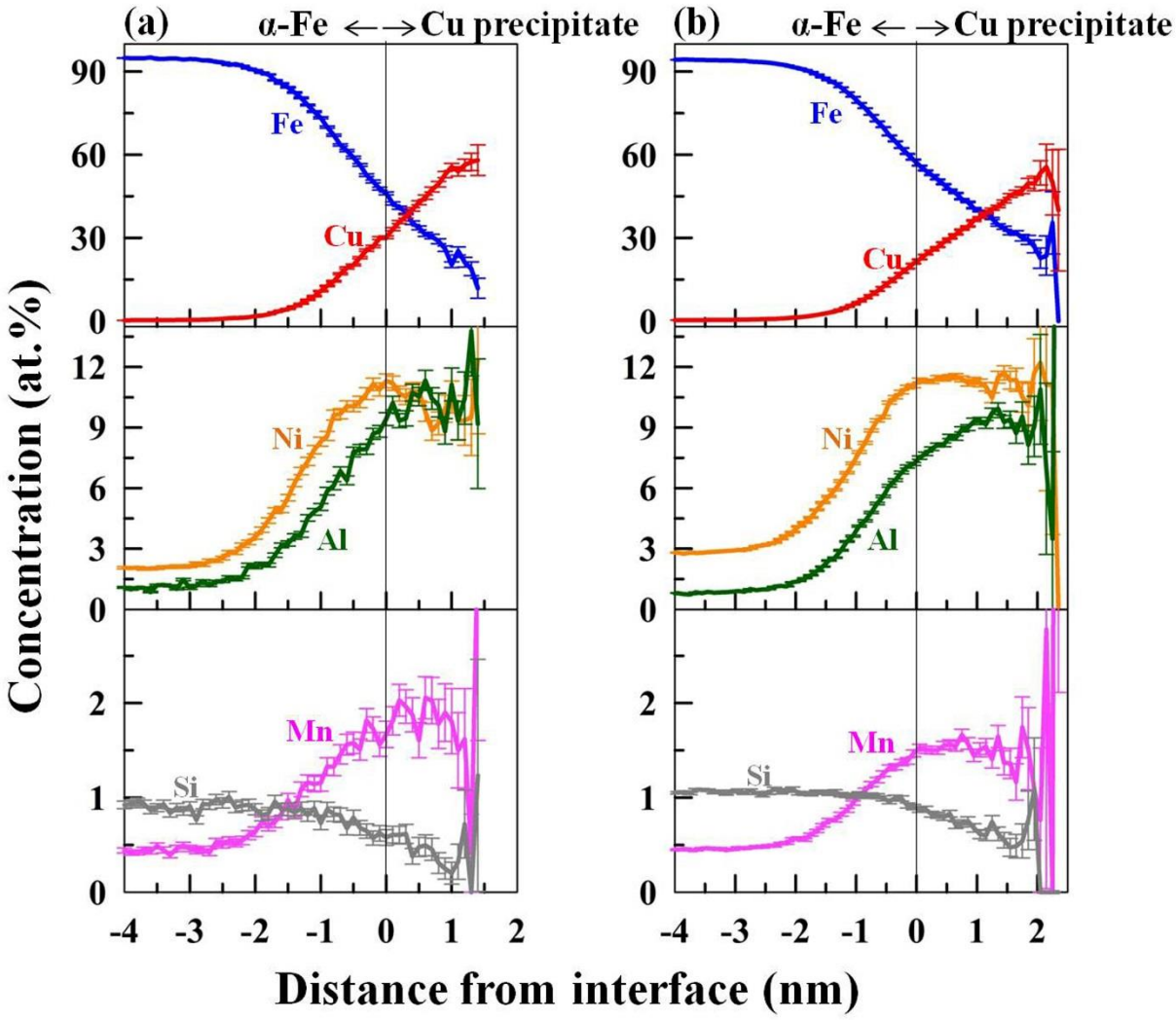

Figure 7- Proximity histogram concentration profiles of Fe, Cu, Ni, Al, Mn, and Si across the α-Fe/Cu precipitate interface, obtained from the Cu precipitates in the (a) FZ 500 and; (b) HAZ 500 regions of the NUCu-140 GTA weld sample that was directly aged for 10 hours at 500°C. The origin of the proxigrams is taken as the inflection point of the Fe concentration profile.

Conclusions

A study was conducted on hardness recovery and re-precipitation behavior of Cu precipitates in welds of NUCu-140 steel during multiple weld thermal cycles and isothermal aging treatments. The following conclusions can be drawn from this work:

1. Welds of NUCu-140 exhibit local softening in the fusion zone and heat-affected zone as a result of the fusion weld thermal cycle.

2. Multipass weld simulations did not produce an increase in hardness of the heat-affected zone after a high initial peak temperature followed by a lower secondary peak temperature. MatCalc simulations indicate that the time is too short to promote significant re-precipitation of the Cu-rich precipitates during the secondary weld thermal cycle.

3. Isothermal post-weld heat treatments of GTA welds at 773 and 823 K (500 and 550°C) demonstrated an increase in hardness of the fusion zone and heat-affected zone to levels above that of the base metal. Short aging times of 0.25 hour at 823 K (550°C) and 1 hour at 773 K (500°C) were adequate to increase the hardness of these zones to levels above that of the base metal.

4. The base metal hardness remains constant during the PWHT at 773 K (500°C) for aging times up to 16 hours, while there is a decrease in base metal hardness for the 823 K (550ºC) treatment at aging times greater than 1 hour. This is explained by MatCalc calculations, which reveal that Cu precipitates in the BM coarsen much faster during the PWHT at 823 K (550ºC) than at 773 K (500ºC).

5. APT results and MatCalc simulations demonstrated that the softening in the heat-affected zone of the NUCu-140 weld is the result of the dissolution of the Cu-rich precipitates during the heating portion of the weld thermal cycle followed by little or no re-precipitation upon cooling. The dissolution of Cu precipitates in these zones combined with their negligible coarsening at

aging temperature of 773 K (500°C) permits the use of a simple direct-aging treatment at 773 K (500°C) (without a prior solutionizing-quenching step) to recover the hardness in softened zones in NUCu140 without affecting the BM hardness.

References

[1] J.T. Bono, J.N. DuPont, D. Jain, S. Baik, D.N. Seidman, "Investigation of Strength Recovery in Welds of NUCu-140 Steel Through Multipass Welding and Isothermal Post-Weld Heat Treatments", *Metallurgical and Materials Transactions A* (2015) 1-13.

[2] J.D. Farren, A.H. Hunter, J.N. Dupont, D.N. Seidman, C.V. Robino, E. Kozeschnik, "Microstructural Evolution and Mechanical Properties of Fusion Welds in an Iron-Copper-Based Multicomponent Steel", *Metallurgical and Materials Transactions A* 43(11) (2012) 4155-4170.

[3] R.P. Kolli, D.N. Seidman, "The temporal evolution of the decomposition of a concentrated multicomponent Fe–Cu-based steel", *Acta Mater.* 56(9) (2008) 2073-88.

[4] D. Isheim, M.S. Gagliano, M.E. Fine, D.N. Seidman, "Interfacial segregation at Cu-rich precipitates in a high-strength low-carbon steel studied on a sub-nanometer scale", *Acta Materialia* 54(3) (2006) 841-849.

[5] M. Kapoor, D. Isheim, G. Ghosh, S. Vaynman, M.E. Fine, Y.W. Chung, "Aging characteristics and mechanical properties of 1600MPa body-centered cubic Cu and B2-NiAl precipitation-strengthened ferritic steel", *Acta Mater.* 73 (2014) 56-74.

[6] Y. Wen, Y. Li, A. Hirata, Y. Zhang, T. Fujita, T. Furuhara, C. Liu, A. Chiba, M. Chen, "Synergistic alloying effect on microstructural evolution and mechanical properties of Cu precipitation-strengthened ferritic alloys", *Acta Materialia* 61(20) (2013) 7726-7740.

[7] R.P. Kolli, Z. Mao, D.N. Seidman, D.T. Keane, "Identification of a $Ni_{0.5}(Al_{0.5-x}Mn_x)$ B2 phase at the heterophase interfaces of Cu-rich precipitates in an α-Fe matrix", *Applied Physics Letters* 91(24) (2007) 241903.